ROYAUME DU MAROC
Université Mohammed V - RABAT -
جامعة محمد الخامس – الرباط –
Faculté des sciences
كلية العلوم
CENTRE D'ETUDES DOCTORALES - SCIENCES ET TECHNOLOGIES

N° d'ordre : **4079**

THÈSE

en vue de l'obtention du : **DOCTORAT**

Centre de Recherche : **Sciences des Matériaux**
Structure de Recherche : **Matériaux, Nanotechnologies et Environnement**
Discipline : **physique - chimie**
Spécialité : **Science des matériaux et conversion de l'énergie**

Présentée et Soutenue le : *29 / 04 / 2025*

par :

Naoufal ENNOUHI

Doping and Alloying approaches for enhancing the properties of wide-band gap semi-transparent kesterite materials and their applications in next generation of kesterite/c-silicon tandem cells

Devant le JURY :

Mourad EL BELKACEMI	PES	FS, Université Mohammed V de Rabat	Président
Mohamed BENAISSA	PES	FS, Université Mohammed V de Rabat	Rapporteur
Abdelmajid AINANE	PES	FS, Université Moulay Ismail de Meknès	Rapporteur
Zineb EDFOUF	MCH	FS, Université Mohammed V de Rabat	Rapporteur
Hamid Ez-Zahraouy	PES	FS, Université Mohammed V de Rabat	Examinateur
Zouheir SEKKAT	PES	FS, Université Mohammed V de Rabat	Directeur de Thèse

Année Universitaire : 2024 - 25

✉ Faculté des Sciences, avenue Ibn Battouta, BP. 1014 RP, Rabat –Maroc
☎ 00212(0) 37 77 18 76 🖷 00212(0) 37 77 42 61 ; http://www.fsr.ac.ma

Acknowledgments

The work presented in this dissertation is the result of international collaboration between the **Laboratory of Materials, Nanotechnology, and Environment** at Mohammed V University in Rabat (UM5R), **Optics and Photonics center** at the Moroccan Foundation for Advanced Science, Innovation, and Research (MAScIR), and the **Laboratory of Solar Energy Materials and Systems** at the Catalonia Institute for Energy Research in Barcelona (IREC). I am deeply grateful for the financial support provided by the **INFINITE CELL project (H2020-MSCA-RISE-2017 777968)** from the European Commission, the **PPR/2015/59 project** funded by the Moroccan Ministry of Higher Education and Research, and the **INNOVX collaboration**. This thesis was supervised by **Professor Zouheir SEKKAT**, to whom I owe a great debt of gratitude.

As I write this note of gratitude, marking the conclusion of my thesis, I reflect on a period of intense learning and growth scientifically and personally. I extend my deepest thanks to all those who have supported and guided me throughout this journey.

First and foremost, my heartfelt gratitude goes to my thesis director, **Professor Zouheir SEKKAT**, PES at the Faculty of Sciences, Mohammed V University. His recommendation of an engaging research topic, unwavering support, and provision of scholarships through various projects and exchanges were instrumental in shaping this work. His patience, invaluable guidance, constructive criticism, and availability were pivotal to the completion of this thesis. I sincerely thank him for his expertise, kindness, and mentorship.

I wish to express my deep gratitude to the jury members who kindly agreed to evaluate this work. First, I would like to extend special thanks to Professor **Mourad EL BELKACEMI** (PES at the Faculty of Sciences, Mohammed V University) for honoring me by presiding over my thesis defense committee. I also offer my sincere thanks to Professor **Abdelmajid AINANE** (PES at the Faculty of Sciences, Université Moulay Ismail de Meknès) for his thorough review of this manuscript, along with his valuable feedback and guidance. My appreciation goes equally to Professor **Mohamed BENAISSA** (PES at the Faculty of Sciences, Mohammed V University) for his generous time, expert input, and constructive remarks. I am also grateful to Professor **Zineb EDFOUF** (MCH at the Faculty of Sciences, Mohammed V University) for her

willingness to review this work and provide detailed comments and suggestions. Finally, I wish to thank Professor **Hamid EZ-ZAHRAOUY** (PES at the Faculty of Sciences, Mohammed V University) for examining this thesis and offering invaluable observations and insights.

I extend my sincere gratitude to my professors at the **Faculty of Sciences** for their unwavering support and guidance throughout my **bachelor's and master's programs**, which laid the foundation for my academic and research journey.

To my colleagues and friends from the **SEMS group (Solar Energy Materials and Systems)** in Spain, I am truly grateful for your hospitality, discussions scientific and otherwise and your unconditional support during my time at IREC. Your assistance and collaboration were invaluable.

I would also like to thank the **MAScIR Foundation** for providing a conducive working environment, access to state-of-the-art facilities, and strong leadership that contributed to the success of this work. I deeply appreciate the support and guidance offered by the MAScIR platform staff during my stay, as well as the continuous support from the MAScIR administration, which ensured the smooth progression of my Ph.D. project.

I would like to take this opportunity to express my gratitude to the **CeDoc administration staff**. Their efficient and supportive administrative facilities were instrumental in ensuring the smooth progression of my work, without which this dissertation would not have been possible.

My heartfelt appreciation also extends to my colleagues from the **Optics and Photonics Center**: **Dr. Siham Refki**, **Dr. Imane Hammidine**, **Dr. Ben Afkir Nourdine**, and **Mr. Abdeljalile**, **Mme. Amine badir** Your support, collaboration, and encouragement throughout this journey have been invaluable, and I am truly grateful for your contributions.

Dedication

This work is dedicated to the most important people in my life, without whom this journey would not have been possible. To my **mother**, **father**, and **sisters Fatna, Youssra, Hidaya**, as well as my entire **extended ENNOUHI family (my uncles, and cousins),** I express my deepest gratitude. Thank you for your **unwavering support**, unconditional love, and countless sacrifices. Your tireless efforts to provide me with everything I needed, your encouragement during difficult times, and your belief in my abilities have been the foundation of my success. It is because of you that I stand here today, defending the fruit of your endless support and motivation.

I also extend my heartfelt thanks to my **friends**, who have been by my side throughout this journey. Your kindness, encouragement, and camaraderie have been invaluable, providing both strength and joy during this challenging yet rewarding path. Each of you has played a unique role in my life, and I deeply appreciate the laughter, shared struggles, and moments of celebration we've experienced together.

Detailed Abstract

This thesis contributes to the development of low-cost, high-performing kesterite materials as a viable option for future photovoltaic integration and the creation of large-bandgap materials for next-generation tandem solar cells. Building on previous studies and recent advancements in photovoltaic technology, this work proposes and develops innovative approaches and strategies to produce high-quality kesterite materials. These efforts aim to address the challenges limiting the efficiency of kesterite-based solar cells and pave the way for their integration into advanced photovoltaic architectures. The optimization of the sol-gel method formed the foundation of this work, enabling the preparation of kesterite materials on transparent electrodes. This involved careful control over all stages of the process, including solution preparation, deposition, and annealing conditions. The oxidation states of metal ions in the sol-gel solution were monitored to understand their effects on kesterite properties. Two distinct protocols were developed through this optimization, resulting in absorber layers with improved structural, morphological, and optoelectronic properties. Building upon these optimized protocols, we investigated alkali-metal doping (e.g., Na, Li, K) to further enhance material properties. This work introduced a novel approach for incorporating alkali metals during the deposition process. These innovative doping techniques demonstrated significant improvements in the morphological and structural properties of kesterite materials, thereby advancing their potential for photovoltaic applications. Further, cation substitution was explored, with a particular focus on substituting copper (Cu) with silver (Ag). The combination of silver alloying and sodium doping proved particularly effective, yielding high-quality kesterite materials with properties that approach the requirements for high-efficiency devices. To evaluate the potential of these materials in advanced tandem solar cell configurations, optical (FDTD) and electrical (SCAPS-1D) simulations were employed. These simulations examined the integration of kesterite materials with crystalline silicon (c-Si) in tandem architectures, achieving efficiencies exceeding 20% after optimization. This demonstrated the feasibility of kesterite materials in tandem cells, reinforcing their role as a promising candidate for next-generation photovoltaic technologies. Finally, the thesis extended its scope to the development of wide bandgap kesterite materials by completely substituting tin (Sn) with Germanium (Ge). Using physical vapor deposition (PVD) methods such as sputtering, a novel single-step sulfo-

selenization process was developed to achieve a bandgap exceeding 1.7 eV, essential for high-efficiency tandem cells. These materials achieved efficiencies comparable to the best-reported values, validating the effectiveness of this innovative synthesis approach.

In summary, this thesis underscores the importance of doping, alloying, and advanced synthesis techniques in optimizing kesterite materials. It bridges the gap between fundamental material development and their application in high-performance photovoltaic devices. By addressing critical challenges and proposing future research directions, this work contributes to positioning kesterite materials as a viable option for large-scale renewable energy production, with the potential to play a significant role in the global transition to sustainable energy.

Résumé

Cette thèse contribue au développement de matériaux à base de kesterite à faible coût et haute performance, en tant qu'option viable pour une intégration photovoltaïque future, ainsi qu'à la création de matériaux à large bande interdite pour les cellules solaires tandem de nouvelle génération. S'appuyant sur des études précédentes et les récents progrès dans la technologie photovoltaïque, ce travail propose et développe des approches et des stratégies innovantes pour produire des matériaux de kesterite de haute qualité. Ces efforts visent à relever les défis limitant l'efficacité des cellules solaires à base de kesterite et à ouvrir la voie à leur intégration dans des architectures photovoltaïques avancées. L'optimisation de la méthode sol-gel a constitué la base de ce travail, permettant la préparation de matériaux à base de kesterite sur des électrodes transparentes. Cela a impliqué un contrôle minutieux de toutes les étapes du processus, y compris la préparation de la solution, le dépôt et les conditions de recuit. Les états d'oxydation des ions métalliques dans la solution sol-gel ont été rigoureusement suivis afin de comprendre leurs effets sur les propriétés de la kesterite. Deux protocoles distincts ont été développés grâce à cette optimisation, conduisant à des couches absorbantes aux propriétés structurales, morphologiques et optoélectroniques améliorées.

En s'appuyant sur ces protocoles optimisés, nous avons étudié le dopage aux métaux alcalins (par exemple, Na, Li, K) pour améliorer davantage les propriétés des matériaux. Ce travail a introduit une approche novatrice pour incorporer les métaux alcalins au cours du processus de dépôt, une méthode non rapportée dans la littérature. Ces techniques de dopage innovantes ont montré des améliorations significatives des propriétés morphologiques et structurales des matériaux de kesterite, renforçant ainsi leur potentiel pour les applications photovoltaïques. Par ailleurs, la substitution des cations a été explorée, avec un accent particulier sur la substitution du cuivre par l'argent. La combinaison de l'alliage d'argent et du dopage au sodium s'est avérée particulièrement efficace, produisant des matériaux de kesterite de haute qualité avec des propriétés proches des exigences des dispositifs à haute efficacité.

Pour évaluer le potentiel de ces matériaux dans des configurations de cellules solaires avancées, des simulations optiques (TMM, FDTD) et électriques (SCAPS-1D) ont été employées. Ces

simulations ont examiné l'intégration des matériaux de kesterite avec le silicium cristallin (c-Si) dans des architectures tandem, atteignant des efficacités supérieures à 20% après optimisation. Cela a démontré la faisabilité des matériaux de kesterite dans les cellules tandem, renforçant leur rôle en tant que candidat prometteur pour les technologies photovoltaïques de nouvelle génération.

Enfin, la thèse a élargi son champ d'application au développement de matériaux de kesterite à large bande interdite en substituant complètement l'étain (Sn) par le germanium (Ge). En utilisant des méthodes de dépôt physique en phase vapeur (PVD), telles que la pulvérisation cathodique, un procédé innovant de sulfo-sélénisation en une seule étape a été développé pour atteindre une bande interdite supérieure à 1,7 eV, essentielle pour les cellules tandem à haute efficacité. Ces matériaux ont atteint des efficacités comparables aux meilleures valeurs rapportées, validant l'efficacité de cette approche de synthèse novatrice.

En résumé, cette thèse souligne l'importance du dopage, de l'alliage et des techniques avancées de synthèse pour optimiser les matériaux de kesterite. Elle comble le fossé entre le développement fondamental des matériaux et leur application dans des dispositifs photovoltaïques haute performance. En relevant des défis critiques et en proposant des orientations futures pour la recherche, ce travail contribue à positionner les matériaux de kesterite comme une option viable pour une production d'énergie renouvelable à grande échelle, avec le potentiel de jouer un rôle majeur dans la transition mondiale vers une énergie durable.

List of acronyms and abbreviations

1.5AM	Air Mass 1.5 Global	**ETL**	Electron Transporting Layer
BHJ	Bulk Heterojunction	**HTL**	Hole Transporting Layer
CB	Conduction Band	**eV**	Electron volt
DSSCs	Dye-Sensitized Solar Cells	**FF**	Fill Factor
Ea	Activation Energy	**IPCE**	Incident Photon Conversion Efficiency
EA	Electron Affinity	**JSC**	Short-circuit Current
Eg	Band gap energy	**PCE**	Power Conversion Efficiency
EQE	External Quantum Efficiency	**PL**	Photoluminescence
JSC	Short-circuit Current	**VOC**	Open-circuit Voltage
PCE	Power Conversion Efficiency	**PV**	Photovoltaic
SEM	Scanning Electron Microscopy	**UV-Vis**	Ultraviolet-visible
VB	Valence Band	**VOC**	Open-circuit Voltage
p-Si	polycrystalline silicon	**GaAs**	**:** Gallium Arsenide
a-Si	amorphous silicon	**CIS**	Copper Indium Selenide
CIGS	Copper Indium Gallium Selenide	**CZTS**	Cu2ZnSnS4

CZTSe	Cu2ZnSnSe4	**CdTe**	Cadmium Telluride

List of co-authored publications

- **Silver and Sodium incorporation into wide bandgap CZTS absorbers on transparent back electrodes and their application in kesterite/c-silicon tandem solar cells: experiments and simulations.** *(Solar Energy (Q1); Accepted)*

  Naoufal Ennouhi, Yassine Chouimi, Nourdine belafkir , Abdeljalile Er-rfyg, Sanaa Ammari2, Massaab El Ydrissi, and Zouheir Sekkat

- **Feasibility of exceeding 20% efficiency for kesterite/c-Silicon tandem solar cells using an alternative buffer layer: optical and electrical analysis** *(Nanomaterials;Accepted, Q1)*

  Naoufal Ennouhi, Safae Aazou, Abdeljalile Er-rafyg, Zakaria Laghfour, Zouheir Sekkat

- **Influence of Copper and Tin Oxidation States on the Phase Evolution of Solution-Processed Ag-Alloyed CZTS Photovoltaic Absorbers** *(Energies (Q1) Accepted)*

  Abdeljalile ER-rfyg, **Naoufal Ennouhi**, Yassine Chouimi and Zouheir Sekkat

- **A simple and efficient strategy for incorporating alkali metals into sol-gel processed-ACZTS photovoltaic absorbers: the case of sodium and lithium doping** *(Materials science & engineering B (Q2) under revision)*

  Naoufal Ennouhi, Abdeljalile Er-rfyg , Yassine Chouimi , Sanaa Ammari , Safae Aazou, Zouheir Sekkat

- **Synthesis and optimization of a wide-bandgap $Cu_2ZnGe(S,Se)_4$ photovoltaic absorber using single-step sulfo-selenization: effect of stacking order and annealing conditions** *(Materials chemistry and physics (Q1), accepted)*

  Naoufal Ennouhi, Abdeljalile Er-rafyg , Safae Aazou, Victoria Rotaru, Angelica Thomere, Edgardo Saucedo, Maxim Guc, A. Pérez-Rodríguez, Zouheir Sekkat

- **Enhancing the Performance of $Cu_2ZnGeSe_4$ Solar Cells through Lithium Doping: Comparative Analysis on Mo and Transparent Electrodes** *(Jornal of alloys and compounds (Q1), under revision)*

  A. Er-rafyg, **N. Ennouhi**, I.Anafnaf , S. Aazou, Kunal J, Alex Jimenez-Arguijo Maxim Guc, Z. Sekkat, Edgardo Saucedo

Outline:

General introduction, motivations, and thesis objectives

Photovoltaics (PVs) have emerged as promising technologies in transitioning to low-cost and sustainable energy production. However, the PV industry continues to face significant challenges, particularly in achieving higher conversion efficiencies and reducing the manufacturing costs of solar cells. Over the past few decades, significant advancements have been made in PV technologies, beginning with the development of first-generation solar cells based on crystalline silicon (c-Si) [1]. Various alternative solar cell architectures and materials have been proposed and investigated within the scientific community. Some of these technologies have attained higher efficiencies and have entered the commercial market. Silicon-based solar cells represent the most established PV technology, achieving a record efficiency of 27.6% in 2017 [2] and approaching the theoretical limit of 29.3% for single-junction silicon devices [3]. Despite the maturity of silicon photovoltaics, further efficiency improvements are becoming increasingly constrained by this fundamental limit. Moreover, the cost-efficiency ratio of silicon solar cells remains relatively high (about 0.25£ per watt) [1], primarily due to the complex and energy-intensive processes involved in producing high-purity c-Si. To overcome the limitations of silicon-based PVs, the scientific community has explored alternative semiconductor materials that offer improved performance characteristics. In the mid-1990s, the development of second-generation solar cells based on thin films was introduced as a new approach in photovoltaic research, aiming to reduce both material consumption and production costs while maintaining competitive efficiencies. Among the second generation of photovoltaic technologies, copper indium gallium selenide (CIGS) and cadmium telluride (CdTe) have emerged as the most successful, with maximum reported conversion efficiencies of 23% for CIGS and 22% for CdTe [5]. Both technologies have been commercialized for decades and are in direct competition with crystalline silicon (c-Si) solar cells on the global market. However, the widespread adoption and large-scale deployment of these technologies are constrained by significant challenges, particularly cadmium toxicity and the scarcity of key elements such as indium and gallium. These material limitations have encouraged researchers worldwide to search for alternative, low-cost, and nontoxic thin-film materials that could serve as viable substitutes for CIGS and CdTe.

In the 2000s, a new family of materials, known as kesterites, was proposed as promising candidates for the next generation of low-cost thin-film solar cells. Kesterite compounds [6], specifically copper zinc tin sulfide/selenide (CZTSSe), have garnered significant attention because of their earth-abundant and nontoxic constituent elements, making them attractive options for sustainable photovoltaic applications. Moreover, kesterites materials exhibit optical and electrical properties comparable to those of CIGS. In this fact, Kesterite materials have been widely studied and reached an efficiency of approximately 15% at the laboratory scale in 2024 [7]. The combination of low-cost materials and favourable optoelectronic properties has established CZTSSe as a strong candidate in the ongoing search for high-efficiency, environmentally friendly solar cells.

In recent years, the introduction of a new third generation of solar cells has emerged, including tandem solar cells (multiple junction), dye-sensitized solar cells (DSSCs or Grätzel cells), organic photovoltaics (OPVs), perovskite solar cells, and quantum dot solar cells. The overarching aim of third-generation solar cells is to overcome the limitations of earlier technologies. Among these solar cells, tandem (multijunction) solar cells have shown great promise in exceeding the efficiency limits of single-junction devices [8]. The tandem concept involves stacking different solar cells with varied bandgaps in specific configurations to harness a broader spectrum of sunlight, thereby maximizing the energy harvested [9]. These tandem solar cells can reach efficiencies exceeding 47% in two-junction systems, with further increases possible by incorporating additional junctions [8].

Narrow-bandgap crystalline silicon (c-Si), with a bandgap of approximately 1.1 eV, has proven to be an ideal candidate for bottom subcells, offering both high efficiency and thermal stability [10]. For top subcells, various wide-bandgap materials have been proposed, with perovskite solar cells being the most explored option. Numerous studies have focused on the integration of perovskite top cells in c-Si/perovskite tandem configurations, capitalizing on the remarkable efficiency improvements observed in perovskite technology [11]. However, long-term stability remains a significant challenge for perovskite-based tandem devices. However, thin-film solar cells based on CdTe and CIGS have been investigated as viable candidates for top subcells in tandem devices [12]. Unfortunately, as previously mentioned, the toxicity and scarcity of key elements pose significant barriers to the widespread adoption of these materials. Kesterite thin films, which are composed of earth-abundant, nontoxic elements with increased flexibility in varying their bandgaps, present promising alternatives. For these reasons, researchers have proposed kesterite/c-Si tandem devices as cost-effective and potentially highly efficient

solutions for the next generation of tandem solar cells. However, the power conversion efficiency (PCE) of wide bandgap kesterite-based solar cells remains relatively low, with a maximum efficiency of 11% for pure CZTS absorbers [13], limiting their application as top subcells in tandem architectures. The primary causes of this lower performance are attributed to several issues in the bulk [14] and interface properties[15], as will be discussed in detail in the next sections. To enhance the performance of the CZTS top subcell and improve the overall efficiency of CZTS/c-Si tandem devices, addressing these limitations is crucial.

Given these challenges, the main objective of this thesis is to contribute to the development of wide bandgap kesterite materials via various strategies and approaches. The goal is to assess the feasibility of next-generation tandem solar cells based on c-Si as the bottom subcell and kesterite as the top subcell. This work encompasses a range of experimental studies, employing both physical and chemical methods to develop highly efficient kesterite materials and solar cells. Furthermore, optical and electrical modelling, along with simulations, are employed to evaluate the tandem performance of kesterite materials in different tandem solar cell architectures.

This report is divided into six main chapters:

The first chapter highlights the importance of solar energy as a sustainable resource, followed by an overview of the fundamental theory and recent advancements in solar cell technologies. This chapter will conclude by introducing and defining the concept of tandem solar cells, which is the core focus of this thesis because of their potential to greatly increase photovoltaic efficiency.

The second chapter outlines the key properties of kesterite materials and provides an overview of kesterite-based solar cells. This section also explores the challenges in developing highly efficient kesterite solar cells and their potential applications in tandem solar cell technologies.

The third chapter begins by detailing the sol–gel process, starting from the preparation of the solution to the deposition of the precursor onto a substrate via the spin–coating method. Next, an overview of CZTS precursor preparation by sputtering is provided. Finally, we discuss the growth mechanism of kesterite materials and highlight the annealing process, which serves as a common and critical step in both physical and chemical approaches for producing high-quality kesterite materials.

The **fourth chapter** focuses on the experimental optimization of the CZTS sol-gel synthesis, presenting two distinct protocols designed to improve the structural, morphological, and

optoelectronic properties of kesterite absorbers. By comparing the results of these protocols, this chapter underscores the critical factors affecting film quality and, ultimately, device performance.

In the **fifth chapter**, doping and alloying strategies for enhancing semi-transparent kesterite absorbers are discussed. Special attention is given to silver and alkali-metal incorporation, which can significantly modify the band structure and defect chemistry. In parallel, both optical (FDTD) and electrical (SCAPS-1D) simulations are presented to evaluate the feasibility of kesterite/c-Si tandem cells, aiming for efficiencies beyond 20%.

The **sixth chapter** extends the investigation to wide-bandgap germanium-based kesterite (CZGSSe), synthesized using a single-step sulfo-selenization technique. This approach addresses the need for top-cell materials with higher bandgaps in tandem structures, offering a viable route to achieving improved photovoltaic performance.

Finally, the **General Conclusion and Perspectives** summarize the main findings and highlight the future directions for advancing kesterite-based photovoltaic technologies, particularly for tandem solar cell applications.

Chapter 1: Generality, fundamentals, and evolution of solar cell technology

The primary objective of this thesis is to contribute to the development of novel concepts and technologies aimed at enhancing the performance and potential of solar cell technologies. A long history of scientific progress is behind the evolution of solar cells, starting with the discovery of the photovoltaic effect by Becquerel in 1839, followed by Einstein's formulation of the photoelectric effect in 1905. These discoveries have led to significant progress in materials science, particularly in the field of semiconductor physics.

The detailed exploration of semiconductor behavior, particularly its application in p-n junctions, has been pivotal in the advancement of solar cell technology. Understanding p-n junction mechanisms facilitates the practical realization of solar cells, with the first functional device being developed by Bell Laboratories in 1954, which is based on crystalline silicon. Since then, the field of photovoltaics has rapidly evolved, driven by advancements in material engineering, innovative device architecture, and improvements in fabrication techniques.

Building on these scientific foundations, this thesis aims to investigate cutting-edge approaches to further optimize solar cell performance. In this context, this section first emphasizes the importance of solar energy as a sustainable resource. It will then provide an overview of the fundamental theory and recent advancements in solar cell technologies. Finally, we introduce and define the concept of tandem solar cells, which represents the primary focus of the work conducted in this thesis, as tandem architectures hold the potential to significantly increase the efficiency of photovoltaic systems.

I.1. From theory to solar cell technology

I.1.1. Why photovoltaic energy?

Over the past few years, the world has experienced a substantial increase in energy demand, driven by swift economic and industrial growth. Despite this trend, the primary sources of energy globally remain fossil fuels, including coal, natural gas, and oil. Fossil fuels are at the forefront of the energy landscape, making up 78.4% of the world's total energy consumption in 2021 (Figure 1.1) [16]. Notably, fossil fuels, which were formed over millions of years under specific conditions, are inherently nonrenewable even though they are widely used. The finite nature of these resources is becoming an urgent concern as global energy consumption

increases. In addition, the use of fossil fuels for energy production has created several environmental challenges, particularly air pollution caused by the emission of greenhouse gases [17]. These issues demonstrate the urgent need to investigate alternative renewable energy sources that can minimize environmental impacts and reduce the dependence on finite fossil fuels. In this vein, renewable energies such as wind, biomass, and solar power have garnered increased amounts of attention as alternative sources of energy. Figure 1.1 illustrates a noteworthy shift, with 18% of the total energy consumption being derived from renewable sources in 2022. Within the realm of renewable energy, solar power is emerging as a crucial choice for future large-scale electricity production. It is an attractive alternative because of its cleanliness, widespread availability, and inexhaustible nature. Furthermore, solar energy can be harnessed either as heat through concentrated solar power (CSP) systems or directly converted into electricity via photovoltaic (PV) systems. However, despite its promise, solar energy faces obstacles in maintaining a significant share of the energy landscape, with only 11% of renewable energy consumption attributed to solar power in 2022 (as depicted in Figure 1.1). The primary challenges revolve around the efficiency and cost of solar cells. To make solar energy a viable and sustainable source for large-scale electricity production in the future, addressing these issues through advancements in PV technology is essential.

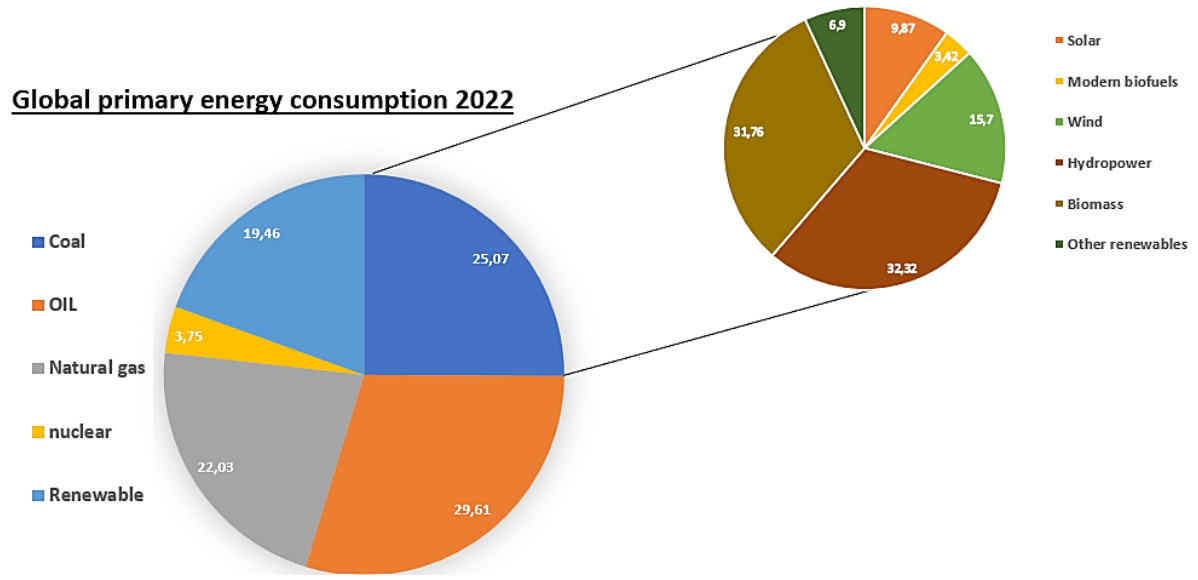

Figure 1. 1: Energy consumption and renewable energy distribution in 2022

I.1.2. Development of photovoltaic technologies

The introduction of photovoltaic solar cells in 1954 marked the beginning of a scientific adventure that led to the development of three different generations of solar cells (Figure 1.2). The silicon solar cell, initiated by Bell Labs in 1954 [1], represents the first generation of silicon

solar cells and is considered a pioneer in this field. The first generation is characterized by the widespread adoption of mono- and polycrystalline silicon solar cells, which have dominated the photovoltaic (PV) market. These cells, developed over decades, form the cornerstone of solar energy technology. The second generation, evolving from the mid-1990s, introduced thin-film solar cells such as cadmium telluride (CdTe) and copper indium gallium selenide (CIGS) solar cells. The primary objective of this generation was to increase cost efficiency and minimize material consumption in solar cell production, expanding the technological and economic feasibility of solar energy. Recently, the third generation of solar cells has emerged as a realm of exploration and innovation. This generation encompasses a diverse array of emerging solar cell technologies, including tandem solar cells (multiple junctions), dye-sensitized solar cells (DSSCs, Grätzel cells), organic solar cells, perovskite solar cells, and quantum dot solar cells. The overarching goal of the third generation is to transcend the limitations imposed by earlier technologies, pushing the limits of efficiency, flexibility, and scalability. Notably, the third generation of solar cells, although promising, remains in the early stages of development, primarily at the laboratory scale. These technologies have yet to be commercialized, signifying ongoing research efforts to refine and optimize their performance before widespread adoption in the solar energy landscape.

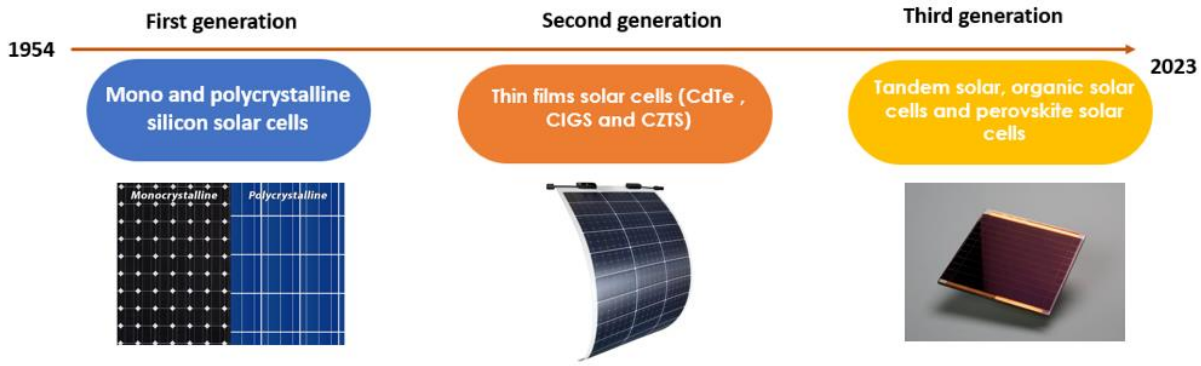

Figure 1. 2: Evolution of photovoltaic generation from 1954

I.1.3. Semiconductor materials

Semiconductors (SCs) have attracted significant interest since their discovery in the early 20th century [18] because of their unique properties and crucial role in various applications, especially photovoltaic solar cells. Unlike conductors and insulators, semiconductors possess an energy bandgap (E_g) that defines the energy difference between the valence band (V_B), where electrons are present, and the conduction band (C_B), where electrons can move freely. This

bandgap typically ranges from 0.6 to 5 eV (Figure 1.3), allowing semiconductors to control their electrical conductivity on external factors, including light, temperature, and doping [18].

The unique properties of semiconductors are essential for their function in photovoltaic solar cells, where they convert sunlight directly into electricity through the photovoltaic effect. When semiconductors absorb photons with sufficient energy, electrons are excited from the valence band to the conduction band, leaving behind holes in the valence band. This electron-hole pair generation is the fundamental process by which solar cells produce electrical current.

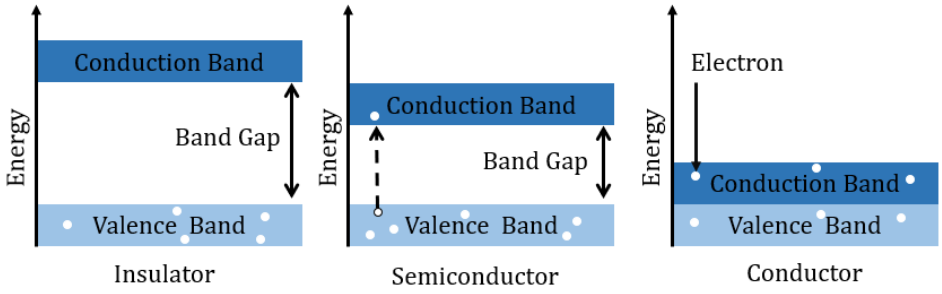

Figure 1. 3: Energy band diagrams for insulators, semiconductors, and conductors

A portion of the periodic table highlighting the elements used in important semiconductors is shown in Figure 1.4, along with a list of selected semiconductors and their energy gaps. Key materials include group IV semiconductors such as silicon (Si) and germanium (Ge), which are fundamental in electronics. Additionally, III-V semiconductor compounds, which are composed of elements from group III (e.g., gallium, Ga) and group V (e.g., arsenic, As), such as gallium arsenide (GaAs), are noted for their high electron mobility and direct bandgaps. II-VI semiconductor compounds, which are made from elements in group II (e.g., zinc Zn) and group VI (e.g., sulfur S), such as zinc sulfide (ZnS) and cadmium telluride (CdTe), are used in optoelectronic applications because of their effective light absorption properties. These materials are chosen for their specific energy gaps, which influence their electrical and optical characteristics, making them essential for various electronic and photonic devices, including photovoltaic solar cells.

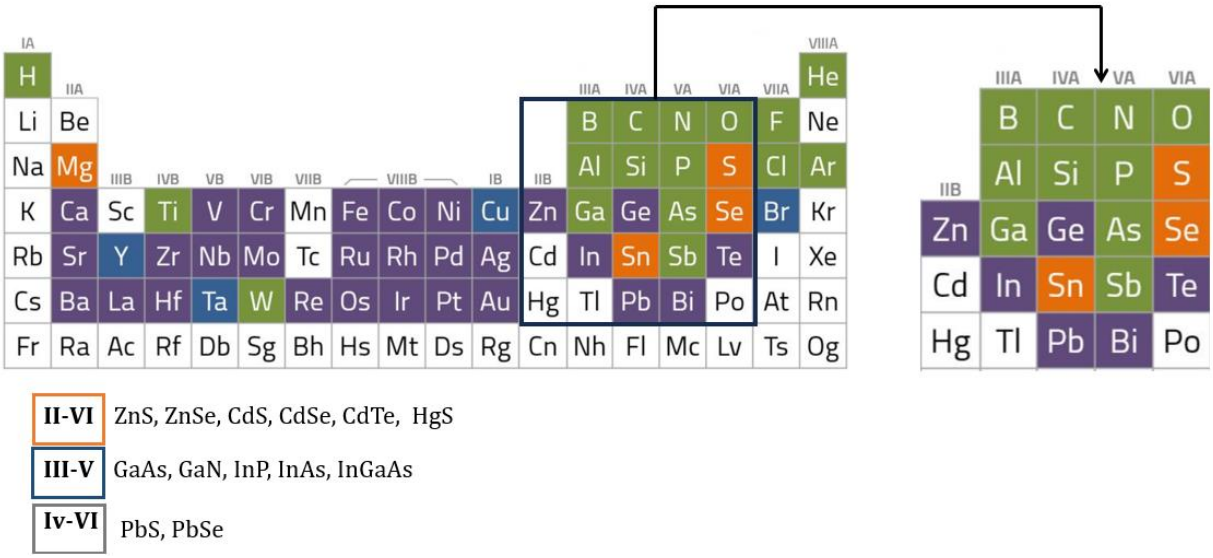

Figure 1. 4: Periodic table highlighting the elements used in important semiconductors

Semiconductor materials can be present in three different forms: intrinsic, n-type, and p-type (extrinsic)

Intrinsic Semiconductors: These materials have an equal number of holes and electrons ($n = p = ni^2$). Silicon (Si) is a well-known intrinsic semiconductor in which the electron and hole concentrations are balanced.

Extrinsic Semiconductors: These are intrinsic semiconductors that have been doped with small amounts of impurities to alter their electrical properties. Doping involves adding atoms from other elements to the semiconductor to increase the concentration of either electrons or holes.

By carefully controlling the type and amount of doping, the electrical properties of semiconductors can be tailored for various applications, including the creation of p-n junctions, which are crucial for photovoltaic solar cells.

I.1.4. Fundamentals of solar cells

The fundamental concept of solar cells is based on the p-n junction in semiconductors [19]. The formation of a p-n junction occurs when a p-type semiconductor and an n-type semiconductor are combined (Figure 1.5). Owing to the concentration gradient at the interface, the majority carriers in the p-type semiconductor (holes) diffuse toward the n-type semiconductor through

the interface, leaving behind negative charges and recombining with electrons. Similarly, most of the carrier electrons from the n-type semiconductor diffuse through the interface onto the p-type semiconductor, rejoin with holes and leave behind positive charges. The space charge region (SCR), also known as the depletion zone, arises when parts of the P–N interface lose a significant portion of their mobile carriers. At the interface between both semiconductors, an electric field is created with an electric force directed from the n side to the p side, and this electric force leads to the diffusion of holes to the n side in the opposite direction of the diffusion force. When this drift–diffusion process reaches equilibrium, the electric field in the p-n junction is called the built-in electric field, and the corresponding voltage is denoted as the built-in voltage (V_{bi}).

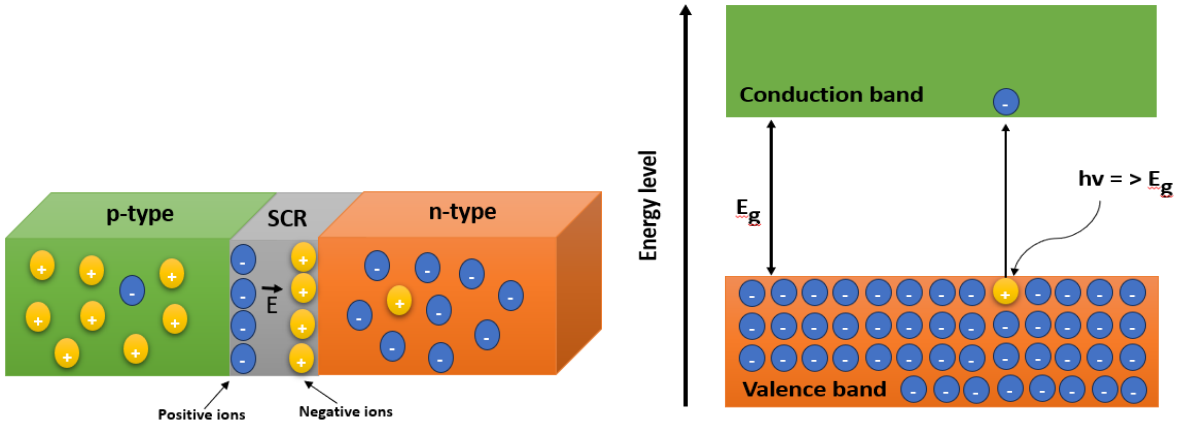

Figure 1. 5: Mechanisms of p-n junction formation and the photovoltaic effect

Solar cells convert sunlight to electricity based on the photovoltaic effect of the p-n junction. Figure 1.5 illustrates the mechanism of the photovoltaic effect in solar cells. When sunlight arrives at the surface of a p-n junction, photons with energies greater than the absorber (p-type) bandgap (Eg) are absorbed. The absorbed photons excite electrons from the valence band to the conduction band, creating a hole in the valence band. This process results in the formation of a photogenerated electron–hole pair (EHP). The built-in electric field of the p-n junction separates the EHP pairs, with electrons accumulating on the n-type semiconductor side and holes accumulating on the p-type semiconductor side. This arrangement generates a photogenerated electric field opposing the p-n junction built in an electric field. Simultaneously, this new electric field enhances the diffusion current, leading to an increase in the integrated electric field. EHP pairs located away from the p-n junction can diffuse to the space charge region and become separated. The distance over which this diffusion occurs is called the carrier

diffusion length. Under open-circuit conditions, a voltage across the p-n junction is established, known as the "open-circuit voltage." This phenomenon is recognized as the photovoltaic effect. In a short-circuit scenario, current flows through an external circuit, illustrating the functionality of solar cells. Notably, the photovoltaic effect is not exclusive to p–n junctions; it can also manifest in metal–semiconductor junctions.

I.1.6. Solar Cell Configurations

The essential framework of a p-n solar cell consists of the following components:

Absorber: This material absorbs most of the light, generating carriers during the process. Ideally, its bandgap falls within the range of 1–1.5 eV for efficient sunlight absorption. Depending on the technology, it can serve as an n-type, p-type, or even an intrinsic semiconductor.

Emitter: Designed to be as transparent as possible, allowing sunlight to reach the absorber

Back and Front Contacts: These contacts are responsible for collecting carriers and assisting their movement into an external circuit. Owing to their high conductivity, metals are commonly used. Transparent conductive oxides are also frequently employed in this process.

Solar cells can be manufactured with various configurations and semiconductor materials, as illustrated in Figure 1.6. The first generation of silicon solar cells is based on a p-Si/n-Si homojunction with the structure p++(BSF)/p-Si/n+-Si/ARC, as depicted in Figure 1.6. The thickness of the p-Si constitutes a significant portion of the solar cell, typically approximately 200 µm, whereas the n-type silicon layer is only 100 nm thick [20]. The second generation of thin-film solar cells relies on an absorber/CdS heterojunction with ZnO and ZnO:Al transparent conducting oxide (TCO) layers [21]. This material includes CdS as an n-type wide band gap buffer layer and chalcopyrite (CIGS or CdTe) as a p-type absorber. Here, the thickness of the absorber is less than 1.5 µm. The third generation is dominated by perovskite solar cells, which are primarily based on the structure: TCO/ETL/perovskite/HTL/top contact[22].

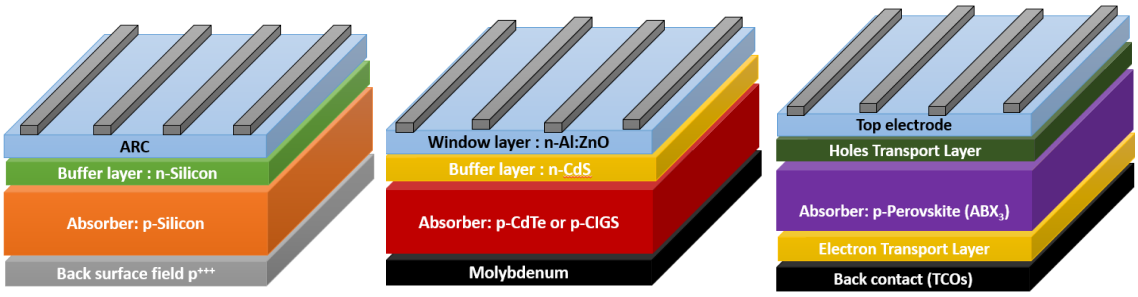

Figure 1. 6: Conventional structures of different generations of solar cells

1.1.5. Solar Cell Parameters

The performance of a solar cell is often characterized via a simplified electric circuit employing a single diode model. In the absence of light (dark conditions), the relationship between the current density and voltage is determined by the ideal Shockley diode equation, expressed as follows:

$$J(V) = J_0(exp^{(\frac{qV}{K_bT}} - 1) \qquad (1)$$

Upon exposure to sunlight, additional charge carriers are generated, contributing to the overall current produced. This is denoted as Jph. The following equation represents the equivalent circuit, which combines the current source and the diode connected in parallel:

$$J(V) = J_0\left(exp^{(\frac{qV}{K_bT}} - 1\right) - J_{ph} \qquad (2)$$

The equation corresponds to a circuit with a current source and a diode connected in parallel. Figure 1.7 graphically illustrates these equations. From this representation, key parameters describing the solar cell's operation can be extracted. The maximum voltage achievable by a solar cell, Voc, is obtained when J = 0, and the maximum current density, Jsc, occurs at V = 0. The product of Voc and Jsc defines the maximum theoretical power (Ptheo) of the cell. Importantly, this theoretical power is unavailable even in ideal devices. Under practical operating conditions, the maximum power extractable from a solar cell (Pmax) is determined by the point on the J–V curve that maximizes the product of J and V. This point is referred to as the maximum power point (MPP). The MPP is characterized by the current density and voltage at maximum power, denoted as Jmp and Vmp, respectively.

The fill factor (FF) is defined as the ratio between the maximum power extracted from a solar cell (Pmax) and its maximum theoretical power (Pt_{heo}):

$$FF = \frac{V_{MMP} \times J_{MMP}}{V_{OC} \times J_{SC}} \qquad (3)$$

This parameter, the fill factor (FF), quantifies the squareness of a J-V curve in relation to an ideal diode. Finally, the power conversion efficiency (η) of a solar cell, which represents the ratio between the maximum power generated by the device (Pmax) and the power incident upon the cell (Pin), is typically expressed as:

$$\eta = \frac{P_{max}}{P_{in}} = \frac{FF \times J_{SC} \times V_{OC}}{P_{in}} \qquad (4)$$

Under standard measuring conditions, Pin corresponds to the power extracted from the integration of the solar spectrum AM1.5G (1000 W/m^2).

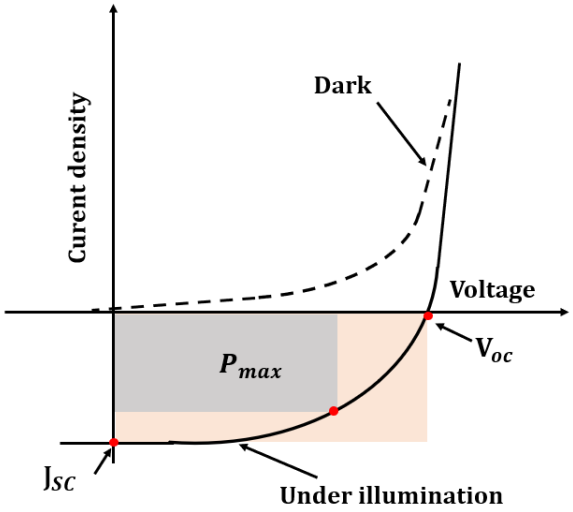

Figure 1. 7: J-V representation of a p-n junction under illumination and in the dark

Until now, the assumption has been that solar cells behave as ideal diodes. However, solar cells experience various losses. These losses can be categorized into two terms: the series resistance (Rs) and the shunt resistance (Rsh). The series resistance encompasses all resistive losses along the device, such as those arising from the electrical resistance of different layers and the contact resistance at the interfaces. On the other hand, shunt resistance accounts for losses caused by alternative current paths, known as shunts. These terms can be incorporated into Eq. (2) as follows:

$$J(V) = J_0\left(exp^{(\frac{qV}{K_bT}} - 1\right) - J_{ph} + \frac{V - JR_S}{R_{sh}}$$

This equation corresponds to the circuit illustrated in Figure 1.8. Eq. (5) is effective for ideal p-n homojunction solar cells where the primary recombination process is radiative and occurs in the neutral region (i.e., an electron falls directly from the conduction to the valence band, emitting a photon). However, in the case of less-than-ideal p-n junctions, such as heterojunctions, significant losses arise due to recombination in the space-charge region (SCR). This recombination can have both radiative and nonradiative components.

Within the nonradiative category, the main recombination mechanisms include Shockley–Read–Hall (SRH), where an electron falls from the conduction band to a mid-bandgap state and subsequently to the valence band, and Auger, in which an electron falls from the conduction to

the valence band, transferring the energy difference to another electron. To account for these losses, Eq. (6) incorporates an additional term known as the diode quality factor, A:

$$J(V) = J_0\left(exp^{\left(\frac{AqV}{K_bT}\right)} - 1\right) - J_{ph} + \frac{V - JR_S}{R_{sh}}$$

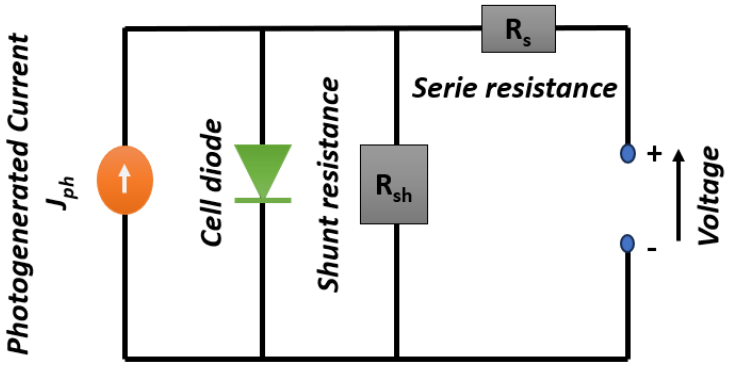

Figure 1. 8: Electrical representation of a p-n junction under illumination

I.1.7. Efficiency Limit of Conventional Solar Cells

Solar cells are designed to harness the power of sunlight and transform it into electricity through the photovoltaic effect. The performance of these solar cells is characterized by various parameters, each of which plays a vital role in determining the performance. Among these parameters are the short-circuit current (Jsc), open-circuit voltage (Voc), fill factor, and overall efficiency. The efficiency is the most crucial parameter because it directly measures how well a solar cell converts sunlight into electricity. It is the ratio of the electrical power output to the solar power input (Figure 1.9), expressed as a percentage. The higher the efficiency is, the more effectively the solar cell can transform sunlight into electrical energy.

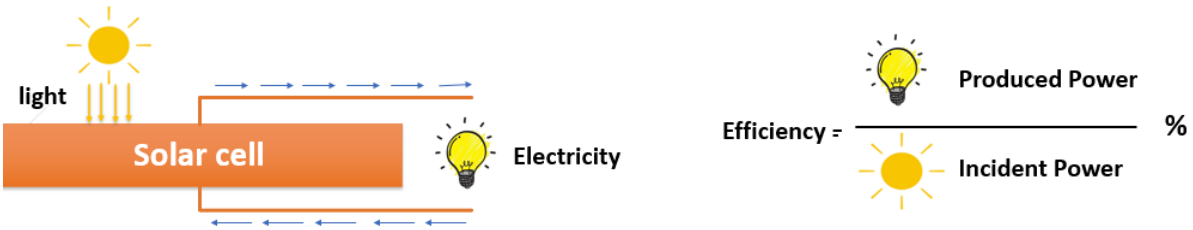

Figure 1. 9: Solar light-to-electricity conversion mechanism and efficiency calculation

In 1961, William Shockley and Hans-Joachim Queisser introduced a significant concept in the field of solar cell research, the calculation of the maximum conversion efficiency of a p–n junction solar cell when exposed to sunlight [23]. This calculation established limits on the efficiency that a solar cell could theoretically achieve based on the inherent properties of the materials used in its construction. These limitations are crucial for understanding the upper boundaries of solar cell efficiency. These methods consider factors such as the energy of sunlight and the electronic properties of the materials involved. While actual solar cells may not reach these theoretical limits owing to practical considerations and material constraints, striving towards these efficiencies remains a central goal in advancing solar cell technology. In essence, the parameters characterizing solar cell performance and the theoretical efficiency limits form the foundation for designing and improving solar cell technologies. As researchers and engineers push the boundaries of material science and engineering, the quest for more efficient and sustainable solar energy conversion continues. Over the past few decades, there have been significant improvements in the conversion efficiencies of solar cell materials. However, these advancements are also approaching their theoretical limits. Figure 1.10 illustrates the historical evolution of various types of solar cells [24]. This indicates that the efficiency progress is either currently converging or will soon converge, primarily owing to constraints imposed by the Shockley–Queisser limit.

As depicted in Figure 1.10.b, currently, the best silicon solar cell achieved in the laboratory has a PCE of 26.7% [25], which closely approaches the efficiency limit of 29.4% for silicon solar cells. However, over the past two decades, the efficiency of c-Si solar cells has improved by only 3%. This finding highlights the challenges associated with further enhancing the efficiency of silicon solar cells. To overcome these efficiency limitations, tandem solar cells have emerged as promising solutions within the photovoltaic (PV) landscape. Traditional single-junction solar cells face inherent efficiency limits because of their inability to efficiently convert a broad spectrum of sunlight into electricity. Tandem solar cells, however, employ different solar cells with varying bandgaps to capture a wider range of solar wavelengths, thus maximizing the energy conversion efficiency. By stacking complementary materials with distinct absorption properties, tandem cells can achieve efficiencies beyond those attainable by single-junction cells alone. This innovative approach has the potential to significantly enhance the performance and competitiveness of PV technology, paving the way for more efficient and sustainable solar energy generation. Through ongoing research and development efforts, tandem solar cells

continue to demonstrate remarkable progress, offering a pathway towards overcoming efficiency barriers and advancing the frontier of renewable energy technology.

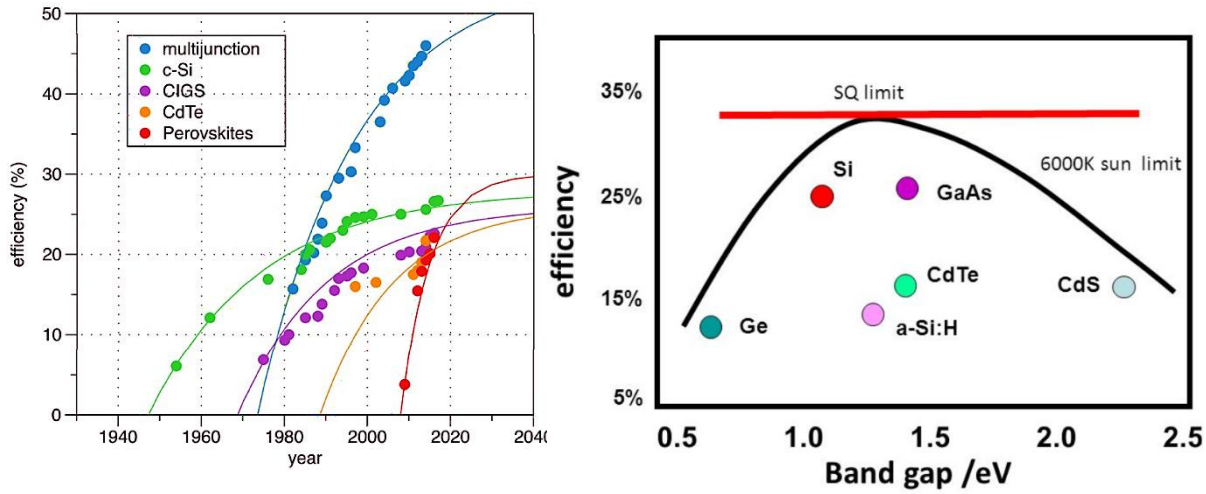

Figure 1. 10: (a) Record efficiencies of III-V multijunctions, crystalline silicon, copper indium selenide (CIGS), cadmium telluride (CdTe) and perovskite solar cells. (b) Theoretical efficiency limits of a single junction in proximity to the Shockley–Queisser li

I.2. Introduction To tandem solar cells

I.2.1. Why tandem solar cells?

The concept of multijunction solar cells represents the most successful approach to surpass the Shockley–Queisser (SQ) limit discussed in the previous section. Unlike single-absorber material devices, multijunction solar cells combine different semiconductor materials to capture a broader range of the solar spectrum. The bandgap of each semiconductor material is optimized to efficiently absorb a specific portion of the spectrum. Spectrum splitting in multijunction cells can be achieved in two main ways. One method involves spatially dividing the solar spectrum via an optically dispersive element, such as a prism, to direct photons of varying energies to the corresponding subcells with appropriate bandgaps. However, despite its conceptual simplicity, this method is often impractical because of the optical and structural complexities involved. A more favoured approach is to stack the subcells vertically, with the bandgap of each subcell decreasing from the top (sun facing side) to the bottom (dark side). In this configuration, as shown in Figure (1.11), sunlight first encounters the cell with the highest bandgap, and as it passes through the device, it is progressively absorbed by materials with lower bandgaps. This

arrangement ensures that high-energy photons are captured by large bandgap materials, minimizing thermalization losses. Additionally, since each upper cell is transparent to photons below its bandgap, photons not absorbed by one cell can still be absorbed by subsequent cells with lower bandgaps. Consequently, this design significantly reduces both thermalization and sub-bandgap losses.

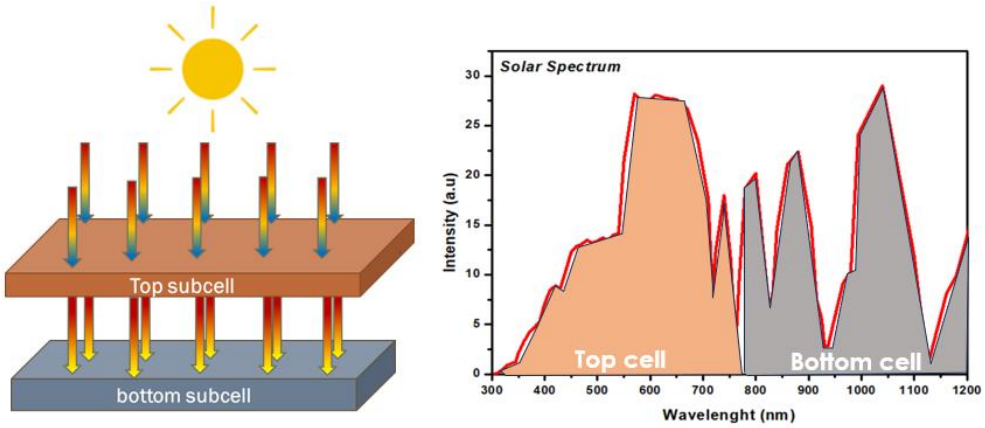

Figure 1. 11: Simplified schematics of the concept of multijunction (tandem) solar cells.

Compared with single-junction cells, these multijunction cells, often referred to as "tandem" solar cells, significantly enhance the theoretical maximum efficiency. By increasing the number of junctions from one to two, the maximum efficiency can improve from 33% to 46% [26]. However, the efficiency increases with additional junctions, reaching approximately 51% for triple-junction cells and 55% for quadruple-junction cells [27]. As illustrated in Figure (1.12), even though the theoretical limit under full concentration (with infinite absorbers and no thermalization losses) is 86.6% [28], practical and economic challenges make the implementation of more than five junctions questionable [29]. For these efficiency improvements to be realized, the bandgaps of the absorbers must be perfectly matched. Figure (1.12) demonstrates how the maximum efficiency limit changes as the bandgap of the subcells varies in double-junction solar cells. In an ideal tandem solar cell, the optimal bandgaps range from 0.9–1.1 eV for the bottom cell and 1.5–1.7 eV for the top cell.

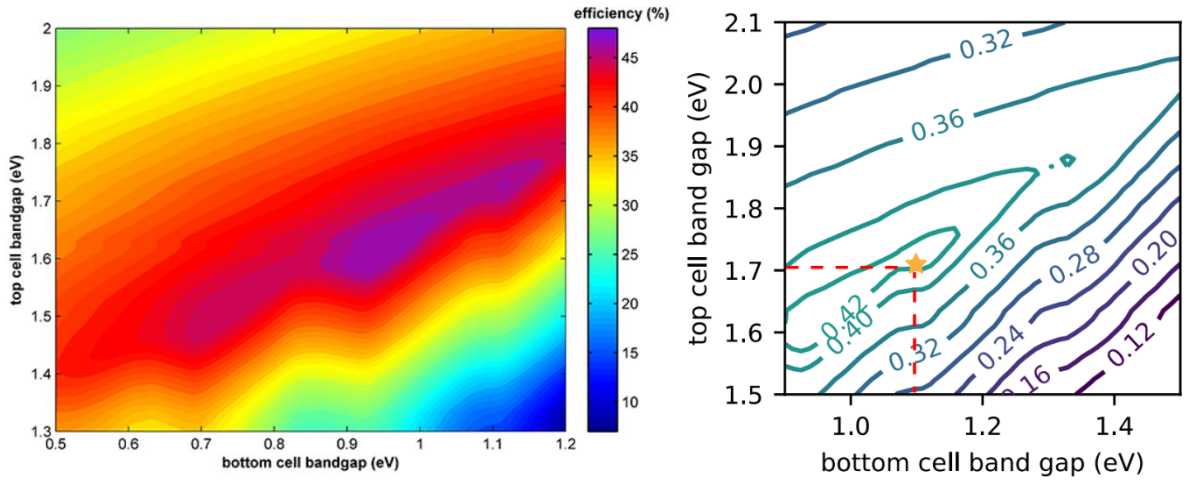

Figure 1. 12: Efficiency contours of an ideal double-junction solar cell as a function of the top and bottom cell bandgaps. [24]

I.2.2. Tandem architecture

Tandem solar cells arranged vertically can be categorized into three main configurations based on their fabrication sequence and interconnection schemes. These configurations, as reviewed in various studies [30] and illustrated in Figure (1.12), include two-terminal (2T), three-terminal (3T), and four-terminal (4T) configurations.

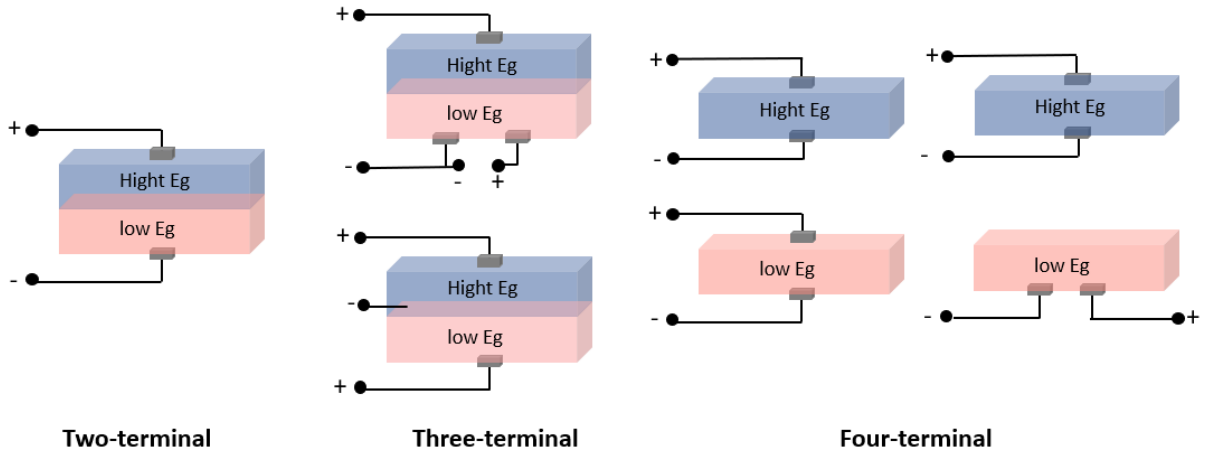

Figure 1. 13: Schematics of different tandem device architectures, namely, the two-terminal, three-terminal, and four-terminal configurations.

I.2.2.1. Two-terminal tandem (2T)

The two-terminal, or monolithic, configuration is the primary type of tandem solar cell. In monolithic tandem cells, two subcells with identical electrical polarities (p/n or n/p) are directly

fabricated on top of each other. These cells are connected in series through a tunnel junction [31] or a recombination layer. The device's overall performance heavily relies on the efficiency of charge carrier transport between the two cells. Since the cells are connected in series, the total voltage (Voc, total) is the sum of the voltages of the individual subcells (Voc, top + Voc, bottom), whereas the total current (Jsc, total) is limited by the cell with the lowest current (Jsc, total = min (Jsc, top, Jsc, bottom)).

One significant limitation of this structure is the current matching problem, where the currents in both cells must be equal. This architecture's efficiency is highly sensitive to spectral variations and changes in the bandgap of the top cell. Achieving current matching requires fine-tuning the bandgap and thickness of the top cell absorber and optimizing the optical properties of other window layers to allow sufficient photons to reach the bottom cell.

Monolithic tandem integration presents several challenges. The fabrication of each layer must not damage the underlying layers, and the surface properties of the substrate must not affect the quality of the subsequent layers. Despite these challenges, monolithic tandems are highly attractive for industrial deployment because of their simple module integration, minimal fabrication steps, layers, and interconnections [32]. Additionally, monolithic structures can achieve greater practical efficiency due to less parasitic absorption, requiring only one transparent electrode and no extralaminating sheets or adhesives [32].

I.2.2.2. Four-terminal (4T) Tandem

In a four-terminal (4T) configuration, the two subcells are fabricated separately and then mechanically stacked on top of each other, each with its own front and rear terminals, as depicted in Figure (1.12). This configuration ensures that the cells are electronically isolated but mechanically coupled, allowing each cell to operate at its maximum power point independently. Consequently, the total efficiency of the tandem cell is the sum of the efficiencies of the individual cells.

Unlike the monolithic structure, the 4T configuration does not impose constraints on the current or the polarity (p/n or n/p) of the subcells [29]. The independent fabrication of each subcell offers greater flexibility in design, material selection, processing, and characterization. This makes the 4T approach particularly advantageous for research and prototyping purposes. However, the 4T structure requires at least three transparent electrodes (the front electrodes of each subcell and the rear electrode of the top cell). This can lead to increased parasitic absorption and ohmic losses in the device.

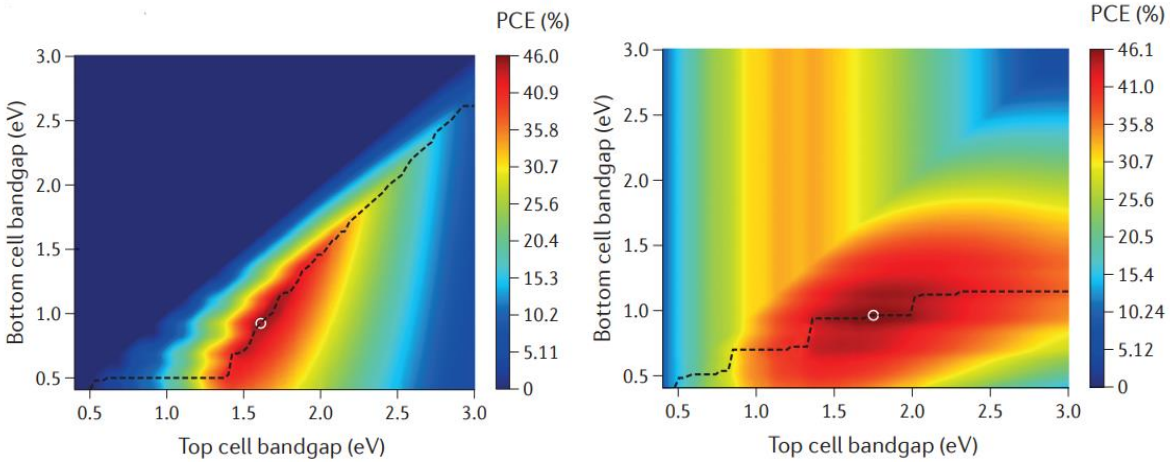

Figure 1. 14: a) and b) Efficiency responsiveness of the 2T and 4T configurations to deviations from ideal bandgap pairs (graphs adopted from [28]).

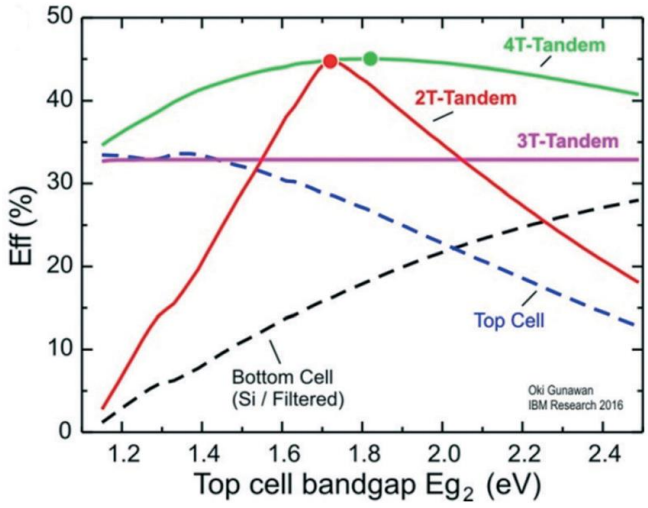

Figure 1. 15: SQ efficiency limits of silicon-based tandem solar cells with 2T, 3T (type A), 3T (type B), and 4T architectures as a function of the bandgap of the top cell (reproduced on the basis of data from [27]).

I.2.3. Possible configuration of tandem solar cells

I.2.3.1. Bottom cell

Silicon solar cells have consistently dominated the photovoltaic (PV) industry, holding a market share of 95%, a figure that is expected to remain stable for the foreseeable future. Although the silicon industry continues to mature, efficiency improvements have been minimal as the technology nears its fundamental limits, such as the 29.4% efficiency ceiling accounting for Auger recombination, which is unavoidable in indirect bandgap materials such as silicon. To achieve efficiencies greater than 30% and reduce the levelized cost of electricity (LCOE), novel approaches such as silicon-based approaches offer promising paths for the silicon industry.

Silicon is an ideal candidate for the bottom cell in a two-junction device for several reasons. Silicon is the second most abundant element in the Earth's crust and is stable, nontoxic, and inexpensive. The extensive knowledge accumulated from the microelectronics industry means that silicon technology is highly developed and well understood. Crucially, a silicon bandgap of 1.1 eV is an excellent match for the bottom cell in a two-junction tandem device. Additionally, silicon cells can be fabricated in various architectures, providing flexibility in tandem design, choice of top cell materials, contact methods (e.g., IBCs), temperature resilience, and device polarity. Given these advantages and the well-established industry, it is unlikely that any new technology will completely replace silicon. Therefore, a more practical approach for the industry is to leverage existing production lines and integrate promising high bandgap materials on top of silicon rather than replacing them entirely.

I.2.3.2. Top cell

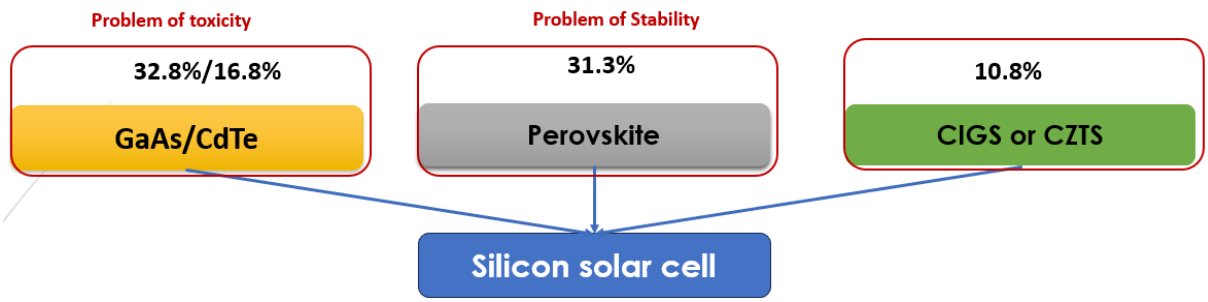

Figure 1. 16: Main Subtop Cell Configurations for Tandem Solar Cells with Silicon as the Bottom Cell

Research has focused on finding suitable top-cell materials with a bandgap of approximately 1.7 eV for pairing with silicon with a bandgap of 1.1 eV. III-V/Si systems have achieved record efficiencies of up to 35.9% but are expensive to manufacture owing to costly deposition methods and lattice mismatch challenges, limiting their terrestrial application. Perovskite solar cells have achieved significant efficiency improvements, surpassing 25% in various tandem architectures and reaching a value of 29.15% [33]. Despite this progress, they face instability issues under light, moisture, and heat, leading to efficiency degradation within 1000 hours [34]. Additionally, the presence of toxic lead in high-performance perovskites raises environmental concerns [35]. Thus, alternative technologies are needed to meet the demands of abundance, low cost, stability, and high performance for sustainable photovoltaic technology.

Thin film chalcogenides (TFCs), such as CdTe, chalcopyrites, and kesterites, emerge as potential alternatives to perovskites in photovoltaic applications. Like those of perovskites and

III-V materials, the bandgap of TFCs can be easily adjusted over a wide range through alloying and stoichiometric modifications [36]. These materials are typically composed of cost-effective elements, and their fabrication processes utilize various low-cost deposition techniques, including solution-based methods such as spray and spin coating, as well as vacuum-based techniques such as sputtering and thermal evaporation, as reviewed in the literature [37]. Historically, chalcogenides have been developed as inexpensive substitutes for conventional silicon technology rather than as tandem partners. Research efforts have focused primarily on enhancing low bandgap materials such as the $CuIn_xGa_{1-x}Se_2$ and CdTe technologies [38]. Consequently, the development of highly efficient high-bandgap chalcogenides suitable for tandem applications is still in progress. Emerging chalcogenide-perovskite hybrids, such as $BaZrS_3$-based alloys, have shown impressive stability against water immersion, high-temperature resilience up to 550°C, very high absorption coefficients (α of 10^5 cm^{-1}), and simulated tandem efficiencies reaching 38% when integrated with silicon in tandem configurations [39]. However, integrating chalcogenides with silicon presents significant challenges. Many chalcogenides require high-temperature annealing steps (>500°C) in reactive atmospheres (e.g., S or Se) during fabrication, which can potentially damage underlying silicon cells in monolithic integration setups. In this context, sulfide kesterite, specifically Cu2ZnSnS4, has emerged as a promising candidate from the chalcogenide family for the top cell in tandem configurations. This choice is based on its excellent optical properties, stability, nontoxicity, abundance in the Earth's crust, and cost-effectiveness comparable to that of silicon cells, which will be elaborated further in subsequent sections.

Chapter 2: Kesterite materials & Kesterite solar cells: General overview

In the previous chapter, the different generations of solar cells and the primary materials employed in their fabrication were discussed in detail. This thesis focuses on tandem solar cell technologies, which necessitate the development of single-junction devices with wide bandgaps to serve as top cells in tandem configurations. Over the past few years, significant efforts have been directed toward identifying and developing wide bandgap materials that can be coupled with silicon to achieve high-efficiency tandem devices. Among the explored materials, perovskite-based solar cells have emerged as promising candidates due to their tunable bandgap and excellent power conversion efficiencies [11]. However, their integration into tandem devices is hindered by critical challenges related to their long-term stability. Thin-film solar cells, such as those based on cadmium telluride (CdTe) and copper indium gallium selenide (CIGS), have demonstrated significant potential for tandem applications [40]. However, these technologies face limitations arising from the toxicity of cadmium and the scarcity of indium and gallium, raising concerns about their environmental impact and scalability for widespread adoption.

In this context, kesterite thin films represent a promising alternative for use as the top cell in tandem solar cells. Kesterite-based materials offer distinct advantages, including excellent long-term stability and the use of earth-abundant, non-toxic elements. Furthermore, their optical bandgap can be adjusted by tailoring their chemical composition, making them particularly suitable for tandem applications. Recent advancements have significantly improved the efficiency of kesterite-based solar cells, with efficiencies exceeding 11% for pure sulfide Cu_2ZnSnS_4 (CZTS) [13] and reaching approximately 15% for selenium-containing $Cu_2ZnSn(S,Se)_4$ (CZTSSe) devices [7].

This chapter provides a comprehensive overview of kesterite materials, emphasizing their structural, optoelectronic, and phase formation properties. Furthermore, it delves into the challenges associated with improving the performance of kesterite-based solar cells. Particular attention is given to doping and alloying strategies, which are the central focus of the subsequent sections, as well as their implications for the integration of kesterite materials into tandem solar cell technologies.

II.1. Evolution of Photovoltaic Alloys: From Binary to Quaternary Structures

The crystalline structure of silicon, characterized by its diamond-type configuration within the cubic crystal system, serves as the foundation for a range of photovoltaic alloys. Binary compounds derived from this structure adhere to the general formula AIIIXV or AIIXVI, where **A** represents cations, **X** denotes anions, and II, III, V, and VI correspond to groups in the Periodic Table of Elements. Among binary photovoltaic alloys, gallium arsenide (GaAs) and cadmium telluride (CdTe) are the most prominent. While GaAs maintains a diamond-like structure, CdTe adopts a sphalerite-type configuration, commonly referred to as the zinc-blende structure, also within the cubic crystal system.

Ternary alloys originate from the sphalerite structure through cation substitution. Specifically, a pair of (2+) cations is replaced by one (1+) cation and one (3+) cation, resulting in the general formula ABX_2. This leads to the presence of two distinct cations, **A** and **B**. In the context of photovoltaics, copper indium disulfide ($CuInS_2$ or CIS) and copper indium gallium disulfide ($CuIn_{1-x}Ga_xS_2$ or CIGS) are noteworthy ternary alloys. These materials crystallize in a chalcopyrite-type structure, which belongs to the tetragonal crystal system. Solar cells based on these materials are commonly referred to as chalcopyrite solar cells.

Quaternary alloys further evolve from the chalcopyrite structure through a substitution process wherein a pair of (3+) cations is replaced by one (2+) cation and one (4+) cation. This results in the general formula A_2BCX_4, comprising three distinct cations (**A**, **B**, and **C**). Among quaternary alloys, copper zinc tin sulfide (Cu_2ZnSnS_4 or CZTS) is the most extensively studied. This material crystallizes in a kesterite structure, a tetragonal crystal system analogous to chalcopyrite. Solar cells utilizing CZTS are referred to as **kesterite solar cells** and represent a promising avenue for sustainable photovoltaic technologies.

The subsequent sections of this thesis will focus on kesterite materials, such as CZTS, with an emphasis on their crystalline structure, properties, and applications in photovoltaic devices.

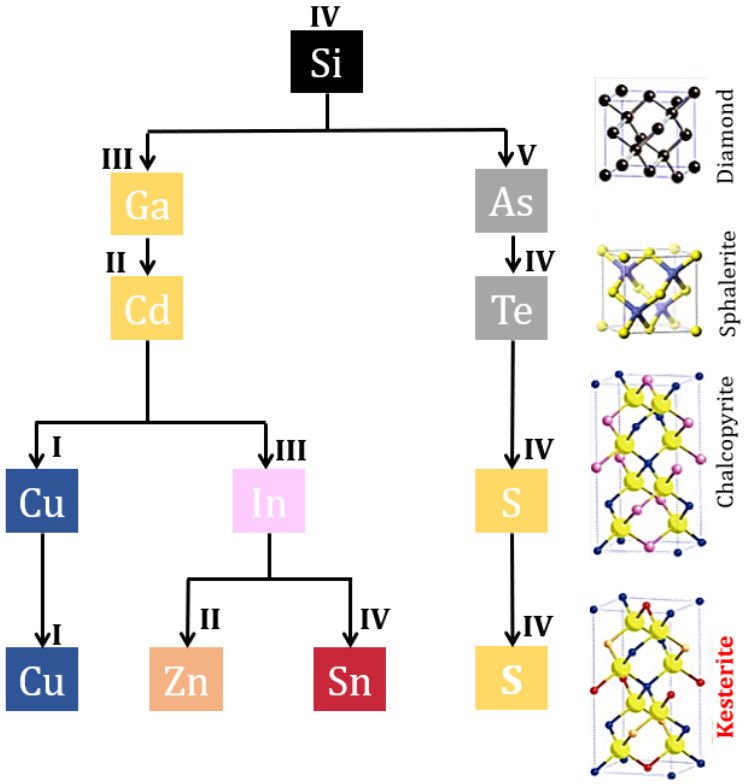

Figure 2. 1: The evolution of the well-known materials used in photovoltaics solar cells antheir chemical structures.

II.2. Kesterite materials: Structural, Optoelectronics properties and Phase formation

II.2.1. Structural properties

Kesterite materials were initially identified as sulfide compounds with the chemical formula $Cu_2(Zn,Fe)SnS_4$, where zinc and iron share the same lattice positions [41]. However, this study focuses on Zn-based kesterite, particularly Cu_2ZnSnS_4 (CZTS) and its derivatives, $Cu_2ZnSnSe_4$ (CZTSe) and $Cu_2ZnSn(S,Se)_4$ (CZTSSe), due to their promising properties for solar cell applications.

The crystal structure of CZTS is predominantly described as kesterite, though it can also form a stannite structure. Both are considered derivatives of the chalcopyrite structure found in $CuInS_2$ (CIS), as illustrated in Figure 2.2. The kesterite structure arises when two trivalent indium (In) atoms in CIS are replaced by two divalent zinc (Zn) atoms, and the remaining In atoms are replaced by one divalent Zn and one tetravalent tin (Sn). The copper (Cu) and anion positions remain unchanged.

The primary distinction between the kesterite and stannite structures lies in the cation arrangement:

- In the kesterite structure, Cu and Sn occupy layers at z=0 and z=1/2, while Cu and Zn occupy layers at z=1/4 and z=3/4.
- In the stannite structure, Zn and Sn alternate at z=0 and z=1/2, while Cu occupies the layers at z=1/4 and z=3/4.

Additional differences are observed in the anion positions:

- In the stannite structure, the anion is located on the (110) mirror plane at position (x, x, z).
- In the kesterite structure, the anion occupies position (x, y, z), which eliminates mirror symmetry.

CZTS exhibits tetrahedral coordination around each sulfur atom, with each sulfur bonded to two Cu atoms, one Zn atom, and one Sn atom. This arrangement supports two possible space groups for CZTS: I4 and I$\bar{4}$2m, highlighting its structural variability. The kesterite structure is energetically favored, as it has a lower formation energy compared to the stannite structure, as confirmed by theoretical calculations [42]. In addition, kesterite structure is reported to be more stable thermodynamically and more suitable for solar cell applications [43]. For these reasons, the next of this report will be focused on the kesterite structure.

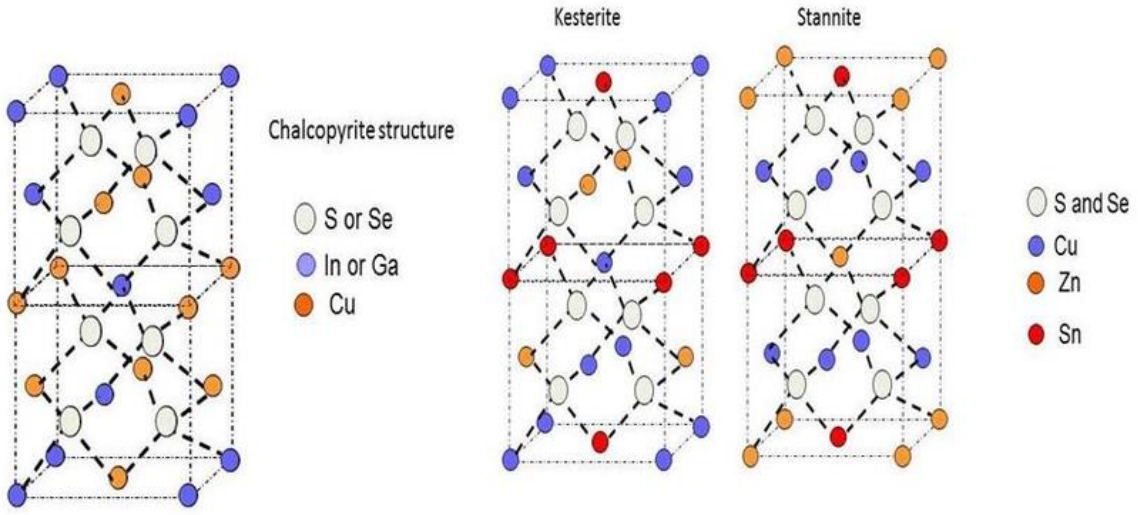

Figure 2. 2: The chemical structures of chalcopyrite and its transformation to the kesterite and stannite structure.

II.2.2. Optoelectronic properties

II.2.2.1. Absorption Coefficient and Optical Bandgap

The absorption coefficient and optical bandgap are fundamental properties of semiconductors, particularly in their application as absorber layers in solar cells. The optical bandgap of the absorber layer determines the maximum theoretical efficiency of a solar cell, as governed by the Shockley–Queisser limit for single-junction photovoltaic devices (refer to Chapter 1). For pure sulfide Cu_2ZnSnS_4 (CZTS) alloys, the absorption coefficient is approximately 10^4 cm^{-1}, and the material exhibits a direct bandgap around 1.5 eV. These properties are optimal for photovoltaic applications, as they enable efficient photon absorption and energy conversion. CZTS, therefore, emerges as a highly promising absorber material for thin-film solar cells.

The Shockley–Queisser model (illustrated in Figure 2.3) highlights the optical bandgap ranges for kesterite alloys, including CZTSe, CZTSSe, and CZTS, which serve as benchmarks for evaluating the performance of photovoltaic devices. Under standard AM1.5G solar illumination, a theoretical efficiency of up to **33%** can be achieved for an ideal CZTS-based solar cell with a 1.5 eV bandgap. These findings underscore the potential of CZTS and its related alloys as cost-effective, environmentally friendly absorber materials for thin-film photovoltaic technologies, capable of achieving high efficiency under optimal conditions.

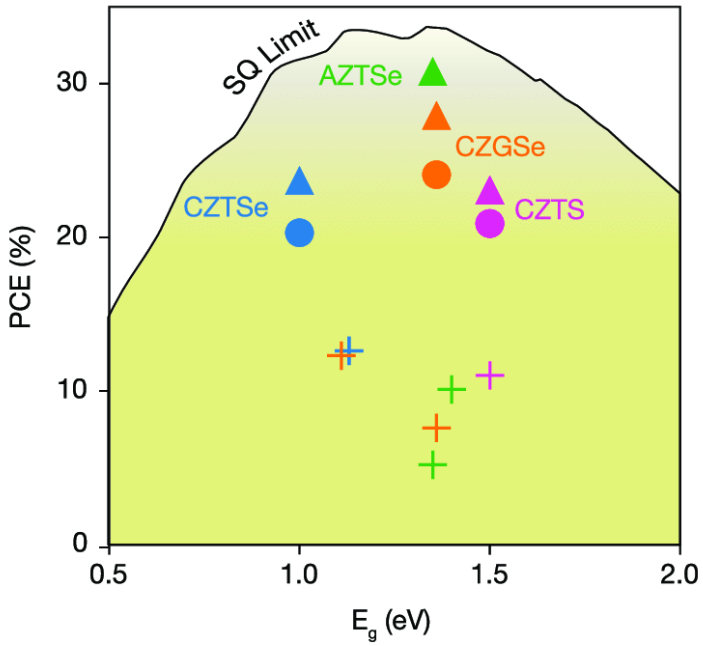

Figure 2. 3: The efficiency limit of different kesterite solar cells according to their bandgap and the absorption coefficient and bandgap of pure CZTS.

II.2.2.2. Electrical properties of kesterite materials

Electrical properties, including carrier type, density, and mobility, are fundamental parameters that influence carrier transport in optoelectronic devices. In solar cells, the carrier type (p- or n-type) dictates the device architecture, while the majority carrier density affects both the recombination lifetime and the depletion width [44]. Carrier mobility, particularly that of minority carriers, plays a critical role in determining the diffusion length, directly impacting current collection efficiency during solar cell operation [45].

In CZTS materials, the predominant carrier type is p-type, with carrier concentrations typically ranging from 10^{16} cm^{-3} to 10^{17} cm^{-3} [46]. This p-type conductivity in CZTS arises from the high density of acceptor defects in the kesterite structure (will be elaborated in the following section). Regarding mobility, various studies using the conventional Hall effect technique have reported values between 1 and 9 cm^2/Vs [47]. These properties make kesterite materials a strong candidate to be used as an absorber layer in thin-film solar cells.

I.2.3. Phase Formation and Defects

II.2.3.1. Phase formation of kesterite materials

The composition of CZTSSe is typically analyzed using the atomic percentages of its cationic elements, copper (Cu), tin (Sn), and zinc (Zn), along with the anionic elements sulfur (S) and selenium (Se). This composition is often depicted in a ternary diagram, which is a section of a quaternary diagram with fixed anion compositions and varying cation compositions. Figure 2.4a shows a ternary diagram of CZTS, where each side of the triangle represents the atomic percentage of one of the three cations in CZTS. In the diagram, every point reflects a specific combination of these cationic percentages, with their sum always equaling unity. The central area marked by an asterisk denotes the region where the CZTS phase exists. However, experimentally achieving a pure CZTSSe absorber is highly challenging due to its narrow zone. According to a thermodynamic calculation by Scragg et al. [48], the kesterite phase of CZTS decomposes at elevated temperatures, leading to the formation of secondary phases. Apart from this narrow zone, six distinct zones are identifiable where minor crystalline phases coexist with CZTS. These zones are labelled in Figure (2.3,a) as Zn-rich, Cu-poor, Sn-poor, etc., and these labels serve to define the compositional positions of the absorber materials throughout this report.

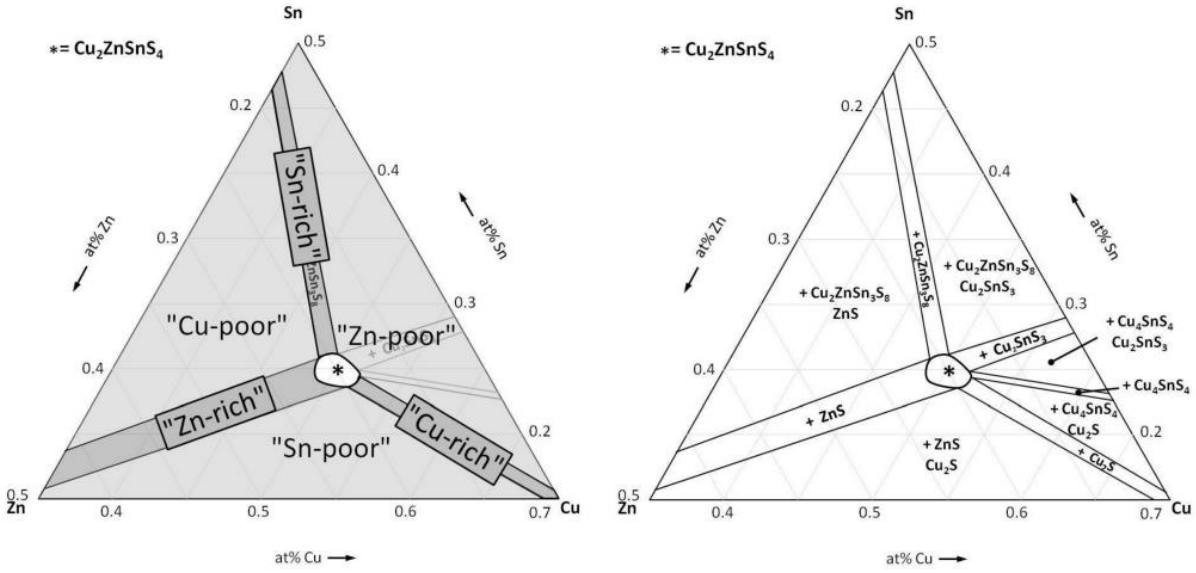

Figure 2. 4: Ternary diagram to define the compositional position of the CZTS absorber and the possible secondary phases arising from this position, adapted from Scragg et al. [47].

Figure 2.4b shows a ternary diagram depicting pure CZTS at various compositional positions. In all regions except for a small area marked by an asterisk representing pure CZTS, up to two additional secondary phases coexist with the CZTS absorber. Experimental investigations have identified the optimal cationic composition for highly efficient CZTS solar cells as Cu-poor and Zn-rich ([Cu]/[Zn+Sn]=0.8 and [Zn]/[Sn]=1.2) [49]. One of the key factors contributing to the superior efficiency in this region is the tendency to induce ZnS as a secondary phase, which is less detrimental than other secondary phases.

II.2.3.2. Defects in kesterite materials

Lattice defects are crucial properties of materials and play a significant role in their application in solar cells. These defects directly impact the generation, separation, and recombination of electron-hole pairs. Theoretical work by Professor S.H. Wei's team (NREL, Boulder Colorado) identified three types of defects: vacancies (V_{Cu}, V_{Zn}, V_{Sn}, and V_S), antisite defects (Cu_{Zn}, Zn_{Cu}, Cu_{Sn}, and Sn_{Cu}), and interstitial defects (Cu_i, Zn_i, and Sn_i) [9]. Certain defects, such as V_{Cu}, V_{Zn}, and Cu_{Zn}, facilitate p-type doping of CZTS, while others, such as Zn_{Cu}, Sn_{Zn}, and Cu_i, result in n-type doping. As depicted in Figure 2.5, the energy of formation for all p-type defects is lower than that for all n-type defects. Consequently, CZTS absorbers consistently exhibit p-type conductivity rather than n-type conductivity.

In general, various defects are commonly observed in CZTSSe absorbers, including vacancies, antisites, interstitials, and defect complexes [50]. These defects can create shallow donor levels, shallow acceptor levels, mid-gap states, and deep trap states within the bandgap of the absorber,

acting as recombination centres that reduce the power conversion efficiency (PCE). Figure 2.5 and Figure 2.6 illustrate the possible intrinsic defects and low-energy intrinsic defects and defect complexes in CZTS absorbers.

The enthalpy of defect formation can be calculated using density functional theory (DFT), which depends on the atomic chemical potential of the cations in the crystal. The Figure 2.5 shows these enthalpies for seven different chemical potentials (A to G), representing the limits of the single-phase domain, adapted from Chen et al. [50]. This analysis identified the p-doped Cu_{Zn} antisite as the most likely point defect for any growth condition of the material. However, Han et al. [51] demonstrated that the hole concentration is primarily controlled by V_{Cu} due to its shallower acceptor level (50 meV) compared to that of Cu_{Zn} (100 meV) (see Figure (2.5)). Intrinsic defects can also form defect complexes. The Figure 2.6 shows the formation energies of different defect clusters. The (Cu_{Zn}+Zn_{Cu}) cluster has the lowest formation energy, suggesting that it is the main defect complex in CZTSSe absorbers. Additionally, Dimitrievska et al. showed that Cu substitutional defects, specifically [V_{Cu} + Zn_{Cu}] clusters, significantly affect the open-circuit voltage (V_{OC}) [52]. It is possible to modify the V_{OC} by adjusting the amount of [V_{Cu}+Zn_{Cu}] defects. Cu-poor conditions during synthesis promote the ordering of Cu/Zn (001) planes by increasing the [V_{Cu}+Zn_{Cu}] cluster, which, in turn, widens the bandgap and increases the V_{OC} of the final device [53].

The primary factor contributing to the lower efficiency of CZTSSe solar cells is the open-circuit voltage (V_{OC}) deficit. The highest V_{OC} achieved with kesterite technology is approximately 60% lower than the maximum theoretical V_{OC} for the given bandgap, and it is also lower than the V_{OC} values achieved by CIGS or CdTe technologies. The main cause of this V_{OC} deficit is the recombination of photogenerated charge carriers within the bulk of the material and at the surface. According to Bourdais et al. [54], deep defects and electrically active grain boundaries are the major contributors to the high nonradiative recombination rates observed in CZTS materials. These defects and grain boundaries create recombination centers that significantly reduce the efficiency of charge carrier separation and collection, leading to an observed V_{OC} deficit.

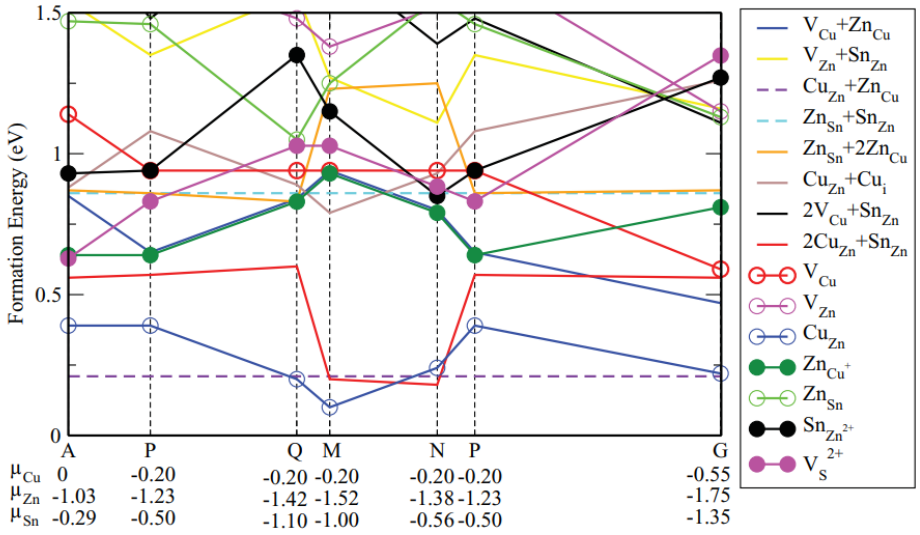

Figure 2. 5: The formation energy of low-energy defects in Cu2ZnSnS4 as a function of the chemical potential of the cations. The Fermi energy is assumed to be at the top of the valence band (strong p-type conditions), and all donor defects are fully ionized [53].

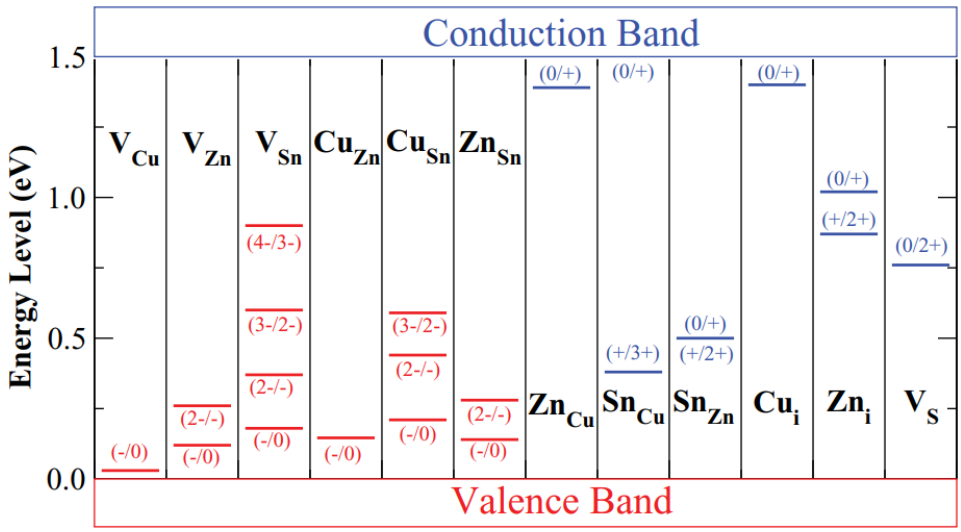

Figure 2. 6: The ionization levels of intrinsic defects in the bandgap of Cu2ZnSnSe4. The red bars show the acceptor levels, and the blue bars show the donor levels, with the initial and final charge states labelled in parentheses. This figure is adapted from [53].

II.3. Overview of the challenges associated with CZTS solar cells

II.3. 1. The structure of CZTS solar cell in tandem configuration

As in all other second-generation thin-film solar cells, CZTS solar cells are composed of five critical thin-film layers. One of the key components is the back contact, typically made of molybdenum (Mo) due to its high electrical conductivity and excellent thermal stability [55]. The molybdenum layer is usually deposited using physical vapor deposition (PVD) techniques,

such as sputtering. The most important part of the device is the absorber layer, which consists of CZTS (Cu_2ZnSnS_4). This layer is crucial for light absorption and typically has a thickness ranging from 1 to 1.5 µm. Directly on top of the absorber layer, a thin n-type CdS buffer layer is deposited. The thickness of the CdS layer is usually around 60 nm, and it is often applied using chemical bath deposition (CBD), which provides optimal coverage and uniformity. The front contact of the CZTS solar cell is formed by a transparent conductive oxide (TCO) layer, generally made from materials like zinc oxide (ZnO) and indium tin oxide (ITO). These materials are favored for their combination of high transparency and conductivity, allowing light to pass through while efficiently collecting and transporting electrical charge.

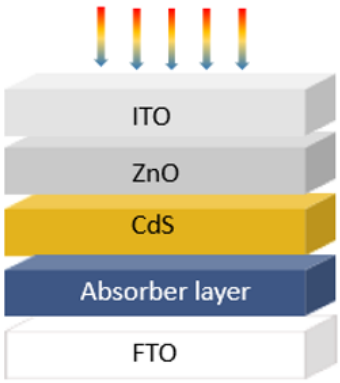

Figure 2. 7: The conventional structure of kesterite solar cell.

In conventional thin films solar cells, the back electrode is typically made of a metal such as molybdenum (Figure 4). This metal electrode is opaque, preventing any light from passing through to the c-Si bottom subcell. For the development of tandem solar cells, this poses a significant challenge. The objective is to develop the top cell (with absorbers such as CZTS, CIGS, or perovskite) on transparent electrodes, allowing light to transmit to the c-Si bottom subcell. The opaque back electrodes serve as a crucial component in single-junction solar cells. It provides the necessary electrical contact and structural support for the active layers. However, its opacity makes it unsuitable for tandem solar cells, where light needs to pass through the top cell to be absorbed by the bottom cell.

To address this limitation, the advancement of tandem solar cells requires the transition from opaque to transparent electrodes (Figure 5). This transition requires materials that exhibit both high electrical conductivity and optical transparency. Indium tin oxide (ITO) and fluorine-doped tin oxide (FTO) are prime candidates for this role due to their superior transparent conductive properties. The utilization of these materials enables the fabrication of transparent back contact, which is critical for the effective functioning of tandem solar cells.

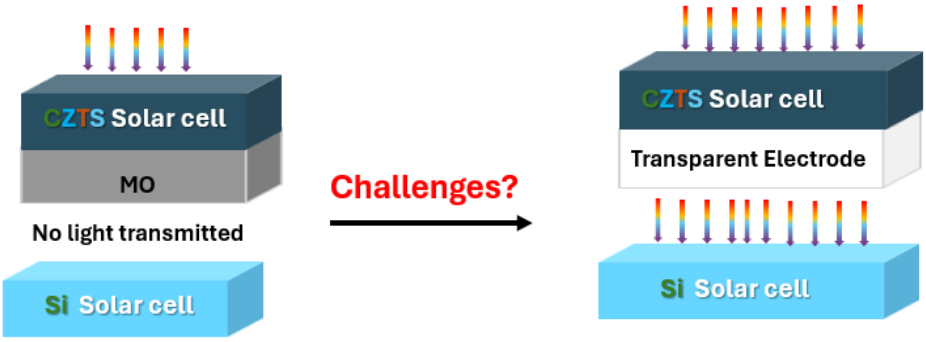

Figure.5. The challenges to develop tandem configuration using CZTS as top solar cells

II.3.2. The limiting factors of CZTS solar cell efficiencies

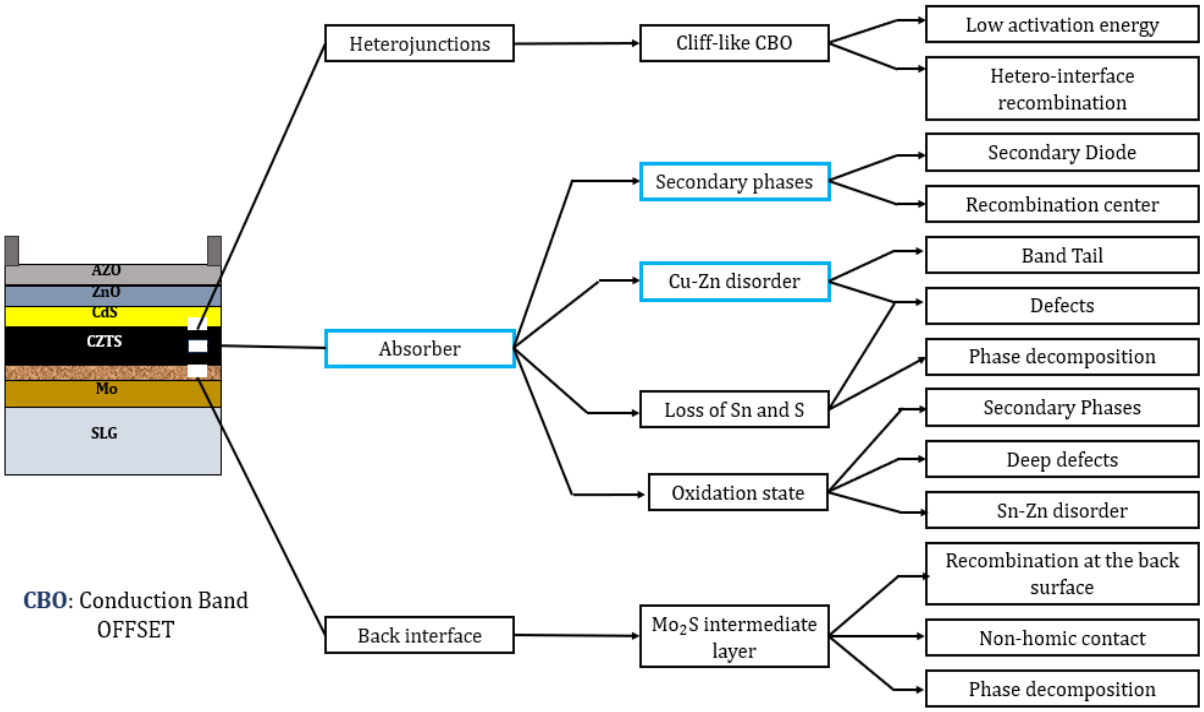

Figure 2. 8: The main factors limiting the efficiency of CZTS solar cells and their effect on the solar cell working.

In thin-film solar cells, the conversion efficiency is highly influenced by the properties of each material within the device structure. For kesterite-based solar cells, several challenges persist, particularly those associated with the absorber layer and its interfaces. This section provides an overview of these issues, focusing on the absorber-related problems as well as the interface challenges. Figure 2.8 illustrates the key challenges identified in kesterite-based solar cells, as reported in prior studies [7,15,47,49]. The analysis begins with a discussion of the challenges intrinsic to the absorber layer, such as defect states, low carrier mobility, and secondary phase formation. This is followed by an examination of the issues at the absorber-buffer heterojunction, including recombination losses and poor band alignment. Figure 2.8 provides a visual summary of these challenges, offering insights into the fundamental limitations of kesterite-based devices and potential strategies for their mitigation.

II.3.2.1 Challenges Related to the Absorber Layer

II.3.2.1.1. Secondary Phases

The synthesis of single-phase kesterite (CZTS) thin films is essential for achieving high-efficiency solar cells. However, the quaternary nature of kesterite alloys, which include multiple elements, poses significant challenges in producing a pure, single-phase material. Under the thermodynamic conditions typically employed for kesterite synthesis, the formation of several secondary phases is often unavoidable. These secondary phases can impact the performance of the solar cell. The commonly observed p-type secondary phases are $Cu_{2x}S$, SnS, and Cu_2SnS_3, which exhibit bandgaps ranging from 1.0 to 1.3 eV. These phases can act as recombination centers, reducing the open-circuit voltage (Voc) and negatively affecting the overall device efficiency [56]. The presence of CuS, a conductive phase, further exacerbates performance issues by lowering the short-circuit current (Jsc) of the solar cell. On the other hand, n-type secondary phases such as SnS_2 (with a bandgap of 2.5 eV) and ZnS (with a bandgap of 3.7 eV) introduce additional challenges. These phases can result in the formation of unwanted secondary diodes within the absorber layer, disrupting charge transport. Furthermore, high-resistance phases like ZnS contribute to increased absorber resistivity, leading to a reduction in both the current density (Jsc) and the fill factor (FF) of the solar cell [57]. Given the critical importance of achieving a pure kesterite phase for thin-film solar cell applications, eliminating secondary phases during the synthesis process remains a significant challenge. Developing strategies to suppress the formation of these secondary phases is essential for optimizing the electrical and optical performance of CZTS-based solar cells.

II.3.2.1.2. Cu-Zn disorder

In the kesterite structure, the similarity in ionic radii and electronic configurations between Cu^{+} and Zn^{2+} cations facilitate their mutual substitution within the lattice. This phenomenon results in the formation of Cu-Zn disorder, where Zn^{2+} ions partially occupy the 2c sites, and Cu^{+} ions partially occupy the 2d sites [58]. This cation exchange process gives rise to what is often referred to as "disordered kesterite". The Cu-Zn disorder leads to the formation of antisite defect pairs (CuZn + ZnCu) that compensate each other. These defect pairs exhibit low formation energies, making their occurrence highly probable during material synthesis. The disorder generates density tails of localized states within the absorber's bandgap, which act as recombination centers and limit the absorber's performance. Specifically, these localized states reduce the open-circuit voltage (Voc) by effectively narrowing the apparent bandgap of the material. As a result, controlling and minimizing Cu-Zn disorder is critical for improving the efficiency of kesterite-based solar cells, as the Voc is directly linked to the material's optoelectronic properties.

II.3.2.1.3. Multivalence of Cu and Sn

To synthesize a high-quality CZTS absorber, it is crucial to address fundamental challenges, including achieving a single-phase material with minimal harmful defects. The local chemical environment plays a significant role in influencing defect formation and determining the crystallographic phase. A particular challenge arises in alloys where cations can exhibit multiple oxidation states. In Cu_2ZnSnS_4 (CZTS), two of its constituent elements, copper (Cu) and tin (Sn), can exist in different oxidation states: Cu^{+} and Cu^{2+}, and Sn^{2+} and Sn^{4+}. In contrast, zinc (Zn) poses no such complication as it exists exclusively in the Zn^{2+} state.

The oxidation states in CZTS are typically Cu^{+}, Zn^{2+}, Sn^{4+}, and S^{2-}, which form the intended kesterite structure. However, the presence of Cu^{2+} can lead to the formation of Cu^{2+}-bonded secondary phases, such as CuS, which can degrade device performance. Similarly, secondary phases bonded with Sn and Zn can arise under certain conditions. Beyond secondary phase formation, the oxidation states of Sn, particularly Sn^{2+}, contribute to antisite defect formation and substantial lattice disorder. The presence of Sn^{2+} increases the likelihood of SnZn antisite defects, where Sn occupies Zn lattice sites [59]. The possibility of developing SnZn antisite defects increases significantly in this case. Minimizing the formation of such defect clusters and controlling the oxidation states of Cu and Sn are essential to improving the efficiency of CZTS-based solar cells.

II.3.2.2 interface challenges: Band Alignment at the p-n Heterojunction

At the p-n heterojunction of a solar cell, the energy bands of the absorber and buffer layers align to form a band offset, which can be described in terms of the conduction band offset (CBO) and valence band offset (VBO). The alignment at the heterointerface is critical for charge separation and carrier transport. Figure 2.9.a illustrates the heterojunction band diagram.

Two primary types of CBO are observed:

Positive CBO (Spike-like): This occurs when the conduction band maximum (CBM) of the buffer (n-type) is higher than that of the absorber (p-type), resulting in a spike-like alignment. A small positive CBO is ideal, as it prevents recombination while maintaining efficient charge transport.

Negative CBO (Cliff-like): This occurs when the CBM of the buffer is lower than that of the absorber, creating a cliff-like alignment. Under illumination, this configuration facilitates electron-hole recombination at the interface, particularly in the presence of defects, leading to significant recombination losses (Figure 2.9.b).

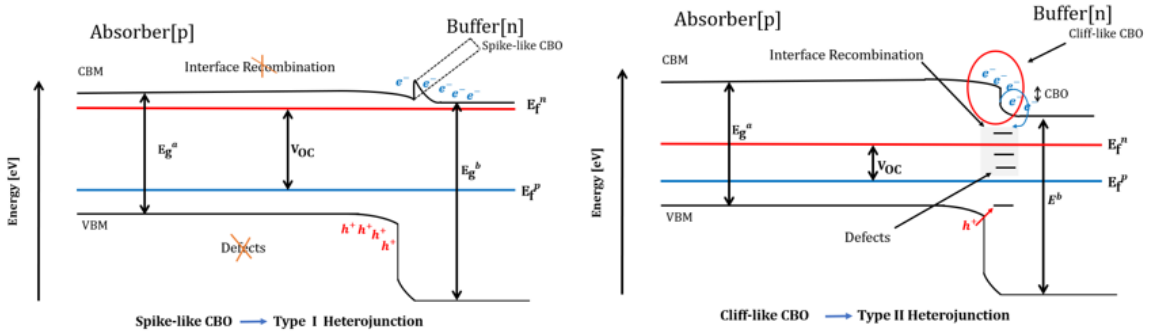

Figure 2. 9: Band diagram at the absorber/buffer heterojunction for type I (left) and type II (right) devices

An ideal CBO for heterojunction solar cells is a slightly positive spike-like alignment, as shown in Figure 2.9.a. However, if the spike becomes excessively high, photogenerated electrons from the absorber face a significant barrier, impeding their flow to the front contact. Theoretical analysis by Minemoto et al. [60], in CIGS chalcopyrite solar cells demonstrated that high efficiencies are achieved when the CBO at the CIGS/CdS interface is between 0 and 0.4 eV. A CBO exceeding 0.4 eV results in a reduced short-circuit current (Jsc) due to the high barrier at the heterointerface.

In CZTS kesterite solar cells, the band alignment at the CdS/CZTS heterointerface is similarly critical. The CdS buffer layer typically forms a positive spike-like CBO with the absorber, with an optimal offset range of 0.2–0.3 eV, facilitating effective charge separation and minimizing recombination losses. Proper control of the heterojunction band alignment remains a key challenge in optimizing the performance of CZTS-based solar cells.

II.4. Improving the Properties of Kesterite Materials

The efficiency of kesterite solar cells remains limited due to the persistent open-circuit voltage (Voc) deficit, with the current record efficiency at 14.9% in 2023 [7]. significantly lower than the 23.35% achieved by CIGS solar cells [61]. Tackling this performance gap necessitates addressing challenges such as the conduction band offset (CBO) at the CdS/CZTS heterointerface, intrinsic defects, and nonradiative recombination at interfaces. This section explores approaches to improving kesterite materials through band alignment optimization and doping/alloying strategies.

II.4.1. Band Alignment Optimization

The band alignment at the buffer-absorber heterointerface plays a critical role in determining charge separation and transport. An unfavorable cliff-like CBO between the CdS buffer and the CZTS absorber promotes recombination, leading to significant efficiency losses. Experimental efforts have focused on replacing CdS with alternative buffer materials that offer wider bandgaps and improved alignment. For instance, In_2S_3 has been used to optimize the interface and enhance Voc [62]. Similarly, materials such as ZnO_xS_{1-x}, ZnSnO [63], and $Cd_{1-x}Zn_xS$ have shown potential. Among these, $Zn_{1-x}Sn_xO$ and $Cd_{1-x}Zn_xS$ buffer layers have demonstrated significant Voc improvements, effectively mitigating recombination losses while facilitating better charge transport. These substitutions have proven to be effective in addressing band alignment issues, thus improving the overall efficiency of CZTS solar cells.

II.4.2 Doping and alloying

Cation substitution has emerged as a promising strategy to address intrinsic defects and optimize the electronic properties of kesterite materials. Replacing copper (Cu) with silver (Ag) forms Ag_2ZnSnS_4 (AZTS), which reduces deep-level defects and stabilizes the crystal structure due to the larger ionic radius of Ag^+ (1.14 Å compared to 0.74 Å for Cu^+). Ag substitution also enhances p-type conductivity and increases Voc by reducing Cu-Zn disorder and suppressing antisite defects such as CuZn and ZnCu, particularly at substitution levels greater than 6% [68, 75]. Theoretical studies indicate that Ag substitution raises the formation energy of antisite defects and clusters, such as AgZn + ZnAg, further improving defect suppression [66].

In addition to Ag, sodium (Na) has been extensively studied as a dopant in kesterite and CIGS solar cells. Sodium diffusion from the substrate during synthesis passivates grain boundary defects, improves grain size, and enhances carrier concentration. This is attributed to the formation of low-temperature Na_2Se_x liquid phases that act as fluxing agents, promoting absorber morphology improvements [67]. Furthermore, sodium treatment improves optoelectronic characteristics by reducing interface defect density [68], [69].

Similarly, lithium (Li) doping has demonstrated remarkable potential in CZTSSe solar cells. The ionic radius of Li^+ (0.73 Å) is close to that of Cu^+ (0.74 Å), allowing it to integrate into the lattice effectively. Studies have shown that Li doping enhances photovoltaic performance, achieving an efficiency increase of 11.8%, primarily through improved carrier concentration and mobility [67]. Li incorporation also tunes the bandgap without significantly altering the crystal growth process.

Alloying, which involves substituting isoelectronic cations to induce ionic size mismatches, is another critical strategy for bandgap engineering and defect suppression. For example, substituting tin (Sn) with germanium (Ge) has been shown to improve energy level alignment and reduce defect densities, leading to enhanced charge separation and transport. Substituting zinc (Zn) with cadmium (Cd) improves lattice matching with other components, reducing strain and defect formation. These substitutions fine-tune the material properties, making kesterite solar cells more efficient and stable.

II.4.3 Doping vs. Alloying

Doping and alloying are widely employed but distinct strategies. Doping modifies the material's electrical properties, such as charge transport and carrier concentration, without altering its crystal structure or optical characteristics. On the other hand, alloying introduces cation substitutions to achieve bandgap tuning and defect suppression. For instance, doping with alkali metals such as sodium (Na), lithium (Li), or potassium (K) enhances grain size, passivates defects, and increases hole carrier concentration [64,70–73]. In contrast, Ag alloying suppresses defect clustering and improves conductivity, while Ge alloying fine-tunes energy levels for better charge transport.

II.4.4. Challenges and Opportunities

Despite significant progress, challenges remain in distinguishing the effects of doping and alloying from other influences, such as changes in crystallization pathways and substrate-derived alkali diffusion. Continued research into these strategies is necessary to fully realize the potential of kesterite solar cells. By optimizing band alignment, reducing defects, and improving carrier

dynamics through cation substitution and doping/alloying, kesterite solar cells can achieve higher efficiencies and become a competitive alternative in photovoltaic technology.

In this thesis, we aim to study and further develop the strategies outlined above to address the key limitations of kesterite solar cells. Each approach, including band alignment optimization, cation substitution, doping, and alloying, will be explored in detail to assess their impact on the material properties and device performance. The subsequent sections of this report are structured to focus on the effects of each approach individually, providing a comprehensive analysis of their influence on bandgap tuning, defect suppression, carrier dynamics, and overall photovoltaic efficiency. By systematically investigating these strategies, this thesis seeks to contribute to the advancement of kesterite-based solar cell technologies and provide insights into their potential for achieving higher efficiencies and improved stability.

Chapter 3: Synthesis and Characterization of Kesterite Thin films

Over the past few decades, kesterite materials have been synthesized using various techniques, each imparting distinct effects on the properties of the final absorber layer. For the formation of CZTSSe thin films and their integration into photovoltaic (PV) devices, both physical and chemical deposition methods have been extensively explored.

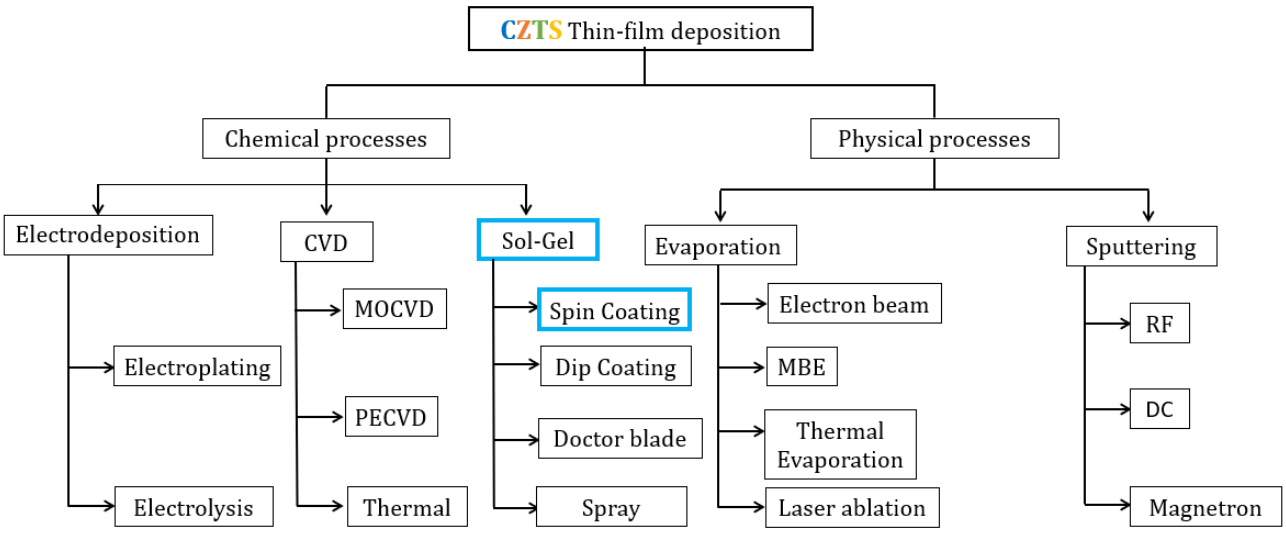

Figure 4. 1: Kesterite solar cell thin-film deposition techniques

Vacuum-based deposition techniques, such as sputtering and thermal evaporation, have demonstrated their ability to produce high-performance kesterite thin films, contributing to enhanced efficiencies in solar cell applications. However, nonvacuum methods have gained significant attention in recent years as cost-effective alternatives for fabricating thin films. While vacuum-based techniques are known for their high precision, they are associated with high costs, low material utilization, and substantial energy consumption. In contrast, nonvacuum approaches are cost-efficient, energy-saving, and capable of producing uniform, high-quality thin films. Among these, solution-based techniques such as the sol-gel method have emerged as particularly promising due to their simplicity, scalability, and the ability to control process parameters effectively. Consequently, there is growing interest in utilizing sol-gel techniques for the fabrication of CZTS thin-film solar cells, given their potential for reducing production costs while maintaining excellent material quality.

In this chapter, we focus on the preparation of CZTS materials using the sol-gel spin-coating method for Sn-kesterite and Sputtering method for Ge-Keserite. The chapter begins with a detailed description of the sol-gel process, covering each step from the preparation of the solution to the deposition of the precursor. This is followed by an overview of the CZGSSe precursor preparation through sputtering, emphasizing the critical parameters and their impact on material quality. Lastly, the growth mechanism of kesterite materials is discussed, with a particular focus on the annealing process, a crucial step common to both physical and chemical approaches for producing high-quality kesterite absorbers. This chapter aims to provide a comprehensive understanding of these synthesis methods and their role in optimizing the properties of CZTS thin films.

III.1. Generality of the sol-gel method

The history of sol-gel technology traces its evolution from its origins in the 1970s as a method for preparing homogeneous glasses and ceramics at lower temperatures than traditional melting and sintering processes [74]. By 1984, the scope of sol-gel processing had expanded to include inorganic-organic hybrid materials, and by 1995, its applications had diversified into fields such as electronics, chemistry, mechanics, and medicine. Today, sol-gel technology is not only used to enhance the performance of existing functional materials but also to discover new materials with tailored properties.

In sol-gel systems, a sol is defined as a stable dispersion of colloidal particles within a liquid, while a gel refers to a solid network immersed in a continuous liquid phase. Gelation typically occurs through the formation of covalent bonds between sol particles, although reversible bonds, such as van der Waals forces, may also contribute. The stability of sols is a critical factor and is typically maintained through electrostatic repulsion or the use of organic additives to prevent aggregation. Gelation may also be induced by solvent evaporation, particularly during the production of thin films or fibers. When wet gels are dried, they form xerogels, which shrink significantly due to capillary forces. Alternatively, aerogels retain the gel's original structure when dried under controlled conditions [75]. The sol-gel process generally involves hydrolysis and polycondensation reactions of metal alkoxides or chlorides in solution, resulting in the formation of a sol. The sol then undergoes polymerization to form a wet gel, which is subsequently dried to yield a solid material. Various purification techniques, such as extraction, ultrafiltration, or low-temperature evaporation, can be employed during sol-gel processing to improve material quality [76].

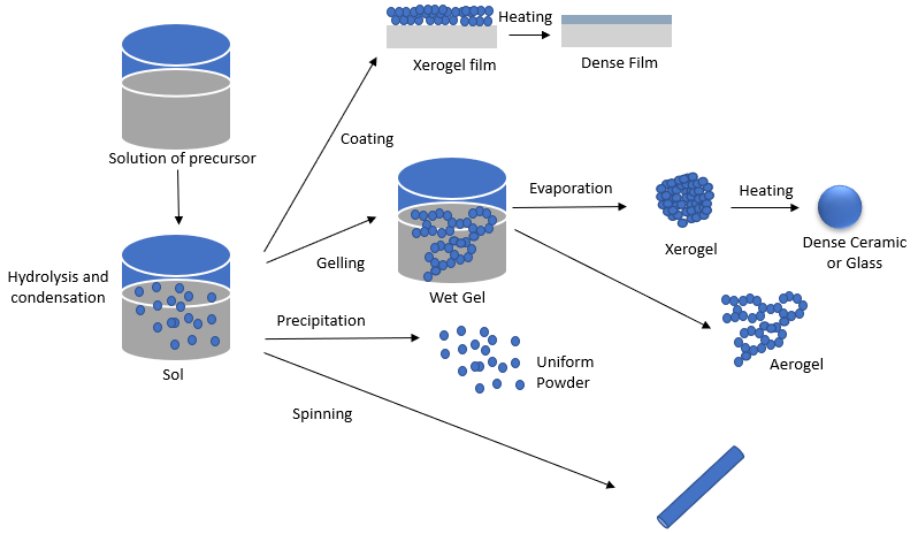

Figure 4. 2: Different sol–gel processing steps were used to control the final morphology of the product.

The sol-gel technique is extensively utilized for thin-film coatings, leveraging metal-organic or inorganic precursors to achieve precise material properties. Metal alkoxides are commonly employed due to their ease of hydrolysis and condensation, which facilitate the formation of amorphous metal oxides. The process involves careful control of the hydrolysis rate, followed by deposition techniques such as spin coating or gravity deposition, and subsequent drying. These steps enable the production of thin films with tailored structural and functional properties, making the sol-gel process a versatile tool for advanced material synthesis.

III.2. Sol-gel for kesterite thin film synthesis

The preparation of CZTS via the sol–gel method involves 3 steps: solution preparation, deposition of the solution on the substrate, and annealing (Figure 3.3). These steps should be carefully controlled to achieve the desired properties of the final prepared absorbers [77].

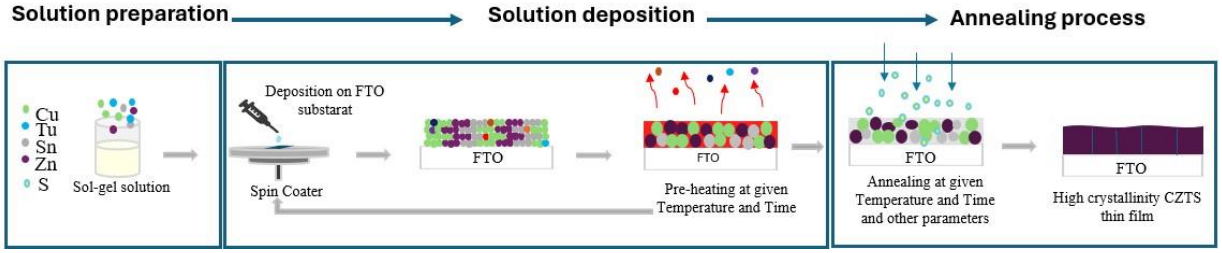

Figure 4. 3: Steps of the sol–gel method for the synthesis of kesterite materials.

III.2.1. Preparation of the solution and deposition for Sn-kesterite synthesis

The first step in synthesizing CZTS absorbers via the sol–gel method involves preparing CZTS solutions. This preparation begins by dissolving various metal salt precursors such as acetates, chlorides, nitrates, and sulfates in organic solvents such as 2-methoxyethanol, DMSO, or DMF [78]. The choice of precursors and solvents is pivotal in achieving high-quality absorbers. Different types of precursors, including chlorides, acetates, nitrates, sulfates, carbonates, organometallic compounds, oxides, elemental forms, and compounds such as citrates and oxalates, can be used. The selection and concentration of these materials affect the properties and performance of the final CZTS thin films.

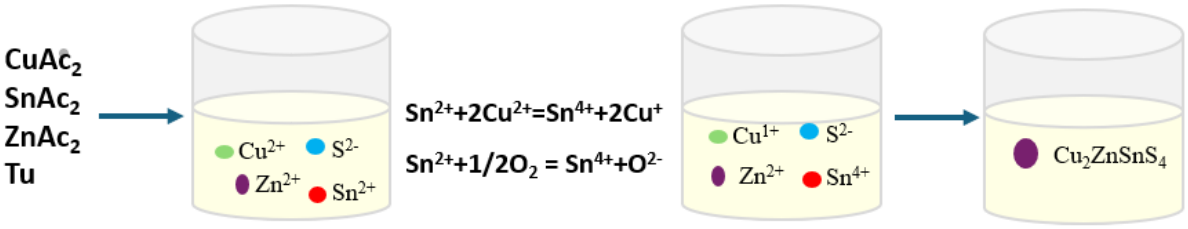

Figure 4. 4: The process of sol-gel solution synthesis for CZTS materials

This reaction process occurred during the sol-gel solution preparation begins with the formation of thiourea-metal complexes. The general steps and reactions are as follows [21]:

1-**Complex Formation (Equation 1)**:

Metal ions (M) such as Cu^{2+}, Zn^{2+}, and Sn^{2+} react with thiourea (Tu) to form thiourea-metal complexes:

$$M–X+Tu \rightarrow [M(Tu)m]–X \qquad (1)$$

Where M represents metal ions (Cu, Zn, and Sn),X represents anions (such as CH_3COO^- or Cl^-), [M(Tu)m]–X represents the thiourea-metal complex.

2-Alcoholysis and Condensation Reactions (Equations 2 and 3):

The thiourea-metal complex undergoes alcoholysis with 2-methoxyethanol (ROH):

$$[M(Tu)m]–X+ROH \rightarrow [M(Tu)m]–OR+H–X \qquad (2)$$

This reaction produces an intermediate complex with an organic chain attached M(Tu)m]–OR and a byproduct acid (H–X).

The resulting complexes then undergo polycondensation:

$$[M(Tu)m]–X+[M(Tu)m]–OR\rightarrow[M(Tu)m]–O–[M(Tu)m]+R–X \quad (3)$$

In this step, complexes link together through an oxygen bridge, resulting in the formation of nanoparticles. Then, during the deposition process these complexes, leading to sulfide formation and volatile byproducts.

Spin-coating is a technique for creating thin uniform films, which typically range from nanometers to micrometers in thickness. The process, which has been in use for more than fifty years, involves applying a polymeric solution onto a rotating substrate. As the substrate spins, the centrifugal force spreads the solution outwards while solvent evaporation leaves behind a thin film. Spin coating is used in various industries, including semiconductor manufacturing and optical devices.

The process includes four main stages: fluid dispensing, spin-up, spin-off, and evaporation. Key parameters such as the volume of dispensed fluid, spin speed, viscosity, and concentration affect the final film thickness and uniformity. Adjusting these parameters allows precise control over the film's properties.

Spin coating is especially important in the production of CZTS (copper zinc tin sulfide) thin films for solar cells. The ability of this technique to produce uniform films helps optimize the performance of CZTS solar cells by controlling the film thickness and morphology. Recent advancements have demonstrated that spin coating can achieve high efficiency in CZTS-based solar cells, making it a crucial method for developing cost-effective and efficient photovoltaic devices.

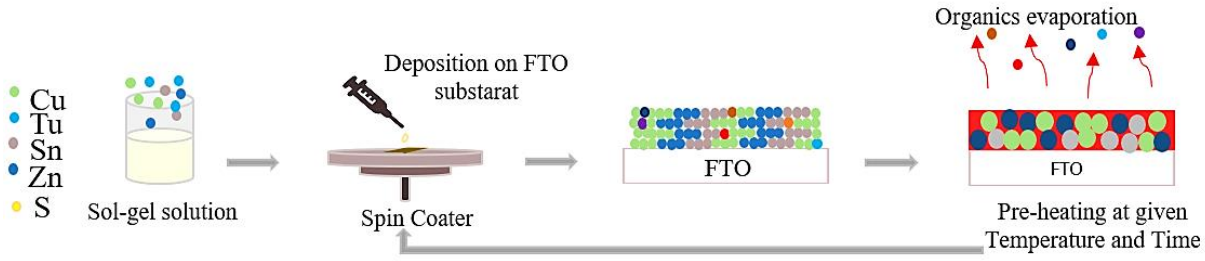

Figure 4. 5: Sequential steps of CZTS sol–gel synthesis for kesterite thin-film formation

III.2. Vacuum-Based Deposition methods (PVD) for Ge-kesterite

Physical vapor deposition (PVD) techniques, operating under vacuum (low or high), were employed to deposit multiple layers critical for the fabrication of kesterite solar cells. PVD

ensures that the chemical composition of the source material is retained in the deposited thin films, a feature essential for maintaining material integrity in multi-layered devices. Among the PVD techniques utilized in this thesis, sputtering played a central role due to its versatility and ability to produce uniform, high-quality thin films.

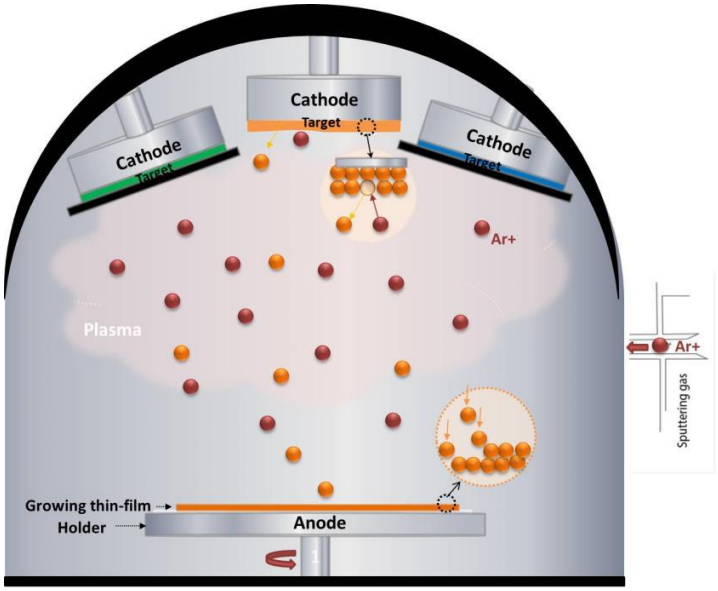

Figure 4. 6: The process of PVD sputtering

II.2.1. Sputtering: Principle and Parameters

Sputtering involves the ejection of microscopic particles from the surface of a target material through energetic particle bombardment, typically achieved using a plasma of non-reactive gas, such as argon (Ar). The ejected particles, possessing high kinetic energy, are deposited onto all exposed surfaces within the chamber, including the substrate, forming homogeneous thin films.

The efficiency and quality of the deposition process depend on several parameters:

- **Target area:** Larger target areas increase the deposition rate (directly proportional).
- **Target-to-substrate distance:** Greater distances reduce deposition efficiency (inversely proportional).
- **Power applied:** Higher power maintains plasma stability and enhances deposition rates (directly proportional).
- **Chamber pressure:** Lower pressure ensures higher deposition rates by reducing collisions (inversely proportional).

- **Deposition time:** Longer durations lead to thicker films (directly proportional).
- **Material properties:** Sputtering rates vary with material characteristics, requiring optimization for each target.

To maintain stable plasma and ensure uniform deposition, direct current (DC) or radiofrequency (RF) generators are employed, chosen based on the material properties of the target.

III.2.2. DC Generator for Ge-Kesterite Deposition

Direct current (DC) sputtering is the preferred method for depositing conductive materials, such as metals, due to its ability to prevent surface charge accumulation on the target. This ensures stable plasma and consistent deposition rates throughout the process. In the case of Ge-kesterite, Mo, Cu, Zn, and Ge thin films were deposited using DC sputtering.

To achieve pure Ge-kesterite precursors with the desired composition, several experiments were conducted to optimize the deposition process. The optimal ratios were determined as:

- **Cu/(Zn+Ge) =1.06**
- **Zn/Ge=0.7**

These ratios were controlled by adjusting the thickness of each metallic layer in the stack. For each substrate configuration, the metallic precursor layers (Cu/Zn/Ge) were sequentially deposited, ensuring precise control of layer thickness and uniformity.

Figure 4. 7: The process of sol-gel solution synthesis for CZTS materials

III.2.2. RF Generator for TCOs deposition

For non-conductive materials, such as transparent conductive oxides (TCOs), radiofrequency (RF) sputtering is employed to address surface charge accumulation, which can destabilize

plasma and lead to inconsistent deposition rates. RF sputtering uses alternating current (AC) to remove charges from the target surface, stabilizing the deposition process. In some cases, pulsed DC sputtering can also be applied for similar effects.

In this thesis, ZnO and In_2O_3:SnO_2 (ITO) thin films were deposited using pulsed DC sputtering, ensuring high-quality, uniform coatings. These TCO layers are critical components for solar cell devices, as they provide high conductivity and transparency, enabling efficient light transmission and charge collection.

III.3. Growth mechanisms and annealing process for kesterite synthesis

Annealing is a thermal treatment process that involves heating a material to a specific temperature, maintaining it at that temperature for a period, and then cooling it at a controlled rate or naturally. The detailed stages and purposes of the annealing process are as follows:

Heating: The material is heated to a temperature above its recrystallization point but below its melting point. This temperature varies depending on the material; for metals, it is typically between 30 and 50% of their melting temperature.

Soaking: The material is held at this high temperature to allow for atomic diffusion. This stage helps homogenize the microstructure, relieves internal stresses, and reduces the number of dislocations. The duration of this phase depends on the material thickness and the desired properties.

Cooling: The material is cooled at a controlled rate, which can vary depending on the desired final properties. Slow cooling often leads to a softer, more ductile material, whereas faster cooling can retain certain phases and properties developed during soaking. Annealing serves multiple purposes in material processing. First, it relieves internal stresses generated during manufacturing processes such as welding, machining, or cold working, contributing to improved structural integrity and stability. Additionally, annealing softens materials, enhances ductility and reduces hardness, thereby facilitating easier manipulation in subsequent manufacturing stages. Moreover, it induces microstructural changes, refines the grain structure, and consequently enhances mechanical properties such as strength, toughness, and hardness. Furthermore, annealing plays a crucial role in improving electrical properties, particularly in materials such as copper, by minimizing impurities and dislocations, thereby increasing electrical conductivity. Collectively, these aspects underscore the importance of annealing as a

versatile thermal treatment method in materials science and engineering. Various types of annealing techniques cater to specific material properties and applications. Full annealing involves heating the material above its critical temperature and then slowly cooling it to refine its microstructure, enhancing its mechanical properties. Process annealing is conducted at lower temperatures to soften work-hardened metals, increasing their ductility for further processing. Stress-relief annealing, which is performed below the recrystallization point, alleviates internal stresses without significantly altering the material's structure. Spheroidizing targets high-carbon steels, forming a spheroidal carbide structure to increase their machinability and ductility. These annealing methods have diverse applications across industries. In metallurgy, they improve the workability and mechanical properties of metals and alloys. In electronics, annealing enhances the electrical properties of semiconductor materials. Moreover, in glass manufacturing, annealing removes internal stresses, bolstering the durability and strength of glass products. Collectively, these annealing techniques play pivotal roles in optimizing material characteristics to meet specific performance requirements in various sectors.

Annealing CZTS (copper zinc tin sulfide) is a critical step in its fabrication process, which is aimed at optimizing its structural and electrical properties. This thermal treatment involves heating the CZTS material to specific temperatures in controlled atmospheres, typically in a tubular furnace (Figure 3.6). Annealing facilitates the rearrangement of atoms within the CZTS lattice, leading to a more ordered crystal structure. This process helps eliminate defects, dislocations, and grain boundaries, ultimately improving the electrical conductivity of the material and increasing its suitability for solar cell applications.

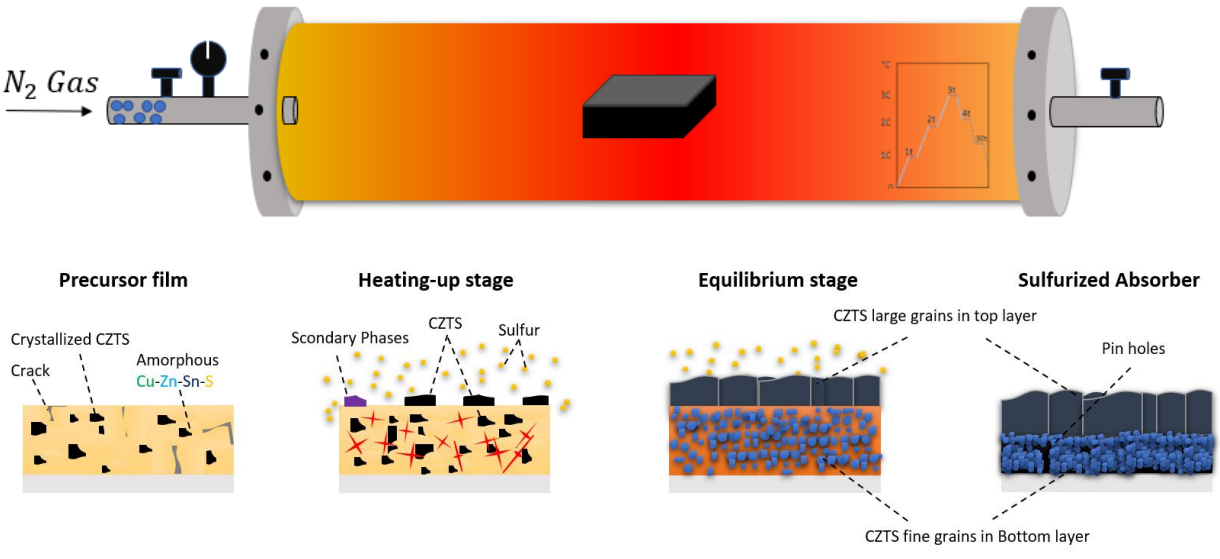

Figure 4. 8: Schematic representation of a sulfurization furnace and a schematic diagram illustrating the grain growth during each stage of the sulfurization process

Following annealing, sulfurization or selenization processes are often employed to tailor the properties of CZTS thin films further. Sulfurization involves the introduction of small quantities of sulfur powder into a graphite box containing the CZTS precursor. These precursors are then heated in a controlled atmosphere inside a tubular furnace, allowing the sulfur atoms to diffuse into the CZTS lattice. This incorporation of sulfur alters the material's composition and bandgap, enhancing its light-absorbing properties and overall efficiency as a photovoltaic material.

A schematic diagram is suggested to illustrate the crystal growth mechanism in the sulfurization process. In most cases, sufficient sulfur vapour uniformly penetrates the precursor film with a loose, porous surface, leading to crystallization that occurs preferentially in the top layer with island-like grains. These small grains eventually mix and ripen to form larger grains. Nucleation and crystallization occur simultaneously on the surface and inside the precursor film; however, fine grains are typically formed in the bottom layer rather than in the large grains in the top layer. This discrepancy can introduce more grain boundaries and bulk defects, which negatively affect device efficiency and represents one of the challenges in kesterite-based solar cells.

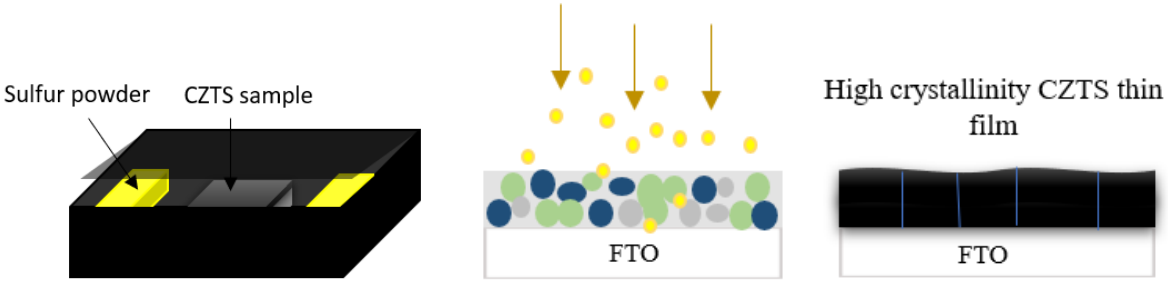

Figure 4. 9: Schematic representation of a graphite box used in the annealing process

III.4. Characterization methods used in this work

III.4.1. X-ray diffraction (XRD)

Physical principle	X-ray Diffraction (XRD) relies on the elastic scattering of X-rays by the core electrons of atoms arranged in a crystalline lattice. The periodic nature of the solid's atomic structure leads to constructive or destructive interference of the scattered X-rays, depending on

	their angle of incidence. This behavior is governed by Bragg's Law: $n\lambda=2d\sin\theta$. Constructive interference occurs when Bragg's condition is met, allowing XRD to determine the crystal structure, lattice parameters, and orientation of the material.
Information	**Crystalline Structure (Phase) and Space Group** The crystalline structure and phase of a material are characterized by its space group, which defines the symmetry of the crystal lattice. Crystals with the same structure exhibit similar XRD patterns, though slight variations may occur due to differences in the core electrons of the constituent atoms. These variations influence the scattering intensity and peak positions. **Lattice Parameters and Cell Volume** Through refinement techniques applied to XRD data, the lattice parameters (dimensions of the unit cell) and cell volume can be accurately determined. These parameters provide essential insights into the material's crystal structure and any potential distortions or changes caused by doping, alloying, or external conditions.
XRD of kesterite compounds	Isoelectronic cations, such as Cu^{+}, Zn^{2+}, and Ge^{4+}, interact with X-rays in a similar manner due to their identical scattering factors. This similarity complicates the differentiation between tetragonal polymorphs like kesterite (I4) and stannite ($I4_2m$), as their XRD patterns are often indistinguishable. Crystals with lower symmetry generate superstructure peaks that can help differentiate phases. However, identifying tetragonal secondary phases with higher symmetry, such as ZnSe ($F\bar{4}3m$) and Cu_2SnSe_3 ($F\bar{4}3m$), remains challenging due to significant peak overlap in the diffraction patterns. This overlap obscures the unique signatures required to discern these phases accurately.

III.4.2. Raman spectroscopy

Physical principle	Raman spectroscopy is based on the inelastic scattering of photons in the UV to NIR range as they interact with the vibrational modes of a solid or molecule. During this process, a photon is scattered with a small energy gain or loss, corresponding to the vibrational energy of the material. The photon is then reemitted at the same angle with a slightly shifted wavelength. The resulting Raman spectrum is unique to each material, with each peak corresponding to a specific vibrational mode. This characteristic spectrum provides detailed information about the material's structural and compositional properties.
Information	**Crystalline Structure (Phase) and Space Group** Raman spectroscopy can identify the crystalline structure and phase of a material through its unique vibrational modes. While crystals with the same structure have similar spectra, slight shifts in vibrational energies occur due to differences in composition or lattice distortions, enabling the differentiation of polymorphs. **Composition and Defect Concentrations (Calibrated)** Calibrated Raman spectra allow the precise determination of chemical composition and the identification of secondary phases or impurities. Additionally, defect concentrations such as vacancies or interstitials can be quantified through specific defect-related peaks or shifts, providing insights into material quality and structural integrity.
Raman of kesterite compounds	Raman spectroscopy is an essential tool for analyzing **kesterite materials**, enabling the detection of: • **Cu and Zn-related defects**: These defects influence the vibrational modes, providing insight into disorder and antisite defects in the crystal lattice. • **Secondary phases**: Multiple laser wavelengths can be used to exploit **energy resonance effects** with the band gap, improving

	the identification of secondary phases like **ZnS**, **Cu_2SnS_3**, or other undesired compounds. This makes Raman spectroscopy highly effective for evaluating the structural quality and phase purity of kesterite absorbers.

III.4.3. Scanning electron microscopy (SEM)

Physical principle	SEM utilizes a **focused beam of high-energy electrons** with wavelengths shorter than those of optical photons to create detailed images of a sample's surface. By scanning the surface, SEM provides high-resolution images and insights into the material's morphology and topography.
Information	**Secondary Electrons (SE):** SE imaging provides detailed information about the topography and morphology of a sample's surface. It is particularly useful for observing the cross-section of thin-film stacks to determine film thickness and layer structure through signal contrast. **Backscattered Electrons (BSE):** BSE imaging offers similar insights into morphology and surface roughness while also providing atomic number contrast, where heavier elements backscatter more efficiently, aiding in material identification. **Auger Electrons:** Detects spatially resolved composition, enabling detailed surface analysis of elemental distribution. **Energy Dispersive X-rays (EDX):** EDX complements SEM by offering spatially resolved compositional analysis, identifying the elemental composition within specific regions.
SEM of kesterite compounds	**Secondary and Backscattered Electrons (SE and BSE):** • Provide insights into grain size and morphology, such as faceted or rounded grains. • Identify single- or double-layer morphologies, revealing grain growth mechanisms.

	• Detect secondary phases, e.g., planar crystals of SnSe or bright impurities of ZnSe. **Auger Electrons:** • Offer surface-sensitive compositional analysis, enabling detailed surface characterization. **Energy Dispersive X-rays (EDX):** • Determine the bulk composition of the material by analyzing emitted X-rays.

III.4.4. UV-Visible spectroscopy

Physical principle	UV-Visible spectroscopy is based on the interaction of ultraviolet (UV) and visible light with matter. When light passes through or is reflected by a material, specific wavelengths are absorbed, corresponding to the electronic transitions between molecular or atomic energy levels. The resulting absorption spectrum provides information about the material's electronic structure, bandgap energy, and concentration of absorbing species.
Information	Spectroscopy in the ultraviolet (UV), visible (Vis), and near-infrared (NIR) regions of light is used to analyze the optical properties of materials: **Transmission Spectroscopy:** Measures the fraction of light that passes through a material, providing information on transparency and optical losses. **Absorption Spectroscopy:** Determines the amount of light absorbed by the material, critical for analyzing bandgap energy and optical transitions. **Reflectance Spectroscopy:** Quantifies the light reflected from the surface, offering insights into surface properties, refractive index, and material roughness. By combining these techniques, a comprehensive understanding of a material's optical behavior across the UV-Vis-NIR spectrum can be

	achieved, essential for applications like photovoltaics and optoelectronics.
UV-Visible of kesterite compounds	**Band Gap and Fluctuations:** The band gap can be determined from the material's absorption spectrum by identifying the onset of significant absorption. Band gap fluctuations, often caused by structural or compositional disorder, are analyzed through the Urbach energy, which quantifies the tailing of electronic states into the band gap. **Reflection Losses:** Reflection losses, arising from light reflected at the surface of a device, are evaluated using reflectance spectroscopy. These losses directly impact the efficiency of optoelectronic devices, as reflected light cannot contribute to carrier generation.

Chapter 4: Experimental optimization of the CZTS synthesis using Sol-gel method

Before initiating experimental studies, extensive optimization efforts were conducted to establish protocols for producing high-quality kesterite materials. The sol-gel process, with its multiple steps, was optimized to achieve the desired material properties. This section focuses on the development of two distinct protocols, differentiated by the oxidation states of the metal ions used during solution preparation. The solution synthesis phase involved careful selection of metal precursors (e.g., acetates, chlorides, nitrates) to ensure homogeneous sol formation. Following this, the annealing conditions were systematically refined, including temperature, duration, atmosphere, and ramp rate, to promote crystallization and phase purity. The optimization of these protocols and processes provides a comprehensive foundation for the synthesis of kesterite thin films with enhanced performance, paving the way for further studies in this thesis.

IV.1. Optimization of Sol-Gel solution Preparation using Sn^{2+} and Cu^{2+}

The preparation of CZTS solutions is a key step in determining the final properties of CZTS absorbers. However, precise control of the mass of the metal salt precursor in sol–gel solutions is essential for synthesizing high-quality Cu2ZnSnS4 (CZTS) thin films. Achieving the correct stoichiometry and composition is crucial for ensuring the optimal performance of the resulting material in photovoltaic applications. Even minor deviations in the mass of the precursors can lead to significant changes in the properties of the final CZTS films, affecting their efficiency and stability. In this section, we focus on the meticulous preparation of the precursor solution for the sol–gel process, starting from the molecular formula of Cu2ZnSnS4. In addition, we will demonstrate how to calculate the necessary masses of the chemical precursors to achieve the desired molar ratios. Additionally, we explored two different protocols with distinct precursor compositions to understand the impact of the protocol on the properties of the final CZTS films. We started our study by preparing a sol-gel solution with the following precursors, which were widely used previously in kesterite synthesis: zinc(II) acetate dihydrate, copper(II) acetate dihydrate, tin(II) chloride dihydrate, and thiourea. On the basis of the Cu_2ZnSnS_4 structure, the desired stoichiometric ratios are Zn/Sn = 1, Cu/(Zn + Sn) = 1, and S/(Cu + Zn + Sn) = 1. By

fixing the mass of zinc(II) acetate dihydrate at 1.18 g (wich is the starting point for our protocol and represents 0.25 mol/l of SnCl2 in 20 ml of solvent), which provides a number of Zn^{2+} ions (3.23×10^{21}), the necessary number of Sn^{2+} ions should be the same as that for Zn^{2+}, the number of Cu^{2+} ions should double, and the number of S^{2-} ions should be four times that of Zn^{2+}. The calculated number of ions and corresponding masses are provided in Table (4.1).

Table 4.1. Calculated Ion Numbers and Corresponding Masses for Sol-Gel Precursors in CZTS Synthesis

Precursor	Number of ions	Masses (g)
Zinc(II) acetate dihydrate	3.23×10^{21}	1.18
Copper(II) acetate monohydrate	6.46×10^{21}	2.14
Tin(II) chloride dihydrate	3.23×10^{21}	1.21
Thiourea	1.292×10^{22}	1.63

For CZTS materials, off-stoichiometry is necessary for p-type conductivity and other optoelectronic properties. For this purpose, the literature often reports a decrease in the number of copper atoms, which is typically approximately 15% less than the stoichiometric composition, and an approximately 85.75% excess of thiourea is incorporated. Several off-stoichiometric compositions have been studied for kesterite materials, and Cu-poor and Zn-rich compositions have been reported to be optimal. This stoichiometry is used in almost all recent works on kesterite materials and can be obtained by reducing the amount of Cu to increase the p-type conductivity of CZTS thin films by increasing the concentration of copper vacancies V_{cu} [79]. In addition to the manipulation of the copper content, the presence of thiourea plays a crucial role in the sol–gel reaction process for CZTS synthesis. Thiourea serves as the sulfur source necessary for the formation of the CZTS structure. During the sol–gel process, thiourea decomposes to release sulfur, which reacts with the metal precursors to form the desired CZTS aggregates in the solution. By providing an excess of thiourea in the solution, complete pre-sulfurization is achieved [80] . Moreover, the role of thiourea extends beyond the sulfur source. It also acts as a complexing agent, facilitating the dissolution of metal salt precursors and promoting homogeneity within the sol-gel solution. On the basis of the previous explanations, in our work, we used the metal salt masses reported in Table 2 to explain the Cu-poor and Zn-rich composition, as presented in Table 3.

Table 4.2. Metal–salt Masses Used for Sol-gel Synthesis of Cu-poor and Zn-rich CZTS

Precursor	Mass (g)	Molar Mass (g/mol)	Number of Ions
Zinc(II) acetate dihydrate	1.18	219.51	3.23×10^{21}
Copper(II) acetate monohydrate	1.83	199.65	5.52×10^{21}
Tin(II) chloride dihydrate	1.21	225.65	3.23×10^{21}
Thiourea	3.04	76.12	2.40×10^{22}

Table 4.3. Resulting Stoichiometric Composition of Cu-poor and Zn-rich CZTS

Zn/Sn	Cu/Zn+Sn	S/Cu+Sn+Zn
1.00	0.85	2.00

Figure 4. 1: Protocol 1 used to prepare the CZTS solution.

IV.2. Optimization of sol-gel solution preparation using Cu^{+1} and Sn^{4+} (Protocol 2)

Another protocol was developed in this work by using Cu and Sn precursors: zinc(II) acetate dihydrate, copper(I) chloride, tin(IV) chloride, and thiourea. The mass of zinc(II) acetate dihydrate is fixed at 1.01 g (0.25 mol/l Zn(oAc) in 10 ml of the solvent, which is reported for many works using CuCl metal–salt precursors), resulting in 2.77×1021 Zn^{2+} ions. On the basis

of the Cu_2ZnSnS_4 structure, the calculated number of ions and corresponding masses for the other precursors are provided in Table (4).

Table 4.4. Calculated Ion Numbers and Corresponding Masses and Volumes for Sol-gel Precursors in CZTS Synthesis

Precursor	Number of ions	Volume (ml)	Masses (g
Zinc(II) acetate dihydrate	2.77×10^{21}	-	1.01
Copper(I) chloride	5.53×10^{21}	-	0.910
Tin (IV) chloride	2.77×10^{21}	0.585	1.198
Thiourea	1.10×10^{22}	-	1.39

With the same strategy used previously, the number of copper atoms was reduced, typically by approximately 10.43% less than the stoichiometric amount, and an approximately 80% excess of thiourea was incorporated.

Table 4.5. Metal–salt Masses Used for Sol-gel Synthesis of Cu-poor and Zn-rich CZTS

Precursor	Number of ions	Volume (ml)	Masses (g
Zinc(II) acetate dihydrate	2.77×10^{21}	-	1.01
Copper(I) chloride	4.95×10^{21}	-	0.815
Tin (IV) chloride	2.77×10^{21}	0.585	1.198
Thiourea	1.99×10^{22}	-	2.52

Table 4.6. Resulting Stoichiometric Composition of Cu-poor and Zn-rich CZTS

Zn/Sn	Cu/Zn+Sn	S/Cu+Sn+Zn
1.00	0.89	1.89

The type of solvent is crucial in determining the properties of the final absorbers. Several solvents have been used in the synthesis of CZTS thin films, each of which has unique benefits for film characteristics. Dimethyl sulfoxide (DMSO), water, and dimethylformamide (DMF) are among the commonly employed solvents. On the other hand, the solvent choice profoundly influences precursor solubility, which strongly limits the use of metal salt precursors (N, Cl, CH3Co, etc.). Dimethyl sulfoxide (DMSO)-based solutions have been proven promising for the preparation of high-quality Cu2ZnSn(S,Se)4 (CZTSSe) absorbers [81]. We started our experiments to prepare a CZTS solution by using dimethyl sulfoxide (DMSO) as a solvent in the sol–gel synthesis process (protocol 1, solution C), which resulted in a yellow solution, and

after deposition by spin-coating, the as–deposited layer was removed after preheating (sample 8). Additionally, some metal salt precursors in the DMSO solution precipitated after 48 h. This finding highlights the limitations of using DMSO as a solvent in this specific protocol and underscores the need for alternative solutions to achieve effective deposition. In the next part of this work, 2-methoxyethanol was used as the solvent because of its favourable attributes, including its high compatibility with metal–salt precursors. With a polarity index of 5.1,2-methoxyethanol offers intermediate polarity, which facilitates the dissolution of both polar and nonpolar compounds and enhances precursor solubility. The solvent volume critically influences the precursor solution concentration and viscosity, thereby impacting film deposition and the resulting film properties. These protocols, which delve into the nature of the precursors, also differ in their sol–gel preparation methods. This distinction in preparation techniques is the objective of the next section. Nevertheless, both methods successfully yielded clear and homogeneous CZTS solutions.

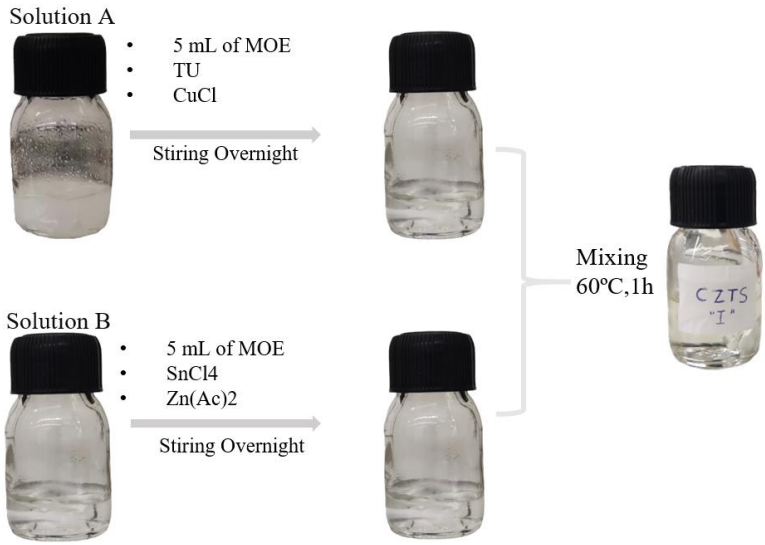

Figure 4. 2: Protocol 2 used to prepare the CZTS solution.

Based on the abovementioned analysis, we successfully prepared CZTS solutions via two distinct protocols, each of which differed in the nature of the precursors and preparation methods. Protocol 1 involved dissolving SnCl2·2H2O in 20 ml of 2-methoxyethanol, followed by the sequential addition of Cu(CH3COO)2·H2O, Zn(CH3COO)2·2H2O, and finally thiourea, with continuous stirring at 60°C for one hour. In Protocol 2, two solutions were prepared and mixed to form the final solution. Solution A was prepared by dissolving thiourea and CuCl in 5 mL of 2-methoxyethanol and stirring overnight. Solution B was prepared by dissolving SnCl4 and Zn(Ac)2 in another 5 mL of 2-methoxyethanol and stirring overnight.

The two solutions were then combined and mixed at 60°C for at least one hour and then filtered through a 0.45 μm nylon filter. These protocols, which involve different approaches to sol–gel synthesis, yield high-quality CZTS solutions. The differences in preparation techniques and their impacts on the final CZTS film properties are discussed in the following sections.

We attempted to prepare a solution using the precursors from Protocol 1 by following the steps of Protocol 2 (Solution D) Figure. (4.3). However, when we mixed the two solutions, we obtained a dark solution. This issue arises because, in Protocol 1, an oxidation–reduction reaction is necessary to achieve the required oxidation states for CZTS. Protocol 2, with its specific precursors, does not require such a reaction and provides the necessary oxidation states. Therefore, using the precursors from Protocol 1 in Protocol 2 does not facilitate the essential oxidation–reduction reaction, resulting in the formation of a dark solution instead of the desired CZTS. More details about this will be discussed later. In the process of synthesizing the sol–gel solution for deposition (protocol 1, solutions A and B) (Figure. (4.3)), several challenges arose that hindered the desired outcome. Notably, as the deposition cycles progressed around the fifth cycle, the material began exhibiting signs of degradation (samples 2, 5 and 7). This unexpected setback prompted a meticulous investigation into the underlying factors contributing to the issue. The degradation could be attributed to several inherent characteristics of the sol–gel process, including the thermal instability and decomposition tendencies of specific precursors such as copper(II) acetylacetonate and tin(II) chloride. Despite diligent optimization attempts to target deposition parameters, the problem persisted until a novel solution was discovered. Remarkably, the addition of 10% sodium (Na) to the precursor solution proved to be a game changer. This simple yet ingenious modification effectively resolved the degradation issue (solution E) (Figure (4.4)), stabilized the solution and prevented material breakdown during subsequent deposition cycles. Although the precise mechanism underlying the stabilizing effect of sodium requires further exploration, its introduction marked a significant milestone in optimizing the synthesis process for enhanced stability and performance. This innovative solution underscores the importance of exploring additives and modifiers to tailor sol–gel methodologies for improved outcomes in various applications.

IV.3. Investigating the phase evolution of kesterite thin films using both developed protocols

In 2012, the efficiency of Kesterite material-based solar cells reached approximately 12.6% [82], with the absorbers in these solar cells being fabricated using the sol-gel method. Since

then, numerous studies have focused on enhancing the performance of kesterite-based solar cells using advanced deposition techniques. However, in 2023, the highest reported efficiency of up to 14.9% was achieved using spin-coated CZTSSe absorbers [83], highlighting the potential of Sol-Gel methods for developing highly efficient Kesterite solar cells. Unlike physical deposition approaches that utilize metal or chalcogen-containing precursors subjected to annealing [84], the sol-gel method requires the use of metal salt precursors dissolved in organic solvents, which may contain additional elements such as C, Cl, H, and O. Despite this complexity, a diverse range of metal precursor salts (e.g., acetate, nitrate, sulfate, chlorides, etc.) and solvents can be employed in kesterite synthesis via the sol-gel method. Consequently, numerous studies have been conducted to identify the optimal precursor salts and solvents for this purpose [80,85]. As the sol-gel reaction process is designed to produce organic products that can fully evaporate during the high-temperature stage used in CZTS fabrication, the oxidation state of the metal salt used in the solution can be a more important factor in controlling the phase evolution of CZTS materials. However, a few studies have reported on the influence of the oxidation state of the metal precursors used during CZTS preparation with sol-gel methods, especially copper (Cu) and tin (Sn) [81]. The most commonly used protocol to prepare CZTS solutions uses Cu^{2+} and Sn^{2+} metal precursors [86], and an oxidoreduction reaction occurs between both elements, which determines the final CZTS materials . This protocol led to a CZTSSe solar cell with 12.6% efficiency. Recently, authors reported a 12.4% efficiency of solution-processed CZTSSe solar cells using Cu^{1+} and Sn^{4+} metal salt precursors [81]. This new approach has achieved the highest reported kesterite solar cell efficiency [87,88] by introducing silver and controlling the selenium vapour pressure. The reported works demonstrate that the transfer from solution to substrate is very different between the two processes. In this study, we investigated the impact of different oxidation states of Sn and Cu during the preparation of CZTS (Cu_2ZnSnS_4) solutions on the transformation from solution to solid precursors and the behavior of the final CZTS absorbers during the high-temperature sulfurization process. Initially, CZTS solutions were prepared using various combinations of Sn and Cu oxidation states (Sn^{2+} + Cu^{2+} and Sn^{4+} + Cu^{1+}). We then studied and analysed how each solution affected the precursors during the deposition process. Finally, we examined the behavior of these precursors during high-temperature annealing using a range of characterization techniques to understand their properties and performance.

IV.3.1. From solution to precursor transfer

One of the critical steps in CZTS preparation using the sol-gel method is the transition from solution to precursor, which is typically achieved through spin-coating techniques followed by preheating at temperatures ranging between 250 and 300°C. According to previous studies utilizing DMSO as a solvent [81], the as-deposited precursors from a solution containing Sn4+ result in the formation of an amorphous CZTS phase, while binary phases tend to dominate in the as-deposited solution containing Sn2+ [87].

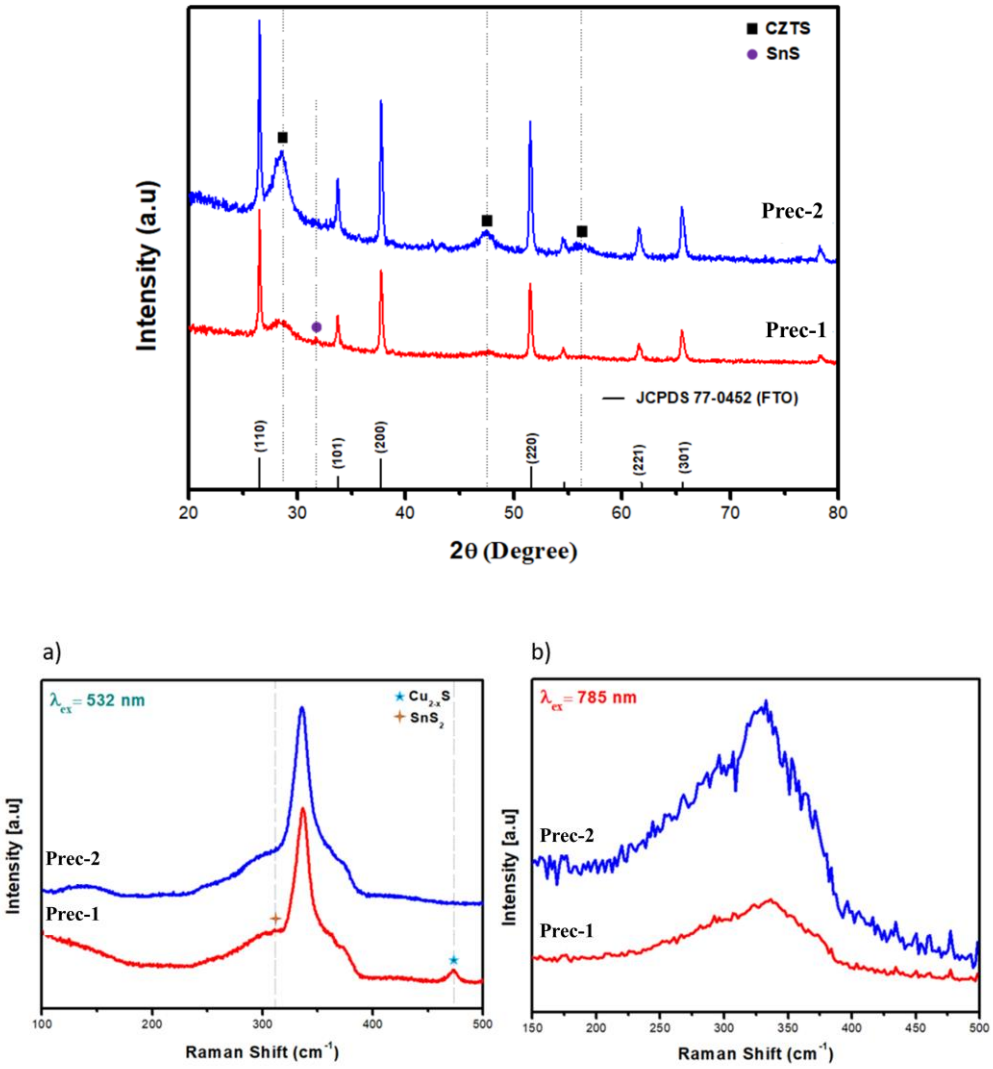

Figure 4. 3: XRD Patterns and Raman spectra of CZTS Precursors Deposited from Sol-1, Sol-2, and Sol-3.

In this work, Cu^{2+} and Sn^{2+} used in Sol-1 serve as sources of Cu and Sn2+ eventually transforming into the necessary Sn4+ for kesterite materials. This transformation occurs

through oxido-reduction reactions of Cu and Sn, as depicted in equation 1. Moreover, the remaining Sn2+ promoted the formation of SnS phases. On the other hand, utilizing Sn2+ and Cu1+ in Sol-3 forces the Sn2+ to transform to the desired Sn4+ through reaction 2 with oxygen during preheating, as reported in [87]. The use of Sn^{4+} and Cu^{+} in Sol-2 can directly facilitate the formation of kesterite phases following preheating.

To delve deeper into the disparities between the three protocols, we employed XRD, SEM, Raman, and EDS analyses of the as-deposited Sol-1 and Sol-2 (Called Prec-1 and Prec-2). Figure 4.3 shows the XRD patterns of the CZTS precursors deposited from Sol-1 and Sol-2. All samples show a broad diffraction peak of kesterite phases [89]. The broad and asymmetric shapes of the peaks indicate the formation of an amorphous kesterite phase, which is consistent with prior observations in spin-coated CZTS solution [81]. However, the shape and intensity of the main diffraction peak corresponding to the (112) orientation differ among the three samples. The peak of sample Prec-3 is more intense than that of Prec-2, while that of Prec-1 is less intense. This suggests that a larger quantity of kesterite phases formed in Prec-3, where all ions have the required oxidation states to form the CZTS phase. In contrast, in Sol-1 and Sol-2, some redox reactions must occur to transform the Sn and Cu ions into the necessary oxidation states, making kesterite phase formation in these precursors more challenging. A similar trend is observed in the Raman spectra obtained with excitation at 785 nm for our as-deposited CZTS precursors (Figure (5.1)). In all samples, a broad peak is observed between 250 and 400 cm^{-1}, encompassing the main vibrational modes of S–S in the kesterite structure [90]. However, the sample prepared using Sol-2 exhibited relatively narrow and symmetric peaks, indicating the presence of a larger quantity of the kesterite phase compared to the sample prepared using Sol-1 and Sol-2. Despite all samples having similar concentrations of metal precursors, this discrepancy can be attributed to differences in the oxidation states of Sn and Cu in the solution. In Sol-3, Sn and Cu ions in the necessary oxidation state for kesterite materials help to form kesterite phases at the lower temperature used in the preheating process (300°C). In Sol-2, Sn in the 2+ oxidation state is converted to 4+ via oxido-reduction with oxygen during preheating. A large portion of Sn ions still in the 2+ oxidation state will lead to the formation of a SnS binary phase with a highly intense peak corresponding to (100) at 31.57° in the XRD pattern. In this case, the Cu ions with the required oxidation state will lead to the formation of the Cu_2S binary phase. The formation of SnS and Cu_2S suggests the existence of ZnS because of the Zn-rich composition, although ZnS cannot be distinguished from CZTS due to diffraction peak overlap [52]. However, in Sol-1, both Cu and Sn ions do not have the necessary oxidation state for kesterite, and the oxido-reduction reactions between both ions in addition to the reaction

with oxygen can lead to the transformation of Cu and Sn to the 1+ and +4 oxidation states. The observed results underscore the strong correlation between the oxidation states of Sn and Cu and the phases present in the CZTS precursors. Notably, the formation mechanism of CZTS absorbers during the annealing process is strongly related to the precursor phases and composition.

$$Sn^{2+}+2Cu^{2+}=Sn^{4+}+2Cu^{+} \quad (1)$$

$$Sn^{2+}+1/2O_2 = Sn^{4+}+O^{2-} \quad (2)$$

The previous results highlighted the significant impact of the oxidation states of Sn and Cu on the phase compositions of CZTS precursors. Figure (5.2) illustrates the transformation mechanisms from solution to precursor for the three different protocols. In Sol-3 (Sn^{4+} + Cu^{1+}), where Cu and Sn ions already have the oxidation states required for kesterite formation, CZTS nanoparticles are formed during the polycondensation process. During the preheating step, these CZTS nanoparticles directly transform into an amorphous CZTS phase. In Sol-2, Cu^{1+} ions are in the required oxidation state, but Sn^{2+} ions must be oxidized to Sn^{4+}. This oxidation occurs through a redox reaction with oxygen. Only a small amount of Sn^{2+} ions are converted to Sn^{4+}, leading to the formation of CZTS nanoparticles. However, since most of the Sn remains in the 2+ oxidation state, SnS phases form, and the excess Cu and Zn ions result in the formation of Cu_2S and ZnS phases. In Sol-1, both Sn^{2+} and Cu^{2+} need to be converted to Cu^{1+} and Sn^{4+}. This transformation involves redox reactions between Cu and Sn, as well as redox reactions of Sn with oxygen. A significant amount of Sn and Cu ions are converted, forming CZTS nanoparticles. However, some ions remain in their initial oxidation states, leading to the formation of CuS, SnS, and ZnS phases in the precursors.

These observations underscore the critical role of oxidation state management in determining the phase composition and quality of CZTS precursors, which in turn affects the main properties of the final CZTS absorbers.

.

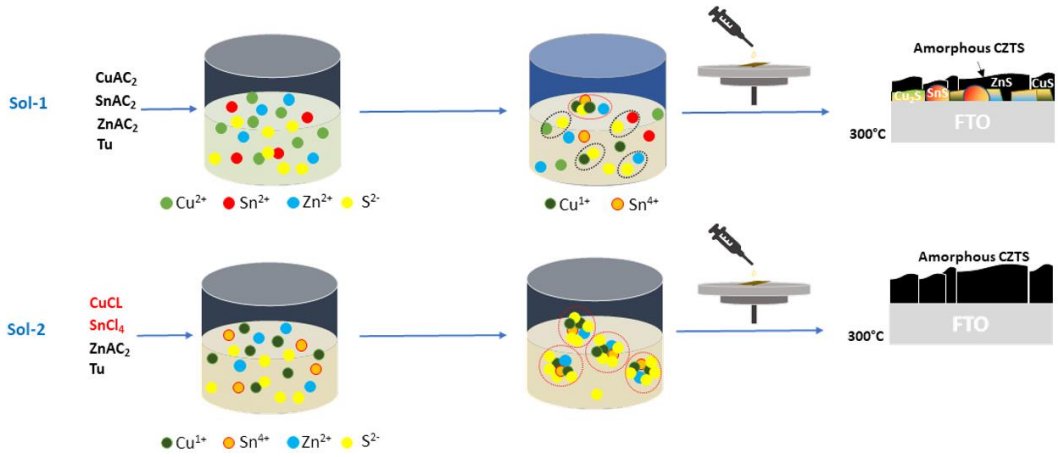

Figure 4. 4: Transformation Mechanisms from Solution to Precursor for Three Different Protocols

IV.3.2. From precursor to absorber transfer

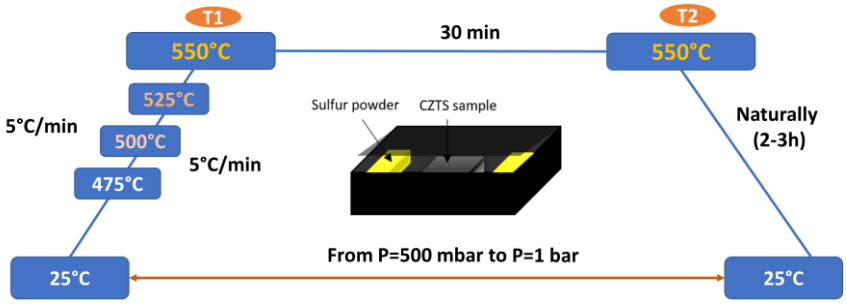

Figure 4. 5: Transformation Mechanisms from Solution to Precursor for Three Different Protocols

In general, during the annealing growth of kesterite materials, CZTS forms at lower temperatures, where most of the phases melt and react with each other, while at higher temperatures, the formation of the kesterite phase helps improve the crystallinity and grain growth of the CZTS materials [91]. The presence of phases with lower melting points in the precursors serves to initiate the formation of kesterite materials at the early stages of the annealing process and leads to the development of high-quality kesterite absorbers at higher temperatures during annealing [92]. Our objective here is to delineate the differences in the formation mechanisms of CZTS materials during the final stage of annealing (from 475 to 550°C) between the widely used methods employing Cu2+ and Sn2+ and the recently implemented protocol utilizing Cu+ and Sn4+, which has shown promise for developing highly efficient kesterite solar cells. Previous studies have investigated the impact of the oxidation states of Sn and Cu on kesterite materials; however, these materials are obtained through a salinization process that leads to the formation of narrow bandgap mixed sulfo-selenide

CZTSSe compounds [93]. In this study, all the absorbers underwent a sulfurization process to transform into CZTS compounds. However, comprehensive investigations in this area are lacking for sulfurized large-bandgap CZTS absorbers. For this purpose, as-deposited Sol-1, and Sol-3 were annealed at different temperatures from 475 to 550°C, and XRD, Raman spectroscopy, SEM and EDX were combined to better understand the influence of the oxidation state of the metal precursors on the properties of the final CZTS thin films at higher annealing temperatures.

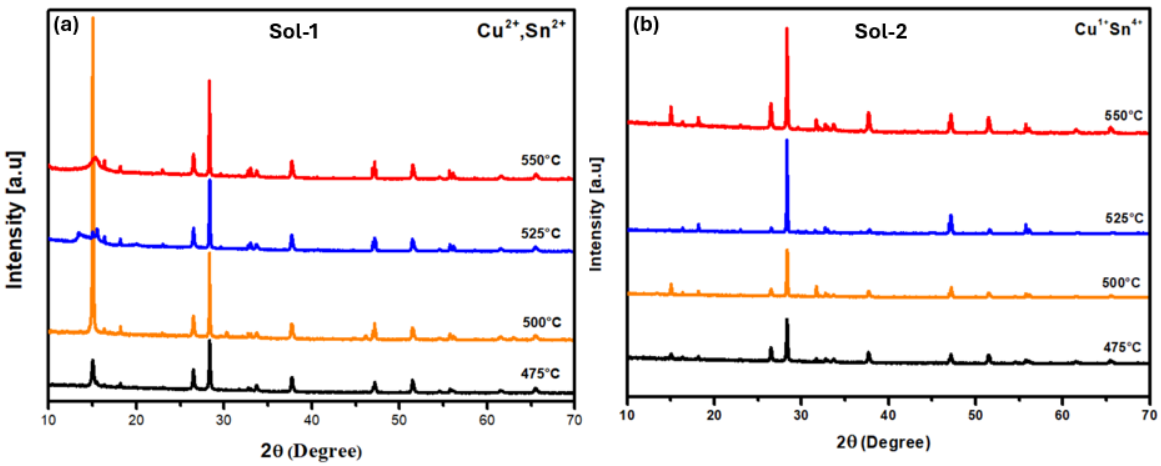

Figure 4.6: XRD Patterns of CZTS Absorbers Prepared with Sol-1 and Sol-2 and Annealed at Different Temperatures

Figure (5.3) shows the XRD patterns of the CZTS absorbers prepared with Sol-1, and Sol-3 and annealed at different temperatures. All samples exhibit similar peaks at 2θ=28.5°, 33.0°, 47.3° and 56.1°, corresponding to the reflections in the (112), (200), (220), and (312) planes, respectively, of the polycrystalline kesterite phase (JPCDS No.26-0575), indicating the formation of crystalline kesterite phases at the lower temperature stage of annealing. This is further confirmed by the Raman spectroscopy results (Figure (5.4)), which show the appearance of vibrational peaks assigned to kesterite vibrational modes [94]. However, the shape and intensity of the main diffraction peak corresponding to the (112) plane vary significantly among the three samples. Starting at 475°C, the samples prepared using Sol-1 show strong diffraction peaks from SnS2, with the disappearance of the SnS peaks, indicating a partial conversion of SnS to SnS_2. Additionally, the sample prepared using Sol-1 exhibited a sharp peak assigned to CZTS or CTS. In contrast, the sample prepared using Sol-3 shows only a small amount of SnS2 but exhibits a sharp peak corresponding to CZTS. Figure (5.5) and Figure (5.6), shows SEM images of the samples. The absorbers prepared using Sol-1 show amorphous Cu2ZnSnS4 with

numerous cracks, as revealed by XRD, with small grains beginning to form. Conversely, the Sol-3 absorber exhibits large grains starting to form from the bottom.

In the Sol-1 solution, the Sn and Cu precursors were both in the +2 oxidation state. Even with a complete redox reaction between Sn^{2+} and Cu^{2+}, residual Sn^{2+} remained in the solution due to the copper-poor composition used in the solution, which is essential for optimal device performance. This indicates that at least two reaction pathways (involving Sn^{2+} and Sn^{4+}) were involved in converting the precursors from the solution to the absorber material. The resulting Sn^{4+} and Cu^{+} formed the CZTS phase, while the SnS produced from the remaining Sn^{2+} converted to the SnS_2 secondary phase [79].

The amorphous CZTS in the Sol-1 precursor film directly converted to crystalline CZTS at the very early stage of sulfurization. Due to the copper- poor availability, the remaining Sn^{4+} formed a very small amount of SnS_2. With increasing temperature to 500°C, the XRD patterns of the Sol-1 show very strong diffraction peaks from SnS_2, revealing the complete conversion of SnS-to-SnS_2, along with an increase in the intensity of the main CZTS peak. Peak splitting arises due to the lower symmetry of CZTS compared to that of the cubic sphalerite-type structure [95]. As a consequence of this tetragonal symmetry, each Bragg peak of the parent structure manifests as two distinct peaks in the diffraction pattern of CZTS.

Additionally, a small peak at 30.8° corresponding to the CuS secondary phase is observed in the sample prepared using Sol-1, indicating the existence of a ZnS secondary phase overlapping with the CZTS phase. This was confirmed by the SEM images, which showed that from 475°C to 500°C, the film morphology changed dramatically and was extremely inhomogeneous, with large hexagonal SnS_2 crystals and some brighter small grains. The brighter regions are identified as high-resistance ZnS [96]. However, the XRD patterns of the Sol-3 sample annealed at the same temperature show a large increase in the intensity of the CZTS signals with peak splitting and a small increase in the intensity of the SnS_2 peak. The SEM image shows larger and more homogeneous grains compared to those in the samples derived from Sol-1, confirming the dominance of single-phase CZTS.

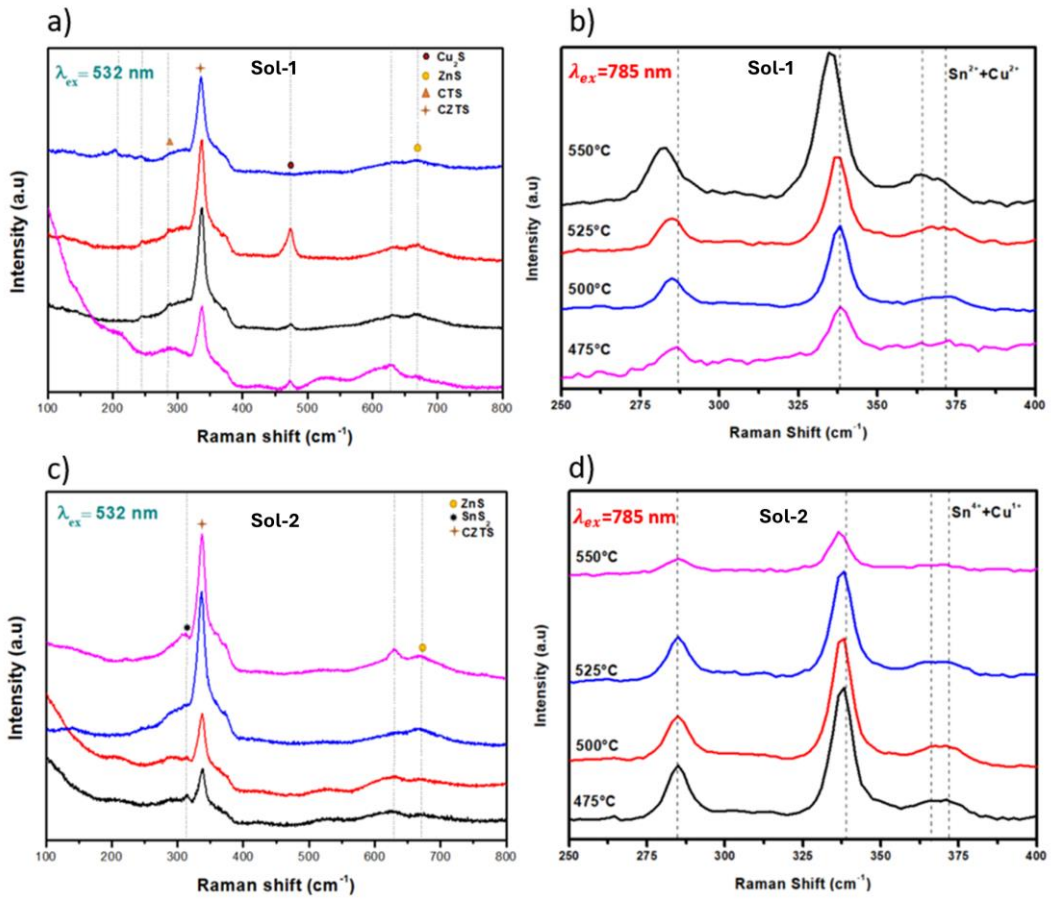

Figure 4. 7: Raman spectra of CZTS Absorbers Prepared with Sol-1 and Sol-2 and Annealed at Different Temperatures

As annealing proceeds to 525°C , all samples exhibit a gradual increase in the intensity of the CZTS signals and symmetry in both the XRD and Raman spectroscopy results, accompanied by a decrease in the intensity of the SnS_2 signals for the Sol-1 and Sol-2 samples. This reveals a gradual fusion of the secondary phases (SnS_2, ZnS, $Cu_{2-X}S$) into CZTS. However, a relatively small decrease in the intensity of the SnS_2 diffraction peak in the spectrum of the Sol-3 sample is observed, indicating that this phase does not completely transform into CZTS in this case. It is important to note that SnS_2 is still detected in these two samples even at the end of the annealing process, indicating that the complete fusion of SnS_2 with CZTS is difficult to achieve. The SEM images of the Sol-1 sample revealed a significant change in morphology, with a homogeneous surface containing large grains assigned to polycrystalline CZTS. On the other hand, the Sol-3 film morphology changed dramatically, showing grain growth from hundreds of nanometers to micrometers on the film surface with a homogeneous, compact, and crack-free morphology, indicating the achievement of single-phase CZTS. This means that the trace

SnS_2 is very likely derived from residual Sn impurities on the film surface, and its influence on grain growth is negligible.

When annealing proceeds to 550°C, the samples from Sol-1 exhibit an increase in the intensity of the CZTS signals and improved symmetry in both the XRD and Raman spectroscopy results. This is accompanied by even larger grain size and a homogeneous surface, indicating the presence of polycrystalline CZTS. However, for the absorber derived from Sol-3, a total decomposition of the CZTS phase is observed in the XRD, Raman, and SEM images, even upon repeating the experiment, indicating that these materials have reached their highest crystallinity at this temperature stage.

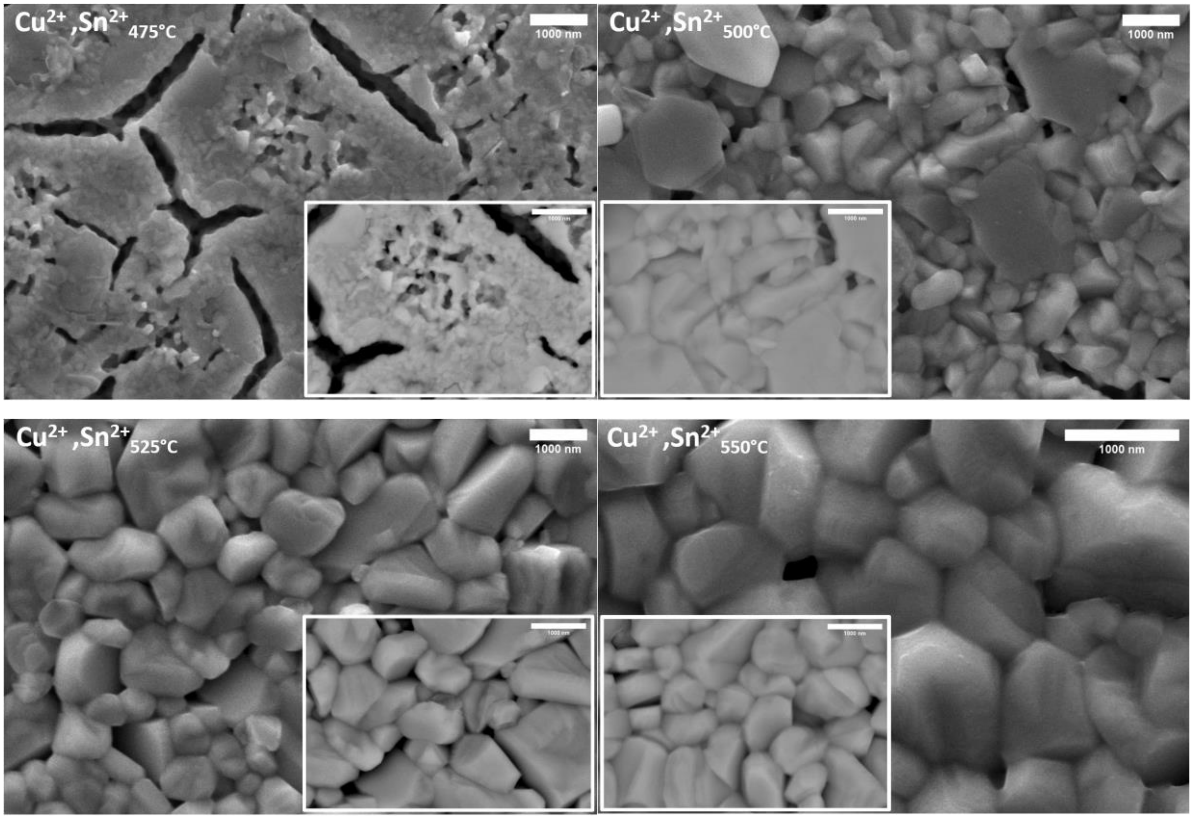

Figure 4. 8: SEM images of CZTS Absorbers Prepared with Sol-1 and annealed in different temperature stage

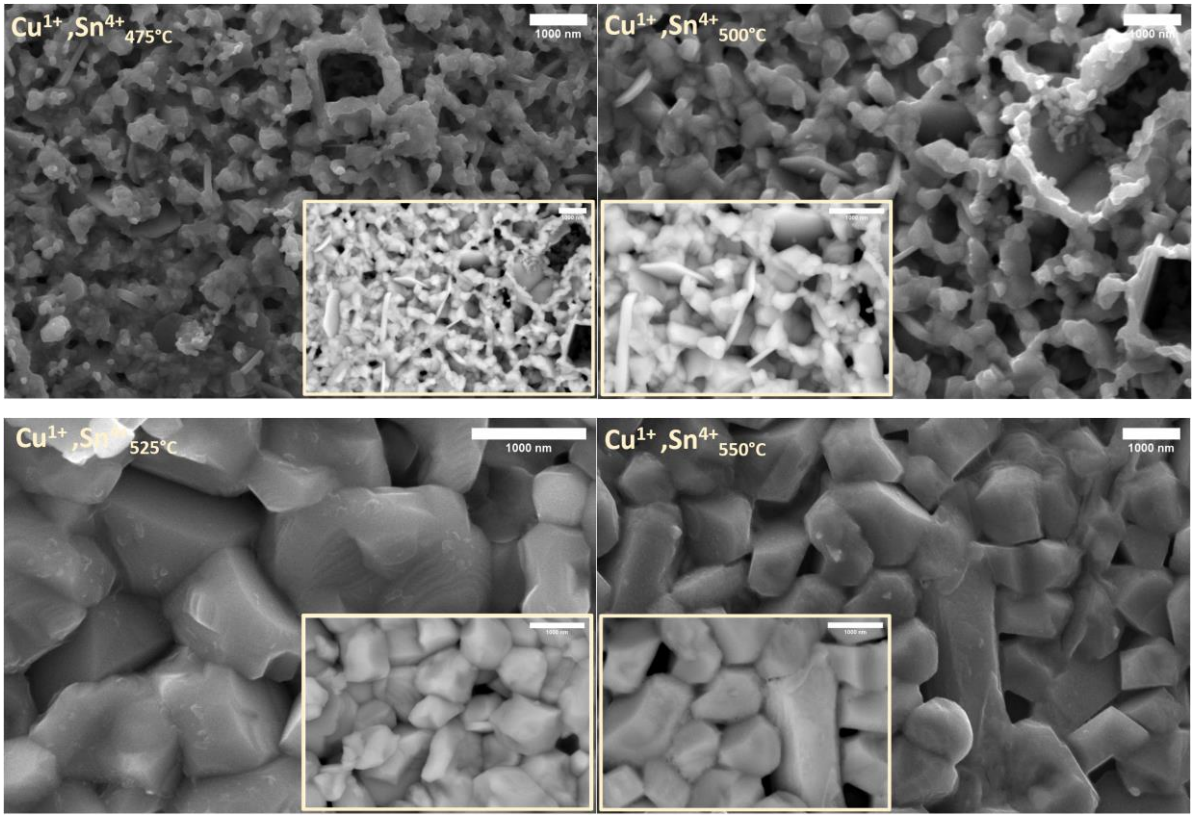

Figure 4.9: SEM images of CZTS Absorbers Prepared with Sol-2 and annealed in different temperature stage

During the annealing process, the transformation from precursor to absorber CZTS formation differs significantly between protocols using Cu^{2+} and Sn^{2+} (Sol-1) versus Cu^{+} and Sn^{4+} (Sol-3). The figures (5.7); summarize the transformation mechanisms from solution to precursor and from precursor to absorber for Sol-1 and Sol-3. In Sol-1, where Cu^{2+} and Sn^{2+} are employed, CZTS has two pathways of formation. The first initially forms as an amorphous phase and then converts to crystalline CZTS. The second pathway is accompanied by the formation of ZnS, CuS, and SnS, which transform into SnS_2 as a secondary phase. As annealing progresses, these secondary phases fuse to form a crystalline CZTS structure. Conversely, in Sol-3, utilizing Cu^{+} and Sn^{4+}, one pathway sees CZTS crystallizing early with minimal secondary phase formation. This results in a nearly single-phase CZTS structure with superior crystallinity at lower temperatures. At higher annealing temperatures, these materials decompose.

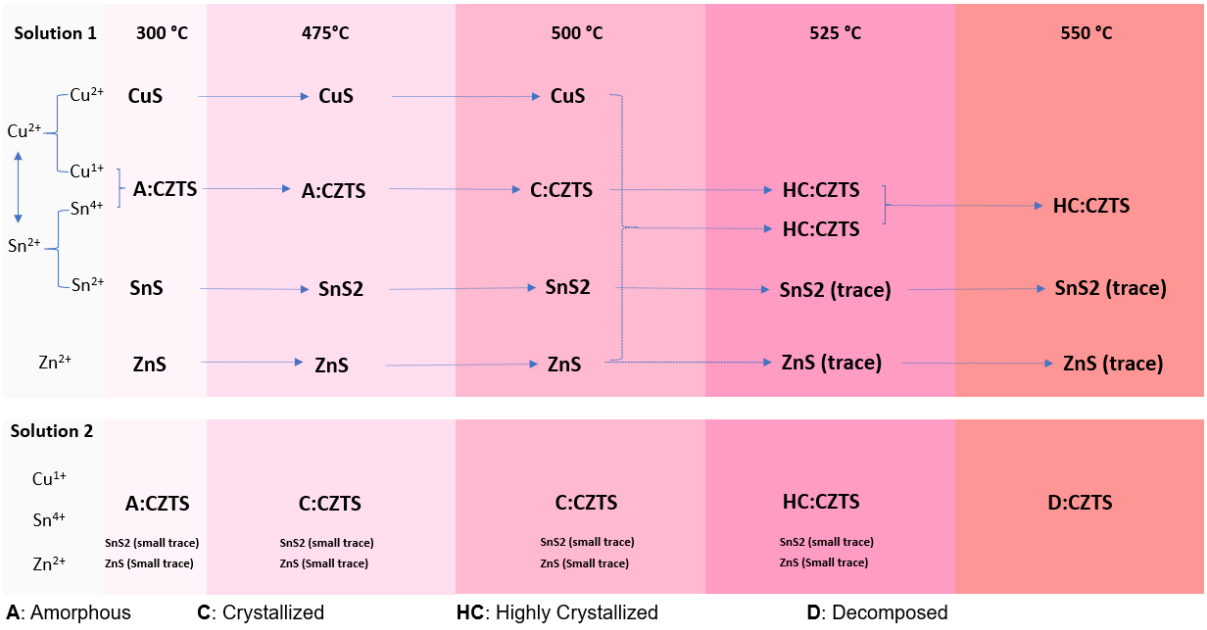

Figure 4. 10: Transformation Mechanisms from Solution to Precursor and from precursor to the absorber for the sol-1 and Sol-3.

In this study, we successfully synthesized Kesterite absorbers using the sol-gel method on a transparent FTO back electrode, with a focus on exploring the effects of different oxidation states of copper (Cu) and tin (Sn) precursors. The results of our structural, morphological, and optical characterizations demonstrated that the oxidation state of these metal ions plays a crucial role in influencing the final properties of the synthesized absorbers. X-ray diffraction and Raman spectroscopy confirmed the formation of kesterite structures with minimal secondary phases. SEM analyses further highlighted the impact of precursor oxidation states on the surface morphology, crystallinity, and grain size of the films. Notably, absorbers synthesized from higher oxidation state precursors exhibited enhanced crystallinity and improved optical properties, suggesting their potential for higher solar cell efficiencies. The findings from this work underscore the importance of precursor chemistry in the sol-gel synthesis of kesterite materials and highlight a promising approach to optimizing the performance of kesterite materials. By utilizing molecular inks and carefully controlling the oxidation states of metal precursors, this study paves the way for more efficient and scalable methods for producing high-quality kesterite absorbers, with implications for advancing the development of low-cost, sustainable thin-film solar cell technologies.

Chapter 5: Doping & Alloying Approaches in Kesterite materials and their Integration in tandem cells: Experimental and Simulation

V.1. Silver incorporation into wide bandgap CZTS absorbers on transparent back electrodes prepared from Sn^{2+} & Cu^{4+} solution and their integration into tandem cells

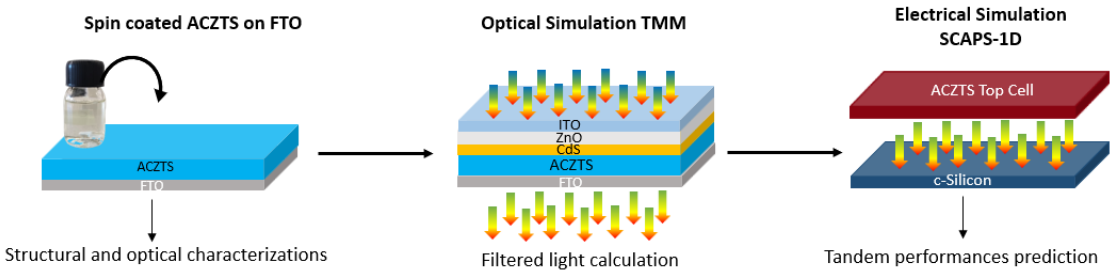

Graphical Abstract: The methodology used in this work.

In recent years, kesterite solar cells have emerged as promising candidates for integration as top subcells into tandem structures with silicon solar cells. However, achieving high-quality kesterite absorbers on transparent substrates has remained a significant challenge. This study addresses this issue by introducing silver into CZTS absorbers developed on FTO back electrodes using the sol-gel method. Structural characterization revealed a significant improvement in the crystallinity and morphology of the kesterite materials with the incorporation of silver. In addition, the Raman spectroscopy results revealed a decrease in Cu//Zn disorder and in Cu_{Zn} defects density in the kesterite materials after Ag incorporation. Optical analysis revealed a slight poster increase in the kesterite optical bandgap due to the presence of silver atoms. Through Finite-difference time-domain (FDTD) optical simulation with realistic optical inputs, the transmitted light from the FTO/CZTS/CdS/ZnO/ITO solar structure was calculated. Then, the performances of the well-established c-Si bottom subcell (with state-of-the-art efficiency) under calculated transmissions was evaluated using SCAPS-1D electrical stimulation. The simulated tandem device shows lower efficiency compared to c-Si solar cell under AM1.5. The findings presented here indicate that the incorporation of silver offers a promising approach for enhancing the properties of kesterite materials on

transparent back electrodes. However, further optical advancements are necessary to fully realize the potential of kesterite materials for tandem applications.

V.1.1. Introduction

Quaternary kesterite compounds such as $Cu_2ZnSnSSe_4$ (CZTSSe)-based solar cells and their derivatives have garnered significant attention as promising materials for use as top cells in the next generation of kesterite/c-Si tandem solar cells [10]. Due to their low cost, abundance of constituents, good optical and electrical properties, and long-term stability, intensive efforts have been made to develop CZTSSe compounds, demonstrating their viability in solar cell applications. Although the efficiency of kesterite material-based solar cells reached 12.6% in 2013 [97], this efficiency has remained the highest reported value for 10 years despite the increasing number of studies reported on kesterite materials. The lower performance of the CZTSSe solar cells is attributed to factors such as the higher V_{oc} deficit (E_g/q-V_{oc}) resulting from the high density of charged bulk defects, particularly the dominant Cu_{Zn} antisite, and the resistive nature of the CZTSSe/CdS heterointerfaces leading to enhanced carrier recombination [98]. Recently, Yauncai et al.[88] reported a significant improvement in kesterite efficiency to 13.6% for small-area solar cells based on $Ag_xCu_{2-x}ZnSnSSe_4$ achieved through epitaxial reconstruction of the heterointerface using lower-temperature junction post annealing. After several months, the same group reported an efficiency of 14.9% through better control of phase evolution during the annealing process [87]. These higher efficiencies represent a strong advance in kesterite solar cell development. The improvements observed in these cells are attributed not only to the announced approaches but also to silver incorporation into the absorbers, as silver alloying (ACZTSSe) significantly enhances kesterite properties, primarily by reducing Cu/Zn disorder and Cu_{Zn} defect density with the introduction of larger Ag atoms [15,89,99,100]. In the Kesterite/c-Si tandem configuration, kesterite solar cells should be developed on transparent electrodes, which act as tunnel junctions in monolithic configurations of tandem solar cells and allow light transmission to c-Si bottom subcells in mechanically stacked configurations [40]. FTO represents the most promising candidate for CZTS top subcells due to its high transparency, low resistivity, and high thermal stability at standard temperatures used to create kesterite materials [101]. However, compared with Mo-based solar cells, CZTSSe solar cells developed on FTO electrodes exhibit some limitations in terms of efficiency, mostly due to the higher work function of FTO and lattice mismatch of the FTO/CZTS interface, complicating charge transfer and increasing nonfavourable carrier recombination [102]. In 2023, Zhou et al. reported an ACZTSSe (E_g=1.16 eV) solar cell on an

FTO substrate with an efficiency of 7.6% using Na doping and Ag alloying, which improved to 11.4% with the addition of a 20 nm MoO_3 nanolayer between the FTO and kesterite materials. This efficiency surpassing the efficiency of other thin-film solar cells on transparent electrodes [103]. Therefore, the combination of Na and Ag in kesterite materials exhibits significant potential for the development of highly efficient kesterite solar cells on transparent electrodes. However, the lower bandgap of the sulfo-selinide Sn-kesterite material CZTSSe makes it unsuitable for top cell applications and these approaches should be transferred to large-bandgap kesterite absorbers.

In this work, we combined Na doping and Ag alloying to enhance the properties of wide-bandgap CZTS materials deposited on FTO back electrodes and evaluated their application in tandem solar cells through optical and electrical stimulation. First, CZTS solar cells with and without Ag silver incorporation on FTO electrodes were prepared using the sol-gel method and analysed by combining XRD, SEM, Raman spectroscopy, AFM, and UV–visible spectroscopy. Then, the obtained optical data for our absorber were used in FDTD simulations to estimate the transmission of the CZTS top cells. Finally, the calculated transmittance spectrum was used in SCAPS-1D electrical simulations to evaluate the c-Si bottom subcell under the transmitted light from top subcell.

V.1.2. Preparation and characterization of Kesterite absorbers

Solution preparation

Solid solution CZTS materials were synthesized using the cost-effective sol-gel method. The CZTS solution was prepared according to the protocol outlined in Figure 1. Initially, Cu $(CH_3COO)_2 \cdot H_2O$ (0.46 mol/l) was dissolved in 20 ml of 2-methoxyethanol, followed by the addition of $SnCl_2$-$2H_2O$ (0.27 mol/l), resulting in a greenish solution. Subsequent colour changes occurred upon the addition of Zn $(CH_3COO)_2 \cdot 2H_2O$ (0.27 mol/l) and thiourea $SC(NH_2)_2$ (2 mol/l), and the entire solution was stirred for one hour at 60°C, yielding a clear and transparent solution. NaCl: H_2O was added to the final CZTS solution with NaCl to CZTS molar ratios of up to 10%. For the ACZTS solution, AgCl with a Cu/Ag ratio of 10% was added after the addition of Cu $(CH_3COO)_2 \cdot H_2O$ in the initial step.

Figure 5. 1: Protocol used to prepare the CZTS Sol-gel solution.

Substrate cleaning and deposition

Prior to deposition, the FTO-coated SLG substrate (surface resistivity ~7 Ω/sq) underwent a thorough cleaning process in an ultrasonic bath. The cleaning steps included immersion in deionized water for 10 minutes, followed by immersion in ethanol for another 10 minutes, and a final rinse in deionized water for an additional 10 minutes. After rinsing with water and drying with nitrogen, the substrate was subjected to UV-ozone cleaning for 10 minutes. The prepared solution was filtered through a 0.45 µm filter and then deposited onto the cleaned FTO substrate via spin-coating at 3000 rpm for 30 seconds. Subsequently, the substrate was preheated in an atmospheric environment on a hot plate set at 300°C for 2 minutes. This deposition process was repeated 10 times to achieve the desired thickness of approximately 1 µm.

Sulfurization process

The as-deposited CZTS precursors were placed in a graphite box (4x5 cm^2) with 500 mg of sulfur powder and inserted into a tubular furnace. Prior to the annealing process, the tube was purged several times with nitrogen. The optimized annealing profile, as depicted in Figure 2, involved a sulfurization process conducted at 550°C for 30 min under a pressure of approximately 1 bar (initially 600 mbar at 25°C). The ramping rate was set to 5°C/min, and the cooling process occurred naturally over approximately 3 hours.

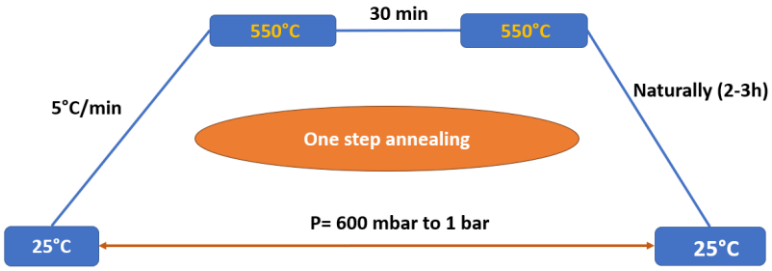

Figure 5. 2: Temperature vs. Time One-Step Annealing Profile

Characterizations

Scanning electron microscopy (SEM) images were acquired using a FEI FEG 450 (Field Emission Gun) microscope with an acceleration voltage of 5 kV. X-ray diffraction (XRD) patterns were collected using a Rigaku SmartLab diffractometer in Bragg–Brentano geometry with a monochromatized CuK-L3 X-ray source (1.540598 Å). The optical properties of the films were investigated using a Perkin-Elmer Lambda 950 UV-visible spectrophotometer. Raman spectroscopy was conducted using a LabRam Aramis microprobe by Horiba Jobin-Yvon Co with 785 nm excitation to study the structural properties and assess the quality of the ACZTS films. Atomic force microscopy (AFM) images were collected using a Veeco Dimension ICON machine.

V.1.3. Results and discussion

The crystal structure and phase composition of the prepared thin films were investigated through X-ray diffraction (XRD) analysis. The obtained diffractograms are shown in Figure 3.a. The diffraction patterns of sulfurized thin films, both with (ACZTS) and without silver (CZTS), revealed narrow peaks corresponding to the (112), (200), (220), and (312) diffraction planes of the polycrystalline kesterite phase (JCPDS # 026-0575). The relatively narrow and symmetric shapes of these peaks confirm the formation of a single-phase structure. Additionally, some peaks corresponding to the FTO substrate were observed in the XRD pattern (JCPDS: 35-1001). While the high incorporation of silver into CZTS compounds typically results in a structural transformation to the stannite phase, no peaks corresponding to stannite phases were observed in this study, likely due to the lower amount of silver used. However, the position, the shape, and the intensity of the main peaks differed significantly between the ACZTS and CZTS samples. In particular, the ACZTS sample exhibited a narrow and much more intense peak corresponding to the (112) orientation (Figure 3.b), indicating a higher crystallinity of the kesterite material after silver incorporation, which is consistent with previous

reports on silver alloyed CZTS absorbers [104]. A slight shift of the principal diffraction peak towards lower angles was observed after silver incorporation, indicating an improvement in the lattice parameter with the introduction of larger silver atoms. A small trace of SnS phase is observed in ACZTS sample with small peak at about 32°, may be due to the substitution of Cu^{2+} with Ag^{+} ions in the solution wish allow some quantity of Sn ions with 2+ oxidation state to form of SnS phases. The lattice parameters, deformation, and crystallite size calculated using the Scherrer formula are presented in Table 1. The lattice parameter 'a' is improved from 5.42 Å for CZTS to 5.47 Å for the ACZTS absorber, where a small decrease in 'c' lattice parameter from 10.86 Å to 10.83 Å is observed for ACZTS, in accordance with the previous reports on Ag alloyed CZTS sample [105]. This variation in the lattice parameter is due to the replacement of Cu-S (2.31 Å) by larger Ag-S (2.57 Å) bond length in the tetragonal structure [89]. Similarly, a significant increase in the crystallite size was observed, increasing from 32 to 69 nm following silver incorporation.

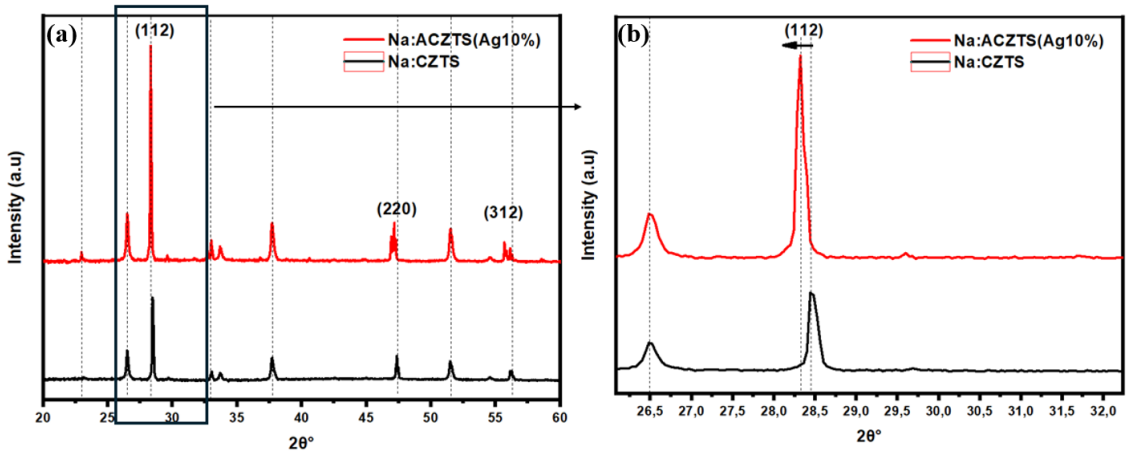

Figure 5. 3: XRD patterns of CZTS and ACZTS thin films (a) entire acquisition scale and (b) magnification on the main peaks.

Table1: Lattice Parameters, Lattice Deformation, and Crystallite Size of CZTS and ACZTS thin films

Samples	a (Å)	c(Å)	c/2a	D(nm)
CZTS	5.42	10.86	1.001	34.7
ACZTS	5.47	10.83	0.989	69.4

As some secondary phases cannot be distinguished from CZTS in XRD analysis (To verify the

formation of a pure CZTS), Raman spectroscopy analysis is necessary. The near-resonance Raman spectra obtained with an excitation wavelength of 785 nm for samples synthesized with and without Ag are depicted in Figure 4. Both samples exhibit Raman peaks at 283, 321, 334, and 370 cm^{-1}, corresponding to the vibrational modes of the kesterite phase [106]. Ag incorporation does not cause any Raman shifts, possibly due to the low content of Ag in CZTS [107]. However, the peak sharpness and intensity are notably enhanced for the ACZTS sample. It is known that the order/disorder of Cu and Zn atoms strongly influences the Raman peaks in kesterite materials, where sharper and more intense peaks indicate a more ordered structure and less defective matrix [108]. In CZTS materials, the dominant defects are associated with CuZn, owing to their lower formation energy resulting from the similar ionic radii of Cu^{+} and Zn^{2+} ions [109]. In the case of the ACZTS material, the substitution of 10% of the copper atoms with larger silver atoms significantly reduced the CuZn defects in the resulting absorbers, explaining the sharper and more intense peaks observed in the Raman spectra. Semiquantitative analysis of the samples was performed by calculating the relative integrated intensity of the second most intense peak in the measured Raman spectra (shown in table 2). Previously, this was shown to be a possible indicator of changes in defects and/or Cu-Zn disorder in kesterite-type compounds [110]. A small decrease in the relative intensity ratio for the ACZTS sample in comparison to that for the CZTS sample. This may be explained by the small changes in the defect concentration, as observed previously for CZTSe compounds [111].

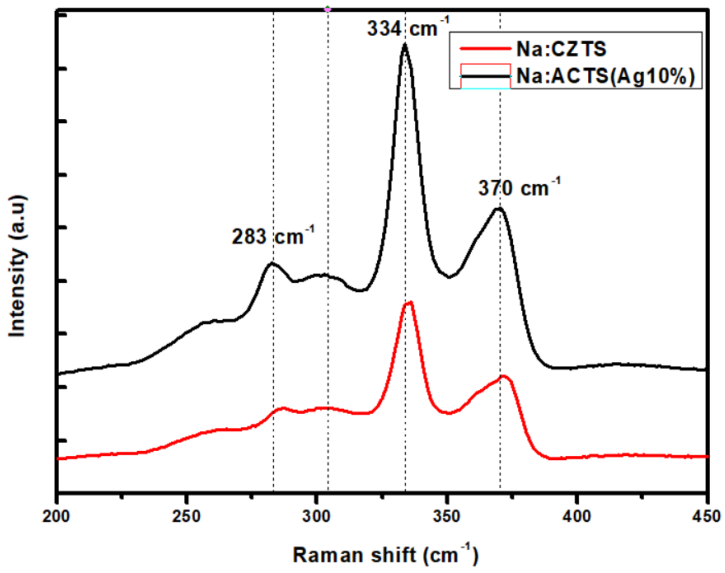

Figure 5. 4: Raman spectra of CZTS and ACZTS thin films

Table 2: the ratio of relative integrated intensity of the second most intense peak in the measured Raman spectra.

Samples	$Q = \frac{I_{283}}{I_{302}}$	$Q' = \frac{I_{334}}{I_{370}+I_{365}}$
CZTS	0.098	0.61
ACZTS	1.012	0.67

The morphology and chemical composition of the prepared CZTS and ACZTS thin films were evaluated using surface SEM images and EDS, and the results are presented in Figure 5.a. and Table 3. Both samples show dense and compact surface morphologies. However, a small density of voids is observed (clear in the CZTS sample), which can be attributed to the volatility of secondary phases or may be the decomposition of CZTS during the high-temperature stage of the annealing process [93]. This phenomenon is most likely due to the greater volatility of the Sn-S binary phases at the annealing temperature [112]. This can be confirmed by the EDS results shown in the table. The Zn/Sn ratio for both samples is 1.43, which is lower than the ratio of the precursors. This problem of tin loss is largely reported in kesterite materials [113], and several groups have attempted to add Sn during the annealing process; however, addressing this problem is still challenging in kesterite materials. The ACZTS sample has large grains (between 800 and 1500 nm), whereas the CZTS sample has relatively fewer grains (between 500 and 1000 nm). The large grains in ACZTS are probably due to the formation of low-melting point phases in the lower temperature stage of the annealing process [114]. However, sodium is present in both samples, and Ag-S is reported to have a lower melting point and help the grain growth of kesterite materials during the annealing process. AFM analysis was conducted to gain a better understanding of the surface topology and roughness of the CZTS and ACZTS thin films, and the results are presented in Figure 5.b. The 3D images of the ACZTS sample exhibit more rough surfaces and fewer grain boundaries than those of the CZTS sample, in accordance with the SEM results. A rougher surface and fewer grain boundaries in the ACZTS sample are detrimental to the absorption and generation of CZTS materials.

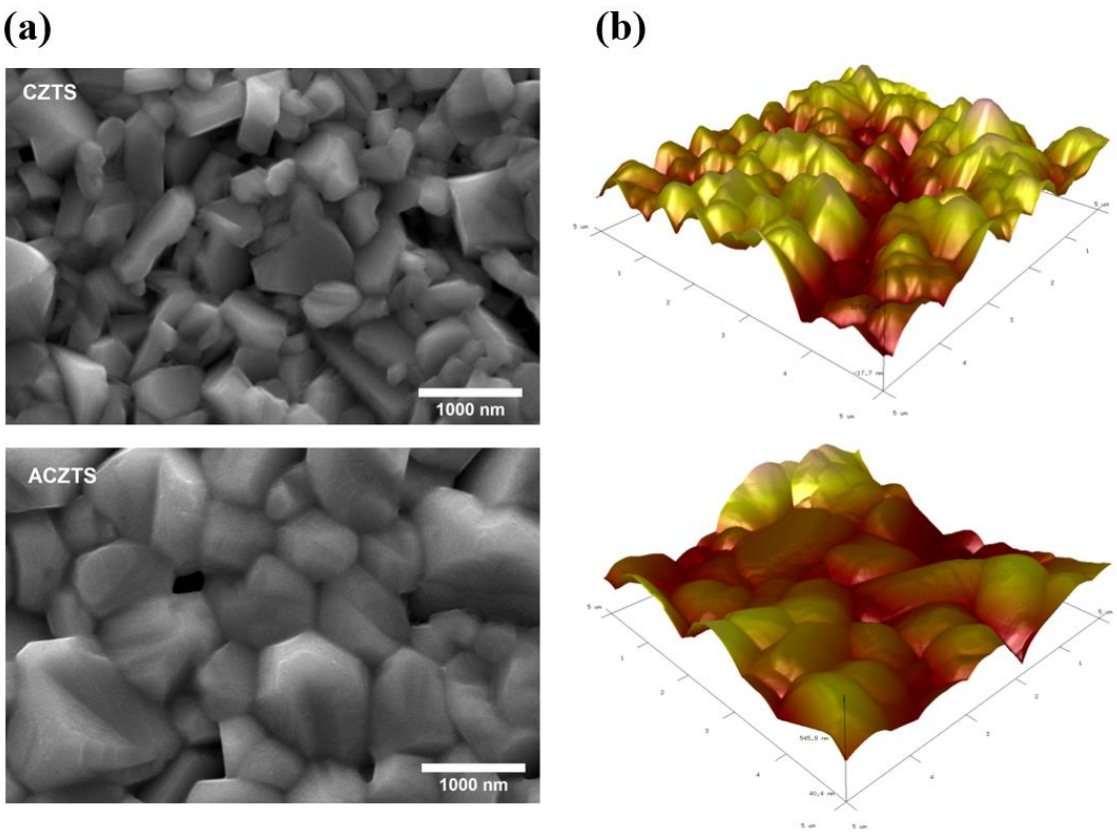

Figure 5. 5: (a) Surface SEM images and (b) 3D-AFM images of CZTS and ACZTS absorbers

Table 3: Cationic ratios of CZTS and ACZTS calculated from EDS results

Ratio	Ag/Ag+Cu	I/II+IV	Zn/Sn	Cu/Zn
ACZTS	6.36	1.18	1.43	2.01
CZTS	--	1.32	1.18	2.43

The optical properties of the ACZTS and CZTS thin films were determined via UV–visible spectroscopy, and the results of the absorption coefficient and band gap calculations are shown in Figure 6. A small increase in the bandgap from 1.53 to 1.57 eV is observed for the CZTS and AZCTS samples, suggesting that the low content of Ag in CZTS does not significantly change the bandgap and that this small change might be due to the reduction in Cu/Zn disorder, which strongly affects the bandgap in kesterite materials [115]. To characterize the band-tailing for these absorbers, the plot ln(α)) vs the bandgap energy to estimate the Urbach tail energy (EU), with a lower value indicating less band-tailing. An estimate of the E_U is obtained by taking the

inverse of the slope of the linear region below the bandgap. We found that the E_U for CZTS devices is ~ 152.7 meV and that for ACZTS devices is ~ 146 meV. This implies a small reduction in band tailing/antisite defects with Ag substitution [110].

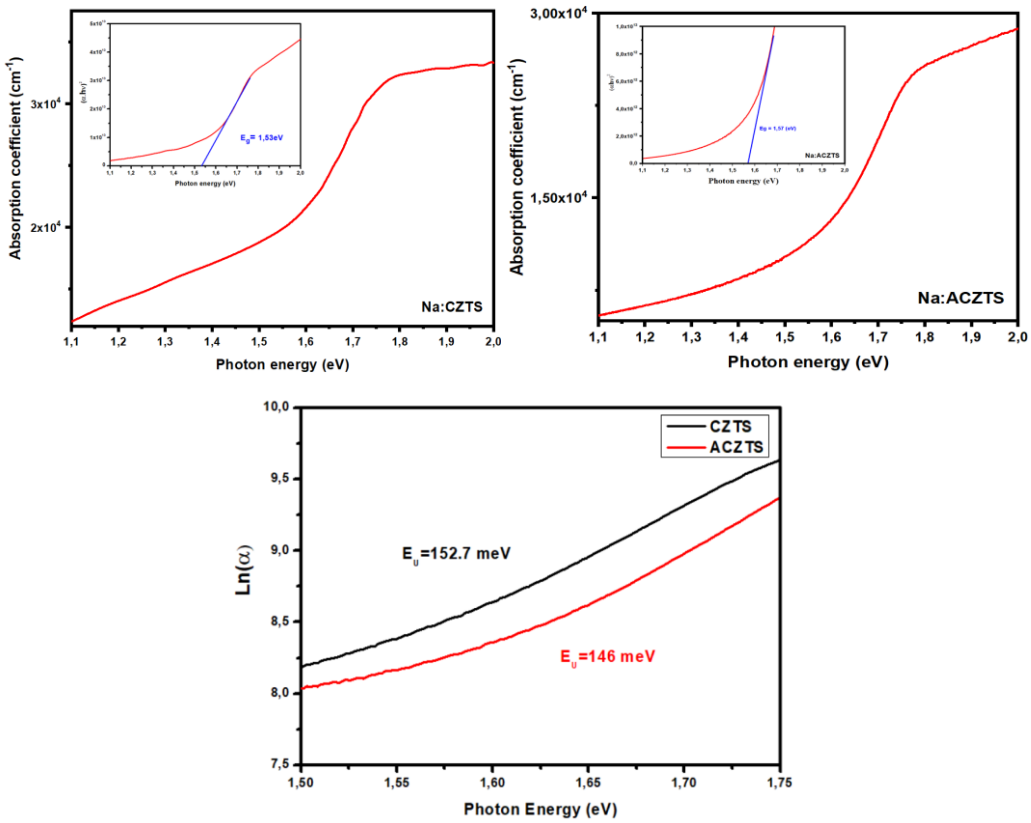

Figure 5. 6: Absorption coefficients, bandgap, and Urbach energy calculations from UV-Visible spectroscopy analysis of CZTS and ACZTS materials

Optical and electrical analysis of CZTS/c-Si tandem cell

In this section, we will use numerical simulations to evaluate the behavior of the above prepared ACZTS absorber in tandem applications. Specifically, we will use FDTD and SCAPS-1D optical and electrical simulations due to their proven accuracy [116–118]

.

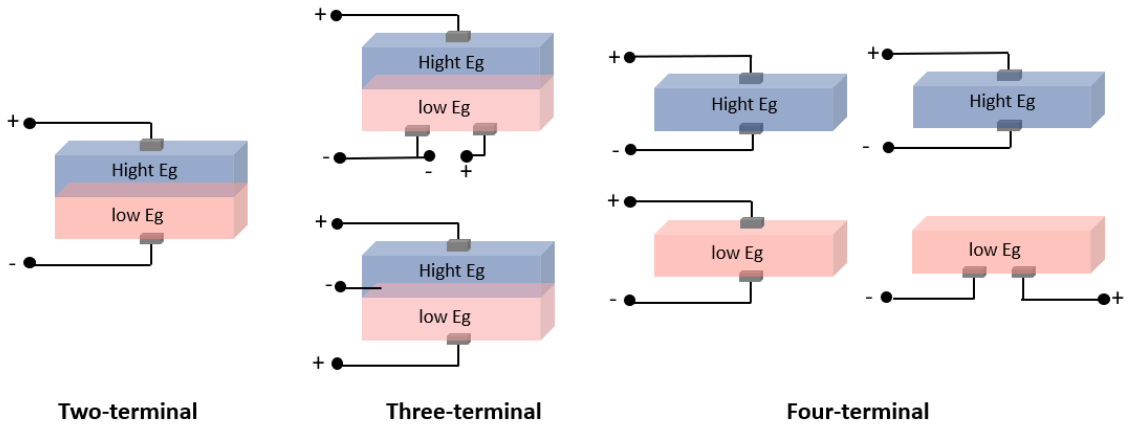

Figure 5. 7: Schematics of different tandem device architectures, namely two-terminal, three-terminal, and four-terminal configurations.

Tandem solar cells can be prepared using different configurations, as shown in Figure 7. The two-terminal (2T), or monolithic, configuration is the primary type of tandem solar cell. In this configuration, the top cell is deposited directly on top of the bottom subcells and connected through a tunnel junction. This configuration is sensitive to the top cell's bandgap and is limited to the matching conditions where both cells produce similar currents. On the other hand, in the four-terminal (4T) configuration, the two subcells are mechanically stacked, and the outputs are collected independently using four electrodes. The four-terminal configuration provides more flexibility in choosing materials with different bandgaps. In this work, we chose to simulate the tandem behavior using our ACZTS material in 4T-configuration with c-Si bottom subcell. Given that the bandgap of our material is about 1.57 eV, the 4T configuration with c-Si as the bottom subcell is more suitable and theoretically leads to higher performance compared to the 2T configuration [119].

The kesterite top subcell (FTO/kesterite/CdS/ZnO/ITO) with ACZTS absorber will be optically modelled using the FDTD method to analyse the spectrum transmitted to the c-Si bottom subcell. The optical data obtained for our absorbers and state-of-the-art data for other materials in the solar structure were used. The refractive index and extinction coefficient of ACZTS are calculated using equations (1) and (2). The CdS, ZnO, and layers were derived from ellipsometry data compiled by Et-taya et al. [120], while those for ITO were obtained from the baseline data for kesterite/c-Si reported in [121]. The thickness of each layer is similar to that of the state-of-the-art CZTS solar cell on a transparent electrode reported in [122], with our absorber's thickness estimated to be approximately 1 µm using profilometry measurements.

$$n = \left(\frac{1+R}{1-R}\right) + \sqrt{\left(\frac{4R}{(1-R)^2} - K^2\right)} \quad (1)$$

$$k = \frac{\lambda\alpha}{4\pi} \quad (2)$$

Where R is the reflectance, α is the absorption coefficient, λ is the wavelength, and n is the refractive index.

The transmission curves in Figure 8.a. correspond to the top subcell structure of FTO/ACZTS/CdS/ZnO/ITO (with an absorber bandgap of calculated using FDTD. Figure 7.b. displays the filtered spectrum from the top subcell, which serves as the incident light for the c-Si bottom subcell simulation in tandem configurations. These curves reveal three distinct regions. For energies higher than the bandgap of ACZTS material (wavelengths < 700nm), there is minimal light transmission due to the high absorption coefficient of ACZTS materials, as observed from UV-Visible data. Around the bandgap (between 700-900 nm), transmission gradually increases, reaching approximately 80% with interference fringes. At higher wavelengths below the bandgap of ACZTS films, transmission curves start to decrease, ranging from 50 to 80%. These results explain the significant decrease in the light transmitted from the top subcells observed in Figure 8.b.

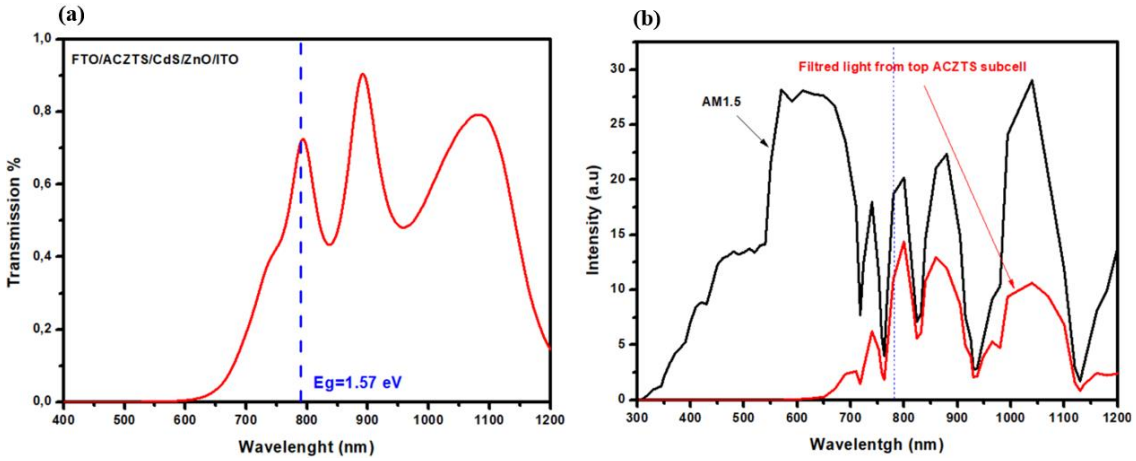

Figure 5. 8: Transmission spectra of ACZTS Solar cell, (b) Filtered light from the top ACZTS top cell calculated using FDTD simulation.

To understand the origins of the above observed results, Figure 9. provides insights into the light absorption distribution within each layer of the top subcell (FTO/CZTS/CdS/ZnO/n-ZnO) and the overall device reflection. At higher wavelengths below the bandgap of the kesterite material (>750 nm), where the light transmitted should be adequate for a better response of the c-Si bottom subcell, the reflection dominates the spectra, with values ranging from 20 to 40%, as well as the absorption of the FTO back electrode, with values ranging from 10 to 20%. The

absorption of TCOs at higher wavelength are mostly shown in previous studies and might be due to some plasmonic phenomena resulted from the higher density of carriers in these materials [123]. However, it is critical to address the issues of the reflection in the IR region through optical engineering to improve the performance of the tandem device.

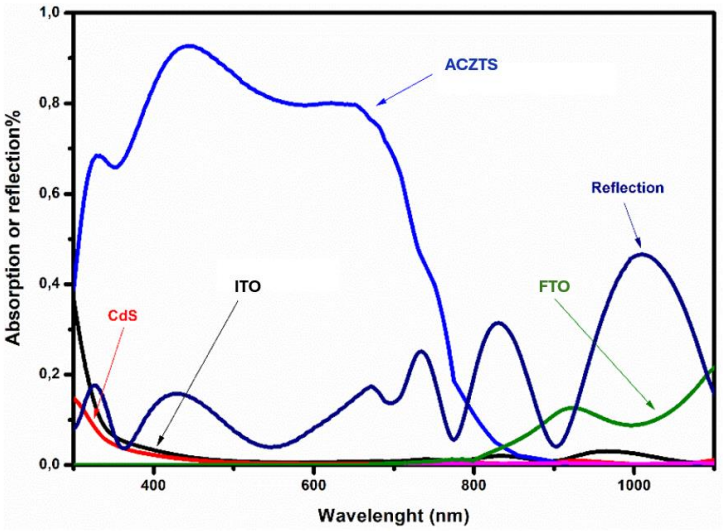

Figure 5. 9: The fraction of light absorbed in each layer and the total reflection of ACZTS solar cell.

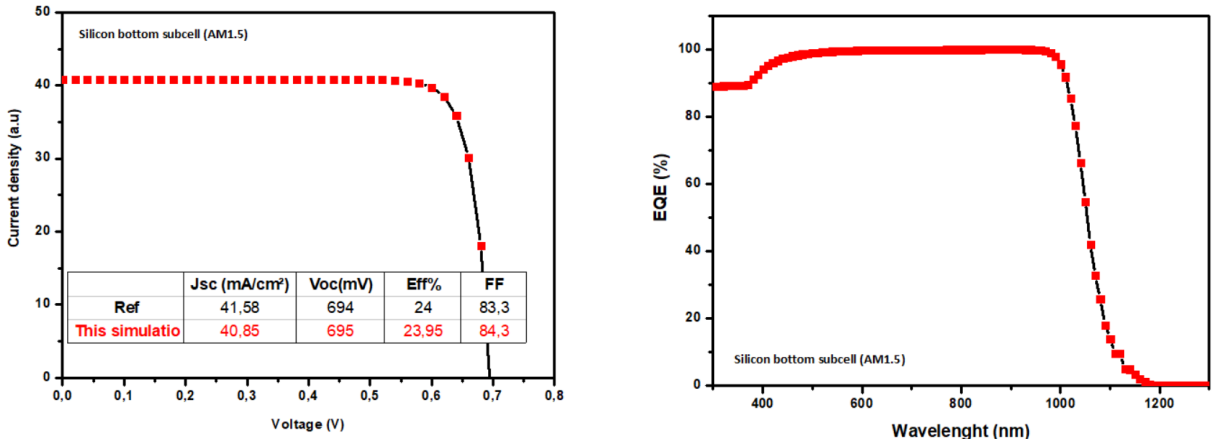

Figure 5. 10: J-V Characteristics and EQE of Simulated c-Si bottom Sub-cell.

The above transmission spectra were used as a filter in the electrical simulation with SCAPS-1D to evaluate the c-Si solar cells in mechanically stacked configuration of ACZTS/c-Si tandem solar cell. The c-Si subcell baseline used in this work reproduces one of the champion lab-scale c-Silicon solar cells [124]. The main electrical parameters used in the simulated are summarized in table 1S. This c-Si bottom subcell exhibited an efficiency of 24.7% with a V_{OC} of 639 mV, a J_{SC} of 41.9 mA/cm^2, and a fill factor of 79.4%. The J-V curve and EQE of the simulated c-Si

bottom subcell are shown in Figure 10. This solar cell exhibits an efficiency of 23.95% with a V_{OC} of 695 mV, a J_{SC} of 40.85 mA/cm^2, and a fill factor of 84.3%, which are in good agreement with the experimental results of the real solar cells.

The J-V curves of c-Si solar cells simulated under AM1.5 solar spectrum and the light transmitted from the ACZTS top subcell are shown in Figure 11.a. A large difference in the PV performances between both simulation results. The c-Si simulated under the filtered spectrum show a very lower efficiency of 6% compared to the reference cell simulated under AM1.5 solar spectrum wish show about 24% efficiency. This large decrease in the efficiency is due to the large decrease in the short circuit density Jsc wish is decreased from 41 to 12 mA after filtering the solar spectrum with the top subcell. However, there is no strong effect on the V_{oc} and FF is observed. The Quantum efficiency of both solar cells is shown in Figure 11.b. At higher energies, all the spectra are absorbed by the top subcell and the electron-hole pair generation and collection are not observed in the QE curves of c-Si subcells. However, at higher wavelength below the bandgap of ACZTS where the higher performance of c-Si subcells are required, the QE curves show values between 60 and 80% wish are lower than the QE of c-Si under AM1.5. These results originate from the higher reflection at lower energies as well as the absorption of the TCOs at this region as observed before.

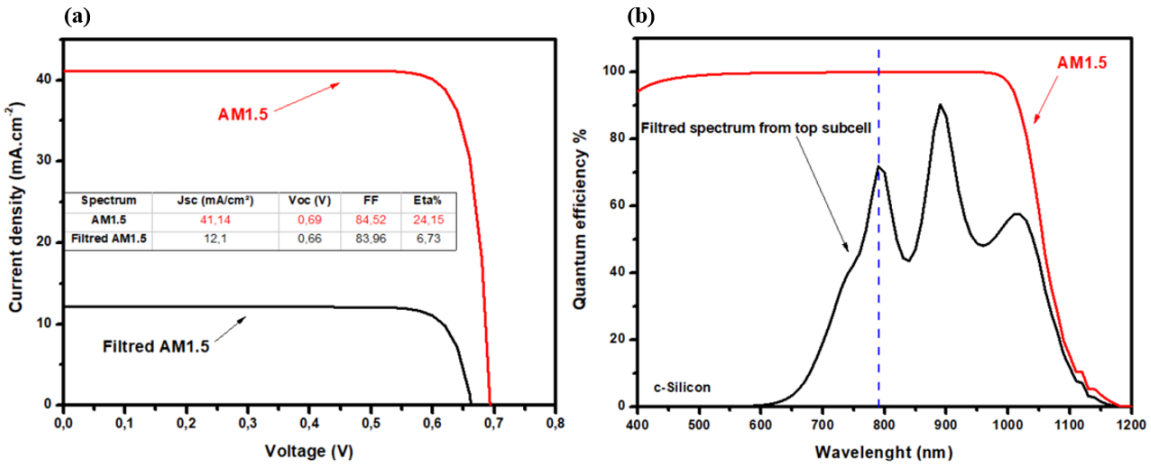

Figure 5. 11: J-V Characteristics and (b) Quantum Efficiency Comparison of c-Si Solar Cells under AM1.5 and Filtered Spectrum by ACZTS Top Subcell.

The obtained results showed that the current density of c-Si solar cell in tandem configuration with ACZTS solar cells is too low. In this case the Jsc of c-Si bottom subcell is lower than the state-of-art current for kesterite top subcells on transparent substrate [122], make it challenging to combine both subcells in 2T-configuration. However, the obtained electrical performance is

combined with the electrical data for the best reported CZTS solar cell on transparent substrate (with similar bandgap) in a 4T-configuration of kesterite/c-Si. The baseline reported by Alex et al [121], reproduces one of the records CZTS solar cell developed on transparent substrate [16]. However, some optical inputs modifications (e.g.: absorption coefficient, optical filters, and interface defects) are used to fit exactly the metric parameters of the real solar cell. The inputs used in this simulation including bulk/interface defects are shown in table 1S and 2S. This solar cell exhibits an efficiency of 7.70%, with V_{OC}=0.68 V, J_{SC}=17.8 mA/cm^2, and FF=63%. A comparison of reported and simulated CZTS solar cell performance is shown in figure 12. The calculated photovoltaic parameters for both cells are summarized in the inset table of figure 11. The simulated device exhibits an efficiency of 7.69% with V_{OC}=0.67 V, J_{SC} =17.85 mA/cm^2, and FF= 63.85%, suggesting that the difference between the experimental and simulated data is insignificant.

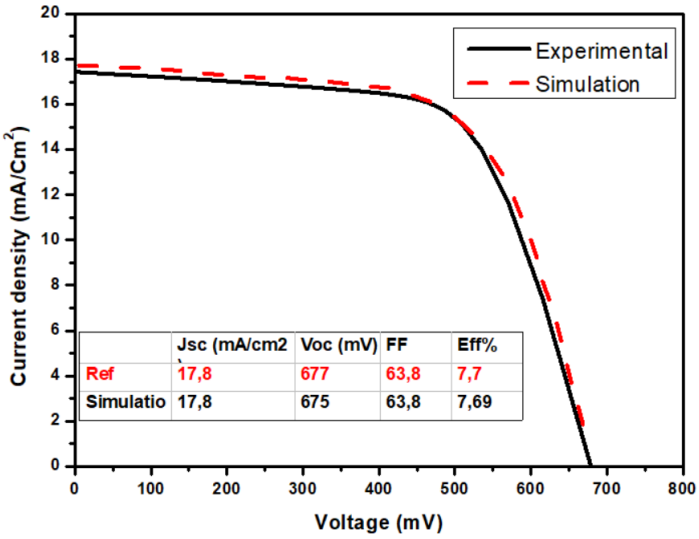

Figure 5. 12: Comparison of Reported and Simulated Performance of CZTS Solar Cells on Transparent electrode.

The photovoltaic parameters of the Kesterite/c-Si tandem device, along with their respective subcells, are summarized in Table 4. The tandem device using ACZTS/CdS as the top subcell exhibits an efficiency of only 14.42%. This lower efficiency primarily arises from the decreased Jsc of the c-Si bottom subcells, attributable to light transmission from the top subcell, consequently impacting the overall performance of the c-Si subcell. Conversely, the lower electrical performance of the kesterite top subcell imposes limitations on the design of highly efficient tandem cells. However, simulation results indicate that further advancements in the

optical and electrical properties of kesterite single-junction cells could enable kesterite/c-Si tandem devices to achieve efficiencies close to those predicted by theoretical studies. This suggests a promising way for overcoming the limitations of single-junction solar cells.

Table 4: Efficiency of Kesterite/c-Si Tandem Device and Respective Subcells.

Cell	**Efficiency%**
Top subcell (Ref) (under AM1.5)	7.69
Bottom subcell (c-Si) (under filtered light)	6.73
Tandem cell	14.42

IV.1.4. Conclusion

In summary, this study has explored the incorporation of sodium doping and silver alloying in large bandgap CZTS materials. This approach has shown promise, resulting in improved structural and morphological properties along with a slight increase in the bandgap. Optical and electrical simulations have been conducted to assess the viability of using ACZTS solar cells as top subcells in mechanically stacked tandem solar cells with c-Si bottom subcells. However, the simulation outcomes have indicated lower efficiencies for ACZTS/c-Si tandem cells, primarily attributed to the decreased performance of c-Si solar cells operating under light transmitted from the top subcell. This underscores the need for further optical and electrical advancements to establish kesterite materials as a feasible option for the development of highly efficient tandem solar cells.

V.2. A simple and efficient strategy for incorporating alkali metals into sol-gel processed-ACZTS absorbers prepared From Sn4+ & Cu1+ solution and their integration into tandem cells

Doping and alloying in sol-gel processed kesterite materials have been the most successful approaches used in recent years to enhance the performance of kesterite solar cells. However, these approaches are limited to incorporating alkali metals during solution preparation, making it challenging to control the incorporation of these elements during the deposition and annealing

steps of the sol-gel process. In this work, we present a straightforward process for incorporating alkali metals into sol-gel processed Ag-alloyed kesterite absorbers by depositing alkali metal layers on top of an ACZTS precursor. This incorporation method significantly improves the properties of ACZTS absorbers compared to the conventional approach used for doping kesterite materials during sol-gel solution preparation. XRD, Raman spectroscopy, SEM, AFM, and UV–Visible analysis were combined to study the properties of the ACZTS samples doped via both approaches. The XRD and Raman results underscore the potential of the proposed method for enhancing crystallinity and reducing Cu/Zn disorder. Additionally, SEM and AFM images show that the morphology and topology of the ACZTS samples are improved, with larger grains and fewer grain boundaries. Optical characterization confirmed that reduced defects with lower Erbach energies were obtained after doping with alkali metals during precursor deposition. The findings reported in this paper emphasize the beneficial effect of doping kesterite materials with alkali metals using the proposed approach, which offers more flexibility in the incorporation of alkali metals in the sol-gel method. However, further work on this strategy can lead to a better understanding and control of the doping approach and the development of high-quality kesterite absorbers.

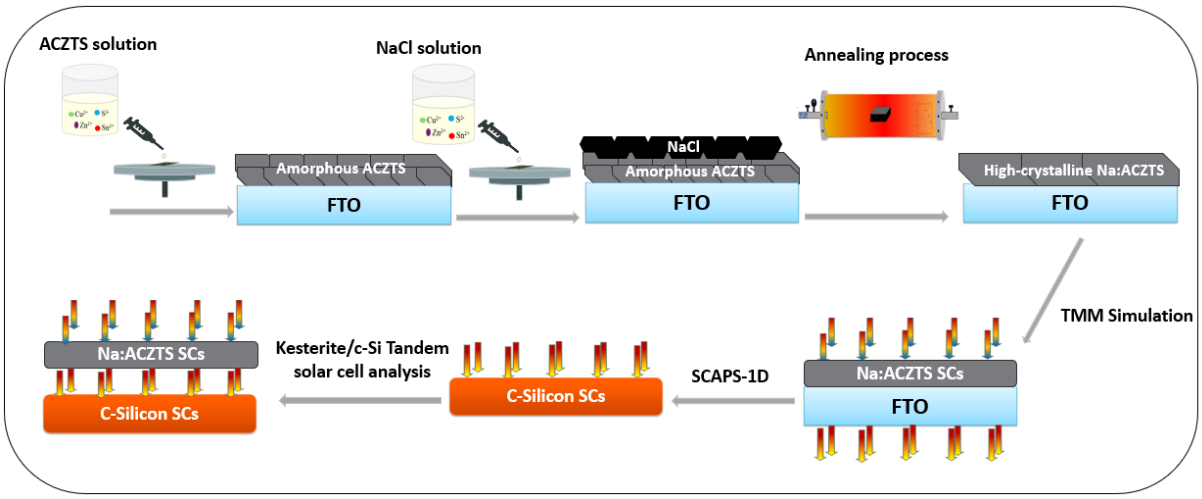

Graphical Abstract: The methodology used in this work to incorporate alkali metals into ACZTS materials.

V.2.1. Introduction

Recent studies on developing highly efficient thin-film solar cells have focused mostly on kesterite-based materials due to their properties similar to those of highly efficient CIGS (Copper Indium Gallium Selenide) solar cells in addition to their cost effectiveness. However,

kesterite solar cells face efficiency limitations, with the highest reported power conversion efficiency (PCE) of only 14.9% using the CZTSSe absorber [7], compared to 23% for CIGS solar cells [5]. Researchers commonly attribute these efficiency limitations to the higher open-circuit voltage (V_{oc}) deficit in kesterite material-based solar cells [15,125,126]. These V_{oc} losses in kesterite solar cells are strongly related to various factors, including bulk and interface defects [127]. Efforts to address this V_{oc} deficit issue have been in progress for decades, with a wide range of strategies proposed to enhance the quality of kesterite absorbers, the primary material in these solar devices. Among these strategies, doping kesterite materials with alkali metals has largely been reported in most studies of kesterite solar cells, and all of these studies support the beneficial effect of alkali metals on kesterite materials by decreasing the voltage deficit, increasing the net hole carrier concentration, passivating grain boundaries, and increasing the grain size [128–130]. Sodium doping is present in almost all works on kesterite solar cells due to its diffusion from the SLG substrate when Mo is used as the back electrode [131]. In addition, lithium (Li) doping has also been reported in many studies leading to high-efficiency solar cells [132,133]. The role of each alkali metal in improving the performance of kesterite solar cells is different. However, alkali metals improve the grain growth of kesterite materials during annealing process by forming lower melting point and improving the chemisorption of chalcogens (e.g., S and Se) [92,114]. The methods for incorporating alkali metals into kesterite materials differ according to the deposition technique used for creating kesterite materials. In solution-processed kesterite materials such as the sol-gel method, alkyl metal salts are used during solution preparation [77,134]. However, in physical vapour deposition techniques, a thin layer of alkali metal (e.g., NaF, LiF, etc.) is generally used [135,136]. In solution-processed kesterite approaches, alkali method incorporation starts from the solution and then leads to a homogenous distribution of Na in the precursors, which is subjected to an annealing process. However, in physical methods, alkali metal layers can be deposited at different positions and thicknesses, and during the annealing process, alkali metals can diffuse into the absorber in different ways. Additionally, these diffusion methods of alkali metals strongly affect the final properties of the absorbers and led to more flexibility in doping kesterite materials [137]. However, the ability to change the diffusion of alkali metals into kesterite absorbers is not present in solution deposition approaches where alkali metals is used in the solution. In this investigation, we investigate a sample strategy for alkali metal doping of spin-coated kesterite materials. The proposed method is based on incorporating alkali metals during solution deposition into a substrate. Spin-coated ACZTS precursors are coated with different layers of alkali-metal chlorides dissolved in an organic solvent. The well-established

alkali metals Na and Li are studied using the proposed approach and compared with the conventional doping strategy of doping in solution. X-ray diffraction (XRD), Raman spectroscopy, scanning electron microscopy (SEM), atomic force microscopy (AFM), and UV–visible spectroscopy (UV–Vis) were combined to understand the influence of the alkali metals on the final absorber properties using different incorporation methods.

V.2.2. Experimental section

Sol-gel solution and ACZTS absorbers preparation

ACZTS thin films were synthesized using the low-cost sol-gel spin coating method, employing copper chloride (CuCl) + silver chloride (AgCl) (0.46 mol/L), zinc acetate dihydrate ($Zn(CH_3COO)_2 \cdot 2H_2O$) (0.27 mol/L), tin (IV) chloride ($SnCl_4$) (0.27 mol/L), and thiourea ($SC(NH_2)_2$) (2 mol/L) as the metal and sulfur sources. Following a similar process as that reported in [81], however, 2-methoxyethanol was used as a solvent instead of DMSO.

To prepare the ACZTS sol-gel solution, two separate solutions were prepared (Figure 1):

For solution 1, thiourea ($SC(NH_2)_2$) and AgCl+CuCl were dissolved in 2-methoxyethanol at a 10% Ag/Cu ratio. For solution 2: $SnCl_4$ was dissolved in 2-methoxyethanol, followed by Zn(CH3COO)2·2 H_2O, maintaining a Zn/Sn ratio of 1.1 and a (Cu + Ag)/(Sn + Zn) ratio of 0.75.

Both solutions were stirred for 24 hours to ensure complete dissolution of the metal-salt precursors. Subsequently, the solutions were mixed and stirred at 60°C for 1 hour in an oil bath. The final solution was then filtered through a 0.45 µm filter.

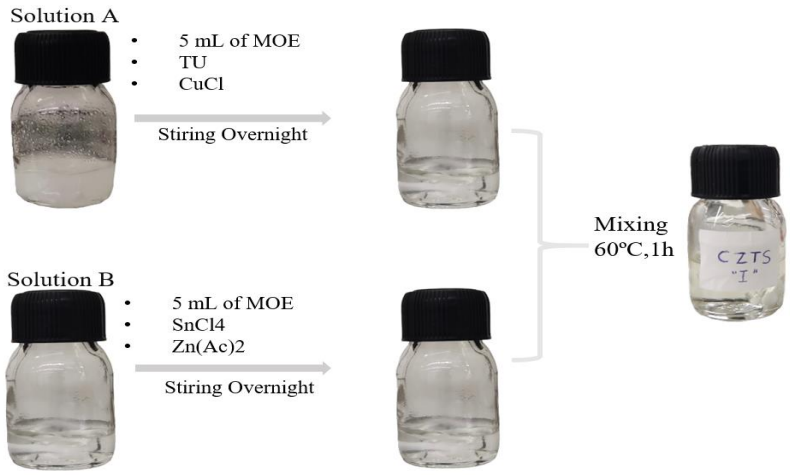

. **Figure 5.13**: Protocol used to prepare CZTS solutions.

To investigate sodium and lithium doping in ACZTS kesterite, 5% NaCl and $LiClO_4$ (Li or Na/Cu =5%) were added to the final solution, resulting in samples referred to as Na:ACZTS-S and Li:ACZTS-S, respectively. For doping using the proposed strategy, 5% NaCl and $LiClO_4$ were dissolved in 2-methoxyethanol, stirred overnight, and then deposited onto the ACZTS precursor under the same deposition conditions.

Prior to deposition, the FTO-coated SLG substrate (surface resistivity of ~7 Ω/sq) underwent a thorough cleaning process in an ultrasonic bath, followed by UV-ozone cleaning for 10 minutes. The filtered solution was deposited onto the cleaned FTO substrate via spin-coating at 3000 rpm for 30 seconds. Subsequently, the substrate was preheated in an atmospheric environment on a hot plate set at 300°C for 2 minutes. This deposition process was repeated 7 times to achieve the desired thickness of approximately 1 µm.

Characterizations

Scanning electron microscopy (SEM) images were acquired using a FEI FEG 450 (Field Emission Gun) microscope with an acceleration voltage of 5 kV. X-ray diffraction (XRD) patterns were collected using a Rigaku SmartLab diffractometer in Bragg–Brentano geometry with a monochromatized CuK-L3 X-ray source (1.540598 Å). The optical properties of the films were investigated using a Perkin-Elmer Lambda 950 UV-visible spectrophotometer. Raman spectroscopy was conducted using a LabRam Aramis microprobe by Horiba Jobin-Yvon Co with 785 nm excitation to study the structural properties and assess the quality of the ACZTS films. Atomic force microscopy (AFM) images were collected using a Veeco Dimension ICON machine.

V.2.3. Results and discussion

During the annealing process, kesterite materials are formed when chalcogens (S or Se) react with the precursors, resulting in the final absorber layers. The nature of the precursor and the annealing conditions significantly affect the properties of these absorbers [96,111,127]. Typically, CZTS materials are deposited on Mo-coated glass substrates, where the porosity of Mo allows alkali-metals to diffuse from the soda-lime glass (SLG) substrate during annealing, leading to remarkable effects. In this work, however, an FTO back contact is used, which may block the diffusion of alkali metals from the SLG. Consequently, the observed effects are primarily due to the alkali metals (sodium and lithium) introduced during the preparation method rather than from diffusion through the substrate.

During the lower temperature stages of the sulfurization process, kesterite materials are formed, while the higher temperature stages lead to improved crystallization and grain growth [138,139]. The presence of alkali metals in CZTS precursors results in the formation of lower melting point phases, which facilitate grain growth and the formation of large grains with compact morphologies. Additionally, the incorporation of silver into kesterite materials has several advantages in enhancing the performance of CZTS thin films. It reduces Cu/Zn disorder and CuZn defects [107,140,141] and decreases Cu vacancies, which is one of the most significant roles of alkali metals in kesterite materials. Silver is also reported to have similar effects as alkali metals in assisting the grain growth of CZTS materials during the annealing process by forming Ag_xS phases with lower melting points [105]. According to [87], kesterite materials can follow several phase evolution pathways during annealing. However, the protocol used to prepare the ACZTS solution in this work involves metal salts that produce metal ions in the solution with the oxidation states required for kesterite materials (Ag-Cu^{1+}, Zn^{2+}, Sn^{4+}). This leads to the formation ACZTS nanoparticles during the polycondensation reaction and leads to form an amorphous ACZTS materials after the deposition of the precursor using spin-coating, which can directly form kesterite materials during the annealing process without passing through binary and ternary phases [81]. Using this protocol can reduce the role of silver in improving grain sizes during the formation of ACZTS materials due to the poor copper stoichiometry used. In this case, silver participates in passivating Cu vacancies and reducing Cu/Zn disorder.

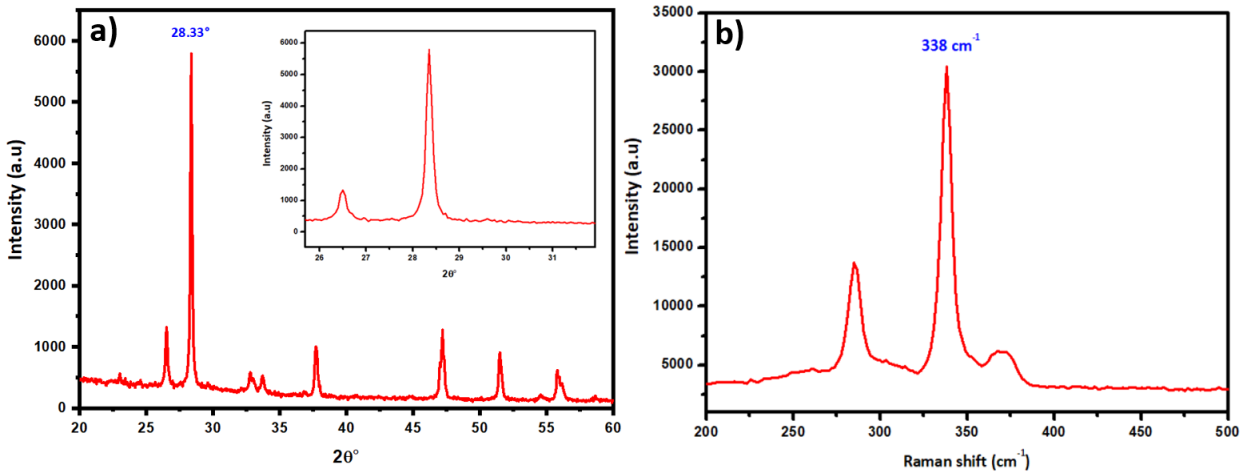

Figure 5.14: XRD patterns (a) and Raman spectra (b) of the undoped-ACZTS sample

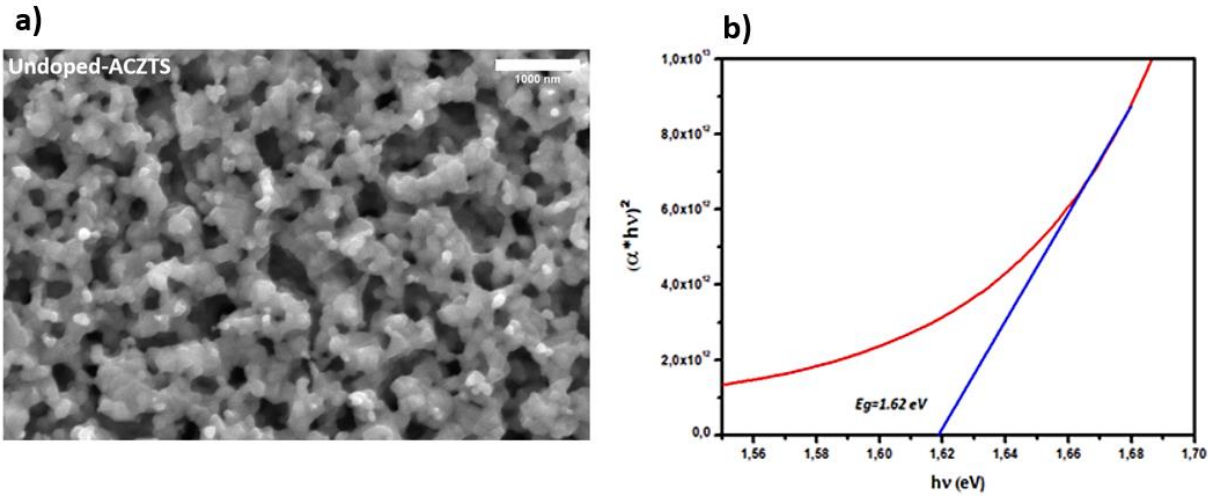

Figure 5. 15: Surface SEM images (a) and energy band bandgap (b) of the undoped-ACZTS sample

We started our experiments by preparing an undoped-ACZTS sample on an FTO back contact, and various characterization techniques were used to investigate the properties of the prepared absorbers. The results of the structural property analyses are shown in Figure 2. The XRD pattern of this sample revealed peaks at 28.33°, 32.9°, 47.3°, and 56.1°, corresponding to the (112), (200), (220), and (312) diffraction planes of kesterite materials, respectively (JCPDS-26-0575). The symmetric and narrow peaks confirm the formation of high crystallinity and single-phase kesterite absorbers. However, additional diffraction peaks corresponding to the FTO substrate are also present (JCPDS-No). In addition, the formation of the single phase of ACZTS was confirmed using Raman spectroscopy (Figure 2b) at an excitation wavelength of 785 nm. The Raman curves exhibit peaks at 283, 321, 334, and 370 cm^{-1}, corresponding to the A1, A2, B1, and B2 vibrational modes of S–S interaction in the kesterite phase [90]. The principal peak sharpness indicates a less defective matrix [17], resulting from the decreased Cu/Zn disorder after incorporating larger silver atoms (ionic radius = 126 pm) and occupying the Cu (ionic radius = 73 pm) positions in the kesterite structures. This prevents the occupation of Cu vacancies by zinc (ionic radius = 74 pm), thereby reducing Cu/Zn antisite defects, which is a major issue in kesterite materials. The reduction of Cu/Zn defects has been observed in previous studies as a primary role of silver alloying in kesterite materials [142].

In contrast to the XRD and Raman results, which showed better structural properties, the SEM image (Figure 3a) revealed a disorganized morphology of the ACZTS sample, with small particles and a high density of voids. This disorganized morphology is reportedly related to the volatility of the Sn-S binary phases from the surface during annealing [112]. The smaller grains observed can be attributed to the absence of liquid phases during the annealing process, as FTO

limits the alkali metal diffusion from SLG. In this case, silver primarily participates in the formation of the kesterite structure. The presence of liquid phases during the annealing process leads to enhanced fusion of smaller grains within larger grains (Ostwald ripening) by creating a capillary force, resulting in larger grains in the final absorbers [143]. These results support the reduced effect of silver in assisting the grain growth of ACZTS materials, and lower melting Ag_2S is not formed during the phase evolution of ACZTS materials using this protocol. Additionally, the SEM images show some ZnS particles on the surface, which appear bright in the SEM images [144], likely due to the Zn-rich composition used in the synthesis of our materials, as shown in the EDX results (Table 1).

The bandgap of the ACZTS sample, as determined from the UV–visible data (Figure 3b), is approximately 1.62 eV, which is greater than the CZTS bandgap. This increase is due to silver incorporation, as reported in many studies on silver incorporation into kesterite materials. This may also be due to the ordered matrix, as it has been reported that kesterite materials with an ordered matrix can lead to a higher bandgap [145]. Generally, the valence band maximum (VBM) of kesterite materials is created by Cu–S bonding. When Cu is substituted by Ag, the VBM energetic level is reduced, leading to an increased bandgap. Additionally, Ag alloying can also improve the conduction band minimum (CBM) level by disordering the anion position when larger Ag atoms are introduced into the kesterite structure [146].

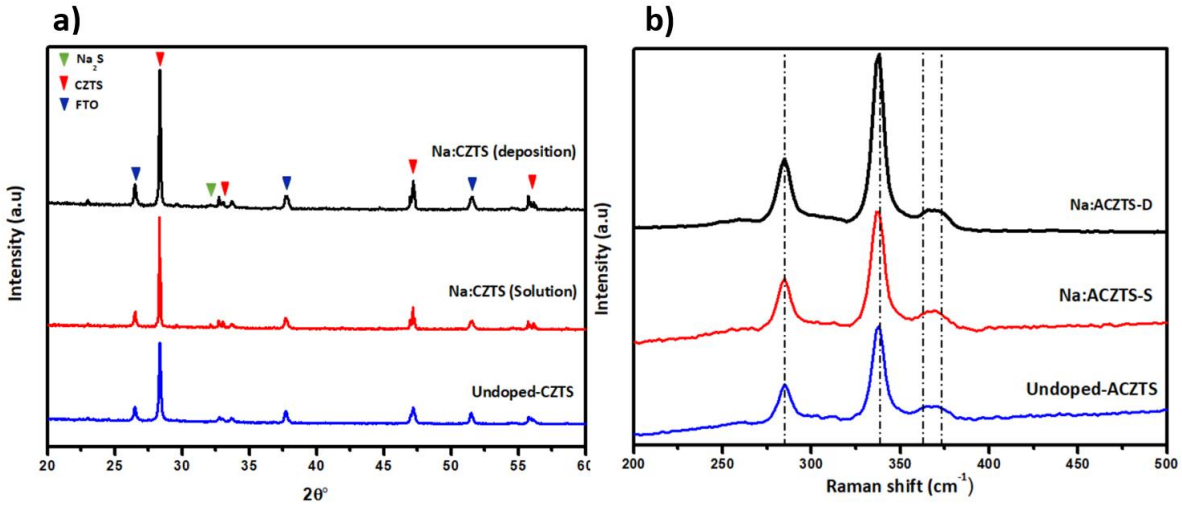

Figure 5.16: XRD patterns (a) and Raman spectra (b) of sodium-doped Na:ACZTS-S and Na:ACZTS-D samples compared to those of undoped CZTS

To evaluate the effect of alkali metal doping and their incorporation method on ACZTS materials, Na- and Li-doped samples were prepared using both the conventional doping strategy, which incorporates alkali metals in a sol-gel solution (Na:ACZTS-S), and the proposed

strategy, which deposits a NaCl layer on top of the ACZTS precursor during the deposition process (Na:ACZTS-D). Their structural properties were studied using XRD and Raman spectroscopy. As presented in Figure 4, the XRD results show diffraction peaks corresponding to the kesterite phase for all the samples. However, compared to the undoped-ACZTS sample, both doped samples exhibit narrow and higher peak intensities, indicating higher crystallinity, a common observation for Na and Li-doped kesterite compounds. These results confirm the incorporation of Na into the bulk of kesterite materials using both doping strategies and demonstrate the diffusion of sodium into the bulk of the materials for the Na:ACZTS-D sample. Additionally, there is no significant change in the main peak positions for all samples, which may be due to the lower amount of sodium used compared to the larger Ag atoms, which significantly affects the lattice parameters [147]. This result is supported by Raman analysis, which does not show any Raman shifts after Na doping. However, the sharpness and intensity of the Raman peaks are notably enhanced for the doped-ACZTS samples. The order/disorder of atoms strongly influences the Raman peaks in kesterite materials, where sharper and more intense peaks indicate a more ordered structure and a less defective matrix. In this case, Na doping leads to a less defective matrix, possibly by passivating Cu vacancies, which is one of the main roles of alkali metal doping in kesterite materials. The sample doped using the proposed strategy (Na:ACZTS-D) exhibited sharper and more intense peaks than did the Na:ACZTS-S sample, suggesting a more ordered and less defective matrix in accordance with the XRD results. These findings can be related to two factors: the diffusion pathway of Na during the annealing process and the greater quantity of Na incorporated, as the EDX results (Table 1) show greater amounts of sodium in the Na:ACZTS-D sample.

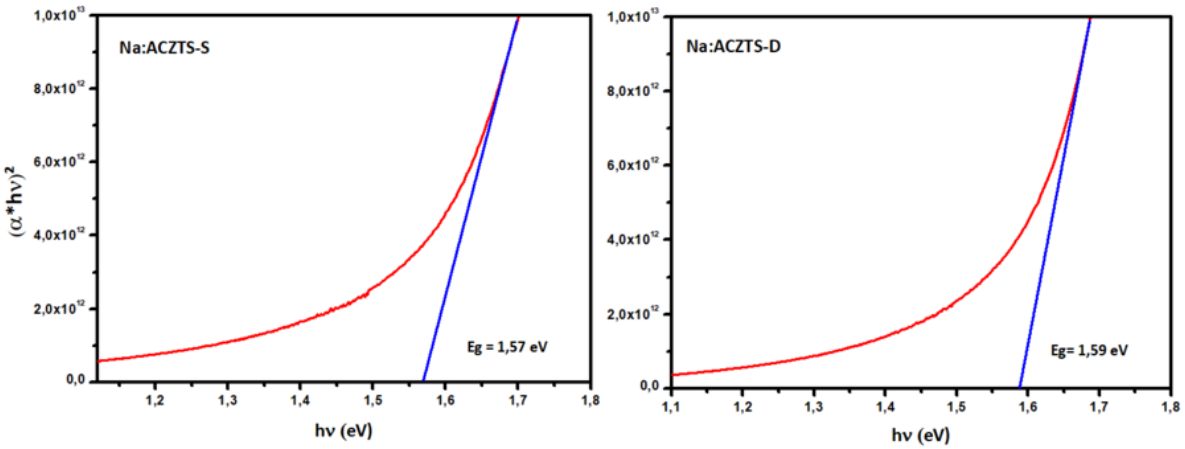

Figure 5.17: Energy bandgap of the sodium-doped Na:ACZTS-S and Na:ACZTS-D samples

The optical bandgap of both doped samples (Figure 5) shows a slight decrease compared to that of the undoped sample. Despite the higher crystallinity and less defective matrix observed for both doped samples, this reduction in the bandgap can be attributed to the role of sodium in substituting Cu in the kesterite structure. Sodium, similar to silver, affects the valence band maximum (VBM) but to a lesser extent than silver, which is known to have a more pronounced impact on the bandgap [148]. Additionally, the Urbach energies of both samples, calculated from the plot of Ln(α) (not shown here), decrease from 404 meV to 337 meV for Na:ACZTS-S and Na:ACZTS-S, respectively. This reduction in the Urbach energy signifies reduced band-tailing and bandgap fluctuations for the sample doped using the proposed strategy [REF]. These bandgap fluctuations are determined by defects having energy levels within the bandgap above or below the valence band (Ev) and conduction band (Ec). This result confirms the decreased defect densities observed in the Raman results for the Na:ACZTS-D sample.

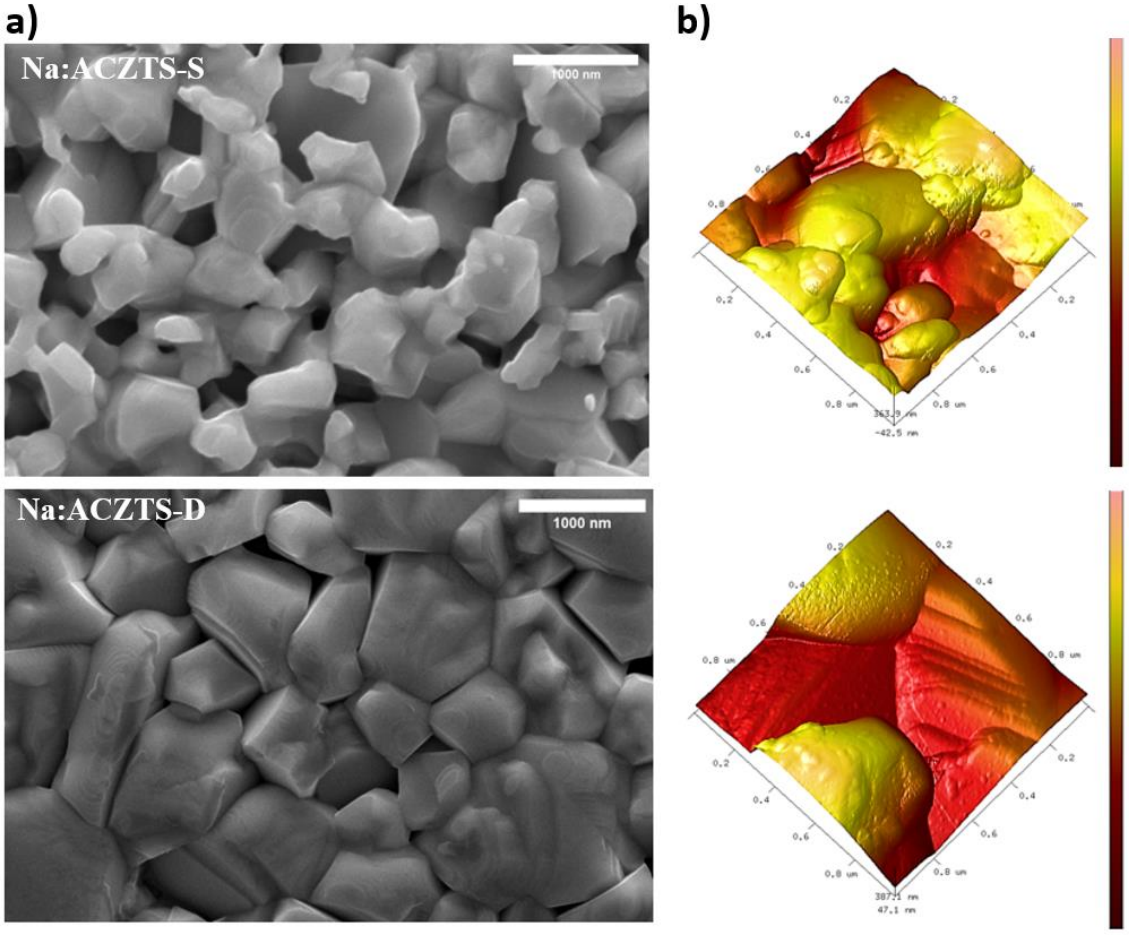

Figure 5.18: Surface SEM images (a) and 3D-AFM images (b) of the sodium-doped Na:ACZTS-S and Na:ACZTS-D samples

Table 2: *Cation ratios of the sodium-doped Na:ACZTS-S, Na:ACZTS-D C and U-CZTS samples from the EDS results*

Samples/Atom%	Cu	Sn	Zn	S	Na	Ag	Zn/Sn	Cu/(Zn + Sn)
Undoped-ACZTS	24.56	8.39	13.07	50.83	-----	3.12	1.55	1.14
Na:ACZTS-S	22.62	9.54	12.40	49.91	2.98	2.52	1.29	1.03
Na:ACZTS-D	22.07	11.08	12.22	48.05	4.05	2.48	1.10	0.94

The surface SEM and AFM images of Na:ACZTS-S and Na:ACZTS-D are shown in Figure 6. Both doped samples exhibit improved morphologies compared to those of the undoped sample (Figure 3a), highlighting the significant role of Na in enhancing grain growth during the annealing process and leading to larger grains in the final absorbers. However, the Na:ACZTS-D sample doped using the proposed strategy displays a more compact and homogeneous morphology with larger grains and fewer grain boundaries than the Na:ACZTS-S sample, as supported by the AFM images. This improvement in morphology is likely related to both the incorporation method of Na and the amount of Na present. The greater amount of Na observed in the Na:ACZTS-D sample may contribute to the observed morphology enhancements. Nevertheless, the difference in the amount of Na alone does not fully account for the significant variation in morphology, suggesting that the method of Na incorporation and its interaction with Ag play a crucial role. Additionally, the presence of a thin layer of NaCl on top of the precursor during the annealing process can lead to the formation of Na_2S at lower temperatures due to the lower melting point of NaCl. This enhances the chemisorption of sulfur on the surface and promotes grain growth in the Na:ACZTS-D sample [149]. On the other hand, doping using the proposed strategy results in a greater quantity of tin (Sn) compared to the other sample, indicating that this technique allows the prevention of Sn-S losses from the surface at higher temperatures. This is reflected in the better morphology and absence of surface voids in the SEM images, which are typically associated with the volatility of Sn-based phases [150]. Therefore, the proposed doping approach has a more beneficial effect than adding Na to the solution.

The results from our analysis demonstrate the advantages of doping kesterite materials with Na during the sol-gel deposition step. However, recent advancements highlight that Li doping has shown even greater benefits for improving kesterite material properties. For instance, efficiencies exceeding 14% have been achieved by combining Li doping with Ag alloying in kesterite-based solar cells [132]. As discussed earlier, the roles of alkali metals in kesterite materials differ after the final kesterite phase is formed, although both Na and Li enhance grain growth. The effectiveness of these alkali metals is influenced by their ionic radii, which affect the melting points of alkali-metal-S phases [REF]. Additionally, previous studies have indicated that Li significantly impacts the optoelectronic properties of kesterite materials compared to those of other alkali metals [151]. The ionic radius of Li (0.90 Å) is very close to that of Cu (0.91 Å), facilitating the ability of Li to occupy Cu vacancies. Moreover, Li can also replace Zn, creating Li_{Zn} antisites that enhance p-type conductivity and improve crystallinity [152]. In the next section, we will use a similar doping approach using smaller Li atoms to assess the potential of this method for lithium doping, as Li has become a particularly promising alkali metal for kesterite materials.

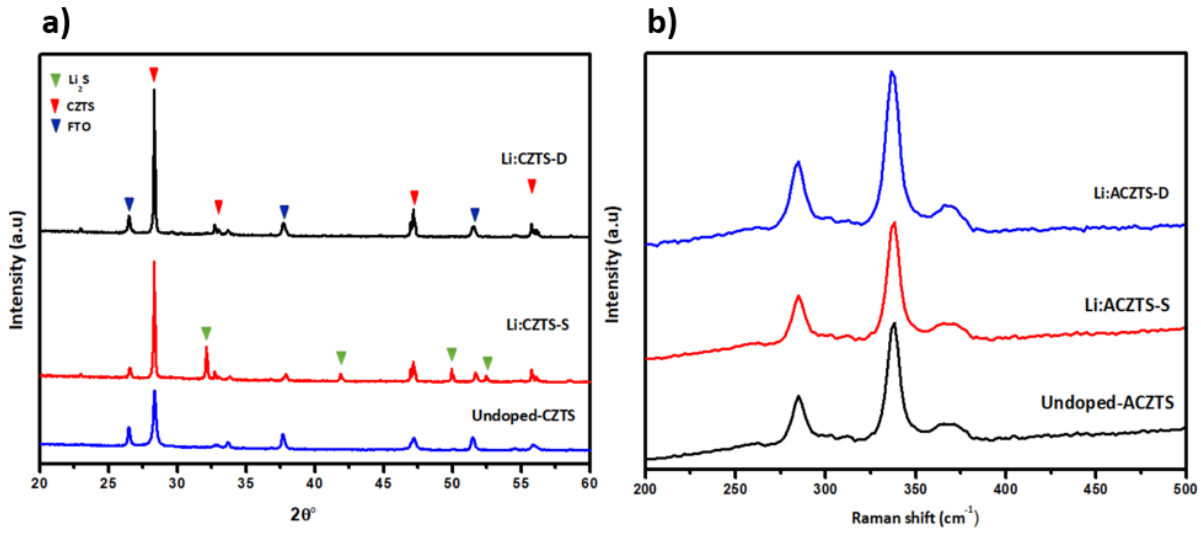

Figure 5. 19: XRD Patterns (a) and Raman Spectra (b) of Litium-Doped Li:ACZTS-S and Li:ACZTS-D Samples Compared to Undoped CZTS

The XRD patterns for the ACZTS samples doped with Li using both doping strategies, as well as the undoped sample, are shown in Figure 7. As with Na doping, the peak intensities are enhanced for both Li-doped samples compared to the undoped sample, indicating improved crystallinity with Li doping. This trend is consistent with previous reports that Li doping enhances the crystallinity of kesterite materials [153]. A comparison between the doping methods revealed that the Li:ACZTS-D sample doped using the proposed strategy exhibited sharper and more intense peaks than did the Li:ACZTS-S

sample. This finding aligns with observations made for Na doping, suggesting that the proposed method is effective for incorporating Li. In this work, for Na doping, NaCl, which is highly soluble in 2-methoxyethanol, was used as the Na source. After deposition and preheating, NaCl forms within or on top of the precursor. During sulfurization, NaCl transforms into Na_2S, which assists in kesterite growth by forming a liquid phase [REF]. In contrast, $LiClO_4$ was used for Li doping. $LiClO_4$, which is more thermally stable and has a higher decomposition temperature (420°C), remains in the films until the later stages of the annealing process. It then decomposes into LiCl, which eventually forms Li_2S [132]. This process is supported by additional peaks may be corresponding to Li_2S observed in the XRD pattern for the Li:ACZTS-S sample. Note that these peaks can be also due to the presence of SnS2 and Ag2S as some of their XRD peaks overlapped. Previous studies on Li doped with $LiClO_4$, in which DMSO was used as a solvent and selenium was used in the annealing process, did not report that these Li_2S phases may be due to different interactions between sulfur or selenium with $LiClO_4$. In the Li:ACZTS-D sample, the $LiClO_4$ phase deposited on top of the precursor is in direct contact with sulfur in the annealing atmosphere, facilitating the decomposition of $LiClO_4$ to LiCl and subsequently to Li_2S at lower temperatures. This interaction may enhance the growth of ACZTS materials. In addition, excess lithium can passivate grain boundaries and vacancies, leading to higher crystallinity and larger grains, as discussed in the next section. Overall, both Li-doped samples show improved crystallinity compared to that of the undoped sample. The issue of Li_2S formation can potentially be addressed by using LiCl instead of $LiClO_4$ or by optimizing the sulfurization temperature. The Raman spectra support these findings, with the Li:ACZTS-D sample exhibiting more intense peaks, indicating a more ordered structure. In contrast, the undoped and Li:ACZTS-S samples show comparable peak sharpness and intensity, potentially due to lower lithium incorporation and the presence of Li_2S, leading to a more disordered matrix.

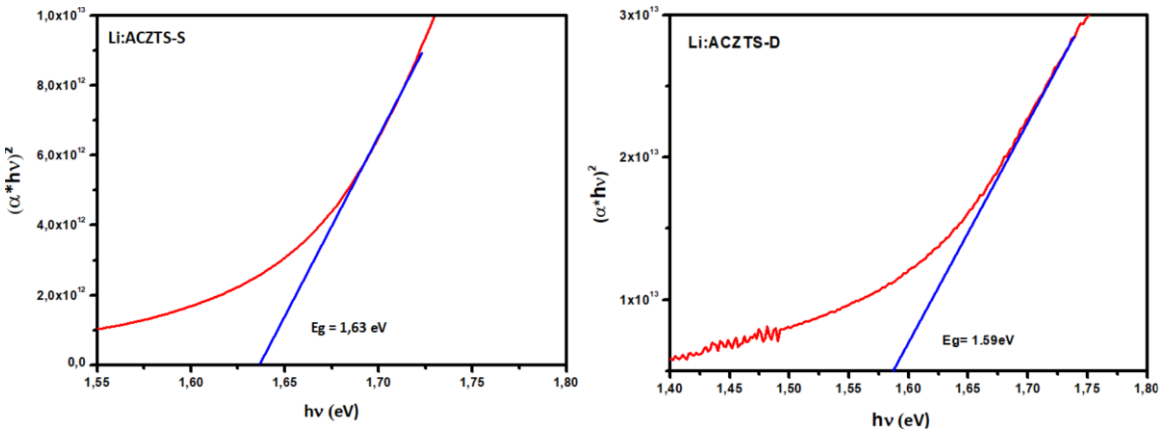

Figure 5.20: Energy band bandgap of the Litium-Doped Li:ACZTS-S and Li:ACZTS-D Samples

The optical bandgap values for the Li-doped samples shown in Figure 8 are 1.63 eV for Li:ACZTS-S and 1.58 eV for Li:ACZTS-D. The bandgap of Li:ACZTS-D is consistent with

the values obtained for Na-doped samples and aligns with the expected bandgap for Ag-alloyed samples at the given silver concentration [154]. The higher bandgap observed for Li:ACZTS-S could be attributed to off-stoichiometry or the presence of secondary phases, as confirmed by previous characterizations. The Urbach energy (Eu) for both samples, which indicates the extent of band-tail states and defect density, reveals values of 426 and 403 meV for Li:ACZTS-S and Li:ACZTS-D samples respectively. This slight reduction in Eu for the Li:ACZTS-D sample compared to that of the Li:ACZTS-S sample confirms the decreased defect density and band-tailing in the sample doped using the precursor method. This improvement supports the effectiveness of the proposed doping strategy in enhancing the optoelectronic properties of kesterite materials.

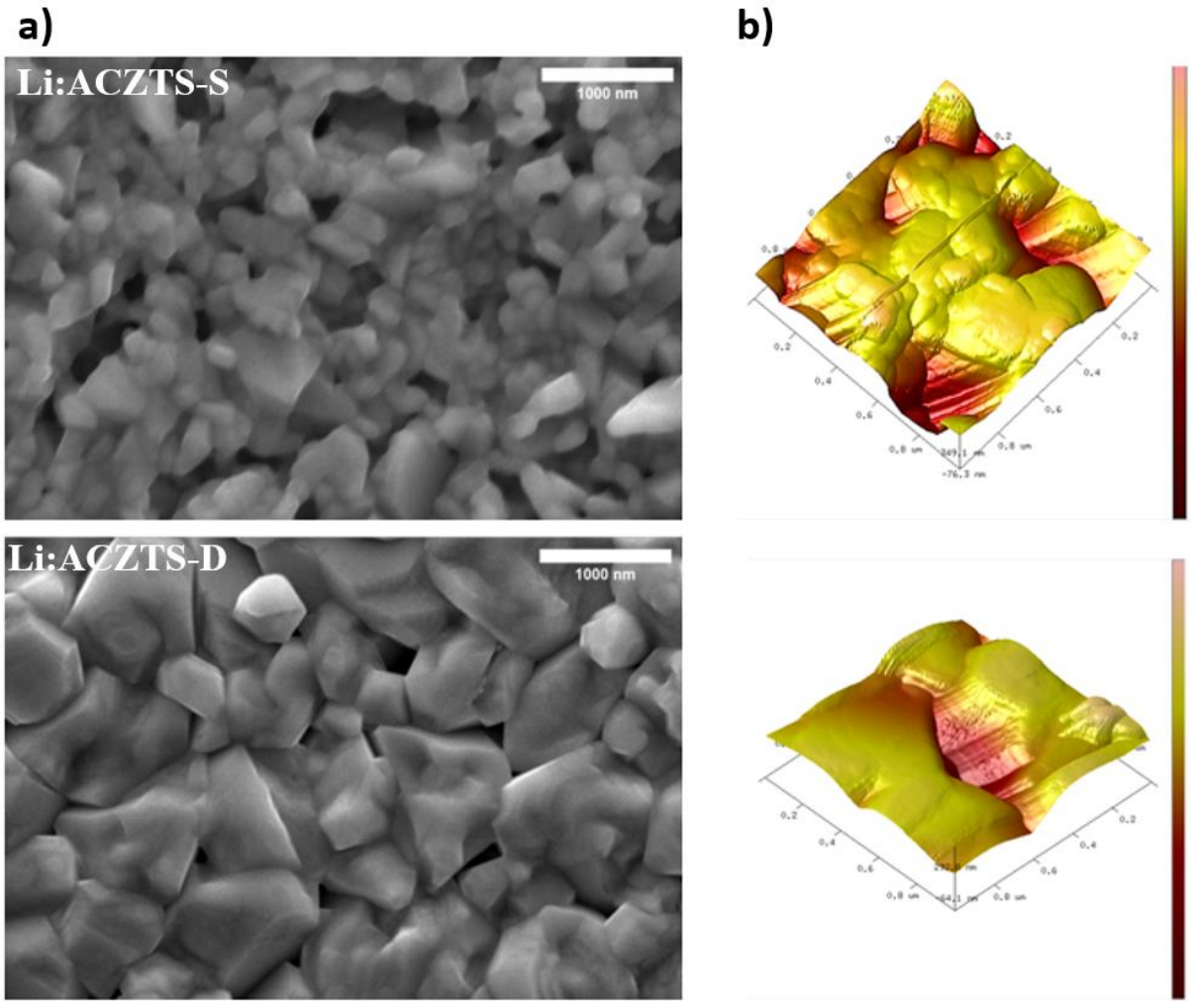

Figure 5.21: Surface SEM images (a) and 3D-AFM images (b) of the Litium-Doped Li:ACZTS-S and Li:ACZTS-D Samples

Table 4: *Cation ratios of the sodium-doped Na:ACZTS-S, Na:ACZTS-D C and U-CZTS samples from the EDS results*

Samples/Atom%	Cu	Sn	Zn	S	li	Ag	Zn/Sn	Cu/(Zn + Sn)
Undoped-ACZTS	24.56	8.39	13.07	50.83	-----	3.12	1.55	1.14
Li:ACZTS-S	22.10	14.16	11.14	49.12	-----	2.60	0.78	0.87
Li:ACZTS-D	22.30	11.33	11.41	50.93	-----	2.41	1.01	0.98

The SEM and AFM images of Li:ACZTS-S and Li:ACZTS-D are shown in Figure 9. Both samples exhibit more organized morphologies and larger grains than the undoped sample, which aligns with the reported benefits of Li doping in improving the grain size of kesterite materials [150]. However, similar to the Na doping results, the sample doped during deposition (Li:ACZTS-D) demonstrates a more compact and dense morphology with larger grain sizes. In contrast, the sample doped during solution preparation (Li:ACZTS-S) displays a less compact morphology with smaller grains and a greater density of voids. These observations can be attributed to the lower solubility in the solvent and higher decomposition temperature of $LiClO_4$, which is distributed within the absorber in the Li:ACZTS-S sample. This can lead to the formation of some grains in some regions within the bulk of the absorber and complicate the formation of Li_2S. Similar results have been reported in [132]. Additionally, these results might be influenced by the amount of Li incorporated using each doping strategy, as was noted in the Na doping results (note that lithium cannot be detected using EDX analysis). From the EDX results (Table X), both doped samples show greater amounts of Sn on the surface compared to the undoped sample. However, the excess Tin in the Li:ACZTS-S sample may lead to the formation of SnS2, which has diffraction peaks similar to those of Li2S (JPCDS 23-0677). To improve the comparability of sodium and lithium doping, it may be beneficial to use LiCl for a more consistent incorporation method for both dopants.

Overall, this work demonstrates the potential of the proposed doping strategy to enhance the structural, morphological, and optical properties of kesterite materials. Future research could further validate the benefits of this doping method in improving the performance of kesterite-based solar cells.

Optical simulation of the transmittance of Na:ACZTS-based solar cells

In this section, we employ the transfer matrix method (TMM) optical modelling to analyse the optical behavior of synthesized sodium-doped Ag-alloyed CZTS (Na:ACZTS-D) absorbers, which exhibit high crystallinity and improved morphology, along with reduced bandgap fluctuations and a relatively high bandgap of 1.59 eV, within tandem solar cell configurations. Specifically, the kesterite top subcell, structured as FTO/kesterite/CdS/ZnO/ITO/MgF_2, is optically modelled via TMM to evaluate the spectrum transmitted to the crystalline silicon (c-Si) bottom subcell. The optical data utilized in the simulations include both our experimentally obtained measurements for the Na:ACZTS absorbers and state-of-the-art data for other materials within the solar cell structure. The refractive index (n) and extinction coefficient (k) of the Na:ACZTS-D absorber were determined via the equations reported in [our paper when published], which were derived from our UV–visible spectroscopy measurements.

For the other layers in the solar cell structure:

- **CdS** and **ZnO:** Optical constants were sourced from ellipsometry data reported by Et-taya et al. [120].
- **ITO** and **MgF2 Layers:** Refractive index and extinction coefficient values were obtained from baseline data for kesterite/c-Si solar cells reported previously [121].

The thickness of each layer in our model mirrors that of the state-of-the-art transparent CZTS solar cells reported in [155]. Specifically, the ACZTS absorber layer was measured to be approximately 1.2 µm thick via profilometry, which aligns with the typical thicknesses employed in high-performance CZTS-based devices. By integrating these optical parameters into the TMM simulations, we aim to accurately predict the transmittance spectrum of the Na:ACZTS top cell and its impact on the overall performance of the tandem solar cell.

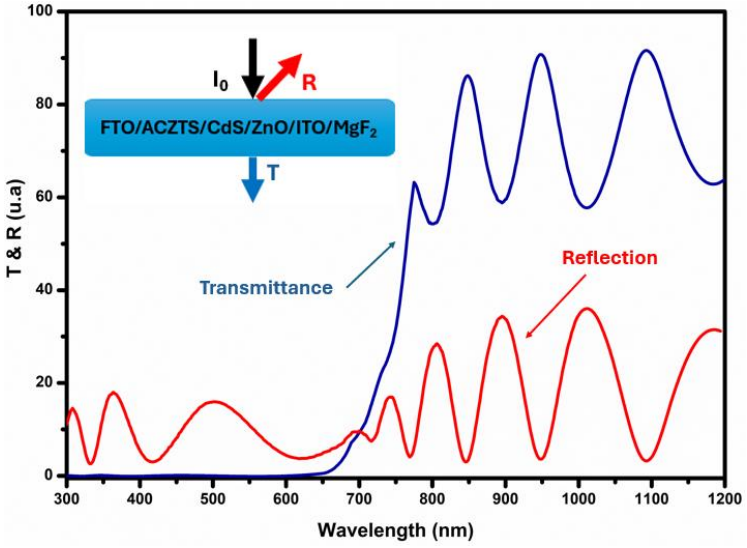

Figure 5.22: Transmittance and Reflection spectrum of FTO/Kesterite/CdS/ZnO/ITO solar cell stack calculated using TMM optical simulation

The transmission curves presented in Figure 8 correspond to the FTO/Na:ACZTS-D/CdS/ZnO/ITO structure and reveal two distinct regions. For photon energies exceeding the bandgap of the Na:ACZTS material (wavelengths <700 nm), minimal light transmission is observed because of the high absorption coefficient of ACZTS. In the near bandgap region (700–750 nm), transmission gradually increases, reaching approximately 80–90%, and is accompanied by interference fringes. These interference patterns arise from the constructive and destructive interactions of incident and reflected light at each interface within the multilayer stack, a phenomenon that occurs when the layer thicknesses are comparable to the wavelengths of the incident light [156]. Similar results have been reported in previous simulation studies on tandem solar cells using the transfer-matrix method (TMM), particularly with kesterite [121] and chalcopyrite [157] in the top cell. At longer wavelengths (>750 nm), which remain below the bandgap of the kesterite material, reflection becomes dominant, with reflectance values ranging from 20% to 40%. This behavior indicates that a significant portion of light is still reflected at wavelengths where the material does not effectively absorb photons. Consequently, these optical characteristics play crucial roles in optimizing the efficiency of tandem solar cell configurations by balancing the absorption and transmission properties to maximize the overall power conversion efficiency.

While the absorber's bandgap is a key parameter that governs material absorption, it is not the only consideration. Multiple optical phenomena, reflection and interference, occur at each interface within the device stack, significantly impacting the amount of light transmitted to the underlying layers [158,159]. When these effects are pronounced, much of the incident light is either reflected out of the device or trapped in undesirable standing wave patterns, reducing the fraction of photons reaching the c-Si bottom cell.

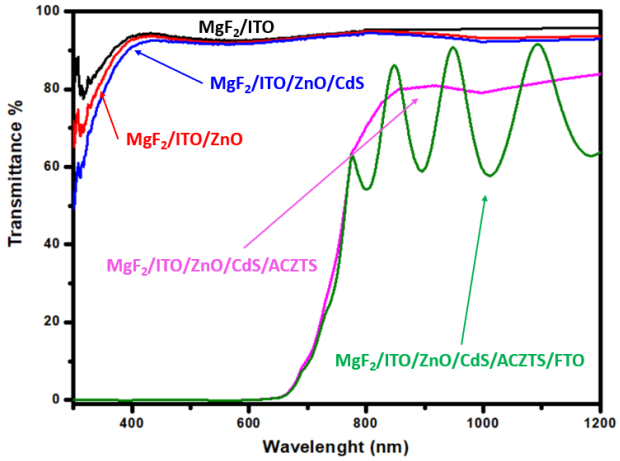

Figure 5.23: Transmittance spectrum of FTO/Kesterite/CdS/ZnO/ITO following the addition of each material in the solar cell stack

To understand which interfaces, contribute most significantly to the observed transmission losses, we implemented a systematic strategy. This approach involves incrementally constructing the solar cell stack layer by layer, starting from the ITO front contact and progressively adding each subsequent material. At each step, we simulate the transmitted light that passes through the partially assembled structure, and we also calculate the corresponding reflection. By comparing the transmission values after each layer is introduced, we can pinpoint where substantial optical losses occur. In other words, this layer-by-layer analysis allows us to identify the specific interfaces or material combinations that most severely prevent light from reaching the bottom subcell. As illustrated in Figure 6, the MgF2/ITO interface contributes to transmission losses in the near-infrared (NIR) region, primarily due to plasma oscillations (PSs) and a higher charge density within the ITO layer [123]. In contrast, the ITO/ZnO interface seems to mitigate losses in the IR domain, albeit accompanied by a slight reduction in transmittance at higher energies. The CdS layer has no significant influence on the overall transmittance and remains effectively neutral. Moreover, the CZTS absorber strongly reduces transmission below approximately 650 nm and introduces substantial losses extending into the NIR range. Finally, the TCO-based back electrode adds further complexity by generating interference patterns and causing a marked decrease in the IR transmittance, thus highlighting the critical role of transparent electrodes in optimizing the device's optical performance and confirm the potential of 2T-configuration in avoiding the optical losses by avoiding the use of transparent contacts compared to the 4T-configuration studied in this work [160].

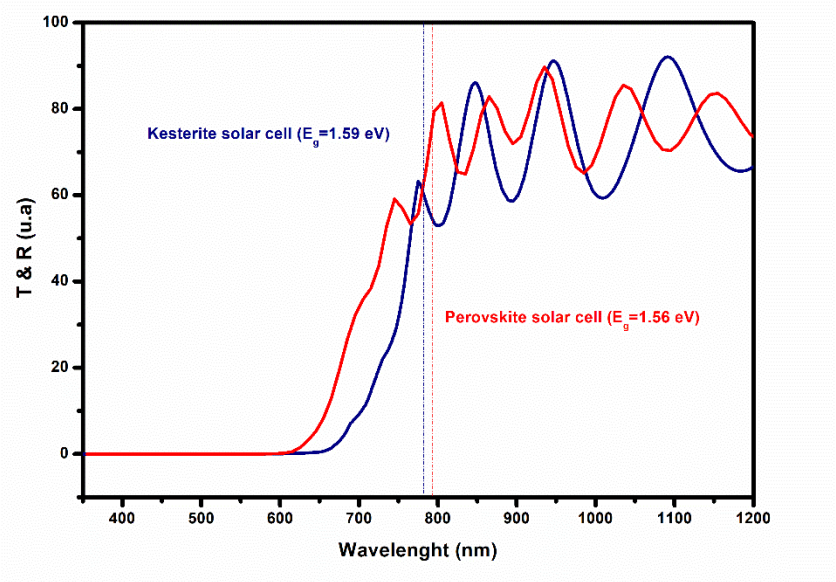

Figure 5.24: Transmittance spectrum of kesterite and perovskite solar cells calculated using TMM simulation

In this section, we compare the simulation results for kesterite and perovskite solar cells in a tandem 4T configuration to understand why perovskite solar cells achieve better performance when combined with a c-Si bottom subcell. This comparison is crucial for identifying the key factors that contribute to the higher performance of perovskite-based tandem devices obtained experimentally [161] and determining what improvements are needed in kesterite-based solar cells to reach similar efficiency levels. Figure 6 shows the transmission spectra of kesterite and perovskite solar cells with a bandgap of approximately 1.59 and 1.56 eV, respectively, which were calculated via TMM optical modelling. The perovskite solar cell considered in this analysis has the structure ITO/MoO_3/$FAPbI_3$/spiro/TiO2, which represents one of the best-performing perovskite solar cells reported [162]. All optical data used for perovskite solar cell simulation are extracted from [121]. As observed in the figure 6, despite the close bandgap of both solar cells, there are noticeable differences in their transmission characteristics. For kesterite, the transmission begins to increase at approximately 700 nm, whereas for perovskite, it starts at approximately 600 nm. This difference is due primarily to fluctuations in the bandgap of kesterite solar cells, which cause a shift in the wavelength at which transmission begins compared with that of perovskite solar cells [163]. At longer wavelengths, both solar cells show similar fluctuations in their transmission spectra. The region between 600 nm and 700 nm appears to be the most significant difference between the two materials in terms of light transmission, which can have a direct effect on the performance of the tandem configuration. The results suggest that kesterite faces a more pronounced challenge in the 600–700 nm range where transmission is lower, whereas at higher wavelengths, the transmission profiles of both solar cells converge.

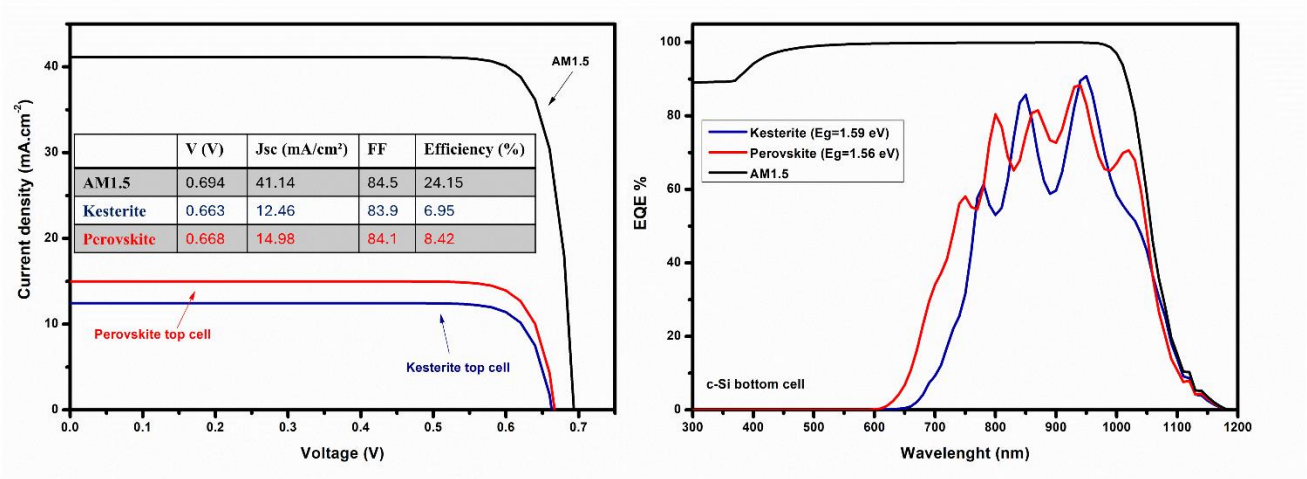

Figure 5.25: J-V curve and EQE of c-Si solar cells simulated using SCAPS-1D simulated under AM1.5, light transmitted from kesterite and perovskite solar cells

The above transmission spectra were used as a filter in the electrical simulation with SCAPS-1D to evaluate the c-Si solar cells in the mechanically stacked configuration of tandem solar cell. The c-Si subcell baseline used in this work reproduces one of the champion lab-scale c-Silicon solar cells [124]. The main electrical parameters used in the simulation are summarized in Table 1S. The results presented in Figure 7 demonstrate that the efficiency of the c-Si solar cell when paired with either kesterite or perovskite top cells are 6.95 and 8.42% respectively. Small differences in current density were observed, suggesting that kesterite has a transmission profile in the same range as perovskite. This indicates that achieving higher efficiency in kesterite/c-Si substrates could be possible without the need for further optimization of transmission properties alone.

Table 1 summarizes the photovoltaic (PV) performances of both kesterite/c-Si and perovskite/c-Si tandem configurations. The kesterite/c-Si tandem achieves an efficiency of 17.8%, while the perovskite/c-Si tandem achieves an efficiency of 31.87%. As discussed earlier, this performance difference arises due to the higher efficiency of the perovskite solar cell, which benefits from a higher bandgap and better transmission properties. Although kesterite materials show similar transmission characteristics to perovskite in the >700 nm range, their overall performance is still limited by factors such as lower efficiency at the top-cell level, even after optimizing the transmission properties. Thus, it is evident that while kesterite is a promising material, it still faces challenges in matching the high performance of perovskite in tandem applications. To bridge this gap, more advanced research should focus on improving both the efficiency and bandgap of kesterite solar cells, possibly through material innovations or novel fabrication techniques, in order to meet or surpass the efficiency levels achieved by perovskite/c-Si tandem cells.

Table 1: Efficiency of Kesterite/c-Si Tandem Device and Respective Subcells.

Efficiency%	**Top cell**	**Bottom cell**	**Tandem cell**
Kesterite/c-Si	10.3 [REF]	6.98	17.8
Perovskite/c-Si	24 [REF]	7.87	31.87

V.2.4. Conclusion

This work explored the incorporation of Sodium (Na) into Ag-alloyed kesterite materials via a simple and efficient doping strategy. This strategy involves depositing Sodium (Na) layers on top of ACZTS precursors prepared on an FTO electrode via sol–gel and spin-coating methods. Our structural analysis results demonstrate the potential of this doping strategy to improve crystallinity and reduce atomic disorder and defect densities, resulting in enhanced morphologies and optical properties for Sodium (Na) doping. Using transfer matrix method (TMM) simulations, we modeled the optical behavior of the Na-doped top cell within a tandem configuration, revealing its impact on the overall light management and transmission to the crystalline silicon (c-Si) bottom subcell. Electrical simulations with SCAPS-1D indicate that, although the Na-doped kesterite top cell exhibits a transmission profile comparable to that of perovskite, the lower efficiency at the top-cell level limits the overall tandem performance. Specifically, while the kesterite/c-Si tandem configuration achieves promising efficiency, it remains below that of the perovskite/c-Si tandem device. These findings highlight the potential of sodium doping for advancing kesterite solar cells and underscore the need for further optimization to bridge the performance gap in tandem configurations.

IV.3. Feasibility of exceeding 20% efficiency for kesterite/c-Silicon tandem solar cells using an alternative buffer layer: optical and electrical analysis

Tandem solar cells can exceed the Shockley-Queisser limit for single junction cells. This study used optical and electrical modeling based on experimental data to enhance Kesterite/c-Si tandem solar cell performance by incorporating a nontoxic TiO2 buffer layer in the Kesterite top subcell. Using SCAPS-1D simulation, we first established baseline data from the best kesterite (CZTS, Eg=1.5 eV) device. After achieving similar metric parameters, we analyzed the impact of replacing CdS with TiO2 on optoelectronic characteristics. We examined various top subcell absorbers (CZTS0.8Se0.2 (Eg=1.4 eV), CZTS (Eg=1.5 eV), CZTS (Eg=1.6 eV), and CZT0.6Ge0.4S (Eg=1.7 eV)) under AM1.5 illumination. To match currents, we simulated the c-Si bottom subcell (19% efficiency) using the transmitted light from the top subcells, calculated via the transfer matrix method (TMM). The TiO2 buffer layer significantly improved the top subcell's electrical and optical performance by reducing parasitic light absorption and heterojunction interface recombination. The optimal tandem device, with a TiO2 buffer layer and a 1.7 eV bandgap (CZT0.6Ge0.4S) top subcell at 0.8 μm thickness, achieved approximately 20% efficiency. These results suggest that TiO2 buffer layers can significantly improve

kesterite/Si tandem solar cells, though further optical and electrical advancements are needed for kesterite materials to be viable in tandem applications.

IV.3.1. Introduction

Among other renewable energies, photovoltaics has been shown to be a crucial alternative for future low-cost power generation. Nevertheless, the technology faces various problems in maintaining this position, the most notable of which is the efficiency of solar cells. Current attempts show that crystalline silicon-based solar cell efficiency is reaching basic limitations based on the Shockley Queisser limit [2]. The tandem idea allows this single junction constraint to be surpassed (multijunction). Tandem devices provide a route to greater conversion performance by maximizing solar spectrum absorption and lowering thermalization losses in the bottom subcell [164]. For these reasons, multiple efforts have been undertaken in recent years to construct novel tandem cell structures [165–168]. Due to the excellent thermal stability of silicon solar cells, which is more compatible with the deposition technique used to build the top subcell, tandem systems based on the silicon bottom subcell idea may be much more useful [169]. The tandem structure with c-Si as bottom subcells (Eg = 1,12 eV) and a top subcell with an absorber with Eg up to 1.7 eV theoretically yield more than 40% efficiency [170]. Perovskite-based solar cells have been proposed as an appealing material for use as wide bandgap top subcells due to their huge band gap tunability and high efficiency exceeding 24.8% [171,172]. Several studies have investigated perovskite as a top subcell in c-Si/perovskite tandem solar cells due to recent outstanding developments in perovskite solar cell performance [168,173]. These structures yield an efficiency of 31.3% in a monolithic structure [174]. However, stability is the major challenge to success with these structures. Regarding the most recent perovskite/Si tandem device breakthroughs, there has been much interest in looking for alternative wide bandgap top-subcell materials that might result in more stable and efficient tandem cells. Thin film solar cells based on CdTe and CIGS is viable options. In fact, a 16.8% efficient $Cd_{1-x}Zn_xTe$/Si [175] and Si/CGSe tandem cell with 10% efficiency has been found [40]. Unfortunately, these materials are hampered by the toxicity and scarcity of their constituent components.

Kesterite thin films could be a good top-subcell material since they have good long-term stability and can be elaborated with low-cost and nontoxic materials. Moreover, the optical bandgap of kesterite varies based on its chemical composition, ranging from about 1 eV for pure CZTSe [77,176] to more than 2 eV for germanium-alloyed CZTGS [177].[178] Kesterite devices have witnessed considerable advances in their efficiency over the course of the last

several years, reaching over 11% for pure sulfide CZTS [179] and more than 13% for the sulfo-selinide ACZTSSe [88]. Researchers have recommended Kesterite/c-Si as a feasible approach toward low-cost and highly efficient tandem devices for the reasons mentioned above.

Finding a suitable tunnel junction to enable smooth carrier transfer between the top and bottom subcells is one of the primary hurdles in the practical development of the CZTS/c-Si tandem device. This interface should have high infrared transparency to allow adequate light absorption in the c-Si bottom cell, strong electrical connections between top and bottom cells, and high resistance to the high temperature thermal treatments applied in top subcell fabrication [101].

The first working monolithic CZTS/c-Si tandem cell with MoS_2/FTO/ZnO intermediate layer with an efficiency of 3.5% has been reported [101]. However, the degradation of the intermediate layers' transmittance and the elements' diffusion into the Si bottom subcell during the high temperature treatments used to develop the top subcell are the main restrictions limiting the tandem device's obtained performances. This problem might be solved by placing a diffusion barrier layer between the bottom cell and top cell. It has been claimed that the TiN nanolayer protects the bottom Si cell from contamination during CZTS growth and acts as an interface recombination layer [180].[181]

Notwithstanding the abovementioned concerns with the intermediate connection, the power conversion efficiency (PCE) of the kesterite solar cells is too low for usage in top subcells. The primary reasons for the poor performance of the CZTS solar cell are the high recombination rate produced by either a high density of bulk and/or surface defects [182,183] and the improper alignment with the CdS buffer layer [184,185]. It is critical to improve the performance of the CZTS top subcell to obtain the desired performance from the CZTS/c-Si tandem device.

Yuancai el al [88] concluded in their analysis of the record ACZTSSe/CdS solar cell that a defective and lattice-mismatched interface is created during CdS deposition and the CdS is not the suitable buffer layer for kesterite based solar cell. Furthermore, numerous effective methods are being researched, such as the possibility of CdS buffer layer replacement. As nontoxic buffer layers, ZTO and ZnS have been investigated [186,187]. According to a recent studies, utilizing a nontoxic TiO_2 buffer layer considerably improves the performance of CIGS solar cells [188]. Additionally, utilizing TiO_2 with a wide band gap may minimize parasitic absorption in the short wavelength region and remove CdS toxicity. Since CZTS and CIGS materials have comparable characteristics, several studies have recently outlined the use of TiO_2 as an electron transporting layer in CZTS solar cells [174]. Moreover, the results obtained with

CZTS/TiO_2 devices are comparable to the ones obtained from CZTS/CdS reference cells, suggesting that, much higher performances could be obtained by applying ALD-TiO_2 buffer layer. Additionally, current modelling methodologies show that using TiO_2 as an electron transport material is a good strategy to improve the performance of CZTS devices [189,190].[191,192]

In this paper, the use of TiO_2 as an alternative buffer layer in kesterite solar cells and its impact on CZTS/Si tandem cells is studied via optical and electrical modeling. The top subcell kesterite is reproduced to fit the reported data from the experiments. Afterwards, adding TiO_2 as a buffer layer for the top subcell is investigated. Moreover, both top subcell structures kesterite/CdS and kesterite/TiO_2, with different bandgaps and thicknesses, of the absorber layer (Kesterite) are simulated and analyzed to calculate the absorbed spectrum from the top subcell. The c-Si bottom subcell is simulated with various spectra of transmitted light from the top subcell. By plotting the current densities of the bottom and top subcells (J_{SC} and J_{MPP}) as a function of the top subcell absorber bandgap and thickness, the current matching condition (both subcells produce similar currents) was obtained. Conclusively, the tandem solar cell characteristics are calculated under current matching conditions.

IV.3.4. Materials and methods

The suggested kesterite/c-Si tandem solar cell is electrically simulated using the Solar Cell Capacitance Simulator (SCAPS-1D) software version 3.3.07 [116]. This software is widely used to model and simulate thin-film polycrystalline solar cells. The results from the simulations with SCAPS are very similar to those of the experiments [120]. The program is based on a numerical resolution of the semiconductor equations, Poisson, and the carrier continuity equations (1, 2, and 3) to calculate the parameters of the simulated solar cells:

The Poisson equation:

$$\frac{d}{dx}\left(-\varepsilon(x)\frac{d\Psi}{dx}\right) = q[p(x) - n(x) + N_D^+(x) - N_A^-(x) + p_t(x) - n_t(x)] \qquad (1)$$

where ε is the dielectric constant, $N_A^-(x)$ and $N_D^+(x)$ are the acceptor and donor concentrations, respectively, Ψ is the electrostatic potential, $p_t(x)$ and $n_t(x)$ are trapped holes and electrons, respectively, $p(x)$ and $n(x)$ are the free hole and electron concentrations, respectively, and q is the electron charge.

The continuity equations for holes (2) and electrons (3):

$$\frac{1}{q}\left[\frac{dJ_p(x)}{dt}\right] = G_L(x) - R(x) \quad (2)$$

$$\frac{1}{q}\left[\frac{dJ_n(x)}{dt}\right] = -G_L(x) + R(x) \quad (3)$$

G(x) is the optical generation rate. E_{Fn} and E_{Fp} are the electron and hole quasi-Fermi levels, respectively, and μp and μn are the mobilities of holes and electrons, respectively. R(x) is the net recombination rate.

Different configurations of Kesterite/c-Si tandem cells can be used (2-terminal and 4-terminal solar cells). In the 4-terminal connection, the two subcells are mechanically stacked, and the outputs are collected independently using four electrodes. On the other hand, the top subcell is deposited directly on the bottom subcell in the 2-terminal configuration, and the two subcells are electrically connected in series. The 4-terminal connection is straightforward to create; however, the electrodes must be carefully chosen to minimize parasitic absorption. Whereas, the 2T-tandem cells, on the other hand, use only one transparent electrode, reducing parasitic absorption and manufacturing costs.

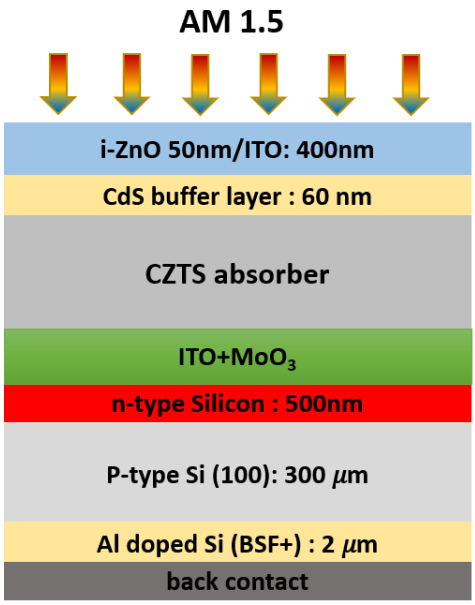

Figure 5.26: Tandem solar cell structure of CZTS/c-Si used in our simulation.

In the current study, we adopted the 2T-tandem structure depicted in Fig. 1. The top subcell had ZnO (50 nm) and ZnO:Al (400 nm) transparent conducting oxide (TCO) layers, CdS (60 nm)

as an n-type wide band gap buffer layer, and kesterite as a p-type absorber. The bottom subcell contains a typical p-n junction of crystalline silicon. Table 1 summarizes the material parameters employed in our simulation. Table 2 summarizes the main defect properties used for the baseline simulation. The input parameters for each layer of CZTS, CdS, TiO_2, and ZnO are chosen based on theories and literature values [190,193–199]. The complicated defect properties of kesterite solar cells are particularly sensitive to several factors, such as the experimental procedure used to prepare the various layers. In this instance, the bulk defect characteristics of kesterite materials are chosen based on Kim et al work [200], and modified to match the reference cell performances at a defect density of 5.10^{15} cm^{-3}. The CdS bulk and Kesterite/CdS interface defects properties are extracted from the baseline reported in [199]. The parameters used in the simulation for the bottom c-Si solar cells are mostly from the default library of SCAPS-1D. The simulated c-Si bottom subcell exhibits an efficiency of 18.7% with a V_{OC} of 639 mV, a J_{SC} of 36.9 mA/cm^2, and a fill factor of 79.4%, which are in good agreement with the experiment of a real solar cell reported in [201].

Materials properties	p-Si	n-Si	CZTS	CdS	i-ZnO	ITO	TiO_2
Thickness (µm)	400	0.5	1.2	0.06	0.05	0.4	0.06
Bandgap (eV)	1.12	1.12	1.5	2.40	3.37	3.37	3.26
Electron affinity (eV)	4.46	4.46	4.1	4.2	4.6	4.6	3.7
Dielectric permittivity	9.1	9.1	7	10	9	9	55
CB (cm^{-3}).10^{19}	2.8	2.8	2.2	2.2	2.2	2.2	2
VB (cm^{-3}).10^{19}	1.040	1.040	1.8	1.8	1.8	1.8	6
Electron mobility (cm^2/Vs)	1500	1500	100	100	150	150	100
Hole mobility (cm^2/Vs)	450	450	25	25	25	25	25
N_d (cm^{-3})	0	5.10^{20}	0	10^{18}	10^{17}	10^{20}	10^{17}
N_a (cm^{-3})	5.10^{16}	0	1.10^{16}	0	0	0	0

Table 2. bulk and interface defects properties used for simulating the baseline solar cells.

Defect properties	Type	Density (cm^{-3})	Energy level (eV)	Capture cross section (cm^2)
Bulk CZTS	Single donor	5.10^{15}	0.900 above Ev	1.10^{-14}
CdS	Neutral	Grading $1.772.10^{15}$ 9.997E+17	1.200 above Ev	$1. 10^{-13}$
CZTS/CdS	Acceptor	2.00E+13	0.300 above the highest Ev	1.00E-14

The practical development of monolithic kesterite/c-Si requires the use of TCOs as intermediate layers, which is now the only approach available. Ah et al. developed a CIGSe/ITO/c-Si tandem device with more than 10% efficiency [40]. According to their electrical analysis, the series resistance of the bottom subcell has the largest impact on tandem efficiency, whereas the electrical loss owing to the tunnel junction resistance is unsignificant. Furthermore, a theoretical study demonstrated that the recombination junction has a strong effect on the fill factor of the monolithic tandem cells; however, employing a recombination junction with a lower interface gap can produce high-efficiency monolithic tandem cells without a strong effect of the RJ [202]. Based on these findings, and since the main tunneling mechanisms needed for monolithic multijunction structure simulations are not implemented in SCAPS-1D, the electrical resistance of the tunnel junction is not considered in the electrical simulation, and we simulate the top and bottom subcells independently.

The kesterite top subcell with the following structure: ITO/MoO_3/kesterite/CdS/ZnO/ITO is modeled optically to calculate the transmitted light for various bandgaps and thicknesses of the absorber layer. In several studies on tandem devices, the transmitted light from the top subcell was calculated using the beer lamber law [193,203,204]. This method contains only absorption at the layers. Thus, no interface reflection and no interference are considered. In this work, the TMM method is used to calculate the transmittance and reflectance of the top subcell. D, and the current matching conditions, where both subcells produce similar J_{SC} or J_{MPP}, are considered. After that, simulate the tandem device at the current-matching points to maximize the current produced in a series-connected mode.

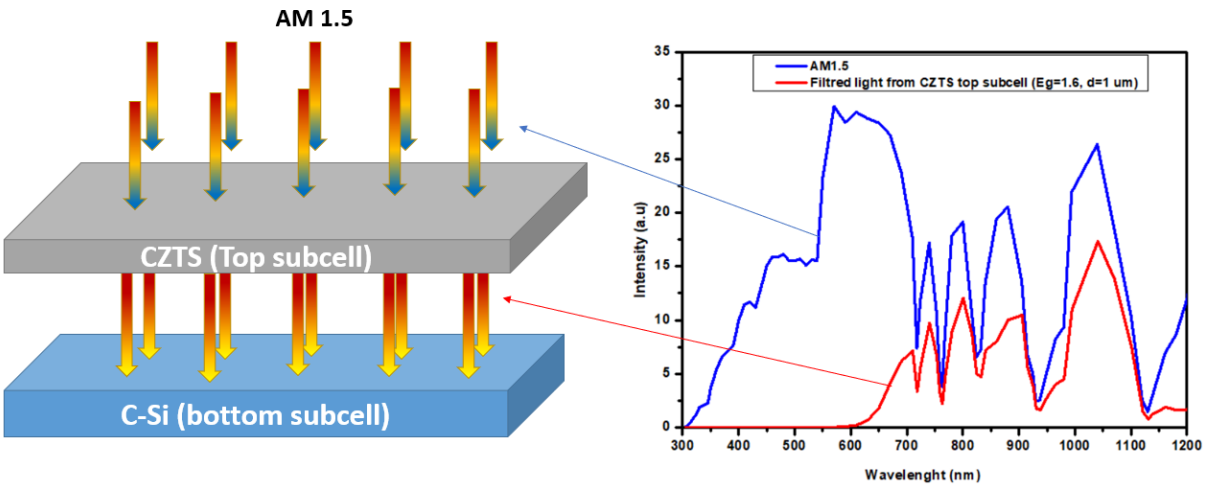

Figure 5. 13: The approach used in this simulation, considering the absorption of the top subcell, the transmitted light to the bottom subcell is calculated and used for simulating the c-Si subcell.

The optical data used in the optical modeling of the top cell are extracted from experimental works; for CdS, ZnO, and Al:ZnO, $CZTS_{0.8}Se_{0.2}$ (Eg = 1.4 eV) and CZTS (Eg = 1.5 eV) layers are based on ellipsometry data collected by Et-taya et al.[120]; the TiO_2 parameters are from [44]; and for the kesterite thin films, CZTS (Eg = 1.6 eV), $CZT_{0.6}Ge_{0.4}$ (Eg = 1.7 eV), ITO, and MoO_3 are from [199]. The absorption coefficients used in this simulation for each material are calculated from the above optical data, and the results are shown in Fig. 3. Since the SCPAS optical model considers only the absorption at the layers, the reflection of the top subcell was calculated using TMM and used as an optical filter in SCAPS simulations for a more accurate calculation results.

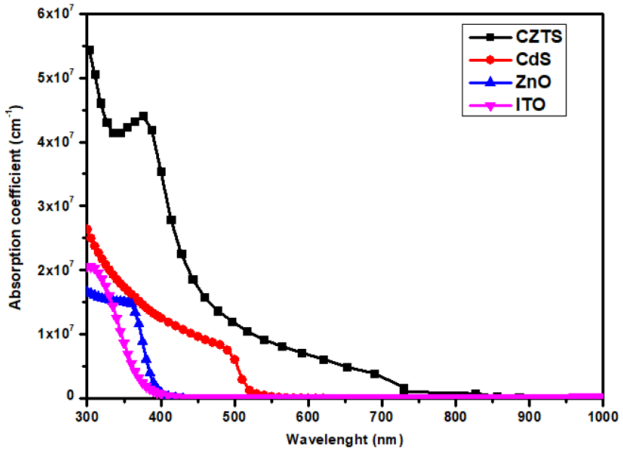

Figure 5.28: The absorption coefficient of the different materials of the baseline CZTS (Eg=1.5eV) solar cell.

V.3.3. Result and discussion

Validation of the simulation model

The world record CZTS (Eg=1.5eV) solar cell reported by Yan et al. [179] was used to validate the input parameters and create a simulation baseline for our study. This solar cell exhibits an efficiency of 11.01%, with V_{OC}= 0.73 V, J_{SC} = 21.74 mA/cm^2, and FF = 69.27%. A comparison of reported and simulated CZTS solar cell performance is shown in Fig. 4. The calculated photovoltaic parameters for both cells are summarized in the inset table of Fig. 4. The simulated device exhibits an efficiency of 11.01% with V_{OC}= 0.73 V, J_{SC}= 21.74 mA/cm^2, and FF= 69.17%, suggesting that the difference between the experimental and simulated data is insignificant. This good match between the experiment and our numerical results confirms the accuracy of the used baseline model.

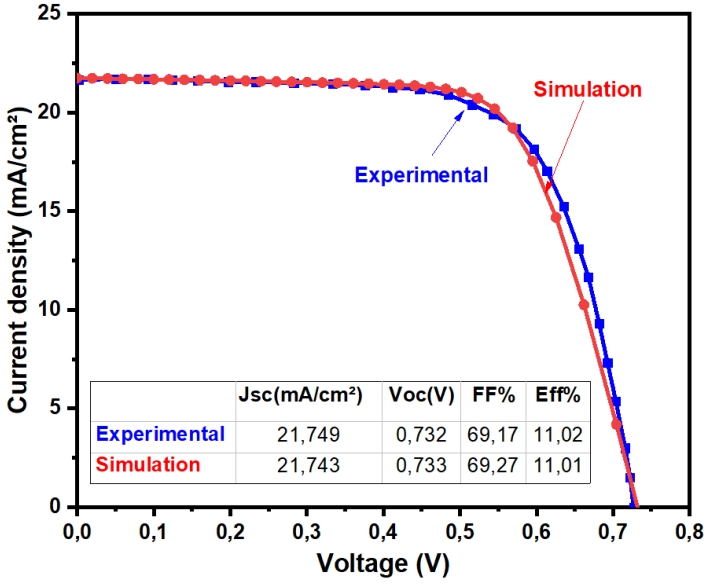

Figure 5. 29: Comparison between the J-V performances of the simulated and reproduced CZTS solar cells [19].

Improving the CZTS performance using an alternative buffer layer.

The output characteristics achieved from the simulated CZTS/CdS solar cell are inadequate for the application of this structure as a top subcell with a silicon solar cell in a tandem design. To develop a tandem structure with acceptable efficiency, it is necessary to improve the CZTS top subcell performance. In this work, we aim to improve the performance of the kesterite device through band engineering employing TiO_2 as a buffer layer. Based on previous research [189,205], we expect that n-type TiO_2 creates an ideal junction with p-type kesterite and may enhance the quality of the kesterite/TiO_2 interface, resulting in a considerable boost in CZTS device performance. To investigate only the effect of TiO_2 on the solar cell performance, we kept all the parameters unchanged, and we replaced CdS with the suggested TiO_2 using the

input parameters listed in Table 1. Fig. 5 illustrates the J-V curve of both the CZTS/CdS and CZTS/TiO_2 structures, and their parameters are listed in the inset table. It should be mentioned that the discrepancies in the PV performance characteristics between the CZTS/CdS and CZTS/TiO_2 devices are significant. The CZTS/TiO_2 solar cell achieves an efficiency value of 14.11%, whereas the reference cell's efficiency is only 11.01%. This high improvement in efficiency is due to a large increase from 68 to 81 in FF and a slight increase from 21.95 mA/cm^2 to 22.85 mA/cm^2 and from 0.73 V to 0.76 V in J_{SC} and V_{OC}, respectively.

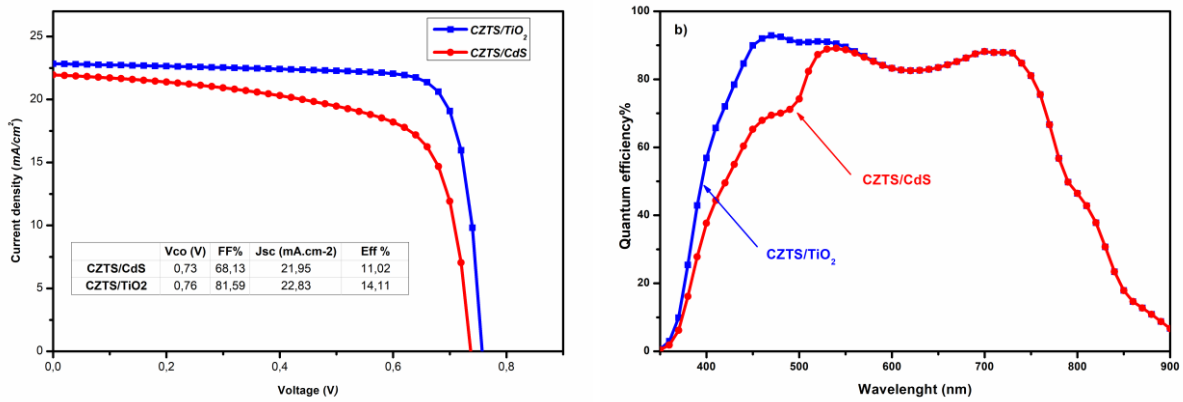

Figure 5. 14: (a) J-V performances of the simulated CZTS solar cells with CdS (red line) and TiO2 (blue line) buffer layers; (b) Quantum efficiencies of CZTS solar cells with CdS (red line) and TiO2 (blue line) buffer layers

The quantum efficiency (QE) of CZTS/CdS and CZTS/TiO_2 is shown in Fig. 5, b. It could be noted that at higher wavelengths, where the absorber dominates the absorption, both devices display almost the same QE. However, at shorter wavelengths, a strong improvement in the QE is seen in the device with the TiO_2 buffer layer, indicating better photogenerated carrier collection and reduced recombination at the heterojunction [206,207]. Furthermore, the introduction of wide bandgap TiO_2 contributes to the enhancement of QE by reducing parasitic absorption in this region (<500nm).

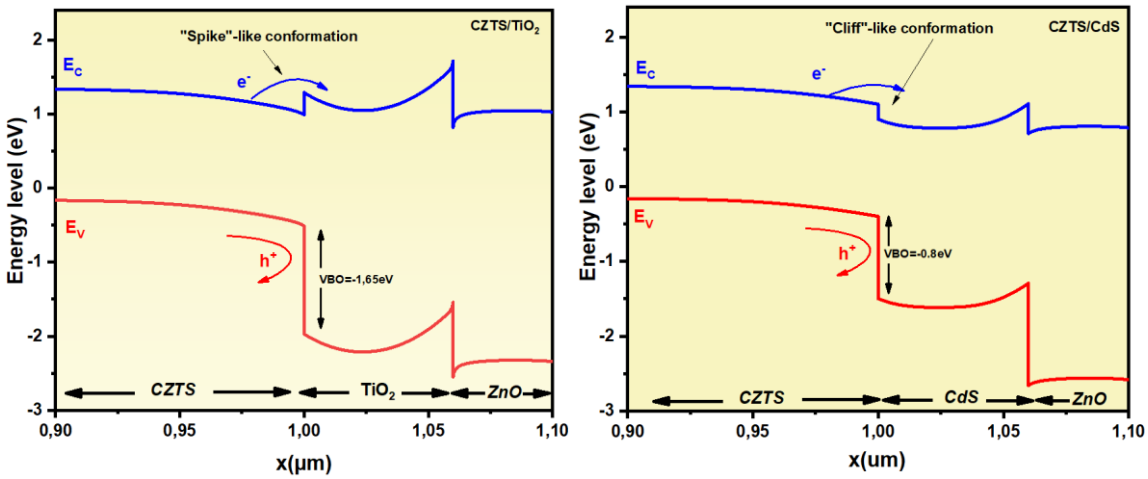

Figure 5. 31: Band diagram at the heterojunction for CZTS/TiO2 (left) and CZTS/CdS (Right)

The band diagrams of CZTS/CdS and CZTS/TiO_2 are shown in Fig. 6 to address these findings. The band alignment at the heterointerface is determined by the bandgap and electron affinity of the absorber and the buffer layer; the obtained conduction band offset (CBO) in CZTS/CdS is a cliff-like configuration, as reported previously [208]. The CBO is changed to a spike-like ($Ec_{Buffer} > Ec_{Absorber}$), with a value of 0.11 eV when the TiO_2 buffer layer is employed. On the other hand, the valence band offset (VBO) of the buffer layer must be designed to prevent photogenerated holes (PGHs) at the absorber/buffer interface. In the case of the CZTS/TiO2 heterojunction, a VBO value of -1.67 eV is obtained, which is greater than that of CZTS/CdS (-0.8 eV). This higher VBO contributes to the improved QE and J_{SC} of the device. The key factor affecting the FF of solar cells is the SRH recombination caused by the device's series resistance, which includes layer and interface resistances. In CZTS devices, the resistive nature of the CZTS/CdS interface resulted in significant recombination and hence reduced the FF [185,209]. The SRH recombination at the heterojunction for both structures are shown in Fig. 7. The device with the CdS buffer layer has a high density of carrier recombination at the interface and in the space charge region (SCR), whereas the device with TiO_2 has a significantly lower density of carrier recombination. These findings explain why the CZTS/TiO_2 device has a greater FF than the traditional CZTS/CdS structure.

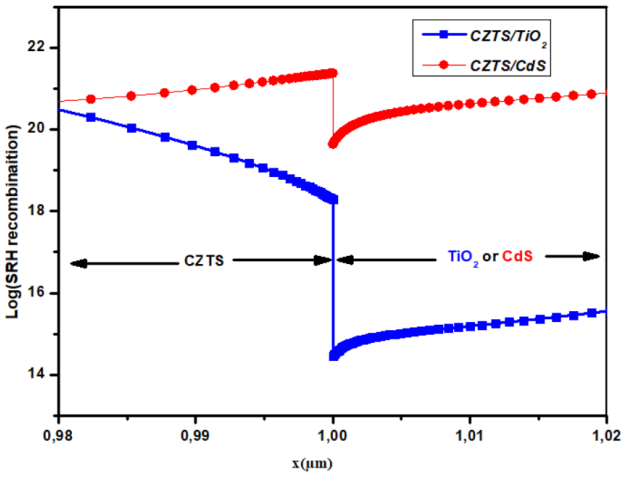

Figure 5. 15: SHR recombination at the heterointerface with CZTS/CdS (red line) and CZTS/TiO2 (blue line) structures

Kesterite/c-Si tandem solar cell analysis

The findings reported above make the Kesterite/TiO_2 solar cell (>14%) suitable for a tandem configuration with silicon solar cells. Nevertheless, to investigate the impact of the suggested buffer layer on the kesterite/c-Si tandem device, it is important to examine the tandem devices using kesterite/CdS and kesterite/TiO_2 top subcell structures. In the practical use of the monolithic kesterite/c-Si device, the top and bottom subcells are connected through a tunnel recombination junction. At this junction, the photogenerated holes collected from the back of the top subcell recombine with photogenerated electrons collected from the front of the bottom subcell [210]. For the best functioning of the tandem device, equal amounts of electrons and holes should be collected by each subcell. Splitting the sun's spectrum by adjusting the bandgap and the thickness of the top subcell is needed to achieve the currant matching conditions. First, the single junction kesterite top subcell with various bandgap materials (CZTSSe, CZTS, and CZTGS) with their corresponding optical properties and electron affinities is simulated; to our knowledge, no detailed study has been performed on how kesterite electron affinity varies with the bandgap. As a result, equation (8) is used to estimate the electron affinities [211]; further information on this equation can be found in [212].

$$\chi s = 4{,}74 - 0{,}43Eg \qquad (8)$$

Fig. 8 displays the metric parameters of both the kesterite/CdS and kesterite/TiO_2 subcells under AM1.5 illumination (with different absorber materials) for various absorber thicknesses. In practical development, it is difficult to maintain the proprieties of kesterite solar cells with thinner absorbers due to incomplete light absorption and the increasing recombination of excess

carriers at the back contact [120]. However, the simulation is performed for thicknesses in the range of 0.4–2 µm. As expected, the J_{SC} of both structures are higher for smaller bandgaps. On the other hand, the FF for the kesterite/CdS configuration was found to decrease when the bandgap was higher. This might be due to the enhanced SHR recombination resulting from the modification of the band alignment. In contrast, the FF of the kesterite/TiO_2 heterostructure shows the opposite behavior; it increases when the bandgap is enlarged, suggesting that TiO_2 and large bandgap kesterite are well aligned. The findings are highly encouraging for the future development of large bandgap kesterite devices employing the TiO_2 buffer layer. J_{SC}, V_{OC} and efficiency follow similar trends for both devices and are improved by improving the absorber layer thickness. However, different behavior of the FF is found in both structures; the FF of Kesterite/CdS starts decreasing at a lower thickness (lower than 0.6 µm) when the bandgap is higher than 1.5 eV. However, the FF of the Kesterite/TiO_2 structure is not strongly affected by the variation in the thickness, and a small decrease is observed for higher thicknesses when the bandgap is approximately 1.7 eV. It is demonstrated that thicker kesterite absorber results in a large series resistance, leading to a decrease in the device FF [190].

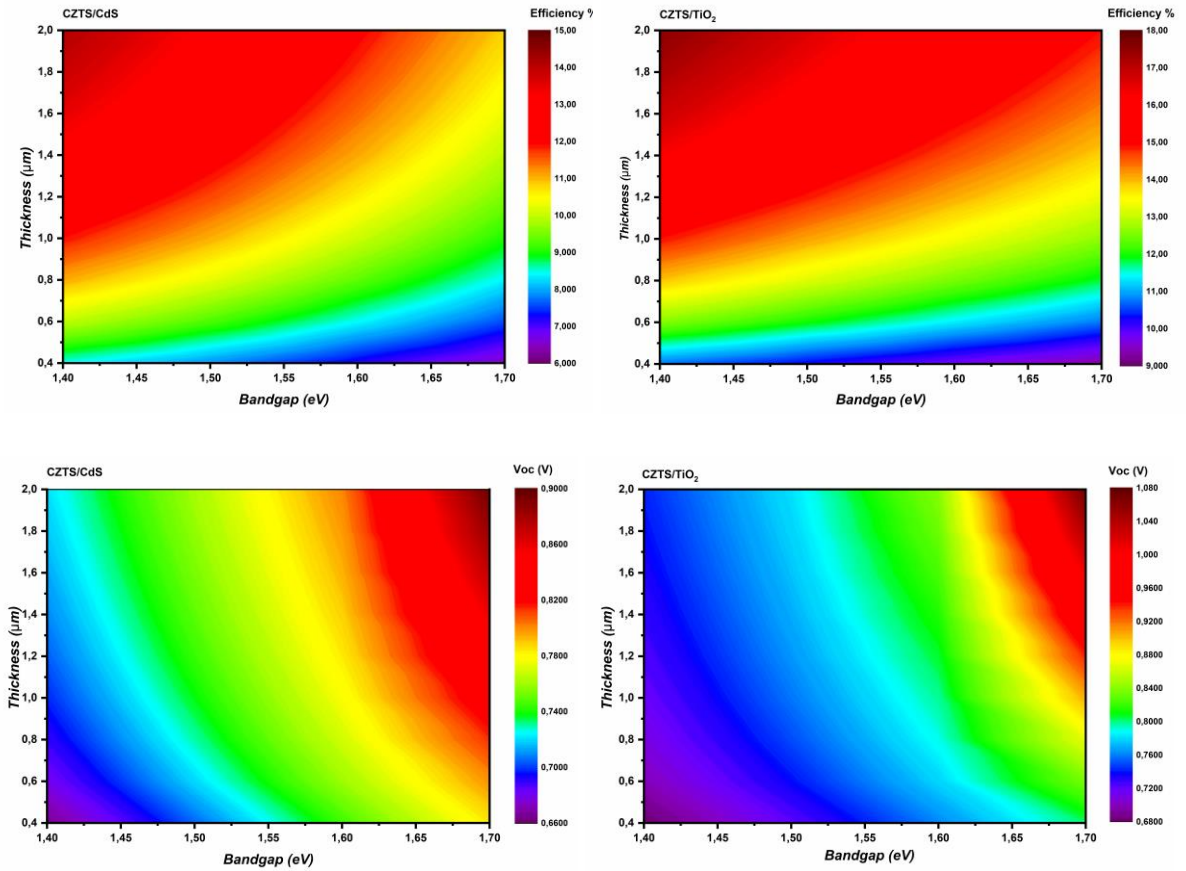

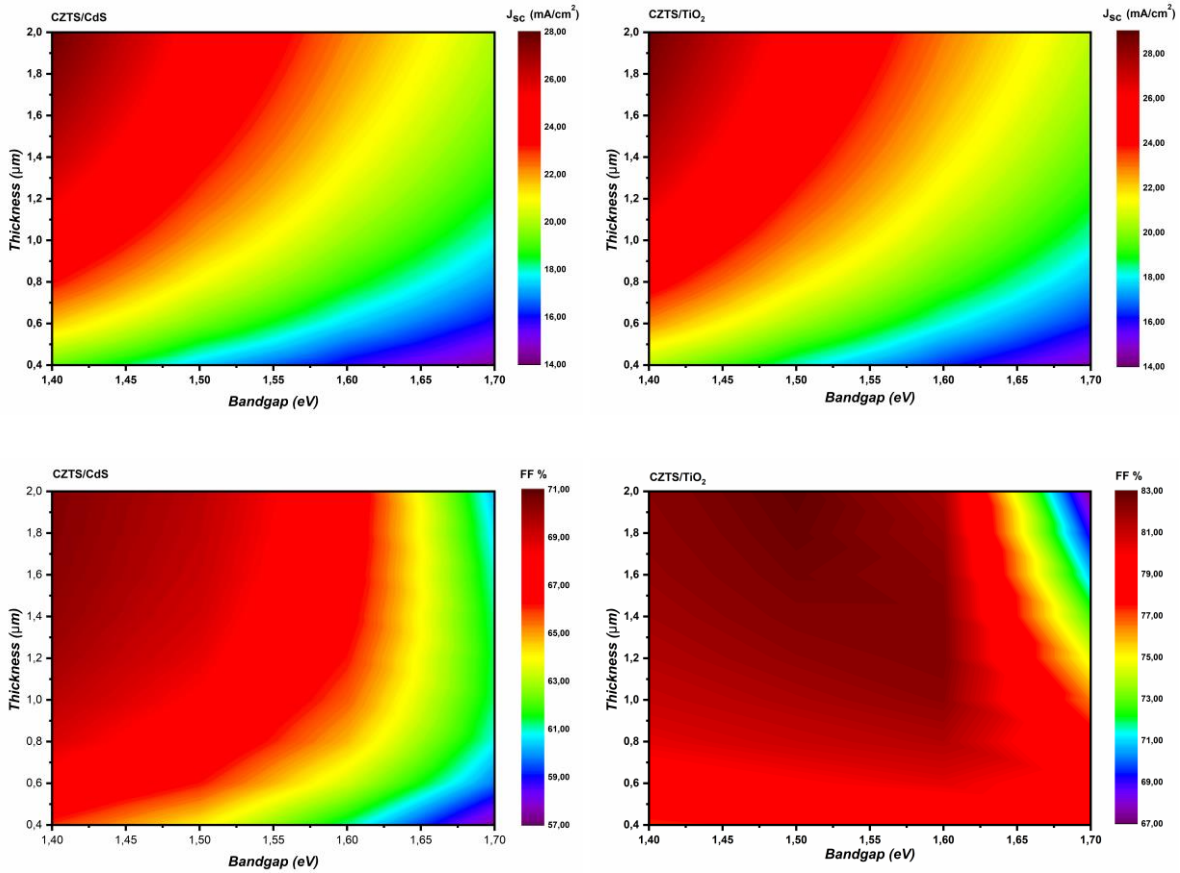

Figure 5. 33: Metric parameters of the top kesterite subcells as a function of the absorber thickness for various band gap absorbers.

To split the spectrum transmitted toward the c-Si bottom subcell, the Kesterite top subcell (ITO/MoO3/kesterite/CdS or TiO_2/ZnO/ITO) with varied thicknesses and absorber materials is optically modeled using the TMM method. Fig. 9, a. depicts the transmission curves of the top subcell for CZTS (Eg = 1.6 eV) and the light transmitted toward the c-Si bottom subcell with CdS and TiO_2 buffer layers. The transmission value is between 0.4 and 0.8, with an interference fringes. The use of wider bandgap TiO_2 materials improves transmission in the visible region when compared to the CdS buffer layer, and this improves light transmission toward the c-Si bottom subcell, as seen in Fig. 9, b. These findings support the benefits of utilizing Kestrite/TiO_2 in tandem devices.

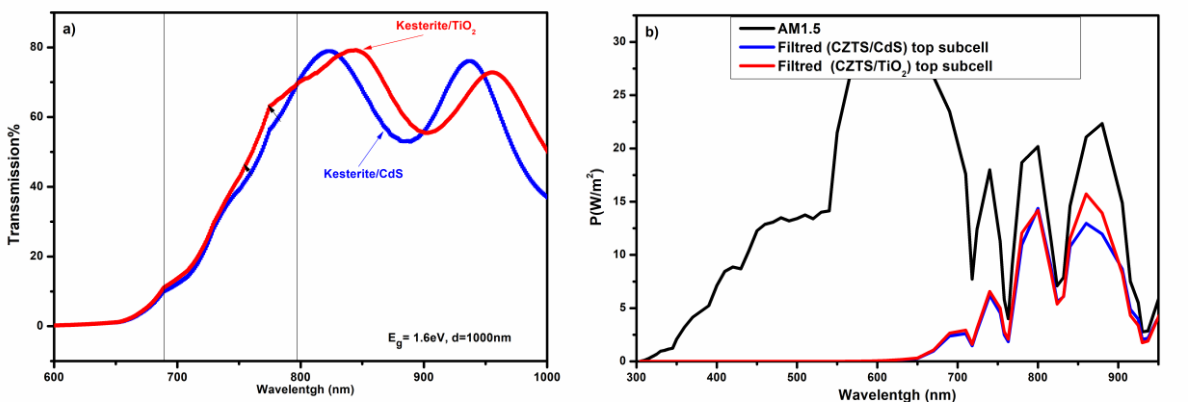

Figure 5.34: Transmission curve of Kesterite solar top subcell (Eg=1.6eV, d=1 µm) with TiO_2 and CdS buffer layer; b) AM1.5 and filtered spectrum from top subcell with TiO_2 and CdS buffer layers

The current-matching conditions under which both subcells generate identical currents are obtained by splitting the solar spectrum. In other words, the transmission spectra are used as a filter in the simulation of the c-Si bottom subcell to attain the current matching conditions. In previous studies, only J_{SC} matching conditions were taken into account in tandem devices [213–215]. However, in our study, the kesterite/CdS structure has a lower FF than the c-Si subcell, in which case the J_{MPP} matching conditions are necessary for the best performance of the tandem device [216]. On the other hand, the FF of the simulated kesterite/TiO_2 configuration is close to the c-Si device FF. Consequently, matching J_{SC} or J_{MPP} will provide similar results. Therefore, both J_{SC} and J_{MPP} matching conditions should be investigated. Fig. 10 presents the J_{SC} and J_{MPP} of the silicon bottom subcell and kesterite top subcell for various top subcell absorber material thicknesses and band gap values. The top subcell's thickness is limited to 1.2 µm to ensure optimum light transmission to the c-Si bottom subcell. There is no current matching for J_{SC} or J_{MPP} between the two subcells when the top subcell band gap is 1.4 eV (CZTSSe) for both configurations of the top subcell (kesterite/CdS and kesterite/TiO_2). Because the light transmitted toward the bottom subcell is insufficient to produce currents similar to those of the top subcells, which is generally higher for lower bandgaps kesterite solar cells. However, because of the lower FF of the kesterite/CdS structure, with CZTS absorber (Eg=1.5 eV), the J_{MPP} matching condition is obtained, where no current matching is found with the CZTS/TiO_2 configuration. With CZTS (Eg= 1.6 eV), both top subcell configurations show two matching conditions, for J_{SC} and for J_{MPP}. Furthermore, when the top subcell absorber bandgap takes a value of Eg=1.7 eV (CZTGS), the light transmitted from the top subcells is adequate to have better performance of the c-Si bottom subcell, the kesterite/TiO_2 subcells show matching

conditions for J_{SC} and J_{MPP}. However, CZTGS/CdS exhibits only the J_{SC} matching conditions due to its smaller FF.

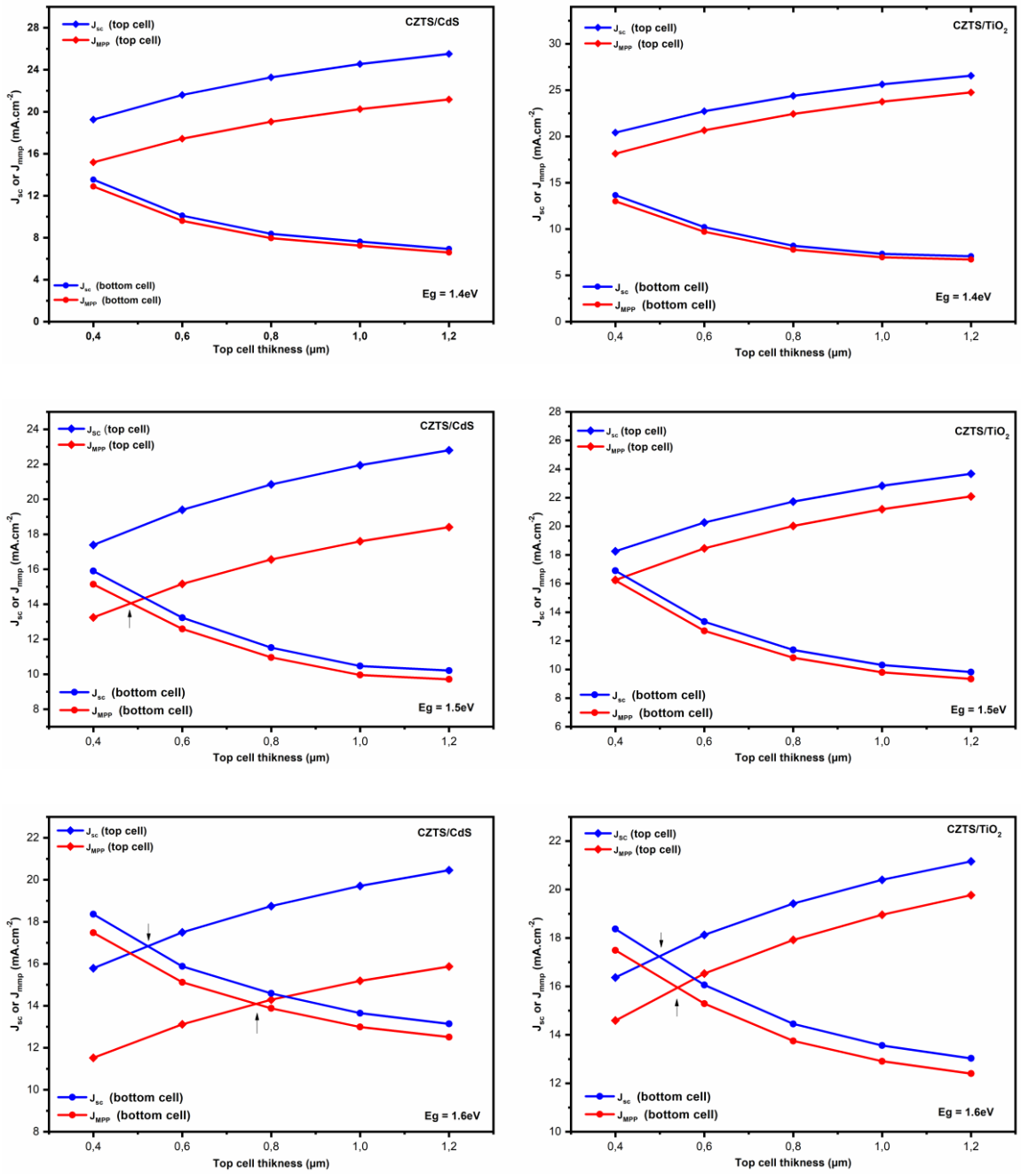

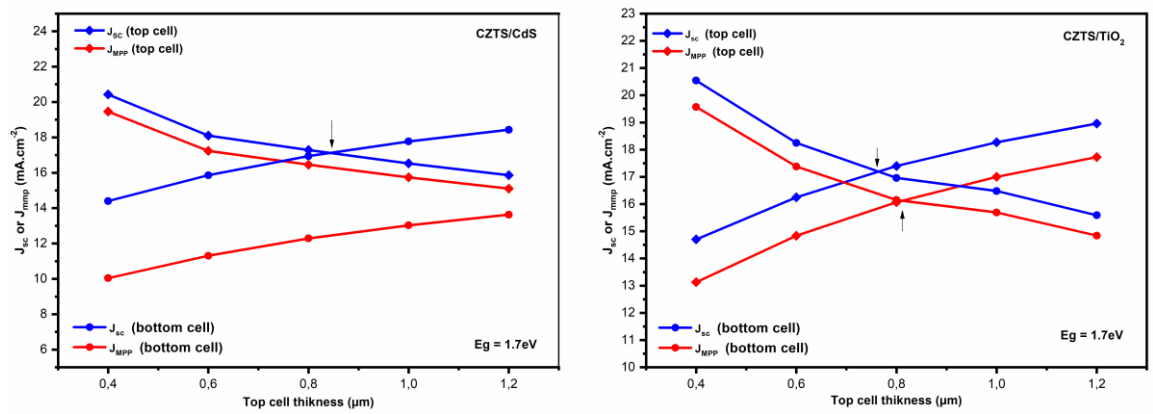

Figure 5.35: JMPP and JSC of the top and bottom subcells for different top subcell band gaps and thickness.

With the present matching conditions acquired, the performance of kesterite/c-Si tandem solar cells were calculated, and the results are given in Table 3. The open circuit voltage of the tandem device is equal to the sum of the open-circuit voltages of both subcells since the top and bottom subcells are series connected. According to the simulation findings, all calculated efficiencies are greater than those of the kesterite single junction. However, when compared to a single-junction c-Si bottom subcell under AM1.5 illumination, the tandem efficiency with kesterite/CdS as the top subcell is still lower because the kesterite top subcell has lower performance for higher bandgaps and for lower thicknesses. However, all tandem devices simulated with the kesterite/TiO_2 top subcell exhibit higher metric parameters than the c-Si single junction under AM1.5, which confirms the advantages of the proposed buffer layer for tandem devices. Under J_{SC} matching conditions, the FF of tandem devices with the kesterite/CdS top subcell is low (60%). However, the FF of tandem devices with kesterite/TiO_2 is greater (of 81%) for both matching conditions (J_{SC} and J_{MPP}). These findings prove the advantages of matching J_{MPP} when two subcells with different FFs are combined.

Table 3. Metric parameters of the tandem solar cells simulated at the obtained matching conditions.

Bandgap (eV)	**top subcell buffer layer**	**Matching conditions**	**Thickness (µm)**	**J_{SC} (mA/cm^2)**	**J_{MPP} (mA/cm^2)**	**V_{OC} (V)**	**V_{MPP} (V)**	**FF %**	**Eff %**
1.5	CdS	J_{MPP}	0.50	14.8	14.06	1.31	1.12	80.	15.74
	TiO_2	J_{SC}	0.50	17.26	15.65	1.37	1.19	79	18.62

1.6	TiO_2	J_{MPP}	0.55	16.75	16.00	1.37	1.19	79	19.36
	CdS	J_{SC}	0.50	16.86	12.54	1.35	1.15	63	14.42
	CdS	J_{MPP}	0.80	14.84	14.11	1.36	1.17	81	16.50
1.7	TiO_2	J_{SC}	0.76	17.18	15.86	1.46	1.25	79	19.82
	TiO_2	J_{MPP}	0.80	16.95	16.14	1.47	1.25	81	20.18
	CdS	J_{SC}	0.84	17.16	12.50	1.42	1.20	61.5	15.00

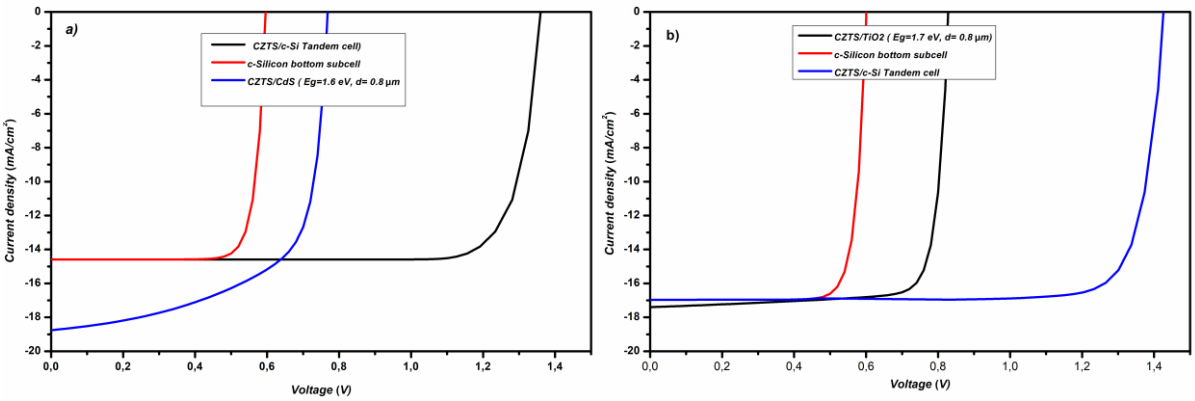

Figure 5.36: J-V curves of the kesterite top subcell, silicon bottom subcell (under transmitted light from the top subcell) and tandem solar cells with TiO_2 (a) and CdS (b) buffer layers

The photovoltaic parameters of the champion tandem devices with CZTS/CdS and CZTGS/TiO_2 structures and their subcells are summarized in Table 3. Their J-V characteristics are depicted in fig.10. The J-V curve of the tandem device is constructed following the assumption that the lower-current subcell dominates the J-V characteristic of the tandem device; more details are reported in [216]. Both solar cells achieved the J_{MPP} matching conditions with the c-Si bottom subcell. However, a significant difference in the performance between both devices was observed. The best tandem device using kesterite/CdS as the top subcell shows an efficiency of only 16.50% with V_{OC}=1.36 V and Jsc=14.84 mA/cm^2. The best tandem device with kesterite/TiO_2 as the top subcell exhibits an efficiency of 20.18% with V_{OC}=1.47 V, J_{SC}=16.95 mA/cm^2, and a fill factor of 81%. This high improvement in efficiency is due to the large improvement in the performance (e.g., fill factor) of the kesterite/TiO_2 top subcell, leading to J_{MPP} matching conditions with the silicon bottom subcell for a higher bandgap (1.7 eV) and moderate thickness. At higher absorber bandgaps of the top subcell, the V_{OC} of the tandem is high due to the top subcell having a greater V_{OC}. Furthermore, the light transmitted from the top subcell will lead to better c-Si subcell performance. The results of this simulation show that

by inserting a TiO_2 buffer layer into the kesterite top subcell, the electrical performance of the kesterite/Si tandem could be enhanced. With further advances in kesterite single-junction performance, kesterite/c-Si tandem devices can reach efficiencies similar to those predicted by theoretical studies and will provide an easy path to overcome the single-junction limit.

The QE curves of the c-Si bottom subcell using the light transmitted from the top subcell with CdS and TiO_2 at the above matching points, the fraction of light absorbed in each layer of the top subcell (ITO/MoO3/CZTS/CdS/ZnO/n-ZnO), and the total reflection of the device are shown in Fig. 12. As can be observed, at higher wavelengths below the bandgap of kesterite material (>750nm), where the light transmits should be adequate for better response of the c-Si bottom subcell, the reflection dominates the spectra with values ranging from 20 to 40%, as well as the absorption of the ITO back electrode with values ranging from 10 to 20%, and this is the reason for the lower QE of the c-Si bottom subcell at this region, as shown in fig. 12, b. These results reveal that it is critical to improve the transmission of the top subcell by reducing the reflection in the IR region through optical engineering to have better performance of the tandem device and show that the development of kesterite/c-Si tandem applications may not require well-developed silicon cells as the efficiency of c-Si does not surpass 9% in the best case.

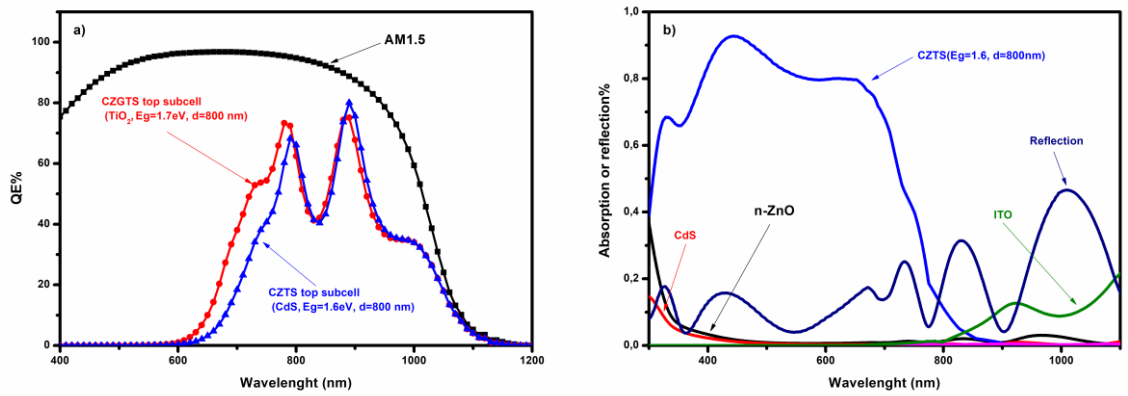

Figure 5.37: QE curves of the silicon bottom subcell (under transmitted light from the top subcell) with TiO_2 and CdS buffer layers; b) the fraction of light absorbed in each layer and the total reflection of the top subcell

V.2.4. Conclusion

Optical and electrical simulations of tandem structures with kesterite as the top subcells, using CdS and TiO_2 as buffer layers and c-Si as the bottom subcell, were examined under different top subcell parameters. The TiO_2 buffer layer was found to improve large bandgap kesterite performance and

show lower interface recombination and parasitic absorption. The tandem devices with Kesterite/TiO_2 simulated under the current matching conditions show higher performance than the tandem devices with the Kesterite/CdS structure, which is limited by their lower fill factor. The best tandem device with the conventional Kesterite/CdS structure (c-Si as the bottom subcell) shows an efficiency of only 16.5%, which is still lower than the c-Si bottom subcell efficiency under AM1.5 illumination (19%). The champion tandem device in our study is obtained with Kesterite/TiO_2, with an absorber bandgap of 1.7 eV (CZTGS) and a thickness of 0.8 µm. This tandem device yields an efficiency of 20.18% with V_{OC}=1.47 V, J_{SC}=16.95 mA/cm^2, and a fill factor of 81%. The findings presented in our study demonstrate the viability of developing highly efficient Kesterite/c-Si tandem solar cells using an alternative TiO_2 buffer layer and indicate that improving the performance of the Kesterite top subcell is essential to ensuring the benefit of the tandem device.

Chapter 6: Development of wide-bandgap Ge-kesterite (CZGSSe) from sputtered metallic stacks

VI.1. Synthesis and optimization of a wide-bandgap Cu2ZnGe (S,Se)4 photovoltaic absorber using single-step sulfo-selenization

Herein, we present a straightforward process for producing wide-bandgap $Cu_2ZnGe(S,Se)_4$ via single-step sulfo-selenization of a chalcogen-free sputtered Cu/Zn/Ge metallic stack. The influence of various annealing parameters on structural and compositional properties of CZGSSe absorbers is investigated, and the solar cell performances are discussed. By analyzing the absorbers, at critical points in the annealing profile, through the combination of SEM images, X-ray diffraction and Raman spectroscopy, we demonstrated the possible factors that constrain the growth and the proprieties of the synthesized CZGSSe absorbers. The experimental observations revealed a strong correlation between the annealing conditions and the introduction of chalcogens (S and Se) into the final absorbers. However, the different thermodynamic properties of S and Se, as well as the Ge layer position in the metallic stack, have a significant impact on the obtained absorber properties. Changing the stacking order of the metallic precursor and optimizing the annealing parameters were found to be more beneficial and led to better absorber properties. In addition, the solar cells prepared using these absorbers demonstrated efficiencies close to those of the best reported S-rich CZGSSe compounds. The results presented confirm the potential of the proposed process for producing CZGSSe solar cells based on a simple and reliable process.

VI.1.1. Introduction

The rapid progress of economic development has increased the energy demand over the past few years. However, well-established crystalline silicon (c-Si) solar cell technologies have almost reached their full power conversion efficiency because of the fundamental properties of Si materials [2]. This challenge has forced researchers to discover new and better-performing materials leading to highly efficient and low-cost solar devices that can be combined with c-Si for tandem concepts, or for widening the penetration of PV energy with semi-transparent or transparent solar cell concepts. Due to their low cost and appealing optoelectronic properties, wide bandgap kesterite materials are potential options for solar applications [217]. Furthermore,

the ability to vary the optical bandgap of kesterite materials makes them suitable for advanced applications, such as the previously mentioned tandem cells (e.g., kesterite/c-Si) [182]. Kesterite-based compounds were largely studied and reached a higher efficiency of 11% for pure-sulfide Cu_2ZnSnS_4 (CZTS)-based solar cells [179] and a maximum efficiency of 14.9% for mixed sulfo-selenide $Cu_2ZnSnS_{1-x}Se_x$ (CZTSSe) [87]. However, the multicharged nature and changes in the oxidation state of tin (Sn), currently limit the kesterite efficiency due to the formation of deep recombination states for photogenerated charges. Additionally, the formation of volatile Sn-S and Se binary phases at the standard temperatures employed in producing kesterite compounds causes composition inhomogeneities and appearance of many secondary phases [218,219]. In addition, the bandgap of Sn-kesterite is limited to a maximum of 1.6 eV, for pure sulfide CZTS absorbers [220], making this material unsuitable for developing highly efficient tandem devices [221]. Various approaches to avoid Sn problems and to improve the kesterite optical bandgap have been investigated, such as partially replace Sn with Ge to produce $Cu_2ZnSn_{1-x}Ge_x(S,Se)_4$ compounds, due to Ge's higher electron affinity and lower propensity toward +II oxidation state [184]. This structure exhibited an efficiency of approximately 12.3% with a Ge/(Sn+Ge) ratio of 0.22 [222]. In many works, Ge has proven to be a critical approach for improving the crystallinity and enlarging the grain size of kesterite materials, resulting in an increase in device efficiency [218,222]. However, controlling Sn and Ge composition during the elaboration process, and the presence of multivalent Sn, still constrain the development of these absorbers. Based on these findings, researchers have attempted to completely substitute Sn with Ge to form pure Ge-kesterite CZGSe and CZGS compounds [127,177,223,224]. A solar cell with a maximum efficiency of 7.5% is obtained using CZGSe materials with a band gap of approximately 1.4 eV [224]. Since the highest efficiency of Sn-Kesterite materials is obtained with an absorber consisting of a sulfur-selenide compound with selenium-rich S/(S+Se) ratios and by varying the bandgap of Ge-Kesterite in the range required for tandem application, recent works have been reported on CZGSSe absorbers [225]. T. Schnabel et al. demonstrated a solar cell with an average efficiency of 2.1% using Se-rich CZGSSe with an S/(S+Se) ratio of 0.3 and a bandgap of 1.54 eV [226]. This efficiency is improved by up to 6% with further buffer layer optimizations [227]. More recently, a maximum efficiency of 3.2% for S-rich CZGSSe-based device was obtained with an absorber bandgap of E_g = 1.98 eV [225]. In the above works, sulfur (or selenium)-containing precursors were subjected to an annealing process under a selenium (or sulfur) atmosphere. Nevertheless, the incorporation of sulfur and selenium into precursors under different annealing parameters

must be carefully studied to develop a simple and reliable procedure that leads to control of the composition and bandgap of CZGSSe absorbers.

In this study, we propose a straightforward and reliable one-step sulfo-selenization process to synthesize solid solutions of CZGSSe thin films using sputtered Cu/Zn/Ge metallic precursor stacks. We also present the possibility of tuning the S/(S+Se) ratio, by controlling the annealing parameters, and we investigate the influence of these parameters (chalcogenide source, pressure, and temperature) on sulfur and selenium incorporation in thin films, through structural and morphological analysis of the synthesized films. Then, solar-cell devices are prepared and characterized with different absorbers. We also report the issues affecting the growth of CZGSSe during the sulfo-selenization process; then, we propose an approach through which moderate efficiencies are obtained. The obtained results indicate the feasibility of the proposed methodology for producing CZGSSe absorbers by a simple thermal process employing metallic precursors, which were previously synthesized by the annealing of chalcogen-containing precursors.

VI.1.2. Experimental section

CZGeSSe absorber synthesis

CZGeSSe thin films were prepared by depositing metallic precursors on Mo-coated soda lime glass substrates. The initial experiments of this study involved the deposition of, Cu/Zn/Ge metallic stack precursors, with Cu-poor and Zn-rich compositions, by direct current (DC) magnetron sputtering (Alliance AC450). The optimal ratios of Cu/(Zn+Ge)=0.65 and Zn/Ge=1.06 were confirmed by X-ray fluorescence (XRF) and measured using the Fischer scope XVD system. The as-deposited metallic precursors were sulfo-selenized using graphite box containing 10 mg of SeS_2 powder to provide an S+Se atmosphere during the thermal treatment. Thermal annealing was carried out in a conventional tubular furnace following different annealing profile processes, as will be discussed later (one-step and two-step processes). In the two-step annealing process, the first step was performed at 1.5 mbar Ar pressure, and the second step at 1 bar Ar pressure. One-step annealing was carried out under 1 bar of Ar pressure. For both annealing profiles, the ramp rate is 20°C/min, and the cooling process occurred naturally, taking approximately 1 and 2 hours, respectively.

CZGeSSe solar cell fabrication

The above absorber-based solar cells were constructed after chemical etching of the absorbers using KCN solution (2% w/v, for 2 min) to remove possible secondary phases and oxides

present on the surface. An n-type 50 nm thick CdS buffer layer was deposited by chemical bath deposition (CBD) from nitrate salts [50]. I-ZnO (50 nm) and In_2O_3:SnO_2 (ITO, 200 nm, 60 Ω/sq) were deposited immediately after CdS deposition using DC-pulsed sputtering (Alliance Concept CT100). The obtained CZGSSe solar cells were scribed (3×3 mm^2) mechanically with a microdiamond scriber (OEG MR200). Antireflective coatings and metallic grids were not used in our work.

Characterization

An XRF system (Fischercope XDV) previously calibrated by inductively coupled plasma–mass spectrometry (ICP) was used to characterize the composition and precursor thicknesses. Scanning electron microscopy (SEM) images were acquired with a ZEISS Series Auriga microscope using an acceleration voltage of 5 kV. X-ray diffraction patterns were collected with a Bruker D8 diffractometer in Bragg–Brentano geometry using a monochromatized CuK-L3 X-ray source (1.540598 Å) and a LynxEye PSD detector. Raman scattering spectra were measured using a FHR 640 monochromator from Horiba Jobin Yvon coupled with a CCD detector. The system was optimized for the UV–visible spectral range, and during this study, 325 and 532 nm excitation wavelengths were used. The applied laser power densities were kept in the range of 100–150 Wcm^{-2}. The measurements were performed in a backscattering configuration through a probe designed at IREC. J-V measurements were performed on the completed devices using a calibrated Sun 3000 class AAA solar simulator (Abet Technologies, 25°C, AM1.5G illumination).

VI.1.3. Results and discussion

Kesterite materials formed during the thermal annealing process, where the chalcogens (sulfur and/or selenium) present in the atmosphere reacted with the precursors to form the final thin films. Undoubtedly, the annealing conditions have a significant impact on the quality of the resulting kesterite absorbers. Previously reported Ge-based kesterite CZGSSe absorbers were synthesized by sulfurizing co-evaporated CZGSe precursors at 480°C [225,228] or by selenizing sulfide precursors deposited via doctor blade method [226,227]. In both cases, a precursor containing sulfur (or selenium) was annealed in a sulfur (or selenium) environment. However, in our work, we aim to produce CZGSSe absorbers through sulfo-selenization of chalcogen-free metallic precursors. All these processes are schematized in Figure 1.

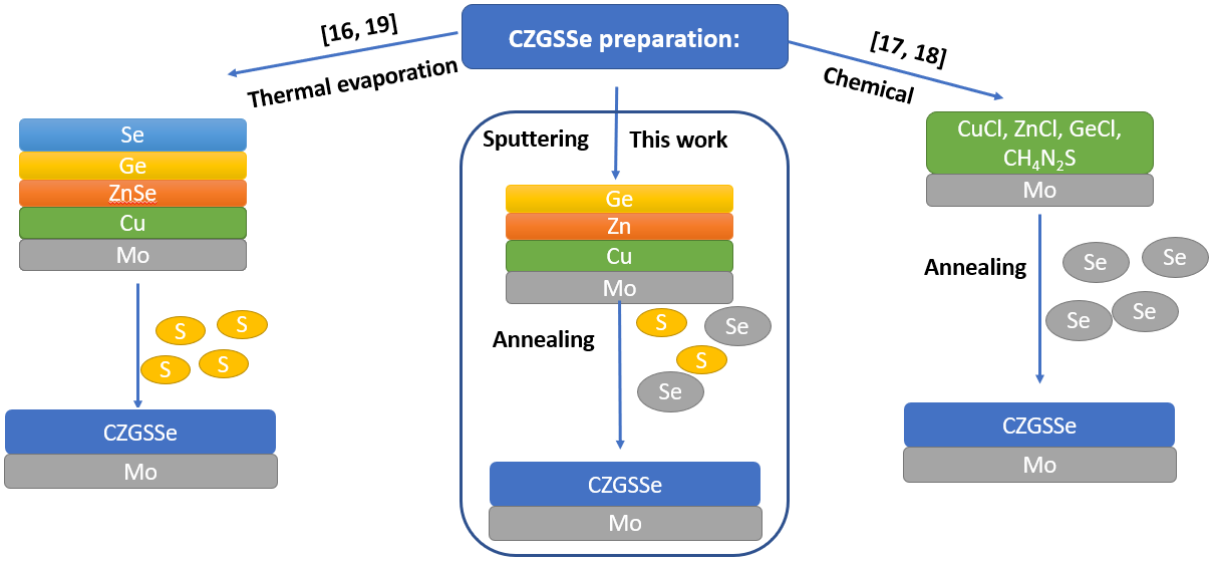

Figure 6.1: Schematic representation of the synthesis process of CZGSSe in literature and in the present work.

According to previous works by our group on CZGSe absorbers [127,184,223], two-step annealing assisted in promoting grain growth and improving CZGSe quality. In fact, the annealing process includes the first step at 330°C and the second step at 480°C; these annealing steps are reportedly efficient and lead to the formation of highly efficient CZGSe absorbers. On the other hand, from previous studies on CZGSSe kesterite materials, temperatures between 480 and 550°C are typically used, and better results have been demonstrated. Based on these findings, we used four different annealing processes to synthesize CZGSSe absorbers (Figure 2). Two-step annealing was performed with a first step at 330°C for 30 min, followed by a second step at 480°C or 550°C for 15 min, called samples A and B, respectively. The one-step annealing at 480°C and 550°C for 15 min were called C and D, respectively. The usual SLG-Mo/Cu/Zn/Ge precursors were introduced within a graphite box with 10 mg of SeS_2 powder to ensure the presence of both S and Se in the environment during the annealing process.

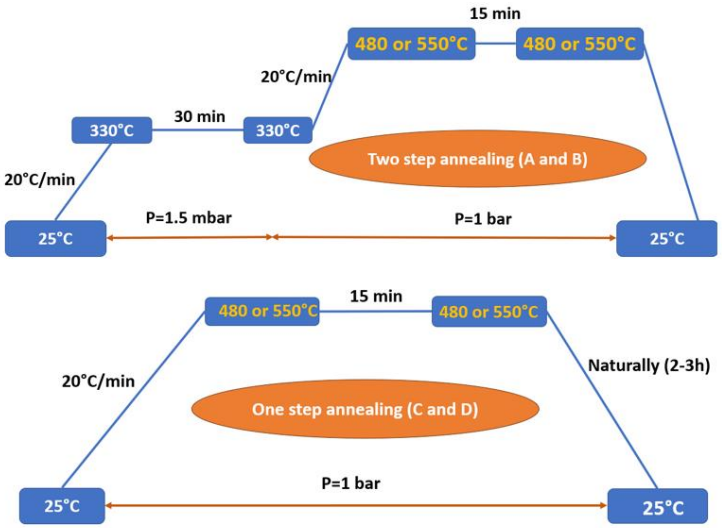

Figure 6.2: Two- and One-step annealing profiles used for the sulfo-selenization of CZG metallic precursors.

The morphology of the CZGSSe thin films prepared with different annealing profiles was evaluated using cross-sectional SEM images, and the results are presented in Figure 3. The thickness of all the samples is estimated to be between 1 and 1.2 µm. However, the morphologies of the samples are significantly different, and the samples annealed via two-step annealing (A and B) exhibit larger grains than the thin films annealed via a one-step process (C and D) do. Sample A has a compact and rough morphology, and voids at the Mo/CZGSSe interface are observed, perhaps due to the diffusion of secondary phases (e.g., $Cu_x(S,Se)_y$) during the high-temperature stage of the annealing process [229]. Sample B had the largest grains, but the homogeneity of the grain distribution at the surface decreased. The CZGSSe samples prepared using one-step annealing (C and D) display nonuniform and poor morphologies and a bilayer structure with small particles at the bottom of the thin films (clear for sample C). Sample D has a slightly better uniformity of grain size; however, a large density of voids and small grains are present in the whole bulk. Overall, as is commonly observed, layers containing sulfur in their structure exhibit smaller grains and rougher surfaces than selenide layers for Sn-pure kesterite and seem to be equivalent when Sn is substituted by Ge.

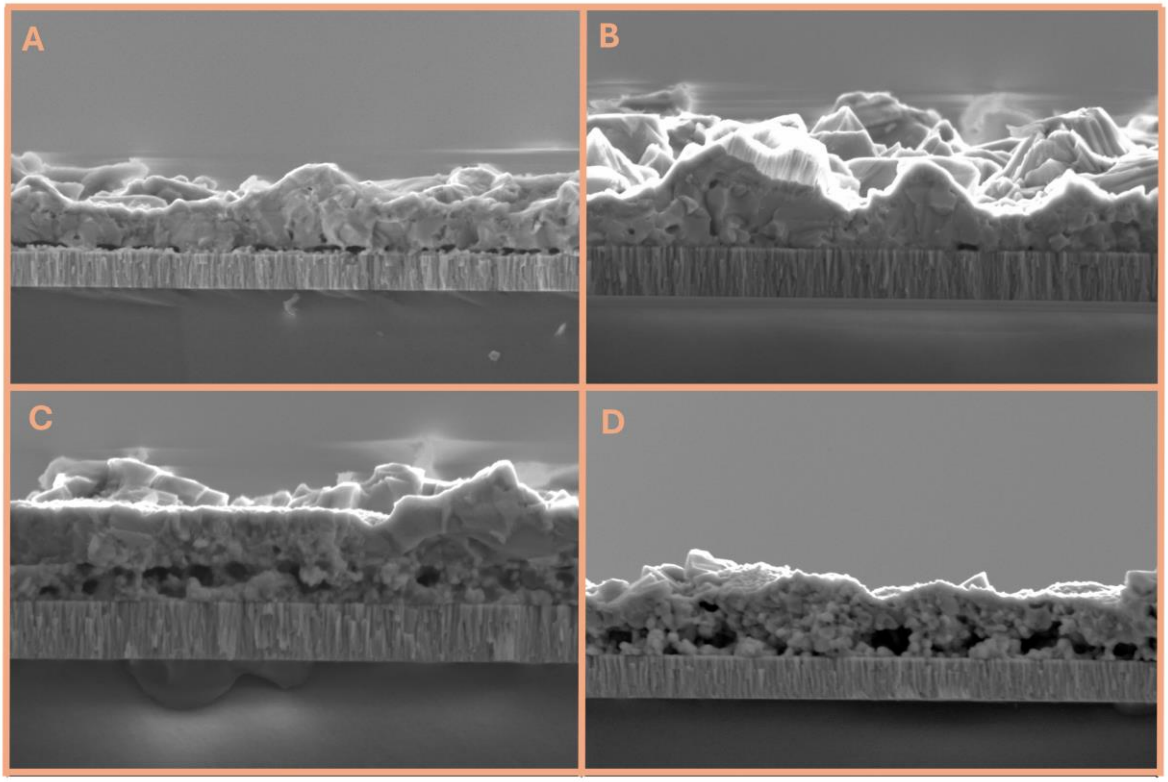

Figure 6.3: Cross-sectional SEM images of CZGSSe thin films annealed using different annealing profiles.

The crystal structure, phase and chemical composition of the prepared thin films were studied via XRD analysis, and the obtained diffractograms are presented in Figure 4. XRD patterns of sulfo-selinized CZGSSe thin films synthesized using various annealing profiles reveal broad peaks corresponding to the (112), (200), (220) and (312) diffraction planes of the polycrystalline kesterite phase [95]. The relatively wide and asymmetric shapes of the peaks can be attributed to the overlapping peaks assigned to phases with different S/Se ratios, confirming that single-phase sulfo-selenide kesterite has not been formed [230]; however, the position and intensity of the peaks are strongly dependent on the annealing profile. Considering only the main diffraction peak corresponding to the (112) orientation (Figure 4), the samples annealed via two-step annealing (A and B) exhibit similar peak positions at approximately 28.16° and 28.15°, respectively, suggesting the formation of a Se-rich phase and indicating that the incorporation of selenium into the samples is predominant (tetragonal space group *I*-42*d* (122); XRD reference). However, the thin films annealed using one-step annealing exhibit the opposite trend; the peaks at 28.56° and 28.98° for samples C and D, respectively, suggest higher sulfur incorporation in the final thin films, which results in the formation of S-rich compounds and can explain the small grains observed in the SEM images as well as a rougher morphology.

Based on previous works and Vegard's law, the S/(S+Se) ratio and bandgap of CZGSSe can be estimated by means of equations (1) and (2) used for the CZTSSe compounds [24,25]. Samples A and B have high Se contents with S/(S+Se) ratios of 36 and 38%, respectively (Table 1), where these ratios are estimated to be approximately 77 and 83% for samples C and D, respectively, indicating greater sulfur incorporation. The obtained results indicate the strong dependency between the introduction of sulfur and selenium and the annealing profile.

$$\frac{S}{S+Se} = (d_{112,CZGSe} - d_{112,CZGSSe})/(d_{112,CZGSe} - d_{112,CZGS}) \qquad (1)$$

$$E_{g,CZGSSe} = (1-x)E_{g,CZGS} + xE_{g,CZGSe} - bx(1-x) \qquad (2)$$

where $d_{112,CZGSe}$ and $E_{g,CZGSe}$ are the d-spacing and bandgap of CZGSe (JCPDS-0322), $d_{112,CZGS}$ and $E_{g,CZGS}$ are the d-spacing and bandgap of CZGS (JCPDS-0324), $d_{112,CZGSSe}$ and $E_{g,CZGSSe}$ are the d-spacing and bandgap of the CZGSSe solid solutions, respectively, and x is the Se content in the CZGSSe thin films. Note that the bowing coefficient b defined for Sn-based kesterites was used in the present calculations [24], which results that obtained E_g values can be slightly different from the real ones.

The XRD results were also used to calculate the lattice parameters of CZGSSe, which are summarized in Table 1. The a lattice parameters for all the samples are between 5.34 and 5.61 Å reported for pure CZGS and CZGSe, respectively. However, this parameter is greater for the two-step annealed samples (A and B), whereas the one-step annealed samples (C and D) exhibit lower values due to the higher S content in these samples.

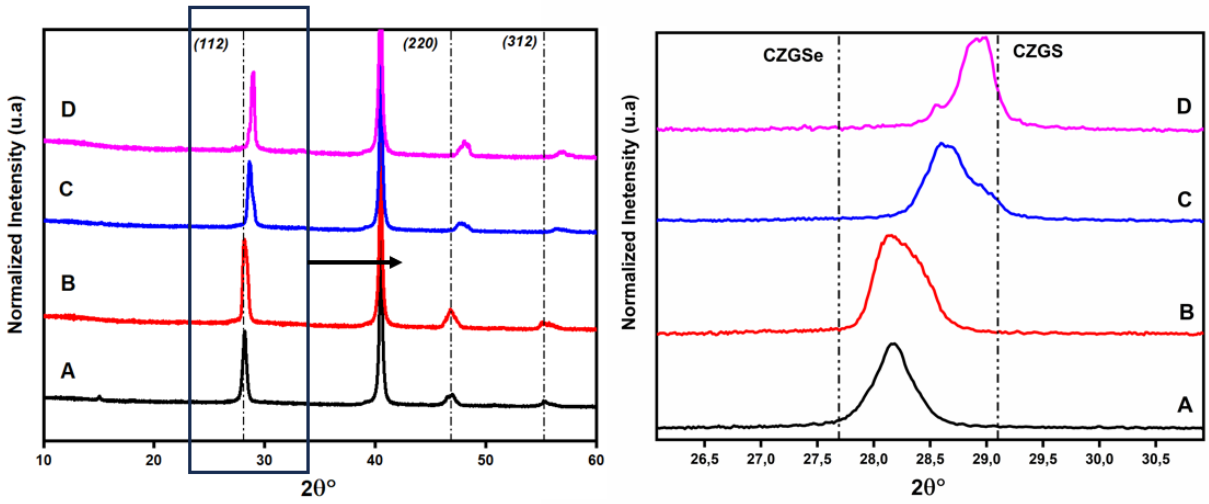

Figure 6.4: XRD patterns of CZGSSe annealed using different annealing profiles.

Table 1. Lattice parameters, S/(S+Se) ratio, and bandgap of CZGSSe prepared using different annealing profiles.

Samples	a (Å)	c(Å)	c/2a	S/(S+Se) (%)	E_g (eV)
A	5.467	11.026	1.008	36	1.66
B	5.487	10.976	0.971	38	1.57
C	5.402	10.846	1.004	77	1.91
D	5.346	10.719	1.004	83	1.97

The solar cells prepared using the above-described absorbers were studied, and their optoelectronic parameters are summarized in Table 2. All the samples exhibited efficiencies less than 1%, which can be attributed to the poor CZGSSe absorber quality, poor morphology, voids at the CZGSSe/Mo back contact and the formation of secondary phases [232,233]. Nevertheless, samples A and C, which were annealed at 480°C, exhibited slightly greater performances than samples B and C, which were annealed at 550°C, confirming the advantages of annealing at 480°C. It is evident that sample A exhibited an efficiency of 0.92% with the highest open-circuit voltage (V_{OC}) of 541 mV and short-circuit current density (J_{SC}) of 4.58 mA/cm^2, but has reduced FF a fill factor (FF) of 31.24% which is mainly due to reduced shunt resistance (R_{Shunt}) of 380.2 Ω as calculated from the J–V data. This suggests that maintaining the two step annealing with the temperature at the second step equal to 480 °C is beneficial, however further optimization are required in order to improve FF

Table 2. J-V parameters of CZGSSe solar cells with absorbers prepared using different annealing profiles.

Sample	J_{sc} (mA/cm^2)	V_{oc} (mV)	FF (%)	Efficiency (%)	R_S (Ohm)	R_{Shunt} (Ohm)
A	4.58	541.48	36.96	0.92	31.24	380.42
B	0.94	374.90	40.55	0.14	87.22	872.83
C	4.43	406.42	33.52	0.60	42.73	190.28
D	0.80	236.05	34.39	0.06	27.24	362.00

Further optimization of the single-step sulfo-selenization process was performed by varying the temperature of the first step. The temperature of the first step is essential in the two-step

annealing process, and this step has a major impact on the quality of the absorbers [234–236]. Fig. 5a shows the XRD patterns of CZGSSe annealed at 480°C using different first-step temperatures (e.g., 180, 230, 280, and 330°C (reference sample)).

The XRD diffractograms measured in the absorbers annealed at lower temperatures for the first step (180 and 230°C) exhibit peaks corresponding to the S-rich kesterite (JPCD987-78) phase, with strong peaks at 29.01° and 29.05°, respectively. For both samples, a small peak corresponding to different phases with different S/(Se+S) ratios is also present, perhaps due to sulfur replacement by selenium at higher temperatures, where the selenium vapor pressure increases, allowing selenium to diffuse into thin films and substitute for S partially [237]. It should be noted that sulfur replacement by the selenium reaction is more favorable due to its exothermic nature [238]. Furthermore, the samples annealed with a first step at 280°C display small broad peaks, indicating poor crystalline quality and the presence of distinct phases with different S/(Se+S) ratios. However, in the reference absorber prepared with 330°C first step annealing, the peaks shift toward lower angles (28.09°), indicating the formation of a Se-rich kesterite phase. As a result, the higher temperature used during the first stage allows selenium to be incorporated in larger quantities during the annealing process, forming Se-rich CZGSSe absorbers. These results can be explained by the different thermodynamic properties of S and Se (e.g., vapour pressure, boiling point) and can open a way to control chalcogen incorporation in samples using the annealing profile. The sample annealed with the first step at 330°C (sample A) is still the best in terms of crystallinity, with the highest intensity of XRD peaks. The optoelectronic parameters of the solar cells prepared with the above absorbers are presented in Table 3. In accordance with the XRD results, the sample A efficiency is still higher than that of the other samples, with domination in all optoelectronic parameters.

Previous findings demonstrated that differences in S and Se thermodynamic properties may constrain the growth of CZGSSe absorbers during annealing, necessitating the investigation of various chalcogen powder sources. To perform this study, the annealing profile of sample A was combined with different sources of S and Se chalcogens (i.e., a mixture of powders of SeS_2+Se, SeS_2+S, S+Se, and $GeSe_2$+SeS_2 was used). Figure 5b shows the XRD patterns of the thin films annealed using different chalcogen sources. Except for the sample annealed using Ge_2Se_4+SeS_2 powders, all the absorbers exhibit poor crystalline quality with small and broad diffraction peaks. However, the sample annealed using Ge_2Se_4+SeS_2 shows a highly intense peak at 28.05°, indicating the formation of a Se-rich kesterite phase. Moreover, the solar cell based on this sample exhibited an efficiency up to 1.2%, which is slightly higher than that of

the reference sample annealed with only SeS_2 powder (sample A), due to significantly increased V_{oc} and improved FF. These results can be attributed to the beneficial effect of adding Ge in compensate the Ge losses during the annealing process. Similar approaches have been made in Sn-kesterite systems, where the addition of Sn-S powder serves a similar compensatory role. The Ge top layer can create several losses resting in a defective CZGSSe/CdS interface which led to higher carrier recombination.

It is important to note that changing the amount of chalcogen powder helps to adjust the pressure during the high-temperature stage annealing process [239] and can have a significant impact on the grain growth of kesterite compounds. The XRD patterns for samples annealed using the same annealing profile as sample A, with various $GeSe_2$+SeS_2 powder quantities ranging from 10 to 500 mg, are displayed in Figure 5c. As a result, the incorporation of sulfur and selenium was not significantly influenced by the powder quantity, as all the samples exhibited similar peak positions. However, the crystalline quality is different when the powder quantity is changed. Thus, the sample annealed with 250 mg of powder has the best crystallinity, as indicated by the highly intense XRD peaks. Based on the J-V curves, the optoelectronic parameters (Table 3) show a significant improvement in solar cell performance for samples annealed with 250 mg of $GeSe_2$+SeS_2 powder, and the best solar cell is obtained with this sample, which exhibits an average efficiency of 1.41%. The observed results demonstrate a notable enhancement in the optoelectronic properties of CZGSSe solar cells with increasing powder quantity to 250mg. This improvement was anticipated to follow a gradual trend. However, our investigation involves three distinct elements (Ge, S, and Se), which led to complex atmospheric phenomena due to the potential influence of multiple factors such as gas composition, pressure, temperature gradients, and particle dynamics.

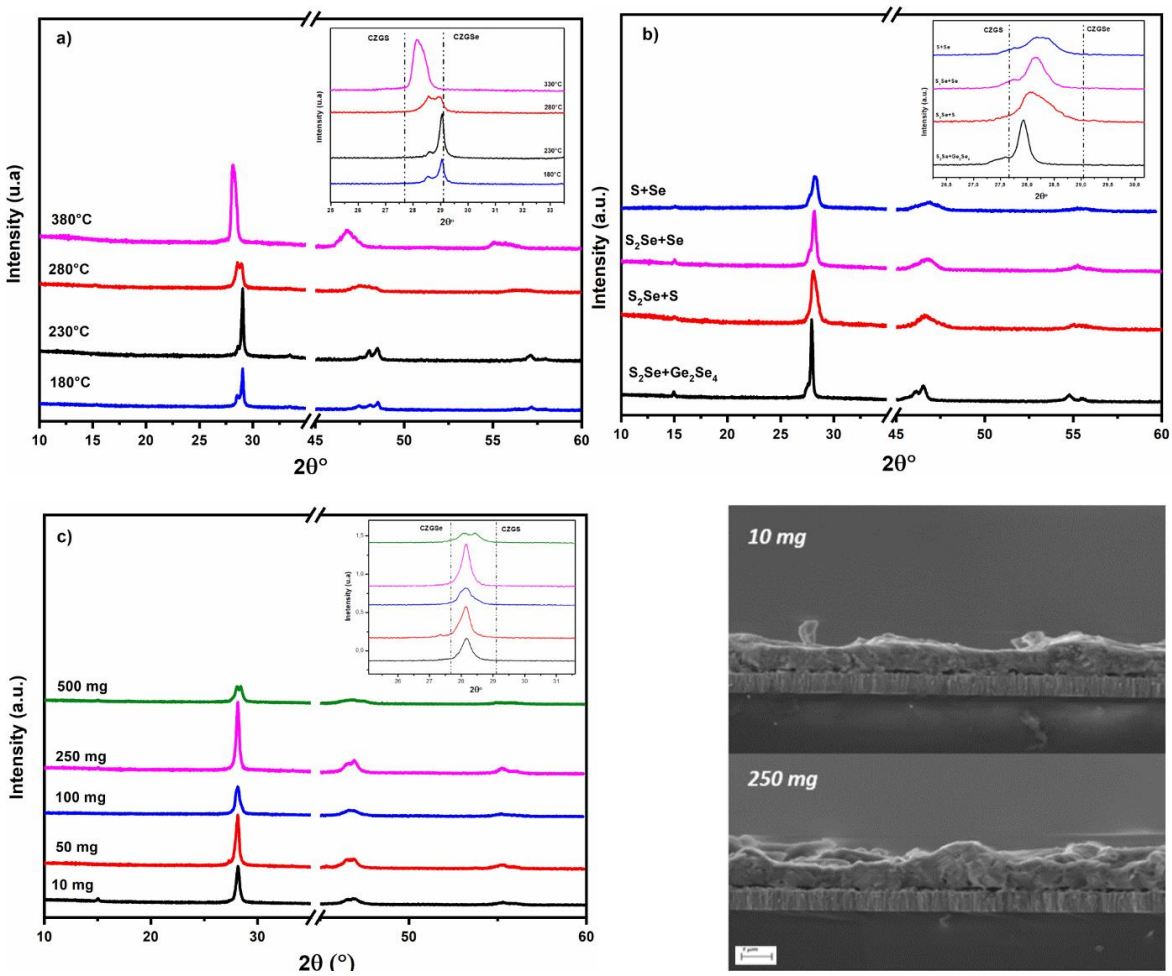

Figure 6.5: XRD patterns of CZGSSe thin films annealed using various annealing parameters: (a) different first step temperatures; (b) different chalcogen source powders; (c) different powder quantities.

Table 3. Optoelectronic parameters of CZGSSe solar cells with absorbers prepared following various annealing optimizations.

Optimization	sample	J_{sc} (mA/cm^2)	V_{oc} (mV)	FF (%)	Efficiency (%)
Temperature (First-step)	**180°C**	0.14	225.24	33.28	0.01
	230°C	1.60	463.83	37.38	0.27
	280°C	0.18	148.96	32.21	0.01
	330°C	4.58	541.48	36.96	0.92
Atmosphere	**SeS2+Se**	5.67	538.80	37.57	1.15
	$GeSe_2$+SeS_2	3.37	720.65	45.66	1.21
	SeS_2+S	2.56	509.92	46.70	0.60
	S+Se	5.98	123.71	25.23	0.18
Powder quantity	**10 mg**	3.37	720.65	45.66	1.21
	50 mg	7.03	418.21	29.71	0.87
	100 mg	6.75	320.31	28.41	0.61
	250 mg	4.25	727.38	45.78	1.41
	500 mg	1.65	198.04	32.29	0.10

To further understand the origin of the limitations in the properties of the prepared CZGSSe thin films and solar cells, an analysis of the absorbers at two critical temperatures during the annealing process was performed by combining SEM, XRD and Raman spectroscopy. Thus, the annealing process was interrupted after the first step (330°C for 30 min (T1)) and compared with the results of two-step annealing (with the second step at 480°C for 15 min (T2)).

At T1, the XRD results (Figure 6) show the appearance of several peaks, most prominently at 27.27°, 28.48°, and 31.70°, which may be due to the formation of separated binary or ternary sulfides (such as Cu_xS, ZnS or Cu_2GeS_3) and selenide (Cu_xSe, ZnSe or Cu_2GeSe_3) phases. The separated phases indicate that sulfur and selenium reacted independently with the metallic layers. The formation of these phases was confirmed by Raman spectroscopy (Figure 8a). The most intense peaks in the Raman spectra are assumed to be related to the pure Ge phase (300 cm^{-1}), confirming that the Ge layer does not completely react with the chalcogens (S and/or Se) [16]. Jinze Li et al. [91] reported that Ge is not as easily selenized as Sn under the same Se pressure. Additionally, the formation of the $Ge(S,Se)_2$ secondary phase with a S-rich composition at T1 was also confirmed, with a Raman peak present at 270 cm^{-1}. This was observed for all the measured points in the sample, indicating a laterally homogeneous

distribution of Ge and $Ge(S,Se)_2$ phases at the sample surface. The less intense peaks observed in the spectra measured under 532 nm excitation (Figure 8a) can also be assigned to the presence of different binary and ternary phases rather than to the kesterite phase, in agreement with the XRD results. The Raman spectra measured at an excitation wavelength of 325 nm also indicate the presence of the ZnS secondary phase in the sample, with the first LO peak occurring at 347 cm^{-1}[240]. The cross-sectional SEM image (Figure 7) shows the formation of two different layers and a large density of voids at contact with Mo, which is mostly due to outwards diffusion of Cu into the surface, as indicated by the diffraction peaks of the $Cu_x(S,Se)$ phases observed via XRD.

At T2, the XRD results confirm the formation of the kesterite phase with a high concentration of selenium as the peak position shifts toward the pure-selenide phase. Moreover, there are no other peaks corresponding to secondary phases present, compared to the XRD results at T1. The Raman spectra of this sample (Figure 8b) confirmed the formation of the kesterite phase since the main peaks of the CZGSSe solid solution assigned to S–S, Se-Se and S-Se interactions were present [16, 36, 37]. In addition, the Raman spectra measured at different points in the sample indicate high lateral homogeneity, with only small changes in the relative intensity of S–S-related peaks, indicating insignificant lateral variations in the S/(Se+S) ratio [241]. However, the presence of a small quantity of the $Ge(S,Se)_2$ secondary phase may also be expected due to the observed Raman peak at 260 cm^{-1} [16], which is also confirmed by the small peak at 15° in the XRD patterns. Based on the Raman spectra measured at an excitation wavelength of 325 nm, the presence of a small quantity of the ZnS secondary phase at individual points in the sample is also expected. The SEM images also show the formation of a dense and homogenous layer with a thickness of approximately 1.27 µm.

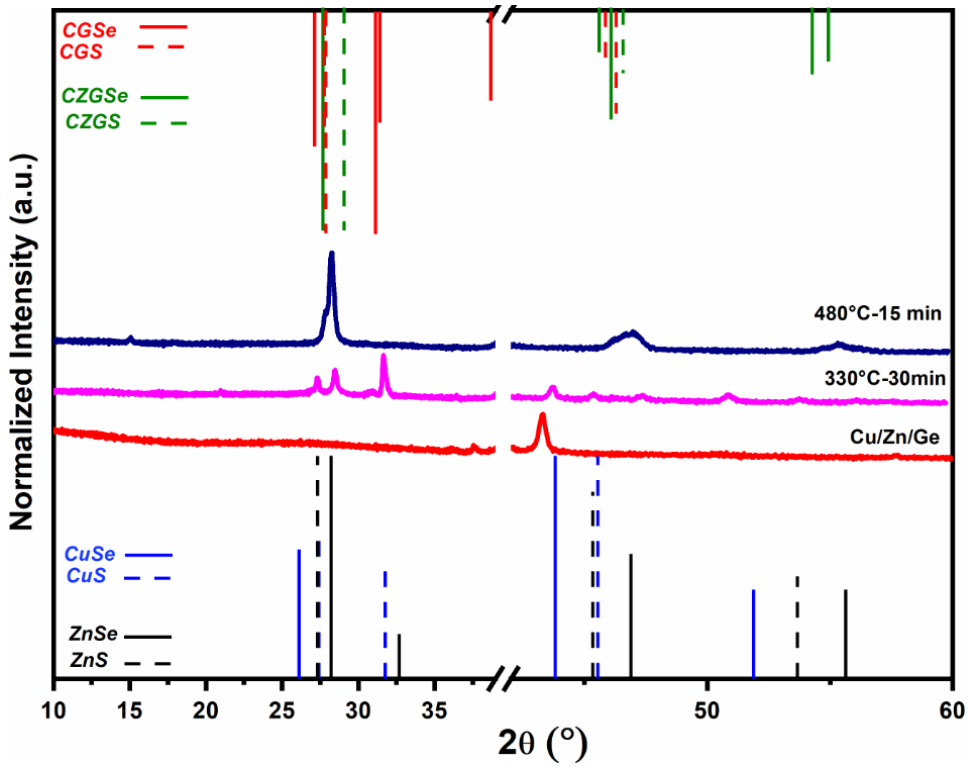

Figure 6.6: XRD patterns of the CZG precursor (red line) and CZGSSe absorbers annealed using a two-step process and stopped after 330°C for 30 min (purple line) and after 480°C for 15 min (blue line).

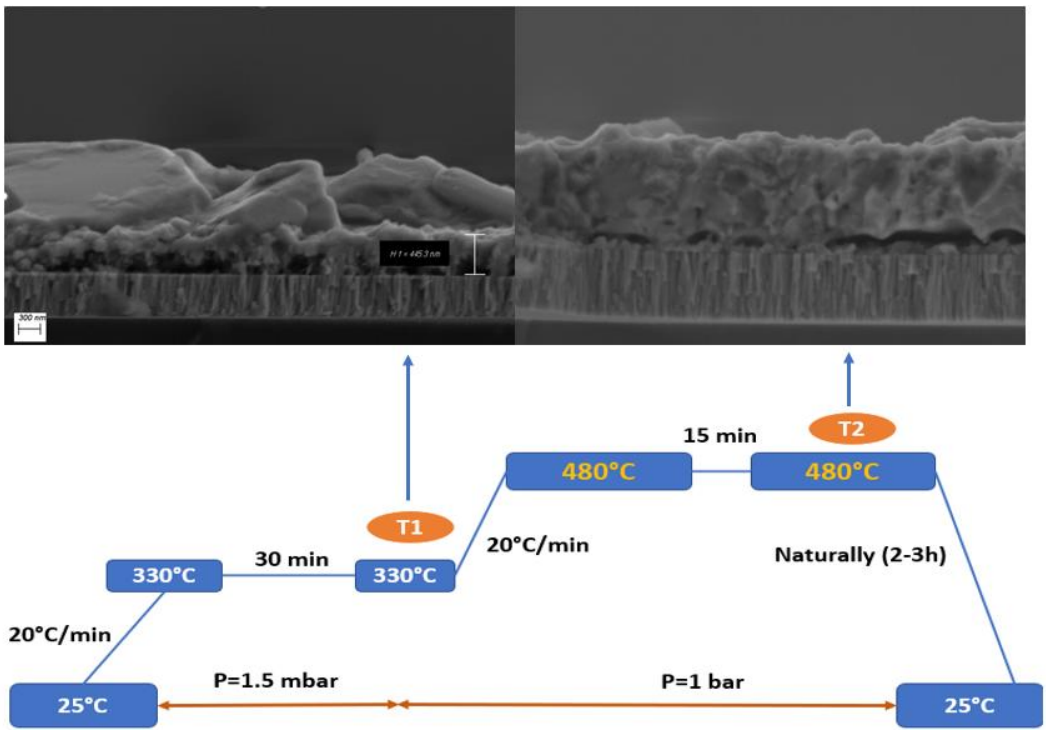

Figure 6.7: Cross-sectional SEM images of CZGSSe annealed in two step process and stopped after 330°C for 30 min and after 480°C for 15 min.

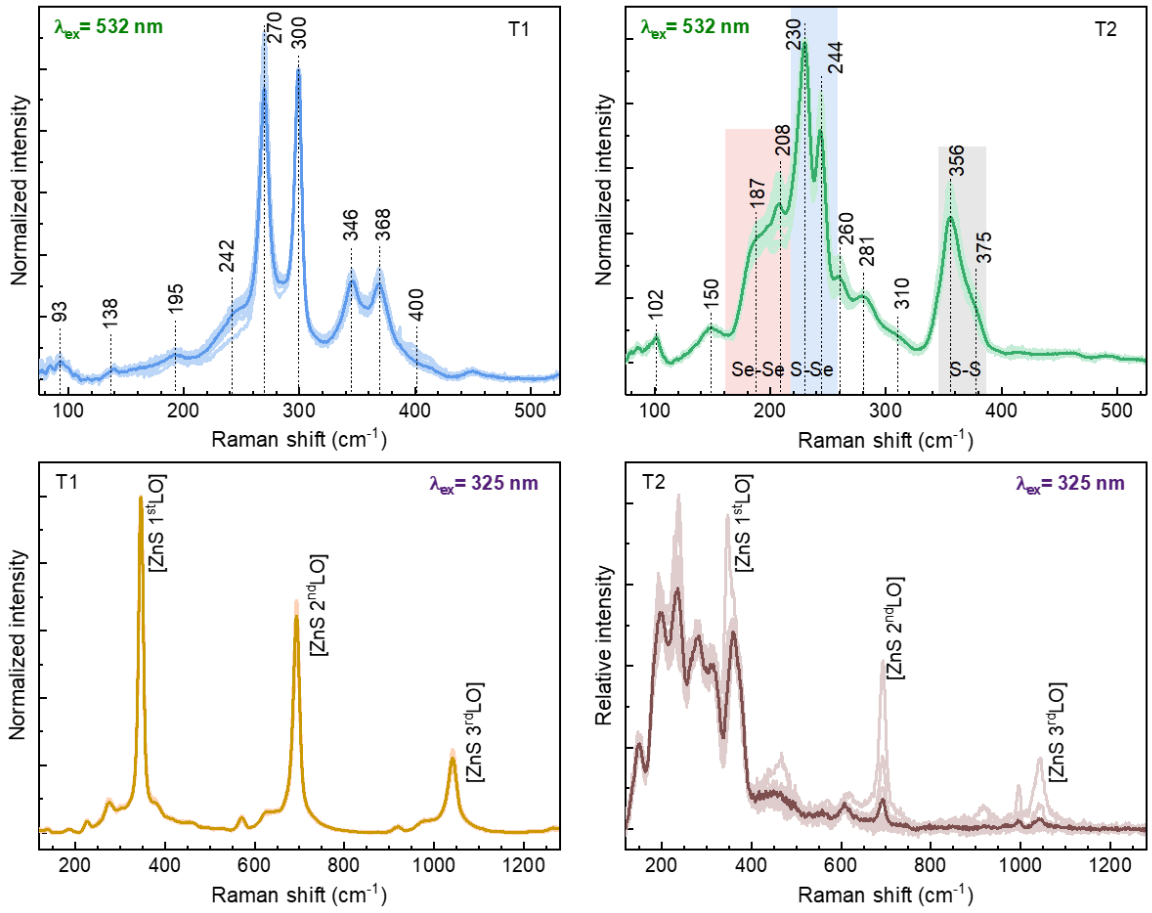

Figure 6.8: Raman spectra of CZGSSe thin films annealed in two-step process and stopped after 330°C for 30 min (left panels) and after 480°C for 15 min (right panels) measured under 532 nm (top panels) and 325 nm (bottom panels) excitation wavelength. The pale-colored spectral curves correspond to the Raman spectra of individual points in the sample and the solid line is the average spectrum.

Figure 9 illustrates the possible formation mechanisms of CZGSSe absorbers during the annealing process based on the above obtained results. At the first step temperature (T1, i.e., 330°C), a high concentration of sulfur is present in the atmosphere, as its vapor pressure is higher at this point than the selenium vapor pressure [243]; however, the Ge top layer reacts with sulfur and selenium to form the GeS_2, $GeSe_2$ and $Ge(S,Se)_2$ phases with S-rich composition. The Zn layer reacts with sulfur, forming the ZnS phase. In addition, Cu reacts with chalcogens to form Cu_xS and Cu_xSe binary phases. With increasing the temperature, the

Se vapor pressure increases, and Se starts to substitute part of S. However, both chalcogens complete their reaction with the rest of the Ge to form $Ge(S,Se)_2$ and react with $Cu_x(S,Se)$ to form $Cu_2Ge(S,Se)_3$, which reacts with ZnS to form CZGSSe. Previously, in Ref. [184], the formation mechanisms of CZGSe compounds were demonstrated by our team, who showed that the Ge-Se liquid phase is formed at a lower temperature and acts as an intermediate catalyst species to form the kesterite phase. In the present study, the formation of Ge-S and Ge-(S,Se) S-rich structures at the surface was observed, the volatility of Ge–S binary phases at temperatures typically used to synthesize kesterite compounds created compositional inhomogeneities, and the appearance of different secondary phases was expected and was confirmed by different characterization techniques.

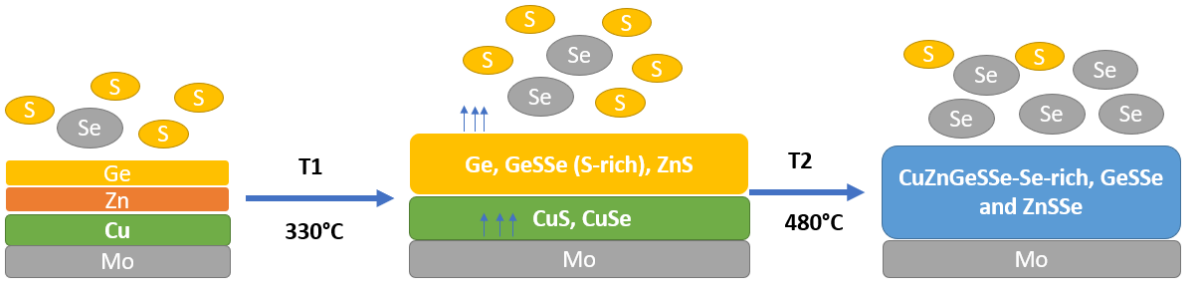

Figure 6.9: Possible formation mechanisms of the prepared CZGSSe during the annealing process.

The above results demonstrate that the Ge layer at the top of the metal stack has a negative effect and constrains the growth of sulfo-selenide CZGSSe absorbers. This layer does not completely react with the chalcogens at the lower temperature of the first step (T1), which is used to synthesize kesterite materials [13,20], and the formation of volatile GeS and Ge(S,Se) phases at the surface can be another factor limiting the crystalline quality of the layer. However, changing the position of the Ge layer in the stacking order can lead to further improvements in the CZGSSe quality. To answer this question, different stacking orders of the metallic precursors shown in Figure 10 (I- CGZ, II-GCZ, III-GCZG, and IV-CZG/CZG) were prepared and annealed with a one-step profile to prepare an S-rich CZGSSe absorber (480°C in the presence of 250 mg of $GeSe_2$+SeS_2 powder).

Figure 6.10: Stacking order of the precursors used in this work.

The XRD patterns of the CZGSSe absorbers synthesized using different stacking orders are presented in Figure 11. All the sample patterns show an XRD peak corresponding to the kesterite phase with an intense peak related to the (112) crystallographic plane. Considering only the (112) diffraction peak, the I-CGZ sample has the highest crystallinity, with a narrow, highly intense peak at 28.52°, confirming the formation of the CZGSSe single phase, with a S/(S+Se) ratio of ~63% (Table 4). Samples II-GCZ and III-GCZG exhibit two distinct kesterite phases with different S/(Se+S) ratios, and the main phases for both samples correspond to S/(S+Se) ratios of approximately 67% and 66%, respectively. Sample IV-CZG/CZG is characterized by lower crystallinity and the presence of multiple kesterite phases with different S/(S+Se) ratios; the dominant phase corresponds to a S/(S+Se) ratio of 97%. From the top-view SEM images of the samples (Figure 12), a similar trend as that of the XRD patterns can be observed. The II-GCZ and IV-CZG/CZG samples exhibit a disorganized morphology with small particles, a large density of voids and inhomogeneity of the surface compared to samples III-GCZG and I-CGZ, which are characterized by a more homogeneous surface, reinforcing the idea of partial decomposition of kesterite and uncontrolled formation of secondary phases. Samples I-CGZ and III-GCZG show better morphologies, with larger grain sizes estimated to be approximately 800 and 600 nm, respectively. The calculated lattice parameters of the dominant phase in all the samples are shown in Table 4. The lattice parameter values of all the samples, except for sample, are close to those of CZGS, confirming the formation of S-rich compounds. Similarly, the E_g values presented in Table 4 were calculated using Eq. (2).

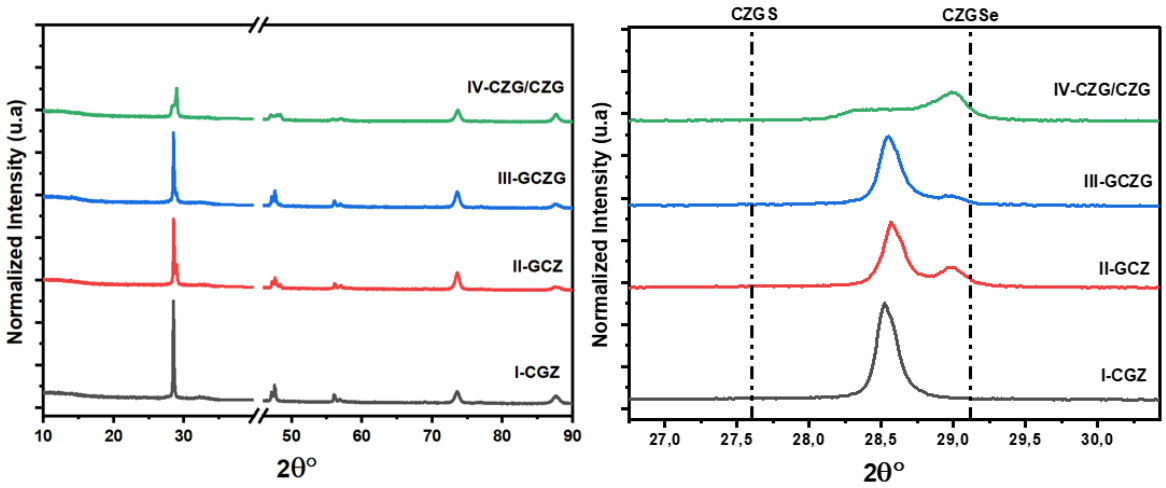

Figure 6.11: XRD patterns of CZGSSe annealed using different stacking orders.

Table 4. Lattice parameters, S/(S+Se) ratio, and bandgap of CZGSSe prepared using different stacking orders.

Stack	a (Å)	c (Å)	c/2a	S/(S+Se) (%)	E_g (eV)
I-CGZ	5.391	10.925	1.013	63	1.82
II-GCZ	5.390	10.880	1.009	66	1.87
III-GCZG	5.393	10.895	1.010	67	1.91
IV-CZG/CZG	5.342	10.690	1.001	97	2.10

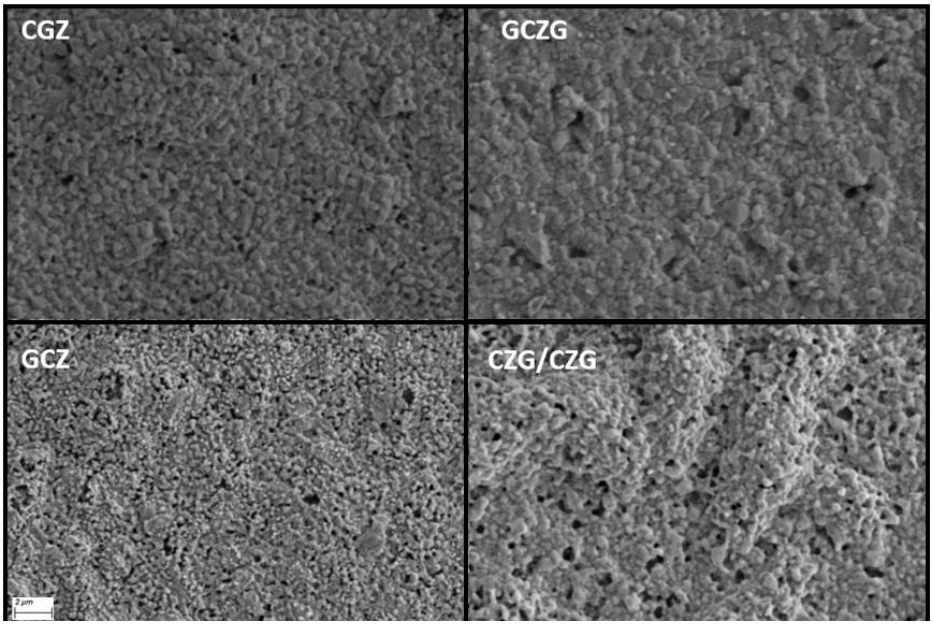

Figure 6.12: Top SEM images of CZGSSe absorbers prepared using different stacking order.

The Raman spectra of the samples synthesized following different stacking orders are characterized by the presence of Raman peaks related to the kesterite phase [16, 36, 37], confirming the results of the XRD measurements. However, a few changes are observed between the Raman spectra of the different samples. Namely, the relative intensity variations of the Se-Se- and S-Se-related peaks indicate changes in the S/(S+Se) ratio between the samples [241]. In this case, sample IV-CZG/CZG was found to have the highest Se content, while the XRD results of this sample show a S-rich content for the dominate phase. This indicates the significant difference in the S/(S+Se) ratio at the surface (where Raman spectroscopy is sensitive) and in the bulk (where XRD is sensitive) of this sample. The remaining samples have comparable S/(S+Se) ratios with reduced Se contents, which is in accordance with the XRD results. Moreover, the presence of the $Ge(S,Se)_2$ secondary phase can also be presumed for all

the samples due to the presence of characteristic peaks at approximately 260 cm^{-1}. In addition, the Raman spectra measured at an excitation wavelength of 325 nm show the presence of a very S-rich Zn(S,Se) secondary phase [244], which is more pronounced for sample III-GCZG than for the other samples.

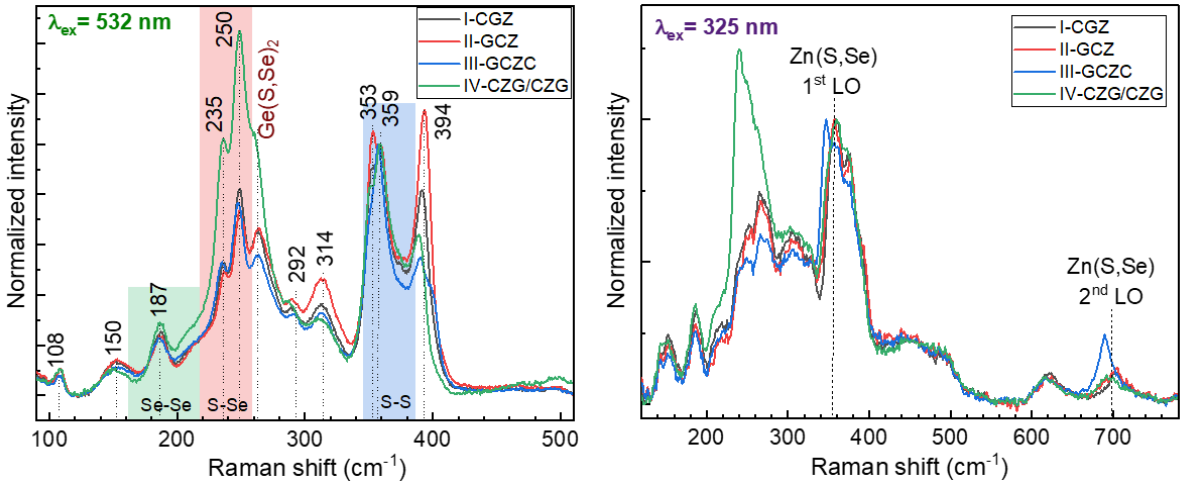

Figure 6.13: Raman spectra of CZGSSe thin films prepared using different stacking orders.

The measured optoelectronic parameters of the solar cells produced using absorbers with different stacking orders are presented in Table 5. As expected from previous characterization results, the II-GCZ and IV-CZG/CZG samples exhibit the lowest solar cell performances, with efficiencies <1%. However, solar cells with I-CGZ and III-GCZG absorbers exhibit better performance. The best solar cell shows an average efficiency of 2.04% for the III-GCZG sample. This device exhibited a high V_{oc} of 730.39 mV and an FF of 43.42%. However, its performance is limited by a lower J_{sc} of approximately 6.44 mA/cm^2. This might be related to the presence of some amount of secondary phases in the absorber, as defined by the Raman spectroscopy, and with non-optimal band alignment with the used CdS buffer layer.

Table 5. J-V parameters of CZGSSe solar cells with absorbers prepared following various stacking orders.

	Jsc (mA/Cm2)	**Voc (V)**	**FF**	**Efficiency%**
I-GCZ	0.18	43.42	31.38	0.03
II-CGZ	6.60	640.44	40.80	1.72
III-GCZG	6.44	730.39	43.42	2.04
IV-CZG/CZG	1.86	245.74	34.54	0.16

Table 6 outlines the highest efficiency achieved in this study, which is comparable to that reported for S-rich CZGSSe compounds prepared using chalcogen precursors. The most efficient S-rich CZGSSe solar cell reported to date, with an absorber bandgap of 1.98 eV, demonstrates an efficiency of 3.2%. In contrast, our work shows an efficiency exceeding 2% at an absorber bandgap of approximately 1.92 eV without additional optimizations.

Achieving high-efficiency CZGSSe solar cells requires enhanced control over the sulfo-selenization process and further optimization to improve the performance of CZGSSe-based solar cells. The incorporation of alkali metals (e.g., Na, Li, etc.) has emerged as a promising approach to improve the crystallinity of CZGSSe absorbers, thereby enhancing solar cell performance, as demonstrated in Ge-kesterite systems [225]. Yuancai el al. [88] concluded, based on their analysis of the recorded $Ag_xCu_{2-x}ZnSn(SSe)_4$/CdS solar cell, that a defective and lattice-mismatched interface is created during CdS deposition. CdS, therefore, may not be the ideal buffer layer for kesterite-based solar cells. Substituting the CdS buffer layer with materials possessing a higher bandgap could offer another approach for improving the efficiency of CZGSSe-based solar cells. Overall, the findings of this study underscore the significant potential of the straightforward sulfo-selenization process for the future development of large-bandgap CZGSSe solar cells.

Table 6. Comparison of the optoelectronic parameters of S-rich CZGSSe solar cells obtained in the present study with those reported in the literature.

REF	**E_g (eV)**	**J_{sc} (mA cm^{-2})**	**V_{oc} (mV)**	**FF (%)**	**Eff (%)**
[225]	1.85	6.6	793	56.3	2.80
[228]	1.98	7.5	817	51	3.20
This work	1.91	6.4	730	43.4	2.04

V.1.5. Conclusion

In summary, large-bandgap $Cu_2ZnGe(S,Se)_4$ thin films were synthesized by simple single-step sulfo-selenization of metallic stacks under different annealing conditions and stacking orders. The introduction of chalcogens, namely, S and Se, into the final absorbers was found to be strongly dependent on the annealing profile. However, the Ge top layer in the metallic stack and the thermodynamic properties of sulfur and selenium are the main features of sulfo-

selenized CZGSSe absorbers and solar cells based on those absorbers. Through annealing condition optimizations and change of Ge layer position in metallic stack, the structural/morphological properties were improved, and the performance of the solar cells was enhanced. The best solar cells were prepared by the sulfo-selenazion of the Ge/Cu/Zn/Ge stack in a 2-step process (at 330 and 480°C) using Ge_2Se_4+SeS_2 powder as a chalcogen source. This solar cell exhibited an efficiency of 2.04% with a high V_{oc} of 730 mV. The findings of this work demonstrate the feasibility of developing efficient CZGSSe solar cells through the sulfo-selenization of chalcogen-free metallic stacks. The obtained performance of the samples is very promising for the future development of these materials, and a good improvement in the optoelectronic properties is obtained only by changing the Ge position in the metallic stack. In addition, other optimizations of the annealing conditions are needed to improve the performance of CZGSSe solar cells.

GENERAL CONCLUSION ANA PERSPECTIVES

This thesis has advanced the development of kesterite-based materials as a viable option for future photovoltaic technologies, with a focus on improving efficiency, optimizing synthesis methods, and enabling their integration into next-generation tandem solar cells. Through the systematic optimization of the sol-gel method, we achieved significant improvements in the structural, morphological, and optoelectronic properties of kesterite materials. By controlling the oxidation states of metal ions, we developed two distinct protocols, each yielding high-quality absorber layers. These foundational advancements highlight the critical role of precise process control in achieving superior material properties. The exploration of alkali-metal doping introduced innovative deposition methods for incorporating dopants such as Na, Li, and K, which proved to enhance grain growth, reduce defect densities, and improve material properties. Furthermore, cation substitution studies particularly the substitution of copper with silver demonstrated significant potential for addressing long-standing challenges such as Cu-Zn disorder and deep-level defects. The synergistic effects of silver alloying and sodium doping led to the fabrication of kesterite materials with unprecedented performance, positioning these approaches as leading strategies for further development. Beyond material synthesis, the integration of kesterite absorbers into tandem solar cell architectures was explored using advanced optical (FDTD) and electrical (SCAPS-1D) simulations. These studies revealed the compatibility of kesterite materials with crystalline silicon (c-Si) as a bottom cell, achieving efficiencies exceeding 20% after optimization. This work demonstrated the potential of kesterite materials for tandem applications, providing a pathway toward their integration into high-performance photovoltaic systems. In addition, the complete substitution of tin (Sn) with germanium (Ge) was investigated to develop wide-bandgap kesterite materials. Using a novel single-step sulfo-selenization process, we successfully fabricated CZGSSe absorbers with a bandgap exceeding 1.7 eV, meeting the requirements for tandem solar cells. These materials achieved efficiencies comparable to the best-reported values, validating the efficacy of the proposed approach.

While this thesis marks significant progress, several challenges remain for the widespread adoption of kesterite materials in photovoltaic applications. Future research should prioritize:

1. Defect Engineering: Advanced techniques to further mitigate bulk and interface defects, including innovative doping strategies and defect passivation approaches, are essential to reduce recombination losses.
2. Secondary Phase Suppression: Refining synthesis protocols to eliminate secondary phases and ensure phase purity will be critical for achieving higher efficiencies.
3. Bandgap Engineering: Further exploration of cation substitution and alloying to optimize bandgap properties for tandem applications is needed to enhance device performance.
4. Scalability: Developing scalable, cost-effective production methods while maintaining material quality will be vital for large-scale adoption.

By addressing these challenges, kesterite materials can move closer to achieving competitive efficiencies and becoming a strong contender for large-scale renewable energy production. Building on the advancements presented in this thesis, future work has the potential to solidify kesterite materials as a cornerstone of next-generation photovoltaic technologies.

APPENDIX 1: Description of Equipment Used in the Synthesis of CZTS Materials on Transparent Electrodes Using the Sol-gel Sulfurization Process

This annex contains visual representations detailing the synthesis process of CZTS material on transparent electrodes. Each image illustrates key stages from the preparation of precursor solutions and their deposition using techniques such as spin coating to the annealing process in a controlled tubular furnace. These images serve to enhance understanding by visually depicting the methodologies and equipment utilized throughout the synthesis process. They are invaluable in complementing the textual descriptions provided, offering a comprehensive overview of the steps involved in fabricating CZTS films.

To determine the FTO side of the transparent electrode, the four-point probe method was used. This technique involves passing a known current through the outer two probes and measuring the voltage across the inner two probes to accurately measure the sheet resistance. By comparing the resistance measurements on both sides of the substrate, the FTO-coated side can be identified due to its significantly lower resistance, ensuring correct orientation for further synthesis processes.

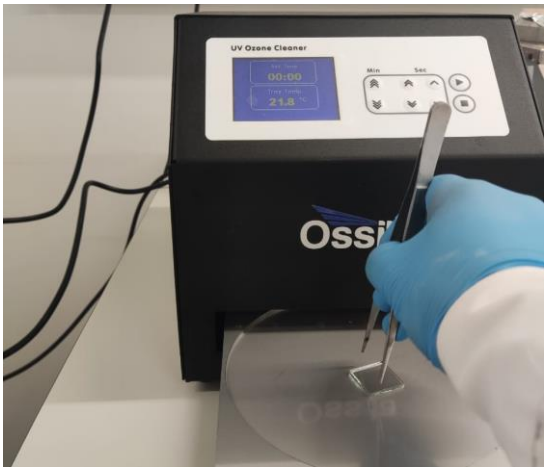

A UV cleaner was used to remove organic contaminants from the surface of the FTO-coated glass substrate. This process involves exposing the substrate to ultraviolet light, which breaks down organic molecules, ensuring a clean and contaminant-free surface. This step is essential for accurate subsequent measurements and synthesis processes.

A spin coating machine is a critical tool in thin film fabrication processes. This machine operates by dispensing a small amount of liquid precursor onto a rotating substrate, causing centrifugal force to spread the material uniformly across the surface. The rotation speed and duration are carefully controlled to achieve the desired film thickness and quality. This precise deposition method ensures even coverage and adherence of the CZTS material on the transparent electrode, facilitating consistent and reliable results in solar cell or optoelectronic device manufacturing.

The as-deposited samples were then placed in a graphite box with a surface area of 5.4 cm^2 in preparation for annealing. This step is crucial for subjecting the samples to controlled heating in an inert atmosphere, typically with a specific temperature and duration optimized for the synthesis of CZTS materials. Annealing in a graphite box helps to minimize oxidation and ensures uniform heat distribution, facilitating the transformation of the precursor layers into the desired crystalline phase.

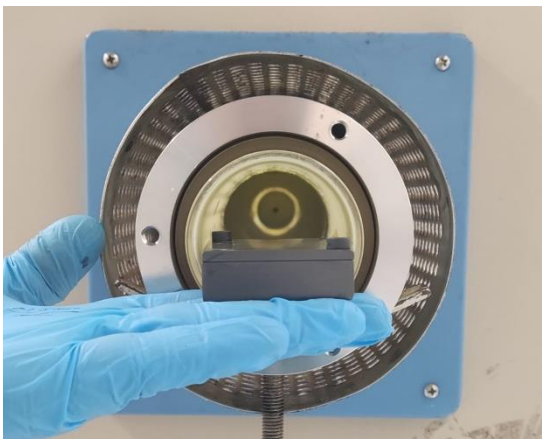

The as-deposited samples were annealed in a tubular furnace at a heating rate of 5°C/min. Annealing in such a controlled environment is critical for the transformation and crystallization of CZTS material deposited on a substrate. This gradual heating rate ensures that the samples are subjected to a uniform temperature increase, minimizing thermal shock and promoting the formation of a homogeneous and stable crystalline structure.

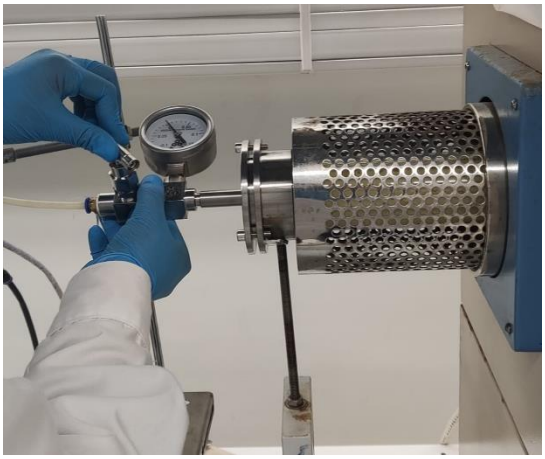

During the annealing process, the quartz tube was purged with nitrogen to create an inert atmosphere and prevent oxidation of the CZTS material. This controlled environment ensures that the samples are heated uniformly under pressure, promoting optimal crystallization. A nitrogen purge is essential for maintaining the integrity and quality of CZTS films.

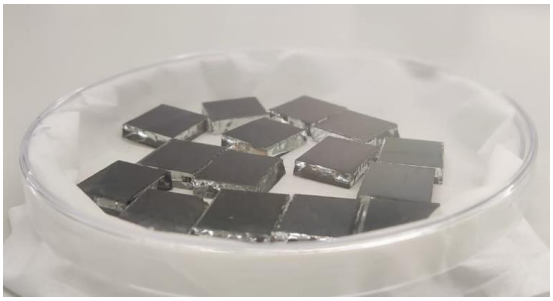

The image depicts the resulting CZTS samples after the complete synthesis process. These samples exhibit a uniform and smooth surface, indicating successful deposition and crystallization. The consistent colouration and texture of the films suggest proper adherence to the transparent electrode and effective sulfurization during annealing.

APPENDIX 2: Description of SCAPS-1D software used in electrical simulation works

Simulation using the SCAPS-1D (Solar Cell Capacitance Simulator in One Dimension) represents a significant technological advancement for the modelling and analysis of solar cells. SCAPS-1D is a software tool developed at the University of Ghent in Belgium that is specifically designed to simulate the electrical performance of solar cells based on various physical parameters and materials. Its importance lies in its ability to provide accurate and detailed predictions about the behavior of photovoltaic devices, enabling researchers and engineers to better understand and optimize their designs. The use of the SCAPS-1D offers several key advantages. First, it allows for the virtual testing of innovative concepts and materials without the costs and time associated with the physical fabrication of prototypes. Second, it helps identify and analyse the mechanisms limiting the efficiency of solar cells, thus facilitating the development of strategies to improve their performance. Finally, by providing a flexible and extensible simulation environment, SCAPS-1D enables the exploration of a wide range of solar cell structures, from traditional technologies to next-generation devices such as perovskite solar cells.

To examine solar cells, numerical analysis software must be able to solve fundamental semiconductor equations. To analyse solar cell performance and potential output, these equations are essential. The Poisson equation for electrostatic potential is the governing equation among these. Poison's equation for electrostatic potential is expressed as equation 1

$$\frac{\mathrm{d}^2\mathrm{V}}{\mathrm{dx}^2} = \frac{\rho}{\varepsilon} \tag{1}$$

ρ is the density of charge (C/cm^3), and ε is the product of the semiconductor dielectric constant and permittivity of free space. The charge neutrality equation ρ can be expressed as given in equation 2 with the assumption that the dopant is totally ionized:

$$\rho = q(p - n + N_D^+ + N_A^-) \tag{2}$$

where q is the electronic charge, p is the concentration of holes, n is the concentration of electrons, $N_A{}^-$ is the ionized acceptor dopant carrier concentration and $N_D{}^+$ is the ionized donor

dopant carrier concentration. By substituting the value of equation 2 in equation 1, equation 3 can be obtained.

$$\frac{\mathrm{d}^2V}{\mathrm{dx}^2} = \frac{q(p - n + N_D^+ + N_A^-)}{\varepsilon} \tag{3}$$

Additionally, the expression for the concentration of carriers (p, n) must be rearranged to solve equation 3 for V as a function of the position of x. The second equation is known as the continuity equation; it is referred to as the governing equation since it analyses drift, diffusion, generation, and recombination simultaneously. The continuity equations for the changes in electron and hole concentrations are represented by equations 4 and 5, respectively.

$$\frac{\partial n}{\partial t} = \frac{1}{q}\frac{\partial J_n}{\partial x} + (G_n - R_n) \tag{4}$$

$$\frac{\partial p}{\partial t} = \frac{1}{q}\frac{\partial J_p}{\partial x} + \left(G_p - R_p\right) \tag{5}$$

The outputs from equations 1, 4 and 5 have nonlinear dependencies on the charge carrier concentration (p, n). Therefore, these equations can be solved with numerical techniques with standard approaches such as equation discretization, device discretization and a set of boundary conditions. To measure the current characteristics of solar cells, a simulator must be able to solve the drift-diffusion equation for the current in solar cells. The equation for drift diffusion of charge carriers is given in equation 6 and equation 7

$$J_n = q\mu_n n\epsilon + qD_n\,\partial n \tag{6}$$

$$J_p = q\mu_p p\epsilon - qD_p\,\partial p \tag{7}$$

The current density for electrons and holes is (J_n,J_p), the mobility of carriers is (μ_n, μ_p), the diffusion coefficient for electrons and holes is (D_n,D_p), and according to Einstein's equation, the diffusion coefficient depends on the mobility of the carriers multiplied by the carrier lifetime. Equation 8 shows the relationship between D_n and the carrier's movement.

$$D_{(n,p)} = \mu_{(n,p)}\frac{kT}{q} \tag{8}$$

The other quantities that need to be solved for equations 3, 4 and 5 are generation and recombination (G, R), which can also be expressed as the net recombination in device (U). This is represented in equation 9 for an n-type semiconductor.

(9)

$$U = \frac{p - p_0}{\tau_p}$$

SCAPS-1D front-end interface

Figure 57 shows the front-end interface of the SCAPS-1D software. It primarily consists of 4 panels, and an overview of these panels is provided below.

The **1**-Problem definition panel is used to define a solar cell structure that we want to define in the SCAPS software, analyse the simulated output, and save the simulated output and clear simulated history data from the SCAPS. To define a solar cell structure, we need to click on a set problem button

The **2**-Action panel is used for reading the scale, and this panel consists of an I − V characteristic scale calibration and setting, a C − V capacitance voltage setting, a C − F capacitance frequency setting and a QE quantum efficiency setting.

3- The illumination panel shows the spectrum setting and direction from which the solar cell structure will be illuminated

4- Working point for setting the operating temperature

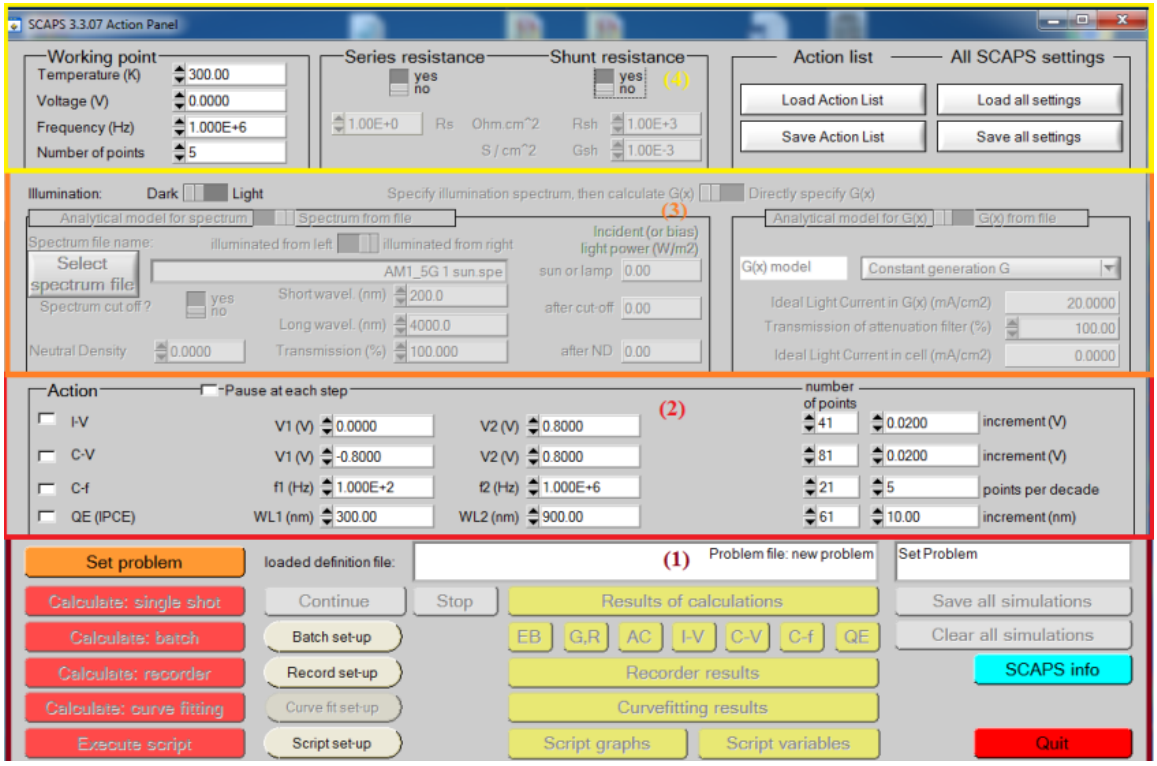

Figure 1. SCAPS front-end interface

1. SCAPS-ID problem setting

Clicking the "set problem" button in SCAPS will cause another interface to open, allowing us to specify or define a problem. We define the structure of our solar cell at this interface, which we term the "Solar cell definition panel." Due to its ability to define and visualize structure, this panel is essential for understanding solar cells. As shown in Figure 4.2, this panel is broken down into three categories for clarification.

The explanations of these categories are listed below.

1- These buttons consist of 5 buttons, and the function of these buttons is to load a structure file from the SCAPS structure definition library or to save already modelled structures in the SCAPS definition library. After loading the file or creating the new structure, we clicked “OK” to return to the main front-end interface for further analysis.

2-This consists of front and back contacts and layers that we will define for our solar cell structure. Figure 58 shows that the SCAPS can support only a 7-layer structure for the numerical analysis of solar cells.

3- This section describes the visualization of the defined solar cell structure with illumination from the front or back contact. In this section, buttons are used to define the illumination from the front or back contact, the applied potential and the current reference.

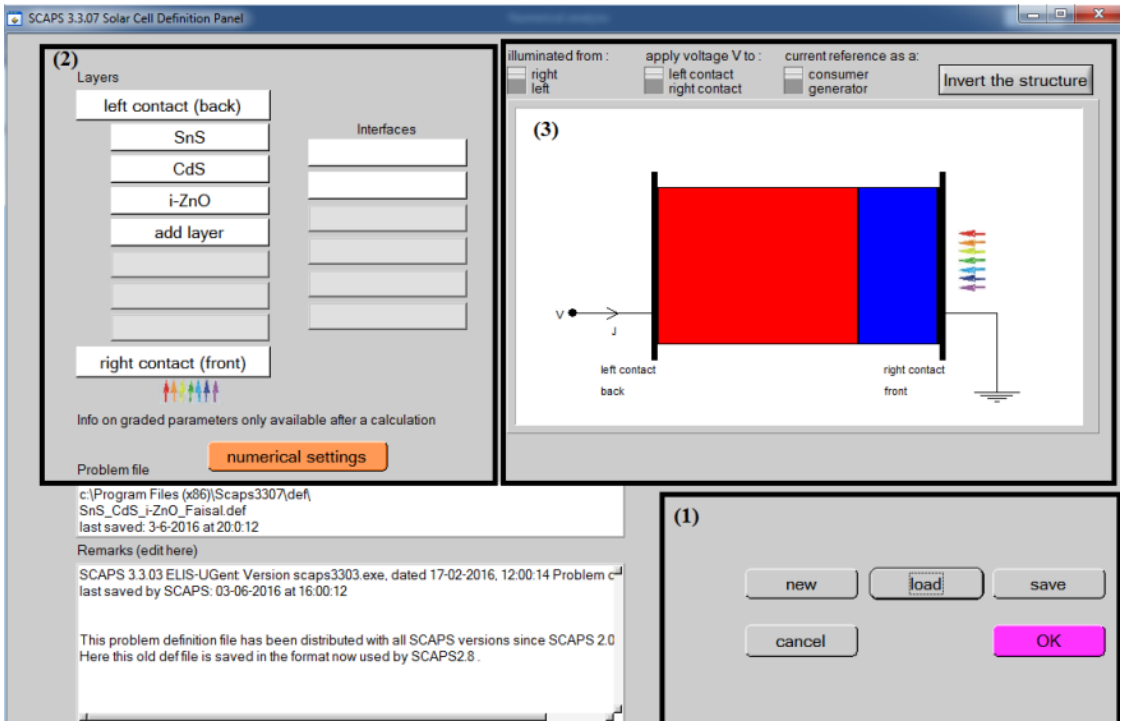

Figure 2. SCAPS solar cell definition panel

2. Adding layers to the structure

As indicated in Figure 58 section 2, we click on the added layer in the SCAPS to designate layers for the development of the solar cell structure. Upon selecting the "Add Layer," a new panel known as the "Layer properties panel" will emerge. We will configure the fundamental physical properties of our layer in this panel, as illustrated in Figure 59.

The next step was to perform numerical analysis for the defined structure after the problem was set up in the SCAPS environment. This involved analysing the impact of various physical parameters, such as the operating temperature, buffer layer thickness, absorber layer doping concentration, and buffer layer, on the performance of the solar cell.

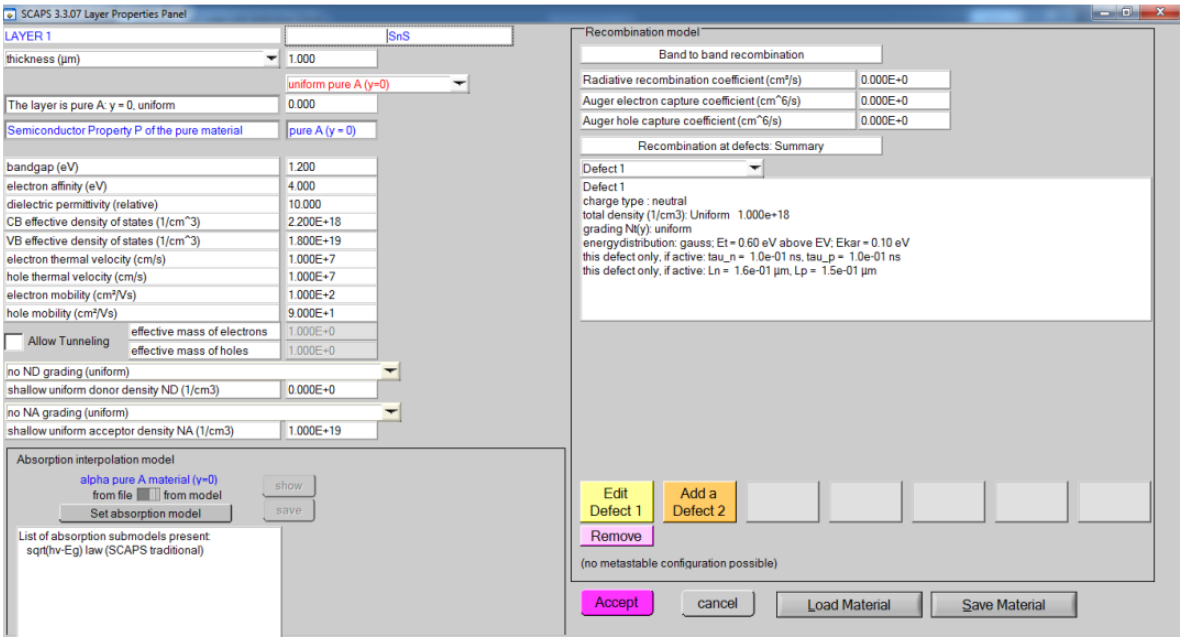

Figure 3. Layer properties panel

REFERANCES:

[1] D.M. Chapin, C.S. Fuller, G.L. Pearson, A New Silicon *p-n* Junction Photocell for Converting Solar Radiation into Electrical Power, Journal of Applied Physics 25 (1954) 676–677. https://doi.org/10.1063/1.1721711.

[2] K. Yoshikawa, H. Kawasaki, W. Yoshida, T. Irie, K. Konishi, K. Nakano, T. Uto, D. Adachi, M. Kanematsu, H. Uzu, K. Yamamoto, Silicon heterojunction solar cell with interdigitated back contacts for a photoconversion efficiency over 26%, Nat Energy 2 (2017) 17032. https://doi.org/10.1038/nenergy.2017.32.

[3] A.R. Zanatta, The Shockley–Queisser limit and the conversion efficiency of silicon-based solar cells, Results in Optics 9 (2022) 100320. https://doi.org/10.1016/j.rio.2022.100320.

[4] E. Aydin, T.G. Allen, M. De Bastiani, A. Razzaq, L. Xu, E. Ugur, J. Liu, S. De Wolf, Pathways toward commercial perovskite/silicon tandem photovoltaics, Science 383 (2024) eadh3849. https://doi.org/10.1126/science.adh3849.

[5] M.A. Green, E.D. Dunlop, M. Yoshita, N. Kopidakis, K. Bothe, G. Siefer, X. Hao, Solar cell efficiency tables (Version 63), Progress in Photovoltaics 32 (2024) 3–13. https://doi.org/10.1002/pip.3750.

[6] H. Katagiri, K. Saitoh, T. Washio, H. Shinohara, T. Kurumadani, S. Miyajima, Development of thin film solar cell based on Cu2ZnSnS4 thin films, Solar Energy Materials and Solar Cells 65 (2001) 141–148. https://doi.org/10.1016/S0927-0248(00)00088-X.

[7] Y. Li, C. Cui, H. Wei, Z. Shao, Z. Wu, S. Zhang, X. Wang, S. Pang, G. Cui, Suppressing Element Inhomogeneity Enables 14.9% Efficiency CZTSSe Solar Cells, Advanced Materials 36 (2024) 2400138. https://doi.org/10.1002/adma.202400138.

[8] A.D. Vos, Detailed balance limit of the efficiency of tandem solar cells, J. Phys. D: Appl. Phys. 13 (1980) 839–846. https://doi.org/10.1088/0022-3727/13/5/018.

[9] N. Ennouhi, S. Aazou, A. Er-rafyg, Z. Laghfour, Z. Sekkat, Feasibility of Exceeding 20% Efficiency for Kesterite/c-Silicon Tandem Solar Cells Using an Alternative Buffer Layer: Optical and Electrical Analysis, Nanomaterials 14 (2024) 1722. https://doi.org/10.3390/nano14211722.

[10] M. Valentini, C. Malerba, L. Serenelli, M. Izzi, E. Salza, M. Tucci, A. Mittiga, Fabrication of monolithic CZTS/Si tandem cells by development of the intermediate connection, Solar Energy 190 (2019) 414–419. https://doi.org/10.1016/j.solener.2019.08.029.

[11] M.K.A. Mohammed, 21.4% efficiency of perovskite solar cells using BMImI additive in the lead iodide precursor based on carbon nanotubes/TiO2 electron transfer layer, Ceramics International 46 (2020) 27647–27654. https://doi.org/10.1016/j.ceramint.2020.07.260.

[12] A.C. Tamboli, D.C. Bobela, A. Kanevce, T. Remo, K. Alberi, M. Woodhouse, Low-Cost CdTe/Silicon Tandem Solar Cells, IEEE J. Photovoltaics 7 (2017) 1767–1772. https://doi.org/10.1109/JPHOTOV.2017.2737361.

[13] C. Yan, J. Huang, K. Sun, S. Johnston, Y. Zhang, H. Sun, A. Pu, M. He, F. Liu, K. Eder, L. Yang, J.M. Cairney, N.J. Ekins-Daukes, Z. Hameiri, J.A. Stride, S. Chen, M.A. Green, X. Hao, Cu2ZnSnS4 solar cells with over 10% power conversion efficiency enabled by heterojunction heat treatment, Nat Energy 3 (2018) 764–772. https://doi.org/10.1038/s41560-018-0206-0.

[14] N. Benhaddou, S. Aazou, R. Fonoll-Rubio, Y. Sánchez, S. Giraldo, M. Guc, L. Calvo-Barrio, V. Izquierdo-Roca, M. Abd-Lefdil, Z. Sekkat, E. Saucedo, Uncovering details behind the formation mechanisms of $Cu_2ZnGeSe_4$ photovoltaic absorbers, J. Mater. Chem. C 8 (2020) 4003–4011. https://doi.org/10.1039/C9TC06728K.

[15] M. Gansukh, Z. Li, M.E. Rodriguez, S. Engberg, F.M.A. Martinho, S.L. Mariño, E. Stamate, J. Schou, O. Hansen, S. Canulescu, Energy band alignment at the heterointerface between

CdS and Ag-alloyed CZTS, Sci Rep 10 (2020) 18388. https://doi.org/10.1038/s41598-020-73828-0.
[16] Hannah Ritchie, Pablo Rosado and Max Roser (2023) - “Energy” Published online at OurWorldInData.org. Retrieved from: “https://ourworldindata.org/energy” [Online Resource], in: n.d.
[17] N. Shen, Y. Wang, H. Peng, Z. Hou, Renewable Energy Green Innovation, Fossil Energy Consumption, and Air Pollution—Spatial Empirical Analysis Based on China, Sustainability 12 (2020) 6397. https://doi.org/10.3390/su12166397.
[18] S.M. Sze, K.K. Ng, Physics of Semiconductor Devices, 1st ed., Wiley, 2006. https://doi.org/10.1002/0470068329.
[19] B. Zaidi, Introductory Chapter: Introduction to Photovoltaic Effect, in: B. Zaidi (Ed.), Solar Panels and Photovoltaic Materials, InTech, 2018. https://doi.org/10.5772/intechopen.74389.
[20] N. Ali, R. Ahmed, J.T. Luo, M. Wang, A. Kalam, A.G. Al-Sehemi, Y.Q. Fu, Advances in nanostructured homojunction solar cells and photovoltaic materials, Materials Science in Semiconductor Processing 107 (2020) 104810. https://doi.org/10.1016/j.mssp.2019.104810.
[21] N. Mufti, T. Amrillah, A. Taufiq, Sunaryono, Aripriharta, M. Diantoro, Zulhadjri, H. Nur, Review of CIGS-based solar cells manufacturing by structural engineering, Solar Energy 207 (2020) 1146–1157. https://doi.org/10.1016/j.solener.2020.07.065.
[22] H.S. Jung, N. Park, Perovskite Solar Cells: From Materials to Devices, Small 11 (2015) 10–25. https://doi.org/10.1002/smll.201402767.
[23] W. Shockley, H.J. Queisser, Detailed Balance Limit of Efficiency of *p-n* Junction Solar Cells, Journal of Applied Physics 32 (1961) 510–519. https://doi.org/10.1063/1.1736034.
[24] N. Guerra, M. Guevara, C. Palacios, F. Crupi, Operation and physics of photovoltaic solar cells: an overview, I+D Tecnológico 14 (2018) 84–95. https://doi.org/10.33412/idt.v14.2.2077.
[25] M.A. Green, E.D. Dunlop, G. Siefer, M. Yoshita, N. Kopidakis, K. Bothe, X. Hao, Solar cell efficiency tables (Version 61), Progress in Photovoltaics 31 (2023) 3–16. https://doi.org/10.1002/pip.3646.
[26] L.C. Hirst, N.J. Ekins-Daukes, Fundamental losses in solar cells, Progress in Photovoltaics 19 (2011) 286–293. https://doi.org/10.1002/pip.1024.
[27] L. Zhu, T. Mochizuki, M. Yoshita, S. Chen, C. Kim, H. Akiyama, Y. Kanemitsu, Conversion efficiency limits and bandgap designs for multi-junction solar cells with internal radiative efficiencies below unity, Opt. Express 24 (2016) A740. https://doi.org/10.1364/OE.24.00A740.
[28] Tandem Cells, in: Third Generation Photovoltaics, Springer Berlin Heidelberg, 2006: pp. 59–67. https://doi.org/10.1007/3-540-26563-5_5.
[29] D.J. Friedman, J.M. Olson, S. Kurtz, High-Efficiency III–V Multijunction Solar Cells, in: A. Luque, S. Hegedus (Eds.), Handbook of Photovoltaic Science and Engineering, 1st ed., Wiley, 2010: pp. 314–364. https://doi.org/10.1002/9780470974704.ch8.
[30] Z. Wang, Z. Song, Y. Yan, S. (Frank) Liu, D. Yang, Perovskite—a Perfect Top Cell for Tandem Devices to Break the S–Q Limit, Advanced Science 6 (2019) 1801704. https://doi.org/10.1002/advs.201801704.
[31] P. Colter, B. Hagar, S. Bedair, Tunnel Junctions for III-V Multijunction Solar Cells Review, Crystals 8 (2018) 445. https://doi.org/10.3390/cryst8120445.
[32] T. Todorov, O. Gunawan, S. Guha, A road towards 25% efficiency and beyond: perovskite tandem solar cells, Mol. Syst. Des. Eng. 1 (2016) 370–376. https://doi.org/10.1039/C6ME00041J.
[33] Y. Cheng, L. Ding, Perovskite/Si tandem solar cells: Fundamentals, advances, challenges, and novel applications, SusMat 1 (2021) 324–344. https://doi.org/10.1002/sus2.25.

[34] M.V. Khenkin, E.A. Katz, A. Abate, G. Bardizza, J.J. Berry, C. Brabec, F. Brunetti, V. Bulović, Q. Burlingame, A. Di Carlo, R. Cheacharoen, Y.-B. Cheng, A. Colsmann, S. Cros, K. Domanski, M. Dusza, C.J. Fell, S.R. Forrest, Y. Galagan, D. Di Girolamo, M. Grätzel, A. Hagfeldt, E. Von Hauff, H. Hoppe, J. Kettle, H. Köbler, M.S. Leite, S. Liu, Y.-L. Loo, J.M. Luther, C.-Q. Ma, M. Madsen, M. Manceau, M. Matheron, M. McGehee, R. Meitzner, M.K. Nazeeruddin, A.F. Nogueira, Ç. Odabaşı, A. Osherov, N.-G. Park, M.O. Reese, F. De Rossi, M. Saliba, U.S. Schubert, H.J. Snaith, S.D. Stranks, W. Tress, P.A. Troshin, V. Turkovic, S. Veenstra, I. Visoly-Fisher, A. Walsh, T. Watson, H. Xie, R. Yıldırım, S.M. Zakeeruddin, K. Zhu, M. Lira-Cantu, Consensus statement for stability assessment and reporting for perovskite photovoltaics based on ISOS procedures, Nat Energy 5 (2020) 35–49. https://doi.org/10.1038/s41560-019-0529-5.

[35] Q. Zhang, F. Hao, J. Li, Y. Zhou, Y. Wei, H. Lin, Perovskite solar cells: must lead be replaced – and can it be done?, Science and Technology of Advanced Materials 19 (2018) 425–442. https://doi.org/10.1080/14686996.2018.1460176.

[36] A. Le Donne, V. Trifiletti, S. Binetti, New Earth-Abundant Thin Film Solar Cells Based on Chalcogenides, Front. Chem. 7 (2019) 297. https://doi.org/10.3389/fchem.2019.00297.

[37] K. Pal, P. Singh, A. Bhaduri, K.B. Thapa, Current challenges and future prospects for a highly efficient (>20%) kesterite CZTS solar cell: A review, Solar Energy Materials and Solar Cells 196 (2019) 138–156. https://doi.org/10.1016/j.solmat.2019.03.001.

[38] M. Nakamura, K. Yamaguchi, Y. Kimoto, Y. Yasaki, T. Kato, H. Sugimoto, Cd-Free Cu(In,Ga)(Se,S) $_2$ Thin-Film Solar Cell With Record Efficiency of 23.35%, IEEE J. Photovoltaics 9 (2019) 1863–1867. https://doi.org/10.1109/JPHOTOV.2019.2937218.

[39] X. Wei, H. Hui, C. Zhao, C. Deng, M. Han, Z. Yu, A. Sheng, P. Roy, A. Chen, J. Lin, D.F. Watson, Y.-Y. Sun, T. Thomay, S. Yang, Q. Jia, S. Zhang, H. Zeng, Realization of BaZrS3 chalcogenide perovskite thin films for optoelectronics, Nano Energy 68 (2020) 104317. https://doi.org/10.1016/j.nanoen.2019.104317.

[40] A.R. Jeong, S.B. Choi, W.M. Kim, J.-K. Park, J. Choi, I. Kim, J. Jeong, Electrical analysis of c-Si/CGSe monolithic tandem solar cells by using a cell-selective light absorption scheme, Sci Rep 7 (2017) 15723. https://doi.org/10.1038/s41598-017-15998-y.

[41] E. Zillner, A. Paul, J. Jutimoosik, S. Chandarak, T. Monnor, S. Rujirawat, R. Yimnirun, X.Z. Lin, A. Ennaoui, Th. Dittrich, M. Lux-Steiner, Lattice positions of Sn in Cu2ZnSnS4 nanoparticles and thin films studied by synchrotron X-ray absorption near edge structure analysis, Applied Physics Letters 102 (2013) 221908. https://doi.org/10.1063/1.4809824.

[42] S. Kumar, D.K. Sharma, B. Joshi, S. Auluck, Theoretical insights into kesterite and stannite phases of Cu2(Sn1– *X* Ge *X*)ZnSe4 based alloys: A prospective photovoltaic material, AIP Advances 6 (2016) 125303. https://doi.org/10.1063/1.4971323.

[43] A.H. Aka, A. Bouich, B. Aka, B.M. Soucase, Synthesis and characterization of kesterite Cu2ZnSn(SxSe1-x)4 thin films with low-cost for efficient solar cells, Results in Optics 13 (2023) 100507. https://doi.org/10.1016/j.rio.2023.100507.

[44] K. Sun, C. Yan, J. Huang, K. Sun, H. Sun, L. Jiang, X. Deng, J. Stride, X. Hao, F. Liu, Minority lifetime and efficiency improvement for CZTS solar cells via Cd ion soaking and post treatment, Journal of Alloys and Compounds 750 (2018) 328–332. https://doi.org/10.1016/j.jallcom.2018.03.401.

[45] M. Grossberg, J. Krustok, C.J. Hages, D.M. Bishop, O. Gunawan, R. Scheer, S.M. Lyam, H. Hempel, S. Levcenco, T. Unold, The electrical and optical properties of kesterites, J. Phys. Energy 1 (2019) 044002. https://doi.org/10.1088/2515-7655/ab29a0.

[46] A. Tang, Z. Li, F. Wang, M. Dou, W. Mao, Preparation of Cu2ZnSnS4 thin films with high carrier concentration and high carrier mobility by optimized annealing, J Mater Sci: Mater Electron 29 (2018) 7613–7620. https://doi.org/10.1007/s10854-018-8753-5.

[47] U. Syafiq, N. Ataollahi, R.D. Maggio, P. Scardi, Solution-Based Synthesis and Characterization of Cu2ZnSnS4 (CZTS) Thin Films, Molecules 24 (2019) 3454. https://doi.org/10.3390/molecules24193454.

[48] I. Repins, C. Beall, N. Vora, C. DeHart, D. Kuciauskas, P. Dippo, B. To, J. Mann, W.-C. Hsu, A. Goodrich, R. Noufi, Co-evaporated Cu2ZnSnSe4 films and devices, Solar Energy Materials and Solar Cells 101 (2012) 154–159. https://doi.org/10.1016/j.solmat.2012.01.008.

[49] H. Katagiri, K. Jimbo, M. Tahara, H. Araki, K. Oishi, The Influence of the Composition Ratio on CZTS-based Thin Film Solar Cells, MRS Proc. 1165 (2009) 1165-M04-01. https://doi.org/10.1557/PROC-1165-M04-01.

[50] S. Chen, A. Walsh, X. Gong, S. Wei, Classification of Lattice Defects in the Kesterite Cu_2ZnSnS_4 and $Cu_2ZnSnSe_4$ Earth-Abundant Solar Cell Absorbers, Advanced Materials 25 (2013) 1522–1539. https://doi.org/10.1002/adma.201203146.

[51] D. Han, Y.Y. Sun, J. Bang, Y.Y. Zhang, H.-B. Sun, X.-B. Li, S.B. Zhang, Deep electron traps and origin of p -type conductivity in the earth-abundant solar-cell material Cu 2 ZnSnS 4, Phys. Rev. B 87 (2013) 155206. https://doi.org/10.1103/PhysRevB.87.155206.

[52] M. Dimitrievska, A. Fairbrother, E. Saucedo, A. Pérez-Rodríguez, V. Izquierdo-Roca, Secondary phase and Cu substitutional defect dynamics in kesterite solar cells: Impact on optoelectronic properties, Solar Energy Materials and Solar Cells 149 (2016) 304–309. https://doi.org/10.1016/j.solmat.2016.01.029.

[53] J. Márquez, M. Neuschitzer, M. Dimitrievska, R. Gunder, S. Haass, M. Werner, Y.E. Romanyuk, S. Schorr, N.M. Pearsall, I. Forbes, Systematic compositional changes and their influence on lattice and optoelectronic properties of Cu2ZnSnSe4 kesterite solar cells, Solar Energy Materials and Solar Cells 144 (2016) 579–585. https://doi.org/10.1016/j.solmat.2015.10.004.

[54] S. Bourdais, C. Choné, B. Delatouche, A. Jacob, G. Larramona, C. Moisan, A. Lafond, F. Donatini, G. Rey, S. Siebentritt, A. Walsh, G. Dennler, Is the Cu/Zn Disorder the Main Culprit for the Voltage Deficit in Kesterite Solar Cells?, Advanced Energy Materials 6 (2016) 1502276. https://doi.org/10.1002/aenm.201502276.

[55] J.-H. Yoon, K.-H. Yoon, W.M. Kim, J.-K. Park, Y.-J. Baik, T.-Y. Seong, J. Jeong, High-temperature stability of molybdenum (Mo) back contacts for CIGS solar cells: a route towards more robust back contacts, J. Phys. D: Appl. Phys. 44 (2011) 425302. https://doi.org/10.1088/0022-3727/44/42/425302.

[56] T.J. Huang, X. Yin, G. Qi, H. Gong, CZTS-based materials and interfaces and their effects on the performance of thin film solar cells: CZTS-based materials and interfaces and their effects on the performance of thin film solar cells, Phys. Status Solidi RRL 08 (2014) 735–762. https://doi.org/10.1002/pssr.201409219.

[57] M. Kumar, A. Dubey, N. Adhikari, S. Venkatesan, Q. Qiao, Strategic review of secondary phases, defects and defect-complexes in kesterite CZTS–Se solar cells, Energy Environ. Sci. 8 (2015) 3134–3159. https://doi.org/10.1039/C5EE02153G.

[58] J.J. Scragg, P.J. Dale, L.M. Peter, Synthesis and characterization of Cu2ZnSnS4 absorber layers by an electrodeposition-annealing route, Thin Solid Films 517 (2009) 2481–2484. https://doi.org/10.1016/j.tsf.2008.11.022.

[59] S. Chen, A. Walsh, X. Gong, S. Wei, Classification of Lattice Defects in the Kesterite Cu_2ZnSnS_4 and $Cu_2ZnSnSe_4$ Earth-Abundant Solar Cell Absorbers, Advanced Materials 25 (2013) 1522–1539. https://doi.org/10.1002/adma.201203146.

[60] T. Minemoto, T. Matsui, H. Takakura, Y. Hamakawa, T. Negami, Y. Hashimoto, T. Uenoyama, M. Kitagawa, Theoretical analysis of the effect of conduction band offset of window/CIS layers on performance of CIS solar cells using device simulation, Solar Energy Materials and Solar Cells 67 (2001) 83–88. https://doi.org/10.1016/S0927-0248(00)00266-X.

[61] M. Green, E. Dunlop, J. Hohl-Ebinger, M. Yoshita, N. Kopidakis, X. Hao, Solar cell efficiency tables (version 57), Progress in Photovoltaics 29 (2021) 3–15. https://doi.org/10.1002/pip.3371.

[62] H. Jia, X. Cao, Z. Shao, S. Long, L. Jin, L. Ma, T. Chang, F. Xu, Y. Yang, S. Bao, P. Jin, Dual-response and Li+-insertion induced phase transition of VO2-based smart windows for selective visible and near-infrared light transmittance modulation, Solar Energy Materials and Solar Cells 200 (2019) 110045. https://doi.org/10.1016/j.solmat.2019.110045.

[63] M. Jurczyszyn, I. Morawski, J. Brona, M. Nowicki, Formation of Cu domains on Ru 10 1 ¯ 0 revealed by stereographic maps of elastically backscattered electrons, Thin Solid Films 537 (2013) 113–118. https://doi.org/10.1016/j.tsf.2013.04.025.

[64] H. Xie, S. López-Marino, T. Olar, Y. Sánchez, M. Neuschitzer, F. Oliva, S. Giraldo, V. Izquierdo-Roca, I. Lauermann, A. Pérez-Rodríguez, E. Saucedo, Impact of Na Dynamics at the $Cu_2ZnSn(S,Se)_4$/CdS Interface During Post Low Temperature Treatment of Absorbers, ACS Appl. Mater. Interfaces 8 (2016) 5017–5024. https://doi.org/10.1021/acsami.5b12243.

[65] T. Gershon, Y.S. Lee, P. Antunez, R. Mankad, S. Singh, D. Bishop, O. Gunawan, M. Hopstaken, R. Haight, Photovoltaic Materials and Devices Based on the Alloyed Kesterite Absorber $(Ag_x Cu_{1-x})_2 ZnSnSe_4$, Advanced Energy Materials 6 (2016) 1502468. https://doi.org/10.1002/aenm.201502468.

[66] T. Zhu, W.P. Huhn, G.C. Wessler, D. Shin, B. Saparov, D.B. Mitzi, V. Blum, I_2–II–IV–VI_4 (I = Cu, Ag; II = Sr, Ba; IV = Ge, Sn; VI = S, Se): Chalcogenides for Thin-Film Photovoltaics, Chem. Mater. 29 (2017) 7868–7879. https://doi.org/10.1021/acs.chemmater.7b02638.

[67] C.M. Sutter-Fella, J.A. Stückelberger, H. Hagendorfer, F. La Mattina, L. Kranz, S. Nishiwaki, A.R. Uhl, Y.E. Romanyuk, A.N. Tiwari, Sodium Assisted Sintering of Chalcogenides and Its Application to Solution Processed $Cu_2ZnSn(S,Se)_4$ Thin Film Solar Cells, Chem. Mater. 26 (2014) 1420–1425. https://doi.org/10.1021/cm403504u.

[68] I. Repins, C. Beall, N. Vora, C. DeHart, D. Kuciauskas, P. Dippo, B. To, J. Mann, W.-C. Hsu, A. Goodrich, R. Noufi, Co-evaporated Cu2ZnSnSe4 films and devices, Solar Energy Materials and Solar Cells 101 (2012) 154–159. https://doi.org/10.1016/j.solmat.2012.01.008.

[69] T. Maeda, A. Kawabata, T. Wada, First-principles study on alkali-metal effect of Li, Na, and K in Cu_2ZnSnS_4 and $Cu_2ZnSnSe_4$, Phys. Status Solidi C 12 (2015) 631–637. https://doi.org/10.1002/pssc.201400345.

[70] S.G. Haass, C. Andres, R. Figi, C. Schreiner, M. Bürki, Y.E. Romanyuk, A.N. Tiwari, Complex Interplay between Absorber Composition and Alkali Doping in High-Efficiency Kesterite Solar Cells, Advanced Energy Materials 8 (2018) 1701760. https://doi.org/10.1002/aenm.201701760.

[71] Y.E. Romanyuk, S.G. Haass, S. Giraldo, M. Placidi, D. Tiwari, D.J. Fermin, X. Hao, H. Xin, T. Schnabel, M. Kauk-Kuusik, P. Pistor, S. Lie, L.H. Wong, Doping and alloying of kesterites, J. Phys. Energy 1 (2019) 044004. https://doi.org/10.1088/2515-7655/ab23bc.

[72] S.G. Haass, M. Diethelm, C. Andres, Y.E. Romanyuk, A.N. Tiwari, Potassium post deposition treatment of solution-processed kesterite solar cells, Thin Solid Films 633 (2017) 131–134. https://doi.org/10.1016/j.tsf.2016.11.012.

[73] S.-Y. Kuo, M.-Y. Hsieh, Efficiency enhancement in Cu_2ZnSnS_4 solar cells with subwavelength grating nanostructures, Nanoscale 6 (2014) 7553–7559. https://doi.org/10.1039/C4NR00566J.

[74] S. Sakka, History of the Sol-Gel Chemistry and Technology, in: L. Klein, M. Aparicio, A. Jitianu (Eds.), Handbook of Sol-Gel Science and Technology, Springer International Publishing, Cham, 2018: pp. 3–29. https://doi.org/10.1007/978-3-319-32101-1_87.

[75] Studies in surface science and catalysis, in: Studies in Surface Science and Catalysis, Elsevier, 1999: pp. 261–268. https://doi.org/10.1016/S0167-2991(99)80316-4.

[76] Z. Su, K. Sun, Z. Han, H. Cui, F. Liu, Y. Lai, J. Li, X. Hao, Y. Liu, M.A. Green, Fabrication of Cu_2ZnSnS_4 solar cells with 5.1% efficiency via thermal decomposition and reaction using a non-toxic sol–gel route, J. Mater. Chem. A 2 (2014) 500–509. https://doi.org/10.1039/C3TA13533K.

[77] Z. Laghfour, S. Aazou, M. Taibi, G. Schmerber, A. Ulyashin, A. Dinia, A. Slaoui, M. Abd-Lefdil, Z. Sekkat, Sodium doping mechanism on sol-gel processed kesterite Cu2ZnSnS4 thin films, Superlattices and Microstructures 120 (2018) 747–752. https://doi.org/10.1016/j.spmi.2018.05.018.

[78] T. Todorov, H.W. Hillhouse, S. Aazou, Z. Sekkat, O. Vigil-Galán, S.D. Deshmukh, R. Agrawal, S. Bourdais, M. Valdés, P. Arnou, D.B. Mitzi, P.J. Dale, Solution-based synthesis of kesterite thin film semiconductors, J. Phys. Energy 2 (2020) 012003. https://doi.org/10.1088/2515-7655/ab3a81.

[79] M.V. Yakushev, M.A. Sulimov, J. Márquez-Prieto, I. Forbes, J. Krustok, P.R. Edwards, V.D. Zhivulko, O.M. Borodavchenko, A.V. Mudryi, R.W. Martin, Influence of the copper content on the optical properties of CZTSe thin films, Solar Energy Materials and Solar Cells 168 (2017) 69–77. https://doi.org/10.1016/j.solmat.2017.04.022.

[80] Y.B.K. Kumar, P.U. Bhaskar, G.S. Babu, V.S. Raja, Effect of copper salt and thiourea concentrations on the formation of Cu_2 $ZnSnS_4$ thin films by spray pyrolysis, Physica Status Solidi (a) 207 (2010) 149–156. https://doi.org/10.1002/pssa.200925194.

[81] Y. Gong, Y. Zhang, E. Jedlicka, R. Giridharagopal, J.A. Clark, W. Yan, C. Niu, R. Qiu, J. Jiang, S. Yu, S. Wu, H.W. Hillhouse, D.S. Ginger, W. Huang, H. Xin, Sn4+ precursor enables 12.4% efficient kesterite solar cell from DMSO solution with open circuit voltage deficit below 0.30 V, Sci. China Mater. 64 (2021) 52–60. https://doi.org/10.1007/s40843-020-1408-x.

[82] W. Wang, M.T. Winkler, O. Gunawan, T. Gokmen, T.K. Todorov, Y. Zhu, D.B. Mitzi, Device Characteristics of CZTSSe Thin-Film Solar Cells with 12.6% Efficiency, Advanced Energy Materials 4 (2014) 1301465. https://doi.org/10.1002/aenm.201301465.

[83] Y. Li, C. Cui, H. Wei, Z. Shao, Z. Wu, S. Zhang, X. Wang, S. Pang, G. Cui, Suppressing Element Inhomogeneity Enables 14.9% Efficiency CZTSSe Solar Cells, Advanced Materials 36 (2024) 2400138. https://doi.org/10.1002/adma.202400138.

[84] S.W. Shin, S.M. Pawar, C.Y. Park, J.H. Yun, J.-H. Moon, J.H. Kim, J.Y. Lee, Studies on Cu2ZnSnS4 (CZTS) absorber layer using different stacking orders in precursor thin films, Solar Energy Materials and Solar Cells 95 (2011) 3202–3206. https://doi.org/10.1016/j.solmat.2011.07.005.

[85] J. V Gohel, Effect of Type of Solvent on the Sol-Gel Spin Coated CZTS Thin Films, PAIJ 1 (2017). https://doi.org/10.15406/paij.2017.01.00023.

[86] H. Xin, J.K. Katahara, I.L. Braly, H.W. Hillhouse, 8% Efficient Cu_2 $ZnSn(S,Se)_4$ Solar Cells from Redox Equilibrated Simple Precursors in DMSO, Advanced Energy Materials 4 (2014) 1301823. https://doi.org/10.1002/aenm.201301823.

[87] J. Zhou, X. Xu, H. Wu, J. Wang, L. Lou, K. Yin, Y. Gong, J. Shi, Y. Luo, D. Li, H. Xin, Q. Meng, Control of the phase evolution of kesterite by tuning of the selenium partial pressure for solar cells with 13.8% certified efficiency, Nat Energy 8 (2023) 526–535. https://doi.org/10.1038/s41560-023-01251-6.

[88] Y. Gong, Q. Zhu, B. Li, S. Wang, B. Duan, L. Lou, C. Xiang, E. Jedlicka, R. Giridharagopal, Y. Zhou, Q. Dai, W. Yan, S. Chen, Q. Meng, H. Xin, Elemental de-mixing-induced epitaxial kesterite/CdS interface enabling 13%-efficiency kesterite solar cells, Nat Energy 7 (2022) 966–977. https://doi.org/10.1038/s41560-022-01132-4.

[89] J. Kumar, S. Ingole, Structural and optical properties of (AgxCu1-x)2ZnSnS4 thin films synthesised via solution route, Journal of Alloys and Compounds 727 (2017) 1089–1094. https://doi.org/10.1016/j.jallcom.2017.08.222.

[90] M. Dimitrievska, A. Fairbrother, X. Fontané, T. Jawhari, V. Izquierdo-Roca, E. Saucedo, A. Pérez-Rodríguez, Multiwavelength excitation Raman scattering study of polycrystalline kesterite Cu2ZnSnS4 thin films, Applied Physics Letters 104 (2014) 021901. https://doi.org/10.1063/1.4861593.

[91] J. Li, H. Shen, J. Chen, Y. Li, J. Yang, Growth mechanism of Ge-doped CZTSSe thin film by sputtering method and solar cells, Phys. Chem. Chem. Phys. 18 (2016) 28829–28834. https://doi.org/10.1039/C6CP05671G.
[92] M. Johnson, S.V. Baryshev, E. Thimsen, M. Manno, X. Zhang, I.V. Veryovkin, C. Leighton, E.S. Aydil, Alkali-metal-enhanced grain growth in Cu_2ZnSnS_4 thin films, Energy Environ. Sci. 7 (2014) 1931–1938. https://doi.org/10.1039/C3EE44130J.
[93] Y. Gong, Y. Zhang, Q. Zhu, Y. Zhou, R. Qiu, C. Niu, W. Yan, W. Huang, H. Xin, Identifying the origin of the V_{oc} deficit of kesterite solar cells from the two grain growth mechanisms induced by Sn^{2+} and Sn^{4+} precursors in DMSO solution, Energy Environ. Sci. 14 (2021) 2369–2380. https://doi.org/10.1039/D0EE03702H.
[94] M. Dimitrievska, G. Gurieva, H. Xie, A. Carrete, A. Cabot, E. Saucedo, A. Pérez-Rodríguez, S. Schorr, V. Izquierdo-Roca, Raman scattering quantitative analysis of the anion chemical composition in kesterite Cu2ZnSn(SxSe1−x)4 solid solutions, Journal of Alloys and Compounds 628 (2015) 464–470. https://doi.org/10.1016/j.jallcom.2014.12.175.
[95] S. Schorr, The crystal structure of kesterite type compounds: A neutron and X-ray diffraction study, Solar Energy Materials and Solar Cells 95 (2011) 1482–1488. https://doi.org/10.1016/j.solmat.2011.01.002.
[96] S. Agrawal, D.O. De Souza, C. Balasubramanian, S. Mukherjee, Effect of secondary phases controlled by precursor composition on the efficiency of CZTS thin film solar cell, Solar Energy Materials and Solar Cells 267 (2024) 112719. https://doi.org/10.1016/j.solmat.2024.112719.
[97] W. Wang, M.T. Winkler, O. Gunawan, T. Gokmen, T.K. Todorov, Y. Zhu, D.B. Mitzi, Device Characteristics of CZTSSe Thin-Film Solar Cells with 12.6% Efficiency, Advanced Energy Materials 4 (2014) 1301465. https://doi.org/10.1002/aenm.201301465.
[98] J. Guo, L. Wang, L. SiQin, C. Yang, Y. Wang, Y. Wang, S. Li, R. Liu, C. Zhu, H. Luan, CdS(In)/CZTSSe bandgap alignment engineering for performance enhancement of solar cells without ZnO layer, Solar Energy Materials and Solar Cells 269 (2024) 112787. https://doi.org/10.1016/j.solmat.2024.112787.
[99] C.J. Hages, M.J. Koeper, R. Agrawal, Optoelectronic and material properties of nanocrystal-based CZTSe absorbers with Ag-alloying, Solar Energy Materials and Solar Cells 145 (2016) 342–348. https://doi.org/10.1016/j.solmat.2015.10.039.
[100] Y.E. Romanyuk, S.G. Haass, S. Giraldo, M. Placidi, D. Tiwari, D.J. Fermin, X. Hao, H. Xin, T. Schnabel, M. Kauk-Kuusik, P. Pistor, S. Lie, L.H. Wong, Doping and alloying of kesterites, J. Phys. Energy 1 (2019) 044004. https://doi.org/10.1088/2515-7655/ab23bc.
[101] M. Valentini, C. Malerba, L. Serenelli, M. Izzi, E. Salza, M. Tucci, A. Mittiga, Fabrication of monolithic CZTS/Si tandem cells by development of the intermediate connection, Solar Energy 190 (2019) 414–419. https://doi.org/10.1016/j.solener.2019.08.029.
[102] I. Becerril-Romero, D. Sylla, M. Placidi, Y. Sánchez, J. Andrade-Arvizu, V. Izquierdo-Roca, M. Guc, A. Pérez-Rodríguez, S. Grini, L. Vines, B. Pusay, R. Almache, J. Puigdollers, P. Pistor, E. Saucedo, M. Espíndola-Rodríguez, Transition-Metal Oxides for Kesterite Solar Cells Developed on Transparent Substrates, ACS Appl. Mater. Interfaces 12 (2020) 33656–33669. https://doi.org/10.1021/acsami.0c06992.
[103] Y. Zhou, C. Xiang, Q. Dai, S. Xiang, R. Li, Y. Gong, Q. Zhu, W. Yan, W. Huang, H. Xin, 11.4% Efficiency Kesterite Solar Cells on Transparent Electrode, Advanced Energy Materials 13 (2023) 2300253. https://doi.org/10.1002/aenm.202300253.
[104] M.H. Sayed, J. Schoneberg, J. Parisi, L. Gütay, Influence of silver incorporation on CZTSSe solar cells grown by spray pyrolysis, Materials Science in Semiconductor Processing 76 (2018) 31–36. https://doi.org/10.1016/j.mssp.2017.12.007.
[105] L.P. Mwakyusa, L. Leist, M. Rinke, A. Welle, U.W. Paetzold, B.S. Richards, M. Hetterich, Impact of silver incorporation at the back contact of Kesterite solar cells on structural and device properties, Thin Solid Films 709 (2020) 138223. https://doi.org/10.1016/j.tsf.2020.138223.

[106] D. Palma-Lafuente, P. Diez-Silva, V. Rotaru, T. Jawhari, T. Bertram, P. Reyes-Figueroa, M. Guc, J.M. Merino, R. Caballero, Sulfurization of co-evaporated Cu2ZnGeSe4 layers: Influence of the precursor cation's ratios on the properties of Cu2ZnGe(S,Se)4 thin films, Solar Energy Materials and Solar Cells 254 (2023) 112243. https://doi.org/10.1016/j.solmat.2023.112243.

[107] A. Guchhait, Z. Su, Y.F. Tay, S. Shukla, W. Li, S.W. Leow, J.M.R. Tan, S. Lie, O. Gunawan, L.H. Wong, Enhancement of Open-Circuit Voltage of Solution-Processed Cu_2ZnSnS_4 Solar Cells with 7.2% Efficiency by Incorporation of Silver, ACS Energy Lett. 1 (2016) 1256–1261. https://doi.org/10.1021/acsenergylett.6b00509.

[108] M. Dimitrievska, F. Oliva, M. Guc, S. Giraldo, E. Saucedo, A. Pérez-Rodríguez, V. Izquierdo-Roca, Defect characterisation in $Cu_2ZnSnSe_4$ kesterites *via* resonance Raman spectroscopy and the impact on optoelectronic solar cell properties, J. Mater. Chem. A 7 (2019) 13293–13304. https://doi.org/10.1039/C9TA03625C.

[109] D. Payno, S. Kazim, S. Ahmad, Impact of cation substitution in all solution-processed $Cu_2(Cd, Zn)SnS_4$ superstrate solar cells, J. Mater. Chem. C 9 (2021) 17392–17400. https://doi.org/10.1039/D1TC04527J.

[110] J.J.S. Scragg, J.K. Larsen, M. Kumar, C. Persson, J. Sendler, S. Siebentritt, C. Platzer Björkman, Cu–Zn disorder and band gap fluctuations in $Cu_2ZnSn(S,Se)_4$: Theoretical and experimental investigations, Physica Status Solidi (b) 253 (2016) 247–254. https://doi.org/10.1002/pssb.201552530.

[111] D. Nowak, F. Atlan, D. Pareek, M. Guc, A. Perez-Rodriguez, V. Izquierdo-Roca, L. Gütay, Influence of the precursor composition on the resulting absorber properties and defect concentration in Cu2ZnSnSe4 absorbers, Solar Energy Materials and Solar Cells 256 (2023) 112342. https://doi.org/10.1016/j.solmat.2023.112342.

[112] J.A. Márquez, J.-P. Sun, H. Stange, H. Ali, L. Choubrac, S. Schäfer, C.J. Hages, K. Leifer, T. Unold, D.B. Mitzi, R. Mainz, High-temperature decomposition of Cu_2BaSnS_4 with Sn loss reveals newly identified compound $Cu_2Ba_3Sn_2S_8$, J. Mater. Chem. A 8 (2020) 11346–11353. https://doi.org/10.1039/D0TA02348E.

[113] V. Kheraj, K.K. Patel, S.J. Patel, D.V. Shah, Synthesis and characterisation of Copper Zinc Tin Sulphide (CZTS) compound for absorber material in solar-cells, Journal of Crystal Growth 362 (2013) 174–177. https://doi.org/10.1016/j.jcrysgro.2011.10.034.

[114] C.M. Sutter-Fella, J.A. Stückelberger, H. Hagendorfer, F. La Mattina, L. Kranz, S. Nishiwaki, A.R. Uhl, Y.E. Romanyuk, A.N. Tiwari, Sodium Assisted Sintering of Chalcogenides and Its Application to Solution Processed $Cu_2ZnSn(S,Se)_4$ Thin Film Solar Cells, Chem. Mater. 26 (2014) 1420–1425. https://doi.org/10.1021/cm403504u.

[115] C. Malerba, F. Biccari, C.L. Azanza Ricardo, M. Valentini, R. Chierchia, M. Müller, A. Santoni, E. Esposito, P. Mangiapane, P. Scardi, A. Mittiga, CZTS stoichiometry effects on the band gap energy, Journal of Alloys and Compounds 582 (2014) 528–534. https://doi.org/10.1016/j.jallcom.2013.07.199.

[116] M. Burgelman, P. Nollet, S. Degrave, Modelling polycrystalline semiconductor solar cells, Thin Solid Films 361–362 (2000) 527–532. https://doi.org/10.1016/S0040-6090(99)00825-1.

[117] L. Et-taya, T. Ouslimane, A. Benami, Numerical analysis of earth-abundant Cu2ZnSn(SxSe1-x)4 solar cells based on Spectroscopic Ellipsometry results by using SCAPS-1D, Solar Energy 201 (2020) 827–835. https://doi.org/10.1016/j.solener.2020.03.070.

[118] S.H. Zyoud, A.H. Zyoud, N.M. Ahmed, A.R. Prasad, S.N. Khan, A.F.I. Abdelkader, M. Shahwan, Numerical Modeling of High Conversion Efficiency FTO/ZnO/CdS/CZTS/MO Thin Film-Based Solar Cells: Using SCAPS-1D Software, Crystals 11 (2021) 1468. https://doi.org/10.3390/cryst11121468.

[119] G.E. Eperon, M.T. Hörantner, H.J. Snaith, Metal halide perovskite tandem and multiple-junction photovoltaics, Nat Rev Chem 1 (2017) 0095. https://doi.org/10.1038/s41570-017-0095.
[120] L. Et-taya, T. Ouslimane, A. Benami, Numerical analysis of earth-abundant Cu2ZnSn(SxSe1-x)4 solar cells based on Spectroscopic Ellipsometry results by using SCAPS-1D, Solar Energy 201 (2020) 827–835. https://doi.org/10.1016/j.solener.2020.03.070.
[121] A. Jimenez-Arguijo, A.G. Medaille, A. Navarro-Güell, M. Jimenez-Guerra, K.J. Tiwari, M. Placidi, M.S. Mkehlane, E. Iwuoha, A. Perez-Rodriguez, E. Saucedo, S. Giraldo, Z. Jehl Li-Kao, Setting the baseline for the modelling of Kesterite solar cells: The case study of tandem application, Solar Energy Materials and Solar Cells 251 (2023) 112109. https://doi.org/10.1016/j.solmat.2022.112109.
[122] E. Ojeda-Durán, K. Monfil-Leyva, J. Andrade-Arvizu, I. Becerril-Romero, Y. Sánchez, R. Fonoll-Rubio, M. Guc, Z.J. Li-Kao, J.A. Luna-López, E. Saucedo, High efficiency Cu_2ZnSnS_4 solar cells over FTO substrates and their CZTS/CdS interface passivation *via* thermal evaporation of Al_2O_3, J. Mater. Chem. C 9 (2021) 5356–5361. https://doi.org/10.1039/D1TC00880C.
[123] Z. Wang, C. Chen, K. Wu, H. Chong, H. Ye, Transparent Conductive Oxides and Their Applications in Near Infrared Plasmonics, Physica Status Solidi (a) 216 (2019) 1700794. https://doi.org/10.1002/pssa.201700794.
[124] M.A. Green, E.D. Dunlop, M. Yoshita, N. Kopidakis, K. Bothe, G. Siefer, X. Hao, Solar cell efficiency tables (version 62), Progress in Photovoltaics 31 (2023) 651–663. https://doi.org/10.1002/pip.3726.
[125] J. Chantana, Y. Kawano, T. Nishimura, A. Mavlonov, T. Minemoto, Impact of Urbach energy on open-circuit voltage deficit of thin-film solar cells, Solar Energy Materials and Solar Cells 210 (2020) 110502. https://doi.org/10.1016/j.solmat.2020.110502.
[126] Y. Gong, H. Xin, L. Ding, V_{oc} deficit in kesterite solar cells, J. Semicond. 42 (2021) 100201. https://doi.org/10.1088/1674-4926/42/10/100201.
[127] N. Benhaddou, S. Aazou, Y. Sánchez, J. Andrade-Arvizu, I. Becerril-Romero, M. Guc, S. Giraldo, V. Izquierdo-Roca, E. Saucedo, Z. Sekkat, Investigation on limiting factors affecting Cu2ZnGeSe4 efficiency: Effect of annealing conditions and surface treatment, Solar Energy Materials and Solar Cells 216 (2020) 110701. https://doi.org/10.1016/j.solmat.2020.110701.
[128] M. Valdés, A. Hernández, Y. Sánchez, R. Fonoll, M. Placidi, V. Izquierdo, A. Cabas-Vidani, M. Valentini, A. Mittiga, P. Pistor, C. Malerba, E. Saucedo, A new approach for alkali incorporation in Cu_2ZnSnS_4 solar cells, J. Phys. Energy 4 (2022) 044008. https://doi.org/10.1088/2515-7655/ac96a4.
[129] Z. Shen, S. Wang, Y. Liu, Y. Sun, J. Wu, H. Guo, K. Zhang, S. Zhang, F. Liu, Y. Zhang, Li2S doping into CZTSe drives the large improvement of VOC of solar cell, Journal of Energy Chemistry 62 (2021) 637–644. https://doi.org/10.1016/j.jechem.2021.04.018.
[130] A. Mule, B. Vermang, M. Sylvester, G. Brammertz, S. Ranjbar, T. Schnabel, N. Gampa, M. Meuris, J. Poortmans, Effect of different alkali (Li, Na, K, Rb, Cs) metals on Cu 2 ZnSnSe 4 solar cells, Thin Solid Films 633 (2017) 156–161. https://doi.org/10.1016/j.tsf.2016.11.027.
[131] N. Bansal, B.C. Mohanty, K. Singh, Diffusional investigation of alkali ions from composition tuned glass substrates to Mo-thin film for solar cell application, Surfaces and Interfaces 24 (2021) 101060. https://doi.org/10.1016/j.surfin.2021.101060.
[132] Y. Gong, A. Jimenez-Arguijo, A.G. Medaille, S. Moser, A. Basak, R. Scaffidi, R. Carron, D. Flandre, B. Vermang, S. Giraldo, H. Xin, A. Perez-Rodriguez, E. Saucedo, Li-Doping and Ag-Alloying Interplay Shows the Pathway for Kesterite Solar Cells with Efficiency Over 14%, Adv Funct Materials (2024) 2404669. https://doi.org/10.1002/adfm.202404669.

[133] W. Li, Z. Su, J.M.R. Tan, S.Y. Chiam, H.L. Seng, S. Magdassi, L.H. Wong, Revealing the Role of Potassium Treatment in CZTSSe Thin Film Solar Cells, Chem. Mater. 29 (2017) 4273–4281. https://doi.org/10.1021/acs.chemmater.7b00418.
[134] G. Tseberlidis, V. Trifiletti, A. Le Donne, L. Frioni, M. Acciarri, S. Binetti, Kesterite solar-cells by drop-casting of inorganic sol–gel inks, Solar Energy 208 (2020) 532–538. https://doi.org/10.1016/j.solener.2020.07.093.
[135] H. Xin, S.M. Vorpahl, A.D. Collord, I.L. Braly, A.R. Uhl, B.W. Krueger, D.S. Ginger, H.W. Hillhouse, Lithium-doping inverts the nanoscale electric field at the grain boundaries in $Cu_2ZnSn(S,Se)_4$ and increases photovoltaic efficiency, Phys. Chem. Chem. Phys. 17 (2015) 23859–23866. https://doi.org/10.1039/C5CP04707B.
[136] J. Xu, S. Shang, J. Yang, J. Liu, S. Jiang, Effect of sodium-doping on the performance of CZTS absorb layer: Single and bifacial sodium-incorporation method, Solar Energy 221 (2021) 476–482. https://doi.org/10.1016/j.solener.2021.04.063.
[137] A. Ruiz-Perona, M. Guc, Y. Sánchez, T. Kodalle, J.M. Merino, M. León, R. Caballero, Wide band gap Cu2ZnGe(S,Se)4 thin films and solar cells: Influence of Na content and incorporation method, Solar Energy 226 (2021) 251–259. https://doi.org/10.1016/j.solener.2021.08.032.
[138] H.R. Jung, S.W. Shin, K.V. Gurav, M.P. Suryawanshi, C.W. Hong, H.S. Yang, J.Y. Lee, J.H. Moon, J.H. Kim, Phase evolution of Cu2ZnSnS4 (CZTS) kesterite thin films during the sulfurization process, Ceramics International 41 (2015) 13006–13011. https://doi.org/10.1016/j.ceramint.2015.06.145.
[139] A. Wang, J. Huang, J. Cong, X. Yuan, M. He, J. Li, C. Yan, X. Cui, N. Song, S. Zhou, M.A. Green, K. Sun, X. Hao, Cd-Free Pure Sulfide Kesterite Cu_2ZnSnS_4 Solar Cell with Over 800 mV Open-Circuit Voltage Enabled by Phase Evolution Intervention, Advanced Materials 36 (2024) 2307733. https://doi.org/10.1002/adma.202307733.
[140] Y.E. Romanyuk, S.G. Haass, S. Giraldo, M. Placidi, D. Tiwari, D.J. Fermin, X. Hao, H. Xin, T. Schnabel, M. Kauk-Kuusik, P. Pistor, S. Lie, L.H. Wong, Doping and alloying of kesterites, J. Phys. Energy 1 (2019) 044004. https://doi.org/10.1088/2515-7655/ab23bc.
[141] W. Li, X. Liu, H. Cui, S. Huang, X. Hao, The role of Ag in (Ag,Cu)2ZnSnS4 thin film for solar cell application, Journal of Alloys and Compounds 625 (2015) 277–283. https://doi.org/10.1016/j.jallcom.2014.11.136.
[142] W.-C. Huang, S.-Y. Wei, C.-H. Cai, W.-H. Ho, C.-H. Lai, The role of Ag in aqueous solution processed $(Ag,Cu)_2ZnSn(S,Se)_4$ kesterite solar cells: antisite defect elimination and importance of Na passivation, J. Mater. Chem. A 6 (2018) 15170–15181. https://doi.org/10.1039/C8TA02950D.
[143] X. Yuan, J. Li, K. Sun, J. Huang, X. Cui, A. Wang, B. Xie, B. Hoex, M. Green, X. Hao, Improved carrier collection efficiency in CZTS solar cells by Li-enhanced liquid-phase-assisted grain growth, EcoEnergy 2 (2024) 181–191. https://doi.org/10.1002/ece2.31.
[144] B. Kim, C. Levard, M. Murayama, G.E. Brown, M.F. Hochella, Integrated Approaches of X-Ray Absorption Spectroscopic and Electron Microscopic Techniques on Zinc Speciation and Characterization in a Final Sewage Sludge Product, J. Environ. Qual. 43 (2014) 908–916. https://doi.org/10.2134/jeq2013.10.0418.
[145] M. Valentini, C. Malerba, F. Menchini, D. Tedeschi, A. Polimeni, M. Capizzi, A. Mittiga, Effect of the order-disorder transition on the optical properties of Cu2ZnSnS4, Applied Physics Letters 108 (2016) 211909. https://doi.org/10.1063/1.4952973.
[146] C.J. Hages, M.J. Koeper, R. Agrawal, Optoelectronic and material properties of nanocrystal-based CZTSe absorbers with Ag-alloying, Solar Energy Materials and Solar Cells 145 (2016) 342–348. https://doi.org/10.1016/j.solmat.2015.10.039.
[147] L.P. Mwakyusa, L. Leist, M. Rinke, A. Welle, U.W. Paetzold, B.S. Richards, M. Hetterich, Impact of silver incorporation at the back contact of Kesterite solar cells on structural and device properties, Thin Solid Films 709 (2020) 138223. https://doi.org/10.1016/j.tsf.2020.138223.

[148] Z. Laghfour, S. Aazou, M. Taibi, G. Schmerber, A. Ulyashin, A. Dinia, A. Slaoui, M. Abd-Lefdil, Z. Sekkat, Sodium doping mechanism on sol-gel processed kesterite Cu2ZnSnS4 thin films, Superlattices and Microstructures 120 (2018) 747–752. https://doi.org/10.1016/j.spmi.2018.05.018.
[149] L. De La Cueva, Y. Sánchez, L. Calvo-Barrio, F. Oliva, V. Izquierdo-Roca, S. Khelifi, T. Bertram, J.M. Merino, M. León, R. Caballero, Sulfurization of co-evaporated Cu2ZnSnSe4 thin film solar cells: The role of Na, Solar Energy Materials and Solar Cells 186 (2018) 115–123. https://doi.org/10.1016/j.solmat.2018.06.015.
[150] Y. Mao, J. Guo, C. Cao, J. Ao, F. Liu, Y. Zhang, Eliminating cracking morphology of solution-processed CZTSSe absorbers by Sn-rich composition engineering, Materials Science in Semiconductor Processing 159 (2023) 107388. https://doi.org/10.1016/j.mssp.2023.107388.
[151] Z. Shen, S. Wang, Y. Liu, Y. Sun, J. Wu, H. Guo, K. Zhang, S. Zhang, F. Liu, Y. Zhang, Li2S doping into CZTSe drives the large improvement of VOC of solar cell, Journal of Energy Chemistry 62 (2021) 637–644. https://doi.org/10.1016/j.jechem.2021.04.018.
[152] M. He, X. Zhang, J. Huang, J. Li, C. Yan, J. Kim, Y. Chen, L. Yang, J.M. Cairney, Y. Zhang, S. Chen, J. Kim, M.A. Green, X. Hao, High Efficiency $Cu_2ZnSn(S,Se)_4$ Solar Cells with Shallow Li_{Zn} Acceptor Defects Enabled by Solution-Based Li Post-Deposition Treatment, Advanced Energy Materials 11 (2021) 2003783. https://doi.org/10.1002/aenm.202003783.
[153] D.S. Dhawale, A. Ali, A.C. Lokhande, Impact of various dopant elements on the properties of kesterite compounds for solar cell applications: a status review, Sustainable Energy Fuels 3 (2019) 1365–1383. https://doi.org/10.1039/C9SE00040B.
[154] J. Kumar, S. Ingole, Structural and optical properties of (AgxCu1-x)2ZnSnS4 thin films synthesised via solution route, Journal of Alloys and Compounds 727 (2017) 1089–1094. https://doi.org/10.1016/j.jallcom.2017.08.222.
[155] A. Xu, X. Li, H. Liu, C. Xiang, C. Ma, Y. Li, X. Pan, W. Yan, S. Wang, W. Huang, H. Xin, Over 10% Efficiency Pure Sulfide Kesterite Solar Cells on Transparent Electrode with Cd–Ag Co-Alloying, Small (2024) 2407075. https://doi.org/10.1002/smll.202407075.
[156] J.M. Ball, S.D. Stranks, M.T. Hörantner, S. Hüttner, W. Zhang, E.J.W. Crossland, I. Ramirez, M. Riede, M.B. Johnston, R.H. Friend, H.J. Snaith, Optical properties and limiting photocurrent of thin-film perovskite solar cells, Energy Environ. Sci. 8 (2015) 602–609. https://doi.org/10.1039/C4EE03224A.
[157] K.J. Tiwari, S. Giraldo, M. Placidi, A. Gon Medaille, A. Thomere, S. Resalati, E. Saucedo, Z. Jehl Li-Kao, Feasibility of a Full Chalcopyrite Tandem Solar Cell: A Quantitative Numerical Approach, Solar RRL 5 (2021) 2100202. https://doi.org/10.1002/solr.202100202.
[158] X. Luo, D. Tsai, M. Gu, M. Hong, Subwavelength interference of light on structured surfaces, Adv. Opt. Photon. 10 (2018) 757. https://doi.org/10.1364/AOP.10.000757.
[159] A.J.N. Oliveira, J.P. Teixeira, D. Ramos, P.A. Fernandes, P.M.P. Salomé, Exploiting the Optical Limits of Thin-Film Solar Cells: A Review on Light Management Strategies in $Cu(In,Ga)Se_2$, Advanced Photonics Research 3 (2022) 2100190. https://doi.org/10.1002/adpr.202100190.
[160] S. Reynolds, V. Smirnov, Modelling of two-and four-terminal thin-film silicon tandem solar cells, J. Phys.: Conf. Ser. 398 (2012) 012006. https://doi.org/10.1088/1742-6596/398/1/012006.
[161] M.A. Green, E.D. Dunlop, M. Yoshita, N. Kopidakis, K. Bothe, G. Siefer, X. Hao, J.Y. Jiang, Solar Cell Efficiency Tables (Version 65), Progress in Photovoltaics 33 (2025) 3–15. https://doi.org/10.1002/pip.3867.
[162] M.A. Green, E.D. Dunlop, M. Yoshita, N. Kopidakis, K. Bothe, G. Siefer, X. Hao, Solar cell efficiency tables (version 62), Progress in Photovoltaics 31 (2023) 651–663. https://doi.org/10.1002/pip.3726.

[163] J. Mattheis, U. Rau, J.H. Werner, Light absorption and emission in semiconductors with band gap fluctuations—A study on Cu(In,Ga)Se2 thin films, Journal of Applied Physics 101 (2007) 113519. https://doi.org/10.1063/1.2721768.
[164] S. Yadav, M.A. Kareem, H.K. Kodali, D. Agarwal, A. Garg, A. Verma, K.S. Nalwa, Optoelectronic modeling of all-perovskite tandem solar cells with design rules to achieve >30% efficiency, Solar Energy Materials and Solar Cells 242 (2022) 111780. https://doi.org/10.1016/j.solmat.2022.111780.
[165] R. Cariou, J. Benick, P. Beutel, N. Razek, C. Flotgen, M. Hermle, D. Lackner, S.W. Glunz, A.W. Bett, M. Wimplinger, F. Dimroth, Monolithic Two-Terminal III–V//Si Triple-Junction Solar Cells With 30.2% Efficiency Under 1-Sun AM1.5g, IEEE J. Photovoltaics 7 (2017) 367–373. https://doi.org/10.1109/JPHOTOV.2016.2629840.
[166] S. Essig, C. Allebé, T. Remo, J.F. Geisz, M.A. Steiner, K. Horowitz, L. Barraud, J.S. Ward, M. Schnabel, A. Descoeudres, D.L. Young, M. Woodhouse, M. Despeisse, C. Ballif, A. Tamboli, Raising the one-sun conversion efficiency of III–V/Si solar cells to 32.8% for two junctions and 35.9% for three junctions, Nat Energy 2 (2017) 17144. https://doi.org/10.1038/nenergy.2017.144.
[167] N. Jain, K.L. Schulte, J.F. Geisz, D.J. Friedman, R.M. France, E.E. Perl, A.G. Norman, H.L. Guthrey, M.A. Steiner, High-efficiency inverted metamorphic 1.7/1.1 eV GaInAsP/GaInAs dual-junction solar cells, Appl. Phys. Lett. 112 (2018) 053905. https://doi.org/10.1063/1.5008517.
[168] R. Lin, K. Xiao, Z. Qin, Q. Han, C. Zhang, M. Wei, M.I. Saidaminov, Y. Gao, J. Xu, M. Xiao, A. Li, J. Zhu, E.H. Sargent, H. Tan, Monolithic all-perovskite tandem solar cells with 24.8% efficiency exploiting comproportionation to suppress Sn(ii) oxidation in precursor ink, Nat Energy 4 (2019) 864–873. https://doi.org/10.1038/s41560-019-0466-3.
[169] C. Battaglia, S.M. De Nicolás, S. De Wolf, X. Yin, M. Zheng, C. Ballif, A. Javey, Silicon heterojunction solar cell with passivated hole selective MoOx contact, Applied Physics Letters 104 (2014) 113902. https://doi.org/10.1063/1.4868880.
[170] S.P. Bremner, M.Y. Levy, C.B. Honsberg, Analysis of tandem solar cell efficiencies under AM1.5G spectrum using a rapid flux calculation method, Prog. Photovolt: Res. Appl. 16 (2008) 225–233. https://doi.org/10.1002/pip.799.
[171] X. Wu, D. Wu, G. Cui, Z. Jiang, C. Zhao, X. Tang, X. Dong, N. Liu, Z. Zuo, L. Kong, M. Gu, Exceeding 20% Efficiency for Highly Efficient and Stable Inverted Perovskite Solar Cells via Sodium Borohydride Induced Interface Engineering, Solar RRL 7 (2023) 2200833. https://doi.org/10.1002/solr.202200833.
[172] M. Jeong, I.W. Choi, E.M. Go, Y. Cho, M. Kim, B. Lee, S. Jeong, Y. Jo, H.W. Choi, J. Lee, J.-H. Bae, S.K. Kwak, D.S. Kim, C. Yang, Stable perovskite solar cells with efficiency exceeding 24.8% and 0.3-V voltage loss, Science 369 (2020) 1615–1620. https://doi.org/10.1126/science.abb7167.
[173] K.A. Bush, A.F. Palmstrom, Z.J. Yu, M. Boccard, R. Cheacharoen, J.P. Mailoa, D.P. McMeekin, R.L.Z. Hoye, C.D. Bailie, T. Leijtens, I.M. Peters, M.C. Minichetti, N. Rolston, R. Prasanna, S. Sofia, D. Harwood, W. Ma, F. Moghadam, H.J. Snaith, T. Buonassisi, Z.C. Holman, S.F. Bent, M.D. McGehee, 23.6%-efficient monolithic perovskite/silicon tandem solar cells with improved stability, Nat Energy 2 (2017) 17009. https://doi.org/10.1038/nenergy.2017.9.
[174] G. Tseberlidis, V. Di Palma, V. Trifiletti, L. Frioni, M. Valentini, C. Malerba, A. Mittiga, M. Acciarri, S.O. Binetti, Titania as Buffer Layer for Cd-Free Kesterite Solar Cells, ACS Materials Lett. 5 (2023) 219–224. https://doi.org/10.1021/acsmaterialslett.2c00933.
[175] J.W. Garland, T. Biegala, M. Carmody, C. Gilmore, S. Sivananthan, Next-generation multijunction solar cells: The promise of II-VI materials, Journal of Applied Physics 109 (2011) 102423. https://doi.org/10.1063/1.3582902.

[176] K. Tsuji, T. Maeda, T. Wada, Optical properties and electronic structures of Cu_2ZnSnS_4, Cu_2ZnGeS_4, and $Cu_2Zn(Ge,Sn)S_4$ and $Cu_2Zn(Ge,Sn)Se_4$ solid solutions, Jpn. J. Appl. Phys. 57 (2018) 08RC21. https://doi.org/10.7567/JJAP.57.08RC21.

[177] N. Saini, N.M. Martin, J.K. Larsen, A. Hultqvist, T. Törndahl, C. Platzer-Björkman, Record 1.1 V Open-Circuit Voltage for Cu_2ZnGeS_4-Based Thin-Film Solar Cells Using Atomic Layer Deposition $Zn_{1-x}Sn_xO_y$ Buffer Layers, Solar RRL 6 (2022) 2100837. https://doi.org/10.1002/solr.202100837.

[178] A.A. Kistanov, W. Cao, M. Huttula, S.Kh. Khadiullin, E.A. Korznikova, A. Smirnov, X. Wang, S. Zhuk, Impact of various dopant elements on the electronic structure of Cu_2ZnSnS_4 (CZTS) thin films: a DFT study, CrystEngComm 22 (2020) 5786–5791. https://doi.org/10.1039/D0CE00802H.

[179] C. Yan, J. Huang, K. Sun, S. Johnston, Y. Zhang, H. Sun, A. Pu, M. He, F. Liu, K. Eder, L. Yang, J.M. Cairney, N.J. Ekins-Daukes, Z. Hameiri, J.A. Stride, S. Chen, M.A. Green, X. Hao, Cu2ZnSnS4 solar cells with over 10% power conversion efficiency enabled by heterojunction heat treatment, Nat Energy 3 (2018) 764–772. https://doi.org/10.1038/s41560-018-0206-0.

[180] A. Hajijafarassar, F. Martinho, F. Stulen, S. Grini, S. López-Mariño, M. Espíndola-Rodríguez, M. Döbeli, S. Canulescu, E. Stamate, M. Gansukh, S. Engberg, A. Crovetto, L. Vines, J. Schou, O. Hansen, Monolithic thin-film chalcogenide–silicon tandem solar cells enabled by a diffusion barrier, Solar Energy Materials and Solar Cells 207 (2020) 110334. https://doi.org/10.1016/j.solmat.2019.110334.

[181] S. Zhuk, T.K.S. Wong, M. Petrović, E. Kymakis, S.S. Hadke, S. Lie, L.H. Wong, P. Sonar, A. Dey, S. Krishnamurthy, G.K. Dalapati, Solution-Processed Pure Sulfide $Cu_2(Zn_{0.6}Cd_{0.4})SnS_4$ Solar Cells with Efficiency 10.8% Using Ultrathin CuO Intermediate Layer, Solar RRL 4 (2020) 2000293. https://doi.org/10.1002/solr.202000293.

[182] S. Giraldo, Z. Jehl, M. Placidi, V. Izquierdo-Roca, A. Pérez-Rodríguez, E. Saucedo, Progress and Perspectives of Thin Film Kesterite Photovoltaic Technology: A Critical Review, Adv. Mater. 31 (2019) 1806692. https://doi.org/10.1002/adma.201806692.

[183] L. Sravani, S. Routray, M. Courel, K.P. Pradhan, Loss mechanisms in CZTS and CZTSe Kesterite thin-film solar cells: Understanding the complexity of defect density, Solar Energy 227 (2021) 56–66. https://doi.org/10.1016/j.solener.2021.08.052.

[184] N. Benhaddou, S. Aazou, R. Fonoll-Rubio, Y. Sánchez, S. Giraldo, M. Guc, L. Calvo-Barrio, V. Izquierdo-Roca, M. Abd-Lefdil, Z. Sekkat, E. Saucedo, Uncovering details behind the formation mechanisms of $Cu_2ZnGeSe_4$ photovoltaic absorbers, J. Mater. Chem. C 8 (2020) 4003–4011. https://doi.org/10.1039/C9TC06728K.

[185] M. Kauk-Kuusik, K. Timmo, K. Muska, M. Pilvet, J. Krustok, R. Josepson, G. Brammertz, B. Vermang, M. Danilson, M. Grossberg, Detailed Insight into the CZTS/CdS Interface Modification by Air Annealing in Monograin Layer Solar Cells, ACS Appl. Energy Mater. 4 (2021) 12374–12382. https://doi.org/10.1021/acsaem.1c02186.

[186] K.S. Gour, R. Parmar, R. Kumar, V.N. Singh, Cd-Free Zn(O,S) as Alternative Buffer Layer for Chalcogenide and Kesterite Based Thin Films Solar Cells: A Review, J Nanosci Nanotechnol 20 (2020) 3622–3635. https://doi.org/10.1166/jnn.2020.17537.

[187] N.M. Martin, T. Törndahl, M. Babucci, F. Larsson, K. Simonov, D. Gajdek, L.R. Merte, H. Rensmo, C. Platzer-Björkman, Atomic Layer Grown Zinc–Tin Oxide as an Alternative Buffer Layer for Cu_2ZnSnS_4-Based Thin Film Solar Cells: Influence of Absorber Surface Treatment on Buffer Layer Growth, ACS Appl. Energy Mater. 5 (2022) 13971–13980. https://doi.org/10.1021/acsaem.2c02579.

[188] J. Löckinger, S. Nishiwaki, T.P. Weiss, B. Bissig, Y.E. Romanyuk, S. Buecheler, A.N. Tiwari, TiO2 as intermediate buffer layer in Cu(In,Ga)Se2 solar cells, Solar Energy Materials and Solar Cells 174 (2018) 397–404. https://doi.org/10.1016/j.solmat.2017.09.030.

[189] H. Bencherif, L. Dehimi, N. Mahsar, E. Kouriche, F. Pezzimenti, Modeling and optimization of CZTS kesterite solar cells using TiO2 as efficient electron transport layer, Materials

Science and Engineering: B 276 (2022) 115574. https://doi.org/10.1016/j.mseb.2021.115574.
[190] Sadanand, D.K. Dwivedi, Numerical modeling for earth-abundant highly efficient solar photovoltaic cell of non-toxic buffer layer, Optical Materials 109 (2020) 110409. https://doi.org/10.1016/j.optmat.2020.110409.
[191] S. Avasthi, W.E. McClain, G. Man, A. Kahn, J. Schwartz, J.C. Sturm, Hole-blocking titanium-oxide/silicon heterojunction and its application to photovoltaics, Applied Physics Letters 102 (2013) 203901. https://doi.org/10.1063/1.4803446.
[192] R. Singh, M. Kumar, M. Saini, A. Singh, B. Satpati, T. Som, Growth of TiO2 thin films on chemically textured Si for solar cell applications as a hole-blocking and antireflection layer, Applied Surface Science 418 (2017) 225–231. https://doi.org/10.1016/j.apsusc.2017.01.307.
[193] A.D. Adewoyin, M.A. Olopade, O.O. Oyebola, M.A. Chendo, Development of CZTGS/CZTS tandem thin film solar cell using SCAPS-1D, Optik 176 (2019) 132–142. https://doi.org/10.1016/j.ijleo.2018.09.033.
[194] T. AlZoubi, A. Moghrabi, M. Moustafa, S. Yasin, Efficiency boost of CZTS solar cells based on double-absorber architecture: Device modeling and analysis, Solar Energy 225 (2021) 44–52. https://doi.org/10.1016/j.solener.2021.07.012.
[195] F. Belarbi, W. Rahal, D. Rached, S. benghabrit, M. Adnane, A comparative study of different buffer layers for CZTS solar cell using Scaps-1D simulation program, Optik 216 (2020) 164743. https://doi.org/10.1016/j.ijleo.2020.164743.
[196] M. Patel, A. Ray, Enhancement of output performance of Cu2ZnSnS4 thin film solar cells—A numerical simulation approach and comparison to experiments, Physica B: Condensed Matter 407 (2012) 4391–4397. https://doi.org/10.1016/j.physb.2012.07.042.
[197] O.K. Simya, A. Mahaboobbatcha, K. Balachander, A comparative study on the performance of Kesterite based thin film solar cells using SCAPS simulation program, Superlattices and Microstructures 82 (2015) 248–261. https://doi.org/10.1016/j.spmi.2015.02.020.
[198] C.A. Benisha, S. Routray, Performance Enhancement of Kesterite Solar Cell with Doped-Silicon Back Surface Field Layer, Silicon 14 (2022) 8045–8054. https://doi.org/10.1007/s12633-021-01583-6.
[199] A. Jimenez-Arguijo, A.G. Medaille, A. Navarro-Güell, M. Jimenez-Guerra, K.J. Tiwari, M. Placidi, M.S. Mkehlane, E. Iwuoha, A. Perez-Rodriguez, E. Saucedo, S. Giraldo, Z. Jehl Li-Kao, Setting the baseline for the modelling of Kesterite solar cells: The case study of tandem application, Solar Energy Materials and Solar Cells 251 (2023) 112109. https://doi.org/10.1016/j.solmat.2022.112109.
[200] S. Kim, J.A. Márquez, T. Unold, A. Walsh, Upper limit to the photovoltaic efficiency of imperfect crystals from first principles, Energy Environ. Sci. 13 (2020) 1481–1491. https://doi.org/10.1039/D0EE00291G.
[201] P. Kanti Basu, Z. Hameiri, D. Sarangi, J. Cunnusamy, E. Carmona, M.B. Boreland, 18.7% Efficient inline-diffused screen-printed silicon wafer solar cells with deep homogeneous emitter etch-back, Solar Energy Materials and Solar Cells 117 (2013) 412–420. https://doi.org/10.1016/j.solmat.2013.06.046.
[202] J. Lauwaert, Fill Factor Loss in a Recombination Junction for Monolithic Tandem Solar Cells, ACS Appl. Energy Mater. 6 (2023) 4211–4218. https://doi.org/10.1021/acsaem.3c00041.
[203] K. Kim, J. Gwak, S.K. Ahn, Y.-J. Eo, J.H. Park, J.-S. Cho, M.G. Kang, H.-E. Song, J.H. Yun, Simulations of chalcopyrite/c-Si tandem cells using SCAPS-1D, Solar Energy 145 (2017) 52–58. https://doi.org/10.1016/j.solener.2017.01.031.
[204] K. Kim, J.S. Yoo, S.K. Ahn, Y.-J. Eo, J.-S. Cho, J. Gwak, J.H. Yun, Performance prediction of chalcopyrite-based dual-junction tandem solar cells, Solar Energy 155 (2017) 167–177. https://doi.org/10.1016/j.solener.2017.05.080.

[205] M. Atowar Rahman, Enhancing the photovoltaic performance of Cd-free Cu2ZnSnS4 heterojunction solar cells using SnS HTL and TiO2 ETL, Solar Energy 215 (2021) 64–76. https://doi.org/10.1016/j.solener.2020.12.020.
[206] G.K. Gupta, A. Dixit, Theoretical studies of single and tandem Cu2ZnSn(S/Se)4 junction solar cells for enhanced efficiency, Optical Materials 82 (2018) 11–20. https://doi.org/10.1016/j.optmat.2018.05.030.
[207] Md.S. Rana, Md.M. Islam, M. Julkarnain, Enhancement in efficiency of CZTS solar cell by using CZTSe BSF layer, Solar Energy 226 (2021) 272–287. https://doi.org/10.1016/j.solener.2021.08.035.
[208] P.K. Kannan, M. Anandkumar, A theoretical investigation to boost the efficiency of CZTS solar cells using SCAPS-1D, Optik 288 (2023) 171214. https://doi.org/10.1016/j.ijleo.2023.171214.
[209] M. Kauk-Kuusik, K. Timmo, K. Muska, M. Pilvet, J. Krustok, M. Danilson, V. Mikli, R. Josepson, M. Grossberg-Kuusk, Reduced recombination through CZTS/CdS interface engineering in monograin layer solar cells, J. Phys. Energy 4 (2022) 024007. https://doi.org/10.1088/2515-7655/ac618d.
[210] M. De Bastiani, A.S. Subbiah, E. Aydin, F.H. Isikgor, T.G. Allen, S. De Wolf, Recombination junctions for efficient monolithic perovskite-based tandem solar cells: physical principles, properties, processing and prospects, Mater. Horiz. 7 (2020) 2791–2809. https://doi.org/10.1039/D0MH00990C.
[211] S. Adachi, Properties of group-IV, III-V and II-VI semiconductors, John Wiley & Sons, Ltd, Chichester, West Sussex, England, 2006.
[212] S. Adachi, Earth-abundant materials for solar cells: Cu2-II-IV-VI4 semiconductors, John Wiley & Sons, Inc, Chichester, West Sussex, United Kingdom, 2015.
[213] M. Elbar, S. Tobbeche, A. Merazga, Effect of top-cell CGS thickness on the performance of CGS/CIGS tandem solar cell, Solar Energy 122 (2015) 104–112. https://doi.org/10.1016/j.solener.2015.08.029.
[214] S. Ho Song, E.S. Aydil, S.A. Campbell, Metal-oxide broken-gap tunnel junction for copper indium gallium diselenide tandem solar cells, Solar Energy Materials and Solar Cells 133 (2015) 133–142. https://doi.org/10.1016/j.solmat.2014.10.046.
[215] M. Al-Hattab, E. Oublal, Y. Chrafih, L. Moudou, O. Bajjou, M. Sahal, K. Rahmani, Novel Simulation and Efficiency Enhancement of Eco-friendly Cu2FeSnS4/c-Silicon Tandem Solar Device, Silicon (2023). https://doi.org/10.1007/s12633-023-02582-5.
[216] K. Kim, J.S. Yoo, S.K. Ahn, Y.-J. Eo, J.-S. Cho, J. Gwak, J.H. Yun, Performance prediction of chalcopyrite-based dual-junction tandem solar cells, Solar Energy 155 (2017) 167–177. https://doi.org/10.1016/j.solener.2017.05.080.
[217] C. Persson, Electronic and optical properties of Cu2ZnSnS4 and Cu2ZnSnSe4, Journal of Applied Physics 107 (2010) 053710. https://doi.org/10.1063/1.3318468.
[218] S. Bag, O. Gunawan, T. Gokmen, Y. Zhu, D.B. Mitzi, Hydrazine-Processed Ge-Substituted CZTSe Solar Cells, Chem. Mater. 24 (2012) 4588–4593. https://doi.org/10.1021/cm302881g.
[219] K. Biswas, S. Lany, A. Zunger, The electronic consequences of multivalent elements in inorganic solar absorbers: Multivalency of Sn in Cu2ZnSnS4, Appl. Phys. Lett. 96 (2010) 201902. https://doi.org/10.1063/1.3427433.
[220] S.I. Swati, R. Matin, S. Bashar, Z.H. Mahmood, Experimental study of the optical properties of Cu_2ZnSnS_4 thin film absorber layer for solar cell application, J. Phys.: Conf. Ser. 1086 (2018) 012010. https://doi.org/10.1088/1742-6596/1086/1/012010.
[221] Z. Wang, Z. Song, Y. Yan, S. (Frank) Liu, D. Yang, Perovskite—a Perfect Top Cell for Tandem Devices to Break the S–Q Limit, Adv. Sci. 6 (2019) 1801704. https://doi.org/10.1002/advs.201801704.

[222] S. Kim, K.M. Kim, H. Tampo, H. Shibata, S. Niki, Improvement of voltage deficit of Ge-incorporated kesterite solar cell with 12.3% conversion efficiency, Appl. Phys. Express 9 (2016) 102301. https://doi.org/10.7567/APEX.9.102301.
[223] I. Anefnaf, S. Aazou, Y. Sánchez, P. Vidal-Fuentes, R. Fonoll-Rubio, K.J. Tiwari, S. Giraldo, Z.J. Li-Kao, J. Andrade-Arvizu, M. Guc, E. Saucedo, Z. Sekkat, Insights on the limiting factors of Cu2ZnGeSe4 based solar cells, Solar Energy Materials and Solar Cells 227 (2021) 111106. https://doi.org/10.1016/j.solmat.2021.111106.
[224] L. Choubrac, G. Brammertz, N. Barreau, L. Arzel, S. Harel, M. Meuris, B. Vermang, 7.6% CZGSe Solar Cells Thanks to Optimized CdS Chemical Bath Deposition, Phys. Status Solidi A 215 (2018) 1800043. https://doi.org/10.1002/pssa.201800043.
[225] A. Ruiz-Perona, M. Guc, Y. Sánchez, T. Kodalle, J.M. Merino, M. León, R. Caballero, Wide band gap Cu2ZnGe(S,Se)4 thin films and solar cells: Influence of Na content and incorporation method, Solar Energy 226 (2021) 251–259. https://doi.org/10.1016/j.solener.2021.08.032.
[226] T. Schnabel, M. Seboui, E. Ahlswede, Evaluation of different metal salt solutions for the preparation of solar cells with wide-gap $Cu_2ZnGeS_xSe_{4-x}$ absorbers, RSC Adv. 7 (2017) 26–30. https://doi.org/10.1039/C6RA23068G.
[227] T. Schnabel, M. Seboui, A. Bauer, L. Choubrac, L. Arzel, S. Harel, N. Barreau, E. Ahlswede, Evaluation of different buffer materials for solar cells with wide-gap $Cu_2ZnGeS_xSe_{4-x}$ absorbers, RSC Adv. 7 (2017) 40105–40110. https://doi.org/10.1039/C7RA06438A.
[228] A. Ruiz-Perona, G. Gurieva, M. Sun, T. Kodalle, Y. Sánchez, M. Grossberg, J.M. Merino, S. Schorr, M. León, R. Caballero, Routes to develop a [S]/([S]+[Se]) gradient in wide band-gap Cu2ZnGe(S,Se)4 thin-film solar cells, Journal of Alloys and Compounds 868 (2021) 159253. https://doi.org/10.1016/j.jallcom.2021.159253.
[229] F. Liu, J. Huang, K. Sun, C. Yan, Y. Shen, J. Park, A. Pu, F. Zhou, X. Liu, J.A. Stride, M.A. Green, X. Hao, Beyond 8% ultrathin kesterite Cu2ZnSnS4 solar cells by interface reaction route controlling and self-organized nanopattern at the back contact, NPG Asia Mater 9 (2017) e401–e401. https://doi.org/10.1038/am.2017.103.
[230] M. Neuwirth, T. Kohl, G. Brammertz, J.D. Wild, M. Meuris, J. Poortmans, B. Vermang, H. Kalt, M. Hetterich, Selenium and Sulphur replacement dynamics in CZTSSe and CZGSSe kesterite materials, in: 2018 IEEE 7th World Conference on Photovoltaic Energy Conversion (WCPEC) (A Joint Conference of 45th IEEE PVSC, 28th PVSEC & 34th EU PVSEC), IEEE, Waikoloa Village, HI, 2018: pp. 0160–0162. https://doi.org/10.1109/PVSC.2018.8548130.
[231] S. Chen, A. Walsh, J.-H. Yang, X.G. Gong, L. Sun, P.-X. Yang, J.-H. Chu, S.-H. Wei, Compositional dependence of structural and electronic properties of Cu 2 ZnSn(S,Se) 4 alloys for thin film solar cells, Phys. Rev. B 83 (2011) 125201. https://doi.org/10.1103/PhysRevB.83.125201.
[232] S.K. Wallace, D.B. Mitzi, A. Walsh, The Steady Rise of Kesterite Solar Cells, ACS Energy Lett. 2 (2017) 776–779. https://doi.org/10.1021/acsenergylett.7b00131.
[233] L. Yin, G. Cheng, Y. Feng, Z. Li, C. Yang, X. Xiao, Limitation factors for the performance of kesterite Cu_2ZnSnS_4 thin film solar cells studied by defect characterization, RSC Adv. 5 (2015) 40369–40374. https://doi.org/10.1039/C5RA00069F.
[234] B. Duan, L. Lou, F. Meng, J. Zhou, J. Wang, J. Shi, H. Wu, Y. Luo, D. Li, Q. Meng, Two-Step Annealing CZTSSe/CdS Heterojunction to Improve Interface Properties of Kesterite Solar Cells, ACS Appl. Mater. Interfaces 13 (2021) 55243–55253. https://doi.org/10.1021/acsami.1c18152.
[235] V. Kumar, U.P. Singh, Optimization of annealing temperature on the formation CZTSe absorber layer, Appl. Phys. A 129 (2023) 414. https://doi.org/10.1007/s00339-023-06694-y.
[236] Y. Mi, Y. Yang, G. Cui, J. Ren, Y. Liu, X. Zhao, X. Tian, T. Bao, Y. Wang, S. Li, C. Zhu, Exploring the optimal two-step selenization process to enhance the performance of ionic

liquid solution based Cu2ZnSn(S,Se)4 thin film solar cells, Journal of Alloys and Compounds 909 (2022) 164740. https://doi.org/10.1016/j.jallcom.2022.164740.
[237] L.S. Brooks, The Vapor Pressures of Tellurium and Selenium, J. Am. Chem. Soc. 74 (1952) 227–229. https://doi.org/10.1021/ja01121a059.
[238] A.K. Singh, G. Aggarwal, R.K. Singh, T.R. Klein, C. Das, M. Neergat, B. Kavaipatti, M.F.A.M. Van Hest, Synthesis of CZTS/Se and Their Solid Solution from Electrodeposited Cu–Sn–Zn Metal Precursor: A Study of S and Se Replacement Reaction, ACS Appl. Energy Mater. 1 (2018) 3351–3358. https://doi.org/10.1021/acsaem.8b00527.
[239] J. Yu, H. Deng, Q. Zhang, J. Tao, L. Sun, P. Yang, J. Chu, The role of tuning Se/(S + Se) ratio in the improvement of Cu2MnSn(S, Se)4 thin films properties and photovoltaic device performance, Solar Energy 179 (2019) 279–285. https://doi.org/10.1016/j.solener.2018.12.076.
[240] A. Fairbrother, V. Izquierdo-Roca, X. Fontané, M. Ibáñez, A. Cabot, E. Saucedo, A. Pérez-Rodríguez, ZnS grain size effects on near-resonant Raman scattering: optical non-destructive grain size estimation, CrystEngComm 16 (2014) 4120. https://doi.org/10.1039/c3ce42578a.
[241] J. Andrade-Arvizu, R.F. Rubio, V. Izquierdo-Roca, I. Becerril-Romero, D. Sylla, P. Vidal-Fuentes, Z.J. Li-Kao, A. Thomere, S. Giraldo, K. Tiwari, S. Resalati, M. Guc, M. Placidi, Controlling the Anionic Ratio and Gradient in Kesterite Technology, ACS Appl. Mater. Interfaces 14 (2022) 1177–1186. https://doi.org/10.1021/acsami.1c21507.
[242] D. Palma-Lafuente, P. Diez-Silva, V. Rotaru, T. Jawhari, T. Bertram, P. Reyes-Figueroa, M. Guc, J.M. Merino, R. Caballero, Sulfurization of co-evaporated Cu2ZnGeSe4 layers: Influence of the precursor cation's ratios on the properties of Cu2ZnGe(S,Se)4 thin films, Solar Energy Materials and Solar Cells 254 (2023) 112243. https://doi.org/10.1016/j.solmat.2023.112243.
[243] P.M. Keane, Y. -J. Lu, J.A. Ibers, ChemInform Abstract: Copper-Containing Group IV and Group V Chalcogenides, ChemInform 22 (1991) chin.199148289. https://doi.org/10.1002/chin.199148289.
[244] M. Dimitrievska, H. Xie, A.J. Jackson, X. Fontané, M. Espíndola-Rodríguez, E. Saucedo, A. Pérez-Rodríguez, A. Walsh, V. Izquierdo-Roca, Resonant Raman scattering of ZnS_xSe_{1-x} solid solutions: the role of S and Se electronic states, Phys. Chem. Chem. Phys. 18 (2016) 7632–7640. https://doi.org/10.1039/C5CP04498G.